PLASMA-ASSISTED MOLECULAR BEAM EPITAXY OF (11-22)-ORIENTED III-NITRIDES

Lise Lahourcade

INSTITUT POLYTECHNIQUE DE GRENOBLE

N° attribué par la bibliothèque
|_|_|_|_|_|_|_|_|_|_|

THESE

pour obtenir le grade de

DOCTEUR DE L'Institut Polytechnique de Grenoble

Spécialité : "Optique et radio fréquences"

préparée au sein du laboratoire

Equipe mixte CEA - CNRS "Nanophysique et semiconducteurs", CEA-Grenoble, INAC/SP2M

dans le cadre de l'**Ecole Doctorale**

"Electronique, Electrotechnique, Automatique, Traitement du signal"

présentée et soutenue publiquement

par

Lise LAHOURCADE

le 6 Octobre 2009

PLASMA-ASSISTED MOLECULAR BEAM EPITAXY OF (11$\bar{2}$2)-ORIENTED III-NITRIDES

DIRECTEUR DE THESE : Eva MONROY

JURY

Mme Anne PONCHET	Rapporteur
Mr Henning RIECHERT	Rapporteur
Mme Eva MONROY	Directrice de thèse
Mr. Daniel BELLET	Président du jury
Mr. François H. JULIEN	Examinateur
Mr. Pierre PETROFF	Examinateur
Mr. Pierre RUTERANA	Examinateur

Avant de rentrer dans le vif du sujet, il convient de remercier les personnes ayant contribué, de quelque manière que ce soit, à l'aboutissement de ce projet. Ce chapitre est à la fois le plus court mais aussi celui qui m'a demandé le plus de temps, j'espère ainsi n'oublier personne.

MERCI…

… à Jean-Michel Gérard et Henri Mariette, respectivement chefs de service et de laboratoire, pour m'avoir accueillie au CEA, et permis de travailler au sein de l'équipe mixte NPSC « Nanophysique et Semiconducteurs ».

… aux membres du jury : un grand merci à Anne Ponchet et Henning Riechert pour avoir rapporté ce travail, et pour les discussions constructives que nous avons pu avoir. Merci aussi à François Julien, Pierre Ruterana, Pierre Petroff et bien sûr Daniel Bellet, qui a accepté de présider le jury. Daniel, je tiens également à te remercier pour ton cours de photovoltaïque (ma nouvelle voie ?), ainsi que pour le temps que tu as su trouver pour discuter avenir et autres. Cependant, le jury ne serait pas complet sans ...

… Eva, mon membre de jury préféré :-) C'est grâce à toi que tout à commencé, il y a bientôt 4 ans. Un immense merci pour ta disponibilité et tes encouragements, mais aussi pour m'avoir offert la possibilité d'assister à de nombreuses conférences. Tu m'as montré que notre machine, certes beaucoup plus grosse que nous, pouvait être apprivoisée et je te remercie pour la confiance que tu m'as rapidement accordée.

… Yoann : impossible de parler de la machine sans mentionner ton aide précieuse au quotidien. Tu m'as appris les dessous de la MBE lors des multiples ouvertures qui, aussi improbable que ça puisse paraître, me manquaient déjà en période de rédaction. Je te remercie pour ta patience et ta disponibilité, et pour la créativité et l'enthousiasme qui te caractérisent et te donnent envie de toujours améliorer notre outil de travail. Je n'oublierai pas ici Yann et Jean, qui se sont montrés disponibles et efficaces plus d'une fois pour détecter et réparer les pannes. Ainsi, quand le bâti était en forme, j'ai eu la chance de faire pousser des hexagones penchés comme vous pourrez le lire dans la suite. Hors, pas de substrat = pas d'échantillon, donc je remercie vivement Marlène pour les multiples découpes et pour m'avoir formée.

… à tous ceux, ici ou ailleurs, qui ont permis la caractérisation des échantillons, sans quoi l'épitaxieur ne pourrait progresser :

Commençons par ceux qui étaient loin. ευχαριστώ πολύ *à l'équipe de Philomela Komninou, et notamment à George, pour leurs études TEM très approfondies au coeur du projet DOTSENSE. Aux équipes de Pierre Ruterana et de François Julien (cités plus haut), pour leurs travaux de TEM et d'optique intersoubande, respectivement : vous n'avez pas attendu COSNI pour vous intéresser à mes échantillons et je vous en suis très reconnaissante. Merci beaucoup à Julien Pernot qui m'a non seulement prêté sa manip d'effet Hall, mais qui s'est réellement investi dans l'interprétation des résultats. Mesures qui n'auraient pas été possibles sans l'aide de Louis, le pro de la microsoudure !*

On arrive maintenant au 3ème étage où se cachent les salles d'AFM et XRD. Merci à Cyrille Beigné et Lucien Notin qui m'ont donné la possibilité de passer de longues journées devant l'AFM, à suivre les déplacements nanométriques de la pointe... Heureusement, j'ai eu la chance de partager quelques unes de ces longues journées avec Benoît Amstatt : je te remercie pour tes explications et toutes les discussions que nous avons eu sur nos sujets quelque peu similaires. J'adresse de vifs remerciements à Edith Bellet-Amalric qui a tout fait pour que je puisse utiliser de façon autonome le diffractomètre X. Un grand merci à Benoît (oui, encore !) et Stéphanie Pouget pour leurs conseils et les échanges toujours fructueux.

*Retour au 4ème étage, pour citer les gens de l'équipe qui ont participé de près à ce travail de thèse. Un immense merci à Julien R., Bruno G. et Joël B. pour avoir réservé des créneaux non négligeables à l'analyse optique de mes échantillons. Je vous remercie tous les trois pour votre disponibilité, et pour le soin que vous avez porté à m'expliquer en détail vos manips ainsi que dans l'interprétation des résultats. Enfin, et en vrac, merci aussi à Sirona pour la PL, Prem pour les manips à Paris et next**nano**^{3}, Sylvain pour les simul et bien sûr Fab pour le HF !*

… à tous ceux, ici ou ailleurs, qui ont rendu ces trois années très agréables, sans quoi l'épitaxieur ne pourrait progresser :

Je tiens à remercier tous les membres de l'équipe pour l'ambiance qui règne au 4ème. A commencer par les « anciens », que je n'ai pas connu longtemps au labo, mais qui m'ont donné envie de rester : je pense notamment à Fabian, Spider-Sébastien, Laurent le cuisinier hors-pair, Yoanna, Rita ou l'éternelle joie de vivre, l'incroyable Momo, Benoît (toujours le même) et bien sûr notre coach musical Fab. Un immense merci aux habitués du café de 11h, toujours en forme, pour discuter ouverture et recherche de fuites, bien sûr... La liste est longue, mais je vais tenter d'oublier personne : Bruno expert homogénéisation du café, Catherine, Gabriel, Henri, Hervé, Julien^2, Joël, Maëlla, Marion, Marlène, Olivier, Périne, Régis, Vincent, Yann, Yoann. N'oubliez pas de continuer la déco « mains » !

Plus personnellement, je suis très heureuse d'avoir partager les bureaux de Yoann et Julien, ce qui m'a permis de mieux les connaître. Aux hommes à barbe qui rodent dans les couloirs, Régis et Joël : vous avez pris le temps de me soutenir et m'encourager en trouvant toujours les mots justes, un immense merci !!! Enfin, Henri, je te remercie très sincèrement pour ta présence et ta disponibilité, ici ou ailleurs.

Je désire maintenant consacrer quelques lignes à mes proches, amis et famille, qui ont ont été présents ces dernières années, que ce soit à Grenoble, en weekends ou en vacances, sur des skis, dans un kayak ou au pied des voies et souvent autour d'un (bon) p'tit plat. Il y a bien sûr les Grenoblois – et je pense surtout à Bab's, Benji, Caro, Claire, Clément, Elodie, Fab, Guillaume, Julien, Laurent, Louis, Manu, Maxime^2, Morgan, Nico, Pascal, Périne, Pierre, Sophie, Thomas – mais aussi ceux qui étaient déjà là avant et qui sont restés présents même en étant parfois très loin : Mathilde, Julie, Mimi, Dany, ma Cot' et bien sûr Sandrine. Un immense merci à vous tous pour les innombrables discussions, souvent très constructives, et simplement tous ces bons moments. Je remercie plus particulièrement Thoms et Elodie, mes « colocs » : merci d'avoir été là pour m'aider dans les moments de doute mais aussi pour partager les plus beaux !

Cette dernière partie s'adresse à ma famille qui m'a soutenue durant 3 ans. Je vous remercie d'avoir été présents le jour de la soutenance, avec vos petits messages ou en me faisant la surprise d'être là ! Je suis heureuse que vous ayez pu découvrir « ma » région pendant ces quelques jours et surtout lors d'un Noël magnifique sous la neige !!! Je souhaite notamment remercier mes grand-parents, pour l'intérêt qu'ils portent à leurs petits-enfants mais aussi pour leur dynamisme. Enfin, mes plus sincères remerciements s'adressent à mon frère – merci Matthieu d'avoir toujours pris autant soin de moi... et Aurélie de t'occuper de lui maintenant qu'on est loin les uns des autres – ainsi qu'à mes parents : merci pour tout ce que vous avez fait pour nous et notamment pour nous avoir toujours encouragés dans nos choix et ainsi nous avoir permis de faire ce qu'on aime dans la vie.

Résumé

Etant donné que cette thèse est intégralement rédigée en anglais, vous trouverez ici un résumé en français des différents chapitres qui la composent. La structure de ce résumé est donc la même que celle du manuscrit, avec, premièrement, une introduction générale, puis l'exposé des différents résultats selon l'ordre chronologique des chapitres, pour finir par les conclusions et perspectives du travail de thèse.

Introduction

Les semiconducteurs nitrures du groupe III (AlN, GaN, InN et leurs alliages) ont connu un développement considérable depuis les vingt dernières années, en raison de leur fort potentiel en termes d'applications. En effet, ces matériaux à bande interdite directe, donc particulièrement adaptés au domaine de l'optoélectronique, couvrent une large gamme du spectre énergétique, allant de 0.8 eV (infrarouge) pour l'InN jusqu'à 6.2 eV (ultraviolet) pour l'AlN.

Aujourd'hui des diodes blanches électroluminescentes (LEDs pour Light Emitting Diodes) à base de nitrures sont largement commercialisées et implantées, par exemple, dans des lampes torches ou lampes frontales. Leur consommation est plus de deux fois inférieure à celle des lampes fluorescentes ou à incandescence, et leur durée de vie plus que doublée. C'est pourquoi certains constructeurs automobiles commencent à intégrer de tels composants dans les phares de leurs véhicules. De plus, les LEDs colorées à base de nitrures ont envahit notre quotidien, des écrans de télévision ou de téléphones portables, aux feux verts de signalisation, en passant par les affichages publicitaires. Dans un contexte socio-économique où le réchauffement climatique et la surconsommation énergétique sont devenus une préoccupation quotidienne, les diodes sont de plus en plus prisées, et on peut notamment espérer que les diodes blanches devraient rapidement trouver leur place en matière d'éclairage public.

Une autre application phare des matériaux nitrures se trouve dans la fabrication de diodes laser bleues (LDs pour Laser Diodes). Les LDs bleues ont remplacé les LDs rouges à base d'arséniures utilisées dans les années 80 pour graver les CDs. La capacité de stockage d'un CD va dépendre de la taille des domaines contenant l'information, donc de la longueur d'onde du faisceau laser utilisé. On est ainsi passé des longueurs d'ondes de gravure avoisinant les 700 nm (laser arséniures) pour des

CDs de 700 Mo de mémoire à des longueurs d'ondes de l'ordre de 400 nm permettant de stocker jusqu'à 50 Go avec la technologie "blue-ray".

Enfin, on peut aussi mentionner l'utilisation de diodes UV nitrures en tant que capteurs pour la médecine ou la biologie, ainsi que le nombre grandissant de composants électroniques haute fréquence pouvant fonctionner à haute puissance, et haute température, grâce à la robustesse des matériaux.

Néanmoins, des limites persistent dans le développement de la technologie nitrure. En effet, les structures synthétisées selon la direction de croissance polaire (0001) [également appelée c] présentent un champ électrique interne qui peut atteindre les 10 MV/cm. Ce champ électrique géant induit une modification des propriétés optiques des zones actives : un décalage de l'émission vers le rouge et une réduction de l'efficacité radiative. Même si les composants nitrures commercialisés sont orientés selon c, il est aujourd'hui important aux yeux de la communauté scientifique de s'affranchir de ce champ électrique, ou du moins le réduire.

Dans ce contexte, mon travail a porté sur l'analyse des modes de croissance de l'AlN et du GaN orientés $(11\bar{2}2)$ dans le but de réaliser des hétérostructures (puits et boîtes quantiques). Les propriétés structurales et optiques ont été analysées, et comparées à celles d'échantillons polaires. De plus, dans le but de sonder le potentiel de l'orientation semipolaire en termes d'applications optoélectroniques (type LEDs ou LDs), une partie de ce travail a été dédiée à l'étude du dopage p et n de couches de GaN, ainsi qu'à la réalisation de zones actives à puits et boîtes quantiques. L'étude des performances optiques de ces structures a montré une forte réduction du champ électrique interne et, par conséquence, les effets qui en résultent.

Durant ma thèse, j'ai ainsi réalisé des échantillons par épitaxie par jets moléculaires assistée par plasma d'azote (PAMBE, pour Plasma-Assisted Molecular Beam Epitaxy). Ces échantillons type couches ou hétérostructures quantiques, ont été caractérisés structuralement *in situ*, via la technique de diffraction d'électrons de haute énergie en incidence rasante (RHEED pour Reflection High Energy Electron Diffraction), et *ex situ*, par diffraction des rayons (XRD, pour X-Ray Diffraction) et microscopie à force atomique (AFM, pour Atomic Force Microscopy). Les études optiques ont été réalisées par photoluminescence intégrée en temps et résolue en temps. En complément, la structure atomique des couches a été étudiée par microscopie électronique en transmission (TEM, pour Transmission Electron Microscopy) par nos collaborateurs du laboratoire CIMAP - CNRS (Caen, France) sous la direction de P. Ruterana et par nos collaborateurs de AUTH (Thessaloniki, Grèce) sous la direction de P. Komninou. Enfin, des mesures d'optique complémentaires ont été réalisées à l'université de Paris-Sud sous la direction de F. H. Julien dans le but de sonder les transitions inter-sous-bandes.

Chapitre 1 : Propriétés des matériaux nitrures du groupe III

Ce chapitre est une introduction aux propriétés des semiconducteurs nitrures du groupe III, *i.e.* GaN, AlN, InN et leurs alliages $Al_xGa_{1-x}N$ et $In_xGa_{1-x}N$. Après avoir décrit les deux principales phases dans lesquelles ils peuvent cristalliser (wurtzite et zinc blende), nous nous intéresserons plus particulièrement aux caractéristiques structurales, électroniques et élastiques de la phase wurtzite. Les différents plans cristallographiques mentionnés tout au long du manuscrit seront notamment présentés dans ce chapitre.

Chapitre 2 : Techniques expérimentales

Ce chapitre se veut être une référence pour les principales expériences décrites dans les chapitres suivants. Dans un premier temps, nous définirons les phénomènes physiques mis en jeu lors du dépôt épitaxial d'un matériau. Les atouts de l'épitaxie par jets moléculaires (EJM), en comparaison aux techniques de dépôt en phase vapeur (CVD, pour Chemical Vapor Deposition), seront exposés. Une attention particulière portera sur la technique de suivi *in situ* de la croissance qu'est le RHEED. Enfin, étant donné que la totalité de ce travail a consisté en des dépôts d'un matériau sur une couche d'un matériau différent (hétéroépitaxie), nous rappellerons les différents modes de croissances possibles, les concepts de relaxation de contraintes et les types de dislocations rencontrés dans les matériaux nitrures. Dans le cas de la croissance par EJM de GaN et AlN, nous discuterons de l'importance de l'orientation cristalline dans la détermination des modes de croissance bidimensionnels et tridimensionnels.

La deuxième partie de ce chapitre est dédiée à la description des principaux équipements utilisés dans ce travail. Ainsi, une description exhaustive du bâti d'EJM qui a servi à la croissance des échantillons sera suivie, de l'explication des techniques de diffraction des rayons X, microscopie à force atomique, photoluminescence (PL) et photoluminescence résolue en temps (TRPL, pour Time-Resolved Photoluminescence). En particulier, la technique de diffraction des rayons X sera détaillée dans le cas de l'étude des matériaux semipolaires. Enfin, nous donnerons les éléments de simulations utilisés pour calculer les structures de bandes des hétérostructures.

Chapitre 3 : Analyse de couches d'AlN($11\bar{2}2$) déposées sur saphir *m*

Dans les hétérostructures à puits ou boîtes quantiques, le GaN (petit gap) constitue le puits ou la boîte et l'AlN (grand gap) sert de barrière. Il est donc nécessaire de contrôler la croissance bidimensionnelle de l'AlN. Dans le cas de la croissance par PAMBE d'AlN polaire ou nonpolaire, la morphologie de surface des couches dépend fortement du rapport III/V utilisé. En particulier dans le cas de l'AlN(0001), des couches bidimensionnelles sont obtenues dans des conditions riches Al. La situation est équivalente pour la croissance de l'AlN plan *m* [orienté $(1\bar{1}00)$], alors que des conditions riches N sont nécessaires pour la croissance de l'AlN plan *a* [orienté $(11\bar{2}0)$]. On comprend ici l'intérêt que l'on devra porter à la croissance de l'AlN($11\bar{2}2$). Une partie des travaux présentés dans ce chapitre a fait l'objet d'une publication [Lah07].

Dans ce chapitre, nous présenterons les modes de croissance de l'AlN sur le saphir *m*, et nous étudierons les propriétés structurales des couches déposées. Dans un premier temps, il sera démontré qu'il est possible d'isoler la phase cristallographique $(11\bar{2}2)$ de l'AlN des phases parasites $(10\bar{1}0)$ et $(10\bar{1}3)$. Nous nous intéresserons en particulier aux conséquences de la nitruration du substrat avant la croissance. En effet, la croissance de l'orientation nonpolaire $(10\bar{1}0)$ semble favorisée par cette étape. En supprimant la nitruration, en utilisant un rapport de flux Al/N adéquat (aux alentours de 0.95) et en suivant un processus particulier il est possible de limiter la propagation de domaines nonpolaires aux premiers 50 nm, et ainsi d'homogénéiser la couche alors orientée $(11\bar{2}2)$. Dans ces conditions, nous avons observé la relaxation des couches après environ 150 nm de croissance, et mesuré des rugosités de surfaces relativement faibles (RMS $\approx$ 2 nm pour 200 nm d'épaisseur) si on considère la forte anisotropie de contraintes dans les couches. Une caractéristique importante des couches est la présence d'une désorientation de la couche par rapport au substrat, dans la direction $<11\bar{2}\bar{3}>_{AlN}$.

L'analyse des relations d'épitaxie entre la couche et le substrat a été réalisée à partir de données de diffraction X et confirmée par les études TEM. Nous remarquerons que les domaines d'AlN plan *m* sont désorientés dans le plan de 90° par rapport au saphir plan *m*, *i.e.* $[0001]_{AlN}$ // $[\bar{1}\bar{1}20]_{saphir}$ et $[\bar{1}\bar{1}20]_{AlN}$ // $[0001]_{saphir}$. L'AlN semipolaire orienté $(11\bar{2}2)$ présente aussi une bonne interface épitaxiale avec le saphir, et son orientation dans le plan est donnée par les relations: $[1\bar{1}00]_{AlN}$ // $[\bar{1}\bar{1}20]_{saphir}$ et $[\bar{1}\bar{1}23]_{AlN}$ // $[0001]_{saphir}$. Enfin, nous avons pu observer sur les premières images prises à l'interface entre les deux domaines [AlN($11\bar{2}2$) et AlN($10\bar{1}0$)] que la jonction est de qualité, avec l'alignement parfait entre les plans $(0002)_{semipolaire}$ et $(01\bar{1}0)_{nonpolaire}$ et les plans $(\bar{1}100)_{semipolaire}$ et $(0002)_{nonpolaire}$.

Ce chapitre a aussi pour but de poser les bases de l'utilisation de la technique RHEED pour cette orientation particulière. En effet, les images que l'on peut ob-

server pendant la croissance sont complètement différentes de celles des orientations polaires et nonpolaires, notamment car elles présentent peu d'éléments de symétrie. Ainsi, nous proposons ici une explication des figures de diffraction, dans le but de différencier, en particulier, les azimuts $<1\bar{1}00>$ et $<11\bar{2}\bar{3}>$ de l'AlN. Grâce à cette analyse, il est maintenant possible de suivre l'évolution des paramètres de mailles lors de la croissance.

Chapitre 4 : Etude du GaN(11$\bar{2}$2)

Dans ce quatrième chapitre, nous présenterons la croissance de couches bidimensionnelles de GaN(11$\bar{2}$2), ainsi que leurs propriétés structurales et optiques. Pour cela, des couches de GaN non dopé, mais également des couches dopées n ou p on été réalisées. Une partie des travaux exposés a été publiée dans [Lah08b].

Dans la première partie, je me focaliserai sur l'étude des modes de croissance du GaN semipolaire, en fonction du rapport de flux Ga/N et en considérant son dépôt directement sur saphir ou sur une couche tampon d'AlN(11$\bar{2}$2). En effet, nous avons pu observer que la croissance sur le substrat saphir plan m amène la formation de domaines semipolaires orientés (10$\bar{1}$3), même dans des conditions optimales de croissance 2D, en régime riche Ga. Nous avons donc montré que la seule façon de s'affranchir de ces domaines parasites est de déposer le GaN sur une couche d'AlN orientée (11$\bar{2}$2). Ainsi, la couche de GaN croît de façon épitaxiale sur l'AlN, *i.e.* en gardant la même orientation (11$\bar{2}$2).

Comme indiqué précédemment, la croissance du GaN(11$\bar{2}$2) est bidimensionnelle si réalisée dans des conditions riche Ga, tridimensionnelle dans des conditions riche N. Dans le but de déterminer les différents régimes de croissance dans les conditions d'excès de Ga, nous avons étudié le mouillage du Ga sur la surface du GaN(11$\bar{2}$2). Le maximum de couverture de Ga qui peut être atteint équivaut à une monocouche d'atomes de Ga orientés selon les plans (11$\bar{2}$2). En comparant avec les taux de couverture sur le GaN(0001), on s'aperçoit que le régime d'accumulation de Ga est atteint pour des flux de gallium plus faibles dans le cas semipolaire que dans le cas polaire. Il est cependant à noter qu'une monocouche orientée (11$\bar{2}$2) est constituée d'atomes arrangés sur deux niveaux selon l'axe de croissance, formant donc une pseudo-bicouche, de la même façon que pour la croissance de GaN(0001) ou GaN(1$\bar{1}$00).

Grâce à l'étude de la cinétique de croissance et à l'analyse de la structure de couches réalisées dans différentes conditions, nous avons établi les quatre différents régimes de croissance du GaN(11$\bar{2}$2):

- Pour III/V $\leq$ 1 (Conditions riche N et à la stoechiométrie), la croissance est tridimensionnelle.
- Pour un excès de Ga inférieur à une monocouche, la croissance est bidimensionnelle, mais les couches de GaN sont rugueuses, et présentent quelques inclusions de GaN(10$\bar{1}$3) dans la matrice de GaN(11$\bar{2}$2).
- Pour un excès de Ga d'une monocouche, la croissance est stabilisée dynamiquement par la couche de mouillage, ce qui conduit à la formation de couches 2D présentant une très faible rugosité de surface.
- Pour un excès de Ga supérieur à une monocouche, on entre dans le régime d'accumulation avec la formation de gouttes de Ga en surface. La surface du

GaN n'étant plus stable pendant la croissance, sa morphologie se dégrade avec l'épaisseur

L'étude de couches de GaN synthétisées dans les conditions optimales de croissance (une monocouche d'excès de Ga) a permis de déterminer la densité de fautes d'empilement dans les couches (environ 3×10^{15} cm^{-1}) ce qui est du même ordre de grandeur que les valeurs trouvées dans la littérature pour des couches réalisées par MOVPE. La photoluminescence des couches est également prometteuse, dominée par la luminescence du bord de bande, et, surtout, sans la luminescence de la bande jaune liée aux défauts que l'on trouve normalement dans les couches de GaN polaires.

L'introduction d'atomes de Si dans la matrice ne modifie pas la cinétique de croissance du GaN(11$\bar{2}$2). En effet, il est possible de stabiliser une monocouche de Ga pendant la croissance, et le régime d'accumulation est atteint pour des flux de Ga équivalents à ceux nécessaires pour la croissance du GaN(0001). Dans les conditions de croissance optimales, nous avons donc pu réaliser des couches épaisses et vérifier l'incorporation des atomes de Si jusqu'à 6×10^{19} cm^{-3} environ.

Comme pour le GaN(0001), l'introduction d'atomes de Mg modifie de manière drastique la croissance du GaN(11$\bar{2}$2), par l'inhibition de la formation de la couche de mouillage. Ainsi, le régime d'accumulation est atteint pour des flux plus faibles que dans le cas de couches non dopées ou dopées Si. Cette modification de la stabilité de la surface pendant la croissance entraîne une modification de morphologie de surface. En effet, sur les échantillons dopés Mg, on observe des sillons perpendiculaires à la direction <11$\bar{2}\bar{3}$>, alors que l'anisotropie de surface des échantillons non dopés ou dopés Si est orientée selon <11$\bar{2}\bar{3}$>. Cependant, les échantillons dopés Mg réalisés à basse température présentent la même anisotropie de surface que pour les couches non dopées.

Des études par SIMS (pour Secondary Ion Mass Scattering) nous ont permis de vérifier l'incorporation homogène du magnésium jusqu'à des concentrations de l'ordre de 10^{20} cm^{-3}. La variation de la quantité de Mg incorporée en fonction des conditions de croissance (température du substrat, flux de Mg) nous a permis de calculer une énergie d'activation de 0.69 eV correspondant à l'incorporation du Mg dans le GaN(11$\bar{2}$2). Cette valeur, très inférieure à celles communément trouvées pour le GaN plan *c*, semble indiquer que l'incorporation du magnésium est plus facile dans le GaN semipolaire que dans le GaN polaire. Les études de TEM n'ont pas révélé la présence des défauts typiques des couches contenant du Mg, à savoir des défauts pyramidaux, ou des domaines d'inversion de polarité. Enfin, les études optiques de couches dopées Mg indiquent que la luminescence est dominée par les transitions DAP (paires donneurs-accepteurs), qui fait intervenir la bande de trous légers du Mg.

Des mesures d'effet Hall ont été réalisées dans le but de déterminer les propriétés électriques de couches épaisses, et d'en vérifier le caractère *p*. Si on compare

l'activation à température ambiance (rapport entre la concentration de trous mesurée par effet Hall et la quantité d'atomes de Mg mesurée par SIMS), on constate une très forte dégradation des performances électriques des couches synthétisées à basse température. *A contrario*, les couches réalisées à hautes températures présentent une énergie d'activation de l'ordre de 4%. Cette valeur élevée et la très forte incorporation d'atomes de Mg constituent un résultat encourageant, notamment quand on connaît les difficultés technologiques associées au dopage Mg des couches de GaN(0001).

Chapitre 5 : Puits quantiques GaN/AlN

Les conditions de croissance 2D maîtrisée pour l'AlN et le GaN ont pu être appliquées à la croissance de puits quantiques de GaN dans AlN. Ce chapitre présente donc les propriétés de ces hétérostructures orientées $(11\bar{2}2)$. Une brève introduction explique les effets de la polarisation interne dans les heterostructures nitrures orientées (0001), et notamment l'origine du décalage de l'émission vers le rouge et de la réduction de l'efficacité radiative. Les travaux exposés dans la suite du chapitre ont été publiés dans [Lah08b].

L'analyse par diffraction X, de même que les observations des couches par TEM, atteste de la bonne qualité des structures, notamment en termes de périodicité. En effet, le contrôle de la croissance 2D nous permet d'obtenir des interfaces abruptes et sans interdiffusion entre le GaN et l'AlN, avec une rugosité d'interface de l'ordre de la monocouche.

Des séries d'échantillons équivalents ont été réalisées avec les orientations $(11\bar{2}2)$ et (0001), de façon à comparer les effets de polarisation interne. Les lignes de luminescence des échantillons polaires sont fortement décalées vers le rouge par rapport à l'émission des séries semipolaires. Ce décalage est d'autant plus important que le puits est large, alors que, au contraire, l'énergie d'émission semipolaire reste au dessus du gap du GaN. On peut conclure ici à une première indication de la réduction du champ électrique dans les structures semipolaires par rapport aux structures plan c. De plus, les mesures de PL résolue en temps donnent des temps de déclin aux alentours de 300 picosecondes pour les puits semipolaires, quand ils atteignent facilement la nanoseconde dans les structures polaires. Cela confirme donc la forte atténuation du champ électrique.

Grâce aux expériences menées à Paris, ce chapitre présente la première observation d'absorption inter-sous-bande dans des puits quantiques nitrures semipolaires. Dans le cas des transitions intra-bande, le champ électrique a tendance à éloigner les niveaux électroniques via la modification du profil de bandes. C'est en effet ce que l'on a pu observer, à savoir un décalage vers le bleu de l'absorption inter-sous-bande polaire par rapport à l'absorption semipolaire, ce qui constitue une preuve supplémentaire de la réduction du champ électrique dans les structures.

Des simulations de la structure électronique des différentes séries d'échantillons ont été réalisées dans le but de corroborer les résultats expérimentaux. On peut ainsi vérifier que l'allure triangulaire des puits polaires est accentuée avec la largeur du puits alors que les puits semipolaires présentent une structure de bande quasi carrée, et ce même pour les puits larges. En y regardant de plus près, cette particularité est due à la compensation de la polarisation spontanée par la polarisation piézoélectrique dans le cas semipolaire. Ayant un signe opposé, leur somme est proche de zéro. Un aspect intéressant également dû à cette compensation est la courbure de bande opposée des puits contraints sur AlN et GaN. En effet, étant donné que les

constantes piézoélectriques sont plus élevées dans AlN que dans GaN, la compensation de la polarisation spontanée est plus importante, ce qui conduit à un champ électrique négatif dans ce cas. La comparaison des simulations des séries polaires et semipolaires prévoit dans ce dernier cas une réduction du champ électrique d'un facteur supérieur à 10.

Chapitre 6 : Boîtes quantiques GaN/AlN

Dans ce chapitre, nous étudierons la croissance et les propriétés des boîtes quantiques semipolaires. Après avoir établi le procédé de croissance permettant l'élaboration des boîtes, leur structure ainsi que leurs caractéristiques optiques seront décrites. Une partie de ce chapitre a fait l'objet d'une publication [Lah09].

Dans un premier temps, la formation de boîtes quantiques a été observée lors du dépôt de quelques monocouches de GaN dans des conditions riches azote. Cependant, ces conditions conduisent à l'apparition, rédhibitoire, d'une deuxième phase cristalline orientée $10\bar{1}3$ qui se propage lors de l'encapsulation des boîtes par l'AlN. Ceci est cohérent avec le mode de croissance rugueux observé dans les conditions riches N et mis en évidence dans le chapitre 4.

Nous avons démontré que le dépôt de quelques monocouches de GaN dans des conditions riche Ga mais proches de la stoechiométrie conduisent à la formation d'une fine couche 2D et la transition 2D-3D est observée après un arrêt de croissance sous vide. La formation de boîtes quantiques est confirmée par l'apparition de réflexions additionnelles sur les images RHEED, dues à la formation des facettes des boîtes lorsqu'on laisse la surface évoluer sous vide.

Les images de TEM haute résolution confirment l'orientation $(11\bar{2}2)$ des boîtes. Cependant, on peut différencier deux familles : certaines boîtes reposent sur les plans $(11\bar{2}2)$ et d'autres sur les plans (1011) de l'AlN. Quel que soit leur plan de croissance, les boîtes s'alignent verticalement selon la direction (0001), *i.e.* avec un certain angle par rapport à la direction de croissance. Leur forme générale est une pyramide tronquée, présentant des interfaces chimiquement abruptes avec la couche d'AlN. Quand on les regarde selon l'azimut $<11\bar{2}\bar{3}>$, les boîtes présentent deux facettes symétriques orientées $(10\bar{1}1)$. Au contraire, elles sont asymétriques selon l'azimut $<\bar{1}100>$, l'une des facettes étant orientée $(11\bar{2}5)$, l'autre $(11\bar{2}0)$.

Des études de photoluminescence ont permis de sonder les propriétés optiques d'hétérostructures à boîtes quantiques. La comparaison de l'émission de super-réseaux à boîtes avec différentes quantités de GaN ne présente pas le décalage vers le rouge généralement observé dans les structures polaires : la luminescence reste au dessus du bandgap du GaN, même dans le cas de grosses boîtes. De plus, nous avons mesuré des temps de déclin courts comparés aux temps de déclin de structures polaires. Toutes ces caractéristiques confirment, au même titre que pour les puits quantiques, la confirmation du champ électrique interne et donc de l'effet Stark confiné dans les boîtes semipolaires.

Enfin, nous avons comparé l'évolution avec la température de l'intensité de luminescence et des temps de déclin pour des structures à boîtes et puits quantiques émettant à la même longueur d'onde. La stabilité dans le cas des boîtes confirme le plus grand confinement des porteurs et la réduction des recombinaisons radiatives dans les boîtes.

Conclusions

Les mécanismes de croissance de l'AlN et du GaN dépendent fortement de l'orientation cristalline. Chronologiquement, le manuscrit traite d'abord de l'AlN car il sert de couche tampon pour la croissance des échantillons, afin d'isoler l'orientation cristalline $(11\bar{2}2)$.

Les couches d'AlN déposées sur saphir m s'arrangent en deux types de domaines d'orientation différente, l'AlN$(11\bar{2}2)$ et l'AlN$(10\bar{1}0)$. L'un des principaux challenges de la croissance de l'AlN est l'isolation de l'orientation $(11\bar{2}2)$ des domaines $(10\bar{1}0)$, dont le ratio décroît en diminuant le rapport III/V. En ajustant le rapport Al/N autour de 0.95, et pour des couches d'épaisseur supérieure à 90 nm, il est possible d'isoler l'orientation semipolaire : des domaines non polaires sont détectés mais confinés à l'interface avec le substrat, car rapidement noyés dans la matrice d'AlN$(11\bar{2}2)$. Dans ces conditions, l'AlN a une croissance bidimensionnelle, et d'après les études par diffraction X et RHEED, les couches sont relaxées à partir de 260 nm. Il est à noter que ces conditions de croissance sont complètement différentes des conditions favorables à la croissance de couches 2D d'AlN(0001) qui nécessite un léger excès d'aluminium.

Les relations épitaxiales entre l'AlN et le saphir m ont été identifiées, dans le cas des phases nonpolaire et semipolaire: l'AlN$(10\bar{1}0)$ présente une rotation dans le plan de 90° par rapport au saphir, de sorte que $[0001]_{AlN}$ // $[\bar{1}\bar{1}20]_{saphir}$. Pour l'AlN$(11\bar{2}2)$ on a pu montrer que $[1\bar{1}00]_{AlN}$ // $\bar{1}\bar{1}20]_{saphir}$ et $[\bar{1}\bar{1}23]_{AlN}$ // $[0001]_{saphir}$. Les images de l'interface entre les deux orientations ont permis d'observer les très bonnes relations épitaxiales entre elles, à savoir l'alignement des plans selon : $(0002)_{semipolaire}$ // $(01\bar{1}0)_{nonpolaire}$ et $(0002)_{nonpolaire}$ // $(\bar{1}100)_{semipolaire}$.

La croissance du GaN directement sur saphir m conduit à la formation de précipités orientés $\{10\bar{1}3\}$ à l'intérieur d'une matrice de GaN$(11\bar{2}2)$. Cependant, le dépôt d'une couche tampon d'AlN$(11\bar{2}2)$ sur saphir avant la croissance du GaN permet de réduire la quantité de précipités. Le GaN$(11\bar{2}2)$ ainsi synthétisé présente les mêmes relations épitaxiales que celles énoncées ci-dessus. Pour ce qui est de l'effet du rapport Ga/N, la croissance riche N est tridimensionnelle, alors que les conditions riche Ga aident à lisser la surface. L'étude du mouillage du Ga sur la surface GaN$(11\bar{2}2)$ a permis de déterminer que la quantité maximale de Ga qui peut être stabiliser en croissance correspond à une monocouche d'atomes de Ga orientée selon le plan $(11\bar{2}2)$. Il est intéressant de noter que l'arrangement des atomes sur cette monocouche forme une pseudo-bicouche (atomes sur deux niveaux le long de l'axe de croissance), comparable à la bicouche observée lors de la croissance de GaN(0001) ou GaN$(1\bar{1}00)$. Les couches de GaN synthétisées avec un excès de Ga assez élevé pour atteindre ce régime stable, mais pas trop élevé pour éviter l'accumulation de Ga, présentent une très bonne morphologie de surface (rugosité RMS inférieure à 1.5 nm). L'étude de la photoluminescence nous a permis d'attribuer l'émission principale des couches à des transitions d'excitons liés à des fautes d'empilement,

fautes d'empilement présentes à hauteur d'environ 3×10^5 cm^{-1}.

Le dopage Si n'affecte pas la cinétique de croissance du GaN, ni ses propriétés structurales. Au contraire, le dopage Mg inhibe la formation de la monocouche de Ga pendant la croissance, de sorte que le régime d'accumulation de Ga est atteint à des flux de Ga inférieurs à ceux du GaN non dopé. En conséquence, la morphologie de surface du GaN:Mg est altérée, même si, en volume, il n'y a aucune trace de domaines d'inversion ou d'inclusions cubiques, que l'on trouve typiquement dans les couches de GaN(0001) dopées Mg. En variant la température de croissance et le flux de Mg, nous avons synthétisé des couches dans lesquelles l'incorporation d'atomes de Mg est homogène jusqu'à environ 10^{20} cm^{-3}, et démontré que l'orientation semipolaire favorise l'incorporation de Mg par rapport au GaN(0001). A température ambiante, l'activation des dopants est de l'ordre de 4%, avec des concentrations de trous allant jusqu'à 10^{18} cm^{-3}.

Des hétérostructures à puits quantiques ont été fabriquées, en appliquant les conditions de croissance de l'AlN et du GaN bidimensionnel. Les études de photoluminescence intégrée et résolue en temps confirment une forte réduction de l'effet Stark confiné quantique (QCSE), en comparaison avec des structures polaires équivalentes. De plus, les résultats expérimentaux sont cohérents avec les simulations de la structure électronique qui prédisent un champ électrique interne allant de 0.6 MV/cm à -0.55 MV/cm, en fonction de l'état de contrainte du superréseau. Enfin, la bonne qualité cristalline des échantillons nous a permis de mettre en évidence, pour la première fois dans des structures semipolaires, l'absorption inter-sous-bande. La réduction du champ électrique interne est confirmée aussi par ces transitions, car elle résulte en un décalage vers le rouge de l'absorption par rapport aux matériaux polaires.

Pour terminer, nous avons montré que la transition 2D-3D correspondant à la croissance de boîtes quantiques GaN/AlN est réalisée en déposant, sur l'AlN, quelques monocouches de GaN dans des conditions très peu riche Ga (donc croissance bidimensionnelle) puis en laissant évoluer la surface sous vide. Les mesures de TEM en haute résolution ont confirmé que les boîtes gardent l'orientation $(11\bar{2}2)$, et qu'elles ont la forme de pyramide tétragonales tronquées. Une particularité intéressante est que leur plan de base est soit le plan $(11\bar{2}2)$ soit le plan $(10\bar{1}1)$, selon que leur cohérence verticale est suivant l'axe de croissance ou suivant le plan *c*. Les super réseaux à boîtes présentent, au même titre que les superréseaux à puits, une forte réduction du QCSE, en comparaison avec les structures polaires.

Perspectives

A en juger par le nombre croissant de groupes s'impliquant dans la recherche sur l'orientation semipolaire (11$\bar{2}$2) depuis les trois dernières années, l'intérêt pour ces structures est certain, et plusieurs perspectives sont à envisager, tant d'un point de vue academique qu'en termes d'applications potentielles.

En vue de l'optimisation de la croissance, il serait particulièrement intéressant de comprendre le mécanisme de nucléation de l'AlN sur saphir m et notamment les mécanismes de relaxation des contraintes. Dans cette lignée, une caractéristique intéressante des couches d'AlN et GaN semipolaires est la désorientation de l'axe <11$\bar{2}\bar{3}$> par rapport à l'axe <0001> du saphir, qui est plus importante dans l'AlN que dans le GaN. L'origin de cette désorientation est actuellement étudiée, et une des hypothèses est que c'est une conséquence de l'accommodation des contraintes le long de la direction <11$\bar{2}\bar{3}$>. Ainsi, il serait intéressant d'étudier la croissance d'AlN sur des substrats saphir m désorientés de quelques degrés dans la direction <0001>.

Les couches de GaN semipolaires présentent une densité de défauts deux fois plus élevée que les matériaux polaires, ce qui est un réel inconvénient pour la fabrication de composants haute performance. Dans l'espoir de diminuer la quantité de défauts dans nos couches, nous avons une collaboration pour utiliser des couches tampons de GaN(11$\bar{2}$2) épitaxiées par MOVPE and HVPE. Il est à noter que la dernière année a connu l'essor du GaN(11$\bar{2}$2) avec la mise sur le marché de couches tampons de GaN, preuve de l'intérêt croissant pour cette orientation.

Au delà de la compréhension des mécanismes de croissance et propriétés physiques de cette nouvelle orientation, les nitrures semipolaires sont des matériaux prometteurs pour la fabrication de composant optoélectroniques. On peut mentionner ici la démonstration de couches épaisses élaborées par HVPE par le groupe de S. Nakamura de l'Université de Californie à Santa Barbara, de même que la fabrication récente de diodes jaunes d'efficacité comparable ou supérieure à celle des diodes phosphures déjà sur le marché. Dans ce contexte, le savoir-faire concernant ce travail trouve toute son utilité, en vue de la croissance de nanostructures utilisées comme zones actives dans les composants optoélectroniques. Ainsi, nous avons commencé la croissance d'alliages d'AlGaN(11$\bar{2}$2), avec 30% et 50% d'aluminium. L'étude des alliages ternaires, AlGaN et InGaN, va donc devenir une priorité, ainsi que les développements, en parallèle, de procédés technologiques en vue de l'intégration des couches minces et nanostructures dans des composants finalisés.

Table of contents

Résumé **iii**

Introduction **1**

1 Properties of III-nitrides **7**
1.1 Crystalline structure . . . 9
1.1.1 Crystallographic phases . . . 9
1.1.2 Lattice parameters . . . 9
1.1.3 Polarity . . . 12
1.2 Electronic properties . . . 12
1.3 Elastic properties . . . 15
1.3.1 Strain and stress . . . 16
1.3.2 Strain in a (0001)-oriented hexagonal system under biaxial stress 17
1.3.3 Strain in nonpolar and semipolar layers under biaxial stress . 17
1.3.4 Plastic relaxation via the formation of dislocations or cracks . 19
1.4 Spontaneous and piezoelectric polarization . . . 21

2 Experimental techniques **23**
2.1 Plasma-assisted molecular beam epitaxy . . . 25
2.1.1 Epitaxial growth . . . 25
2.1.2 Heteroepitaxy . . . 27
2.1.3 *In-situ* characterization: RHEED . . . 27
2.2 PAMBE growth of III-nitrides . . . 30
2.2.1 Growth diagram of *c*-plane nitrides . . . 30
2.2.2 Growth of nonpolar nitrides . . . 33
2.3 Description of the growth methods . . . 34
2.3.1 PAMBE equipment . . . 34
2.3.2 *m*-sapphire substrates . . . 37
2.4 Structural and optical characterization . . . 39
2.4.1 X-ray diffraction . . . 39
2.4.1.1 Diffraction theory . . . 39
2.4.1.2 Description of the diffractometer . . . 40
2.4.1.3 Sample alignment . . . 43
2.4.1.4 Symmetrical and asymmetrical reflections . . . 43

2.4.1.5 Effect of the presence of crystalline defects on reciprocal space maps . . . 44
2.4.1.6 Determination of lattice parameters in the case of semipolar nitrides. . . . 47
2.4.2 Atomic-force microscopy . . . 50
2.4.3 Photoluminescence spectroscopy . . . 53
2.5 Simulation of electronic structures . . . 54

3 Analysis of AlN(11$\bar{2}$2) grown on *m*-sapphire 59
3.1 Growth of AlN on *m*-sapphire . . . 61
3.1.1 Effect of the III/V ratio . . . 61
3.1.2 How to understand the RHEED patterns? . . . 64
3.1.3 Crystallographic orientation relationships . . . 67
3.1.4 Synthesis of two-dimensional AlN(11$\bar{2}$2) . . . 73
3.1.4.1 Effect of the substrate temperature . . . 73
3.1.4.2 Discussion on *m*-sapphire nitridation . . . 73
3.1.4.3 Starting the growth . . . 76
3.2 Crystalline structure of AlN(11$\bar{2}$2) . . . 77
3.2.1 XRD experiments . . . 77
3.2.2 Estimation of the lattice parameters in thick layers . . . 80
3.2.3 Relaxation analysis . . . 81
3.2.4 Surface morphology . . . 83
3.3 Conclusions . . . 84

4 Study of GaN(11$\bar{2}$2) 87
4.1 Growth of GaN(11$\bar{2}$2) . . . 89
4.1.1 Crystalline orientation . . . 89
4.1.2 Ga wetting on GaN(11$\bar{2}$2) . . . 93
4.1.3 Identification of the growth window . . . 98
4.2 Optical properties of GaN(11$\bar{2}$2) thick layers . . . 103
4.3 Doping of GaN(11$\bar{2}$2) . . . 107
4.3.1 Growth kinetics of doped GaN(11$\bar{2}$2) . . . 108
4.3.2 Mg incorporation in GaN(11$\bar{2}$2) . . . 110
4.3.3 Optical properties Mg-doped layers . . . 114
4.3.4 Electrical characterization of Mg-doped layers . . . 116
4.4 Conclusions . . . 118

5 GaN/AlN quantum wells 121
5.1 Quantum Confined Stark Effect . . . 123
5.2 Structural analysis of semipolar quantum wells . . . 124
5.3 Optical investigation . . . 128
5.3.1 Demonstration of the reduction of the QCSE . . . 128
5.3.2 Intersubband transitions . . . 132

5.4 Conclusions 134

6 GaN/AlN quantum dots **137**
6.1 Synthesis of semipolar GaN QDs on AlN(11$\bar{2}$2) 139
6.1.1 Growth of nitride quantum dots 139
6.1.2 Growth of semipolar GaN quantum dots 140
6.2 Structural description of semipolar GaN quantum dots 141
6.3 Optical properties of (11$\bar{2}$2)-oriented QDs 145
6.4 Conclusions 148

Conclusions and perspectives **151**

Bibliography **169**

Glossary **171**

Introduction

III-Nitride semiconductors

The first synthesis of polycrystalline AlN and GaN was reported in 1907 [Fic07] and 1932 [Joh32], respectively. However, it took some additional 40 years for the scientific community to become aware of the potential of III-nitride semiconductors (GaN, AlN, InN and their alloys). In particular, the fabrication of GaN epitaxial layers dates from 1969 by hybrid vapor phase epitaxy [Mar71], 1971 by metal organic vapor phase epitaxy [Man71] and 1975 by molecular beam epitaxy [Yos75]. The achievement of p-type doping in 1989 [Ama89] resulted in an outburst of interest on these materials, which culminated with the fabrication of InGaN-based blue lasers diodes (LDs) [Nak97] by Nichia corporation. Figure 1 illustrates the growing activity on nitrides, represented by the annual number of publications related to GaN since then [Aka07]. The motivation for research on these materials comes from their potential applications. Indeed, the direct bandgap of III-nitride semiconductors covers a broad energetic spectrum, ranging from 0.8 eV (infrared) for InN to 6.2 eV (ultraviolet) for AlN, as illustrated in Fig. 2. Thus, the synthesis of alloys and the bandgap engineering should make it possible to develop light emitting components within this whole range.

Nowadays, nitride semiconductors are widely used in commercial white light emitting diodes (LEDs) integrated in flashlights or headlamps. The main advantage of such components lies in their low consumption and $\approx$ 10 000 hours of lifetime [Nis06, Dam07]. Their efficiency can be as high as 159 lumens/watt compared to 85 lumens/watt for fluorescent lights of 15 lumens/watt for incandescent lights. In a socio-economic context where global warming has become an every-day concern, LEDs should rapidly find their place in public lighting. White LEDs have already convinced the car industry, with their implantation in several car models (Lexus LS600H, Audi R8 [Sem07a]). Nitride-based color (blue, green) LEDs are also commercialized and we can find their application in every corner of our lives: green traffic lights, advertising panels, TV screens, mobile phones. Finally, UV LEDs have particular potential in the medical and chemical application domains.

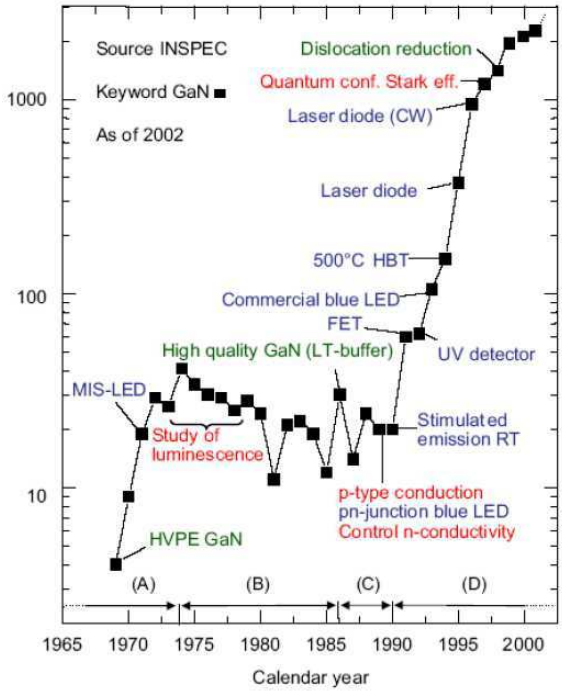

Figure 1: *Number of publications related to GaN published every year since 1970 [Aka07].*

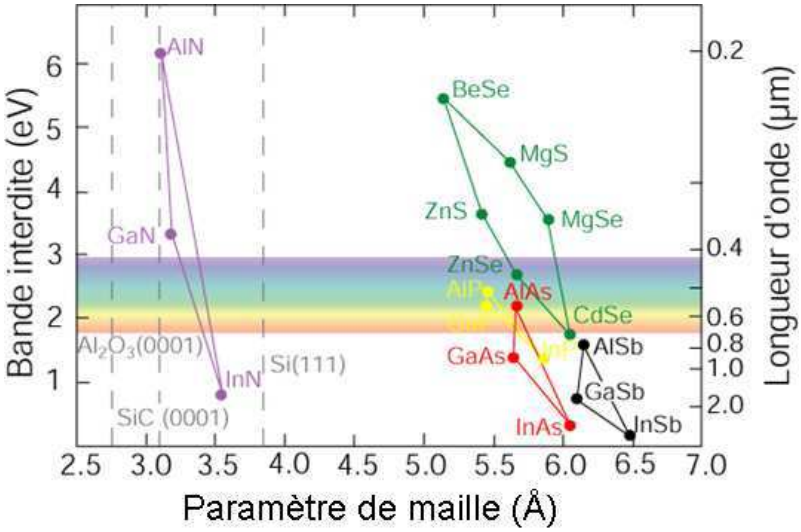

Figure 2: *Bandgap of semiconductor families, given their common in-plane lattice parameters.*

Blue LDs provide another important field of application for nitrides, in terms of information storage. The huge revolution occurred in the 80s, with the fabrication of the compact disks (CDs), burned with arsenide-based red lasers. The disk capacity depends on the wavelength of the laser used for burning: the shorter the wavelength the more information can be stored. Thus, the wavelengths of 780 - 650 nm of red lasers used in classic CDs and DVDs are now overcome by blue lasers with a wavelength of 405 nm (blue-ray technology). For instance, blue-ray disks have a

storage capacity of 50 Go, compared to the CDs with 700 Mo and experimental prototypes have a storage capacity of up to 200 Go! Sony is the main company using this technology (Playstation, Vaio laptops), fabricating up to 1.7 millions of blue lasers per month! The blue LD market should continuously increase and experts predict it will reach 1 billion of dollars by the end of 2011 [Sem07b].

In addition to optoelectronic applications, nitrides are also present on the electronic market, thanks to the development of High Electron Mobility Transistors (HEMT) operating at high frequencies ($\geq$ 100 GHz), delivering high power and standing high temperatures.

Remaining material challenges

One of the drawbacks of the III-nitrides is the lack of low-cost bulk substrates for homoepitaxy. As a result, nitride-based structures are mostly fabricated by heteroepitaxy, on sapphire, Si(111) or SiC substrates. The large lattice mismatch of nitrides with these substrates induces strain, which relax via the introduction of dislocations, whose density can be as high as 10^{10} cm^{-2}. As for comparison, arsenide or phosphide materials usually present dislocation densities of about 10^{2} cm^{-2}. The presence of dislocations reduces the quality and the lifetime of nitride-based devices.

An additional challenge stems for the large lattice mismatch between III-nitride binary compounds (2.4% between GaN and AlN and 11% between InN and GaN). As a result, strain relaxation is important even for very thin layers. For device design, it is important to control of the relaxation mechanisms since they may introduce defects and also modify the electronic structure of the components due to the high piezoelectric constants of III-nitride materials. Besides, the difficulties to synthesize homogeneous alloys has to be mentionned, and particularly in the case of materials containing In. Indeed, In clusters are formed in the InGaN quantum wells (QWs), acting as carrier localisation centers. This enhanced localization is an advantage for the fabrication of LEDs, since the carriers confined in alloy fluctuations become less sensitive to non-radiative recombination centers. However, the resulting broadening of the emission lines and their dependence on the temperature and carrier injection are important drawbacks for devices like laser diodes.

Last but not least, because of their crystalline structure, III-nitride semiconductors exhibit strong spontaneous and piezoelectric polarization along their growth axis, the *c*-axis [Ber97]. In QW structures grown along this direction, the polarization discontinuity at the interfaces can cause electric fields of up to 10 MV/cm [Tch06] along the growth axis. Even if this electric field is interesting for certain applications (HEMTs, sensors), it has deleterious effects on the performance of optoelectronic devices, by reducing the radiative recombination efficiency of the heterostructures, and inducing a red shift of the luminescence, which is called the Quantum Confined Stark Effect (QCSE).

Motivation and Targets

The polarization effects can be reduced by choosing nonpolar growth orientations. Nonpolar orientations are those with the c axis in the growth plane, so that there are no polarization discontinuities at the interfaces of 2D heterostructures. The two candidates are the $(1\bar{1}00)$ m-plane [Chi04] and the $(11\bar{2}0)$ a-plane [Cha06]. GaN/AlGaN $(1\bar{1}00)$- or $(11\bar{2}0)$-oriented QWs present a quasi zero QCSE [Wal00, Cra03]. A reduction of the electric field has also been observed in QDs with the same orientations [Fou05, Gar05, Ams07].

In spite of the reduction of the QCSE in nonpolar nitride structures, their growth remains challenging due to the strong anisotropy of their surface properties, which leads to epitaxial layers with a high density of crystalline defects. An alternative approach is the growth of semipolar planes, which are the $(hkil)$ planes with a nonzero h, k or i and a nonzero l Miller index. Theoretical studies have shown that semipolar orientations may minimize the internal electric field effect by compensating the spontaneous and piezoelectric polarization differences [Tak00]. Semipolar orientations have been reported for films epitaxially grown on spinel or sapphire substrates: GaN$(10\bar{1}1)$ on (100)spinel, GaN$(10\bar{1}\bar{3})$ on (110)spinel [Cha05], and either GaN$(10\bar{1}\bar{3})$ or GaN$(11\bar{2}2)$ on $10\bar{1}0$-oriented sapphire depending on the growth conditions [Bak06]. Light emitting diodes (LEDs) grown on $(10\bar{1}3)$ [Kam05, Cha05], $(10\bar{1}1)$ [Tya07, Wun07, Fun06] and $(11\bar{2}2)$ [Ued06] planes have been demonstrated recently. At the beginning of this thesis, research efforts on semipolar III-nitrides had mainly focused on hydride vapor phase epitaxy (HVPE) and metalorganic vapor phase deposition (MOVPE). However, plasma-assisted molecular-beam epitaxy (PAMBE) presents advantages for certain device structures, particularly in terms of dopant incorporation and nanoscale design.

The target of this work was to study the epitaxial growth of semipolar $(11\bar{2}2)$-oriented nitride thin films and nanostructures (quantum wells and quantum dots) in order to assess their optical and structural properties in comparison with those of polar and nonpolar structures. Efforts were dedicated to the understanding of the growth modes of AlN and GaN with this orientation, and to the study of their fine structure. With a motivation to probe the potential of the $(11\bar{2}2)$ orientation in terms of optoelectronic applications, we also dedicated part of this work to the control of n-type and p-type doping.

During my PhD, my work has concerned the plasma-assisted MBE growth of semipolar nitride layers and heterostructures, and their characterization, using *in situ* Reflection High Energy Electron Diffraction (RHEED), X-Ray diffraction (XRD), Atomic-Force Microscopy (AFM) and photoluminescence. Additional data on the structural quality of the layers was provided by Transmission Electron Microscopy (TEM), performed by our collaborators at CIMAP - CNRS in Caen, France (Prof. P. Ruterana) and Aristotle University of Thessaloniki, Greece (Prof. Ph. Komninou). In order to probe the intersubband transitions, Fourier-Transform In-

fraRed (FTIR) measurements were performed by our collaborators in Paris-Sud University (Prof. F. H. Julien).

Organization of the manuscript

The first two chapters of the manuscript stand for an introduction to the materials and techniques I used. In that purpose, the first chapter introduces group III-nitride semiconductors, and then concentrates on the properties of wurtzite-type nitrides. After a description of the wurtzite structure and the crystallographic planes under study in this work, the electronic structure of these semiconductors is described. A special interest is given to the study of the strain and stress in polar and semipolar layers. Finally, we will explain the origin of the internal polarization.

The second chapter starts with an introduction to the heteroepitaxy principle. Then, I will describe the growth modes of polar and nonpolar nitrides, which constituted the know-how at the beginning of my thesis. A more technical section describes the PAMBE equipment used for the growth of the samples, and the structural and optical characterization setups.

Chapters 3 to 6 contain the results obtained in this work. In the third chapter, I focus on the growth of AlN on *m*-sapphire. After the identification the crystallographic orientations which can be found in the layers, I explain the growth process leading to the formation of two-dimensional AlN($11\bar{2}2$) and identify the crystallographic orientation of the AlN layer relatively to the substrate.

After the investigation of the two-dimensional growth of AlN($11\bar{2}2$) and subsequent structural properties, the fourth chapter focuses on the growth of semipolar GaN. I will determine the best growth window necessary to achieve two-dimensional GaN($11\bar{2}2$) on top of AlN($11\bar{2}2$). The optical emission of the layers will be deeply analyzed, before considering the properties of Mg-doped layers.

The know-how described in the previous chapters is applied to the synthesis of ($11\bar{2}2$)-oriented multiple-QW structures. I will discuss on the determination of the lattice parameters and the strain state of the structures. The optical measurements will be compared to simulations to verify the attenuation of the QCSE.

Finally, the last chapter is dedicated to the study of ($11\bar{2}2$)-oriented GaN/AlN QDs. I will introduce the growth conditions required to form QDs with this orientation. The nucleation process will be described, together with the geometrical structure of the dots, before giving results on their optical performance.

Chapter 1

Properties of III-nitrides

In this chapter, I summarize some of the characteristics of III-nitride semiconductors. I first present the various crystalline structures which these materials can display, and then expose the main structural and electronic properties of wurtzite-type III-nitrides. Finally, I explain the origin of the internal polarization.

Contents

1.1 Crystalline structure 9

1.1.1 Crystallographic phases 9

1.1.2 Lattice parameters 9

1.1.3 Polarity 12

1.2 Electronic properties 12

1.3 Elastic properties 15

1.3.1 Strain and stress 16

1.3.2 Strain in a (0001)-oriented hexagonal system under biaxial stress 17

1.3.3 Strain in nonpolar and semipolar layers under biaxial stress 17

1.3.4 Plastic relaxation via the formation of dislocations or cracks 19

1.4 Spontaneous and piezoelectric polarization 21

1.1 Crystalline structure

In this section, I describe the two main crystalline configurations of III-nitride semiconductors, namely the cubic zinc-blend and the hexagonal wurtzite phases. In particular, I give the values of the various lattice parameters that describe wurtzite-type materials and detail the specific crystallographic planes which will be addressed in this work.

1.1.1 Crystallographic phases

III-nitride semiconductors - AlN, GaN, InN and their alloys - can crystallize in three crystallographic configurations: the hexagonal wurtzite phase (α), the cubic zinc-blend phase (β) and the rocksalt phase (γ). Depending on the substrate and growth conditions, nitride epitaxial layers present either wurtzite or zinc-blend structure. In both configurations, the atoms are tetrahedrically coordinated, but the orientation of the tetrahedrons is rotated by an angle of 60° around the <0001> axis of the wurtzite structure, or the equivalent <111> axis of the zinc-blend structure. As a consequence, the stacking periodicity along the [0001] axis is ABABA... for the wurtzite phase and it is ABCABCA... along the [111] axis for the zinc-blend phase (Fig. 1.1). Even if the wurtzite phase is the most thermodynamically stable configuration of nitride semiconductors [Yeh92], cubic nitrides can be grown by MBE using cubic substrates such as (001)3C-SiC [Dau98, MG02] or (001) GaAs [As97, Sun99]. This work focuses on wurtzite-type nitrides, and the following chapters only address the intrinsic properties of wurtzite materials.

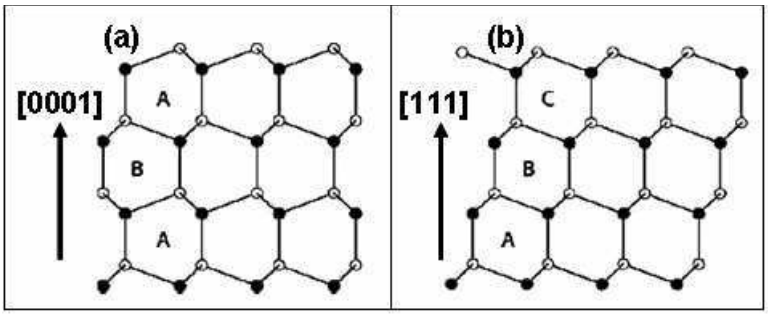

Figure 1.1: *Stacking periodicity for (a) wurtzite ABABA... planes along the [0001]axis ([11$\bar{2}$0] azimuth) and (b) zinc-blend ABCABCA... planes along the [111] axis ([1$\bar{1}$0] azimuth).*

1.1.2 Lattice parameters

The wurtzite structure is represented in Fig. 1.2. It consists of two entangled hexagonal closed packed (HCP) lattices of metal (Al, Ga or In) and Nitrogen (N) atoms with the associated space group $P6_3mc$. The two lattices are shifted along the [0001] $\overrightarrow{c}$-axis by $u = \frac{3c}{8}$.

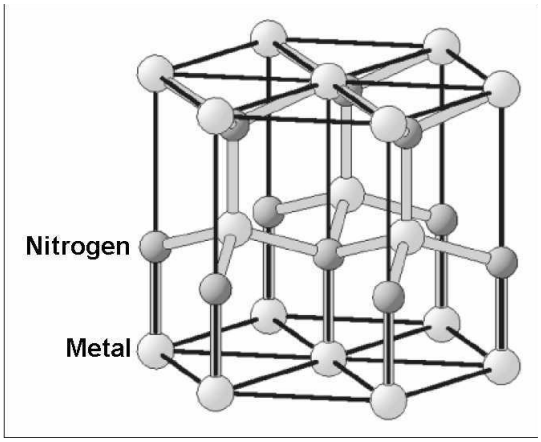

Figure 1.2: *Illustration of the atomic distribution in wurtzite structure [Fou07].*

The hexagonal unit cell is defined by the side of the hexagon, a, and the height of the hexahedron, c, as illustrated in Fig. 1.3. In a hexagonal system, the crystallographic directions and planes are named after the $\{h, k, i, l\}$ Miller-Bravais indices, related to the directions $\{\overrightarrow{a_1}, \overrightarrow{a_2}, \overrightarrow{a_3}, \overrightarrow{c}\}$, respectively. Since $\overrightarrow{a_3} = -\overrightarrow{a_1} - \overrightarrow{a_2}$, the sum of the first three indices is zero: $i = -(h + k)$.

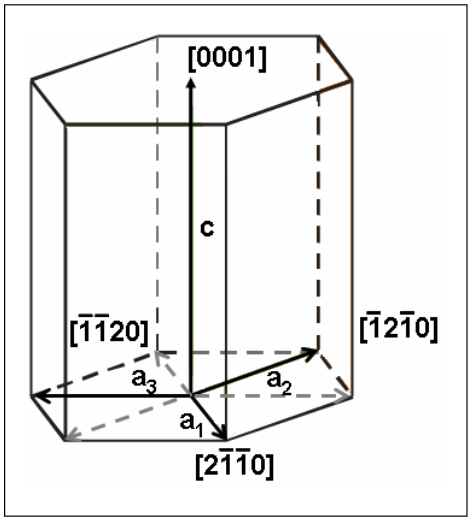

Figure 1.3: *Hexagonal unit cell.*

It is important to emphasize that in the case of a hexagonal system, the [hkil] direction is not perpendicular to the (hkil) plane, except for a few particular plane families. Indeed, the direction strictly perpendicular to the (hkil) plane is the vector $[hki\frac{3a^2}{2c^2}l]$. As an example, Fig. 1.4 illustrates the $(1\bar{1}00)$, $(11\bar{2}2)$ and $(1\bar{1}03)$ planes and Table 1.1 defines the three orthogonal directions for each plane. The z' axis is attributed to the vector normal to the plane, the x' and y' axis to two perpendicular in-plane vectors, and θ is the angle formed by the plane with the c-plane.

The value of the lattice parameters a, c and u is given in Table 1.2 for GaN, AlN and InN. These values correspond to wurtzite materials at room temperature.

The thermal expansion coefficient [$\alpha(a) = \frac{\Delta a}{a}$ or $\alpha(c) = \frac{\Delta c}{c}$] is given in Figure 1.5 as a function of the temperature. In the case of $A_xB_{1-x}N$ ternary alloys, the parameters are determined by Vegard's law:

$$\begin{aligned} a_{A_xB_{1-x}N} &= xa_A + (1-x)a_B \\ c_{A_xB_{1-x}N} &= xc_A + (1-x)c_B \end{aligned} \tag{1.1}$$

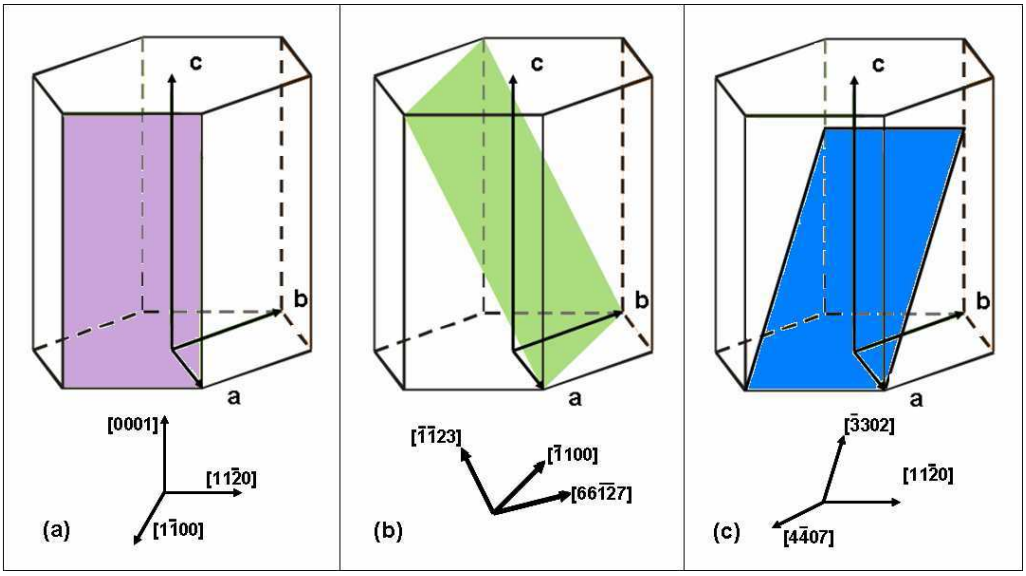

Figure 1.4: *Description of the (1$\bar{1}$00), (11$\bar{2}\bar{2}$) and (1$\bar{1}$03) planes.*

Planes		(11$\bar{2}\bar{2}$)	(1$\bar{1}$00)	(1$\bar{1}$03)
Normal vector	z'	[6 6 $\overline{12}$ 7]	[1 $\bar{1}$ 0 0]	[4 $\bar{4}$ 0 7]
In-plane vectors	x'	[1 $\bar{1}$ 0 0]	[1 1 $\bar{2}$ 0]	[1 1 $\bar{2}$ 0]
	y'	[1 1 $\bar{2}\bar{3}$]	[0 0 0 1]	[$\bar{3}$ 3 0 2]
θ		58.4°	90°	32°

Table 1.1: *Description of the planes and directions under study. θ angles are calculated here for GaN.*

Parameters [$\AA$]	GaN	AlN	InN
a	3.189	3.112	3.540
c	5.185	4.982	5.705
u	0.376	0.380	0.377

Table 1.2: *Lattice parameters of GaN, AlN and InN at room temperature [Mor94].*

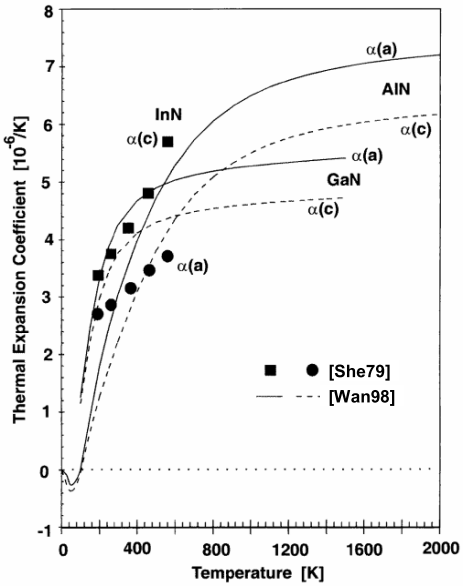

Figure 1.5: *Thermal expansion coefficients versus temperature for AlN, GaN and InN [Amb98]. For each material, $\alpha(a)$ and $\alpha(c)$ are the coefficients with respect to a and c lattice parameters.*

1.1.3 Polarity

Since wurtzite structures do not have a symmetry inversion center, the [0001] and [000$\bar{1}$] directions are not equivalent. The polarity is determined by the direction of the vector associated to the metal-N bond along the <0001> axis. The $\overrightarrow{c}$-axis is defined as positive (metal polarity) when such a vector points from the metal atom towards the N atom, as illustrated in Fig. 1.6. The (0001) face (called metal face) presents different properties than the (000$\bar{1}$) face (called nitrogen face) in terms of surface morphology, chemical reactivity and growth conditions. Metal-polarity surfaces are more chemically-stable than nitrogen-polarity surfaces [Mas05] [Rou98].

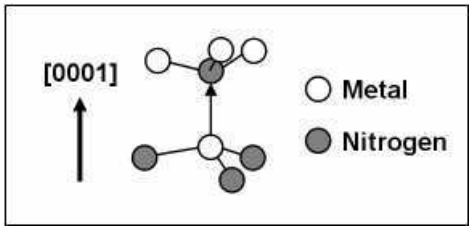

Figure 1.6: *(0001) metal face for III-nitrides.*

1.2 Electronic properties

Group-III nitride semiconductors have a direct bandgap, *i.e.* the minimum of the valence band and the maximum of the conduction band occur in the center of the

Brillouin zone (Γ point in Figs. 1.7(a) and 1.7(b)). Because of the lack of symmetry along $\vec{c}$, there is a degeneracy splitting of the valence band between the heavy hole (Γ_9 symmetry), light hole (Γ_7 symmetry) and spin-orbit (Γ_7 symmetry) subbands. As illustrated in Fig. 1.8, this splitting stems from the crystal-field surrounding the wurtzite crystal on the one hand (Δ_{CF}), and the spin-orbit interaction (Δ_{SO}) on the other hand. This band structure leads to three different excitons formed between electrons of the conduction band and holes of the corresponding valence subband, usually named A, B and C [see in Figure 1.8]. Table 1.3 presents the values of the bandgap (E_g), Δ_{CF} and Δ_{SO} at $T = 300$ K for GaN, AlN and InN.

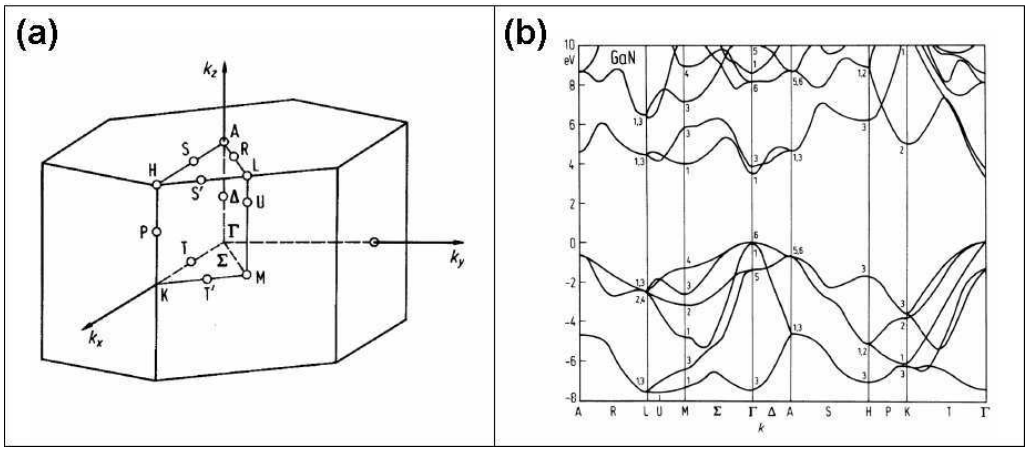

Figure 1.7: *(a) Brillouin zone of wurtzite type GaN. Image copied from http://www.ioffe.ru/SVA/NSM/. (b) GaN band structure [Blo74].*

Experimental values of the effective mass of electrons and holes for wurtzite-type GaN and AlN are summarized in Table 1.4. For most calculations, the effective mass of the electrons, m_e^*, can be considered as approximately constant along all the crystallographic directions. In contrast, theoretical calculations predict that the effective mass of holes should be strongly anisotropic. The dispersion in the experimental values can be additionally explained by the fact that the three valence bands are not parabolic and close to each other.

	GaN	AlN	InN	References
E_g at 300K (eV)	3.51	6.24	-	[Pug99]
	-	-	0.65	[Wan04]
Δ_{SO} (eV)	0.0096	0.018	0.0139	[Rez06]
Δ_{CF} (eV)	0.030	-0.104	0.057	[Pug99]

Table 1.3: *GaN, AlN and InN band characteristics.*

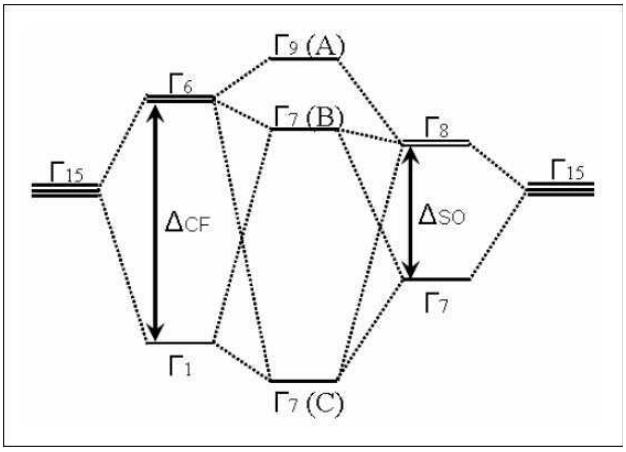

Figure 1.8: *Details on the degeneracy splitting of the valence band of GaN. Δ_{CF} is the splitting due to the crystalline field and Δ_{SO} the splitting due to spin-orbit interaction.*

	Electron effective mass	Hole effective mass
GaN	0.2 m_0 [Per96] [Dre95]	0.3 m_0 [Sal95] 2.2 m_0 [Im97] 0.54 m_0 [Mer96] 0.8 m_0 [Pan75] 1 m_0 [Vur01]
AlN	0.32 m_0 [Vur01] [Dre95]	1.14 m_0 [Kim97]

Table 1.4: *Effective masses for wurtzite GaN and AlN.*

The variation of the bandgap with the temperature is given by Varshni's law:

$$E_g(T) = E_g(0) - \frac{\alpha T^2}{\beta + T} \tag{1.2}$$

where $E_g(0)$ is the bandgap at 0 K. The parameters α and β can be calculated taking into account the electron-phonon interaction. Table 1.5 records some values found in the literature for these three parameters and the corresponding bandgap calculated for $T = 300$ K.

The bandgap of $A_xB_{1-x}N$ ternary alloys can be calculated with the formula:

$$E_g^{A_xB_{1-x}N}(x) = (1-x)E_g^{AN} + xE_g^{BN} - x(1-x)b^{ABN} \tag{1.3}$$

where b^{ABN} is the bowing parameter [Wu03]. The values of b for $Al_xGa_{1-x}N$ and $In_xGa_{1-x}N$ alloys are reported in Table 1.6.

	$E_g(0)$ (eV)	α (meV.K^{-1})	β (K)	$E_g(300K)$ (eV)	References
GaN	3.47	0.59	600	3.411	[Li97]
	3.479	0.87	884	3.413	[Cal97]
	3.489	0.887	874	3.421	[Ler99]
	3.492	0.531	432	3.426	[Tri99]
		0.909	830		[Vur03]
AlN	6.126	1.799	1462	6.03	[Guo94]
		1.999	1429		[Vur03]
InN	0.69	0.414	454	0.641	[Wal04]

Table 1.5: *Example of the calculated values of $E_g(0)$, Varshni parameters α and β, together with the value of the calculated bandgap at room temperature.*

	b (eV)	References
$Al_xGa_{1-x}N$	0.62 ± 0.45	[Lee99]
	0	[Och99]
	1.33	[Sha98]
	0.353 ± 0.024	[Kuo02]
	-0.82	[Onu04]
	0.341 ± 0.035	[Lio05]
	0.351 ± 0.043	[Lio05]
$In_xGa_{1-x}N$	1.21 ± 0.03	[Kuo01]
	1.782 ± 0.076	[Lio05]
	1.916 ± 0.068	[Lio05]
	1.44	[Cae07]

Table 1.6: *Values of the bowing parameter for AlGaN and InGaN alloys.*

1.3 Elastic properties

As we will see in the next chapter, III-nitrides are mainly synthesized by heteroepitaxy. The difference in lattice parameters between the substrate and the epitaxial layer induces stress within the deposited film. The epilayer starts growing coherently, *i.e.* adjusting its in-plane lattice parameter to the in-plane lattice parameter of the substrate. However, this coherent regime implies the accumulation of elastic energy increasing with the layer thickness. At a certain critical thickness, becomes energetically favorable to relax the lattice via the creation of coherent clusters (elastic relaxation) or the formation of dislocations or cracks. This critical thickness depends on both the substrate and the deposited material. Moreover, the lattice mismatch between the different nitride compounds (see Table 1.2) results in additional stress in multilayer structures.

In the following, I will first introduce the relation between strain and stress. Then, two sections address the calculation of strain for polar and semipolar materials under biaxial stress in the hexagonal system. The last part studies the generation

of dislocations and cracks in such systems.

1.3.1 Strain and stress

The relation between the stress ($\sigma_{i,j}$) and the strain ($\epsilon_{k,l}$) is given by Hooke's law:

$$\sigma_{i,j} = \sum_{k,l} C_{i,j,k,l}\epsilon_{k,l} \tag{1.4}$$

where ($C_{i,j,k,l}$) is the fourth-order elastic tensor. To simplify the expression, the deformation and stress tensors are usually expressed as 6-component vectors:

$$\begin{cases} \epsilon_1 = \epsilon_{xx} & \sigma_1 = \sigma_{xx} \\ \epsilon_2 = \epsilon_{yy} & \sigma_2 = \sigma_{yy} \\ \epsilon_3 = \epsilon_{zz} & \sigma_3 = \sigma_{zz} \\ \epsilon_4 = \epsilon_{yz} + \epsilon_{zy} & \sigma_4 = \sigma_{yz} + \sigma_{zy} \\ \epsilon_5 = \epsilon_{zx} + \epsilon_{xz} & \sigma_5 = \sigma_{zx} + \sigma_{xz} \\ \epsilon_6 = \epsilon_{xy} + \epsilon_{yx} & \sigma_6 = \sigma_{xy} + \sigma_{yx} \end{cases}$$

In that way, the elastic tensor becomes a 6×6 matrix, as shown in the example for a hexagonal structure given in Eq. 1.5. Calculated and experimental values of the parameters $C_{i,j}$ for III-nitride materials are reported in Table 1.7.

$$(C) = \begin{pmatrix} c_{11} & c_{12} & c_{13} & 0 & 0 & 0 \\ c_{12} & c_{11} & c_{13} & 0 & 0 & 0 \\ c_{13} & c_{13} & c_{33} & 0 & 0 & 0 \\ 0 & 0 & 0 & c_{44} & 0 & 0 \\ 0 & 0 & 0 & 0 & c_{55} & 0 \\ 0 & 0 & 0 & 0 & 0 & \frac{1}{2}(c_{11} - c_{12}) \end{pmatrix}. \tag{1.5}$$

Coefficients (GPa)	c_{11}	c_{12}	c_{13}	c_{33}	c_{44}	c_{66}	References
GaN	365	135	114	381	109	115	[Yam97] (exp.)
	370	145	110	390	90	112	[Deg98] (exp.)
	396	144	100	392	91	126	[Kim96] (theo.)
	367	135	103	405	95	116	[Wri97] (theo.)
AlN	411	149	99	389	125	131	[McN93] (exp.)
	410	140	100	390	120	135	[Deg98] (exp.)
	398	140	127	382	96	129	[Kim96] (theo.)
	396	137	108	373	116	129	[Wri97] (theo.)
InN	271	124	94	200	46	73	[Kim96] (theo.)
	223	115	92	224	48	54	[Wri97] (theo.)

Table 1.7: *Theoretical and experimental values of the elastic stiffness coefficients of GaN, AlN and InN.*

1.3.2 Strain in a (0001)-oriented hexagonal system under biaxial stress

Given Hooke's law enunciated previously (Eq. 1.4), it is possible to calculate the strain induced in a layer, knowing the stress distribution. During heteroepitaxy of III-nitrides on the (0001) plane, the in-plane stress is uniform ($\sigma_{11} = \sigma_{22} = \sigma$) and there is no stress along the $\vec{c}$ axis or shear stress. In that particular case (biaxial stress configuration), the Hooke law is simplified as in Eq. 1.6, with the coefficients ϵ_i given in Eqs. 1.7 and 1.8 where a_s and c_s are the lattice parameters of the substrate and a and c the lattice parameters of the epitaxial layer.

$$\begin{pmatrix} \sigma \\ \sigma \\ 0 \end{pmatrix} = \begin{pmatrix} c_{11} & c_{12} & c_{13} \\ c_{12} & c_{11} & c_{13} \\ c_{13} & c_{13} & c_{33} \end{pmatrix} \times \begin{pmatrix} \epsilon_1 \\ \epsilon_2 \\ \epsilon_3 \end{pmatrix} \tag{1.6}$$

$$\epsilon_1 = \epsilon_2 = \epsilon_{xx} = \frac{a_s - a}{a} \tag{1.7}$$

$$\epsilon_3 = \epsilon_{zz} = -2\frac{c_{13}}{c_{33}}\epsilon_{xx} = \frac{c_s - c}{c} \tag{1.8}$$

1.3.3 Strain in nonpolar and semipolar layers under biaxial stress

Whereas in the particular case of c-plane nitrides, the in-plane mismatch is equibiaxial, this does not hold for semipolar and nonpolar nitrides. As a result, the in-plane distribution of the elastic strain is anisotropic. In the case of a ($hkil$) plane, we can attribute the z' axis to the vector normal to the surface and the x' and y' axis to the two in-plane vectors, as illustrated in Fig. 1.9 [see in Table 1.1 for the particular case of $(1\bar{1}00)$-, $(11\bar{2}2)$- and $(1\bar{1}03)$-oriented growing surfaces]. In general, the misfits along x' and y' directions (ϵ_{m1} and ϵ_{m2}, respectively) are different.

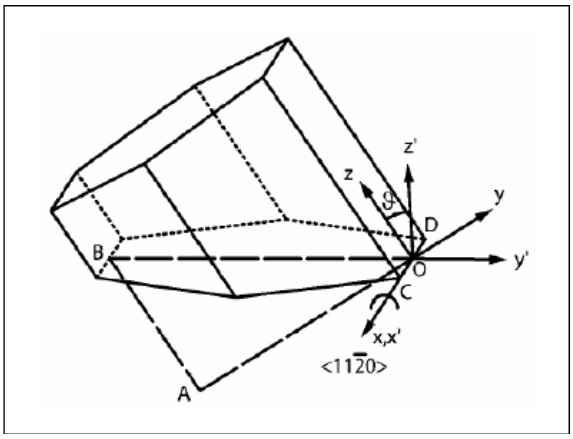

Figure 1.9: *Schematic to illustrate the change of coordinates from the (x, y, z) system to the (x', y', z') system.*

Since the out-of-plane direction is free, the layer is under zero traction stress ($\sigma_{z'z'} = 0$) and the absence of shear stress gives $\sigma_{x'z'} = \sigma_{y'z'} = 0$ together with a zero in-plane shear mismatch $\epsilon_{x'y'} = 0$ [Rom06]. Romanov *et al.* have calculated the strain tensor of a semipolar (or nonpolar) layer in our so-called (*x'*, *y'*, *z'*) system:

- $\epsilon_{x'x'} = \epsilon_{m1}$
- $\epsilon_{y'y'} = \epsilon_{m2}$
- $\epsilon_{z'z'} = \dfrac{(B_{41}\epsilon_{m1} + B_{42}\epsilon_{m2})A_{32} - (B_{31}\epsilon_{m1} + B_{32}\epsilon_{m2})A_{42}}{A_{31}A_{42} - A_{32}A_{41}}$
- $\epsilon_{y'z'} = \dfrac{(B_{31}\epsilon_{m1} + B_{32}\epsilon_{m2})A_{41} - (B_{41}\epsilon_{m1} + B_{42}\epsilon_{m2})A_{31}}{A_{31}A_{42} - A_{32}A_{41}}$

with:

- $A_{31} = C_{11}sin^4\theta + (\dfrac{1}{2}C_{13} + C_{44})sin^2(2\theta) + C_{33}cos^4\theta$
- $A_{32} = (C_{11}sin^2\theta + (C_{13} + 2C_{44})cos(2\theta) - C_{33}cos^2\theta)sin(2\theta)$
- $A_{41} = \dfrac{1}{2}((C_{11} - C_{13})sin^2\theta + 2C_{44})cos(2\theta) + (C_{13} - C_{33})cos^2\theta)sin(2\theta)$
- $A_{42} = (\dfrac{C_{11} + C_{33}}{2} - C_{13})sin^2(2\theta) + 2C_{44}cos^2(2\theta)$
- $B_{31} = C_{12}sin^2\theta + C_{13}cos^2\theta$
- $B_{32} = C_{13}(sin^4\theta + cos^4\theta) + (\dfrac{C_{11} + C_{33}}{4} - C_{44})sin^2(2\theta)$
- $B_{41} = \dfrac{C_{12} - C_{13}}{2}sin(2\theta)$
- $B_{42} = \dfrac{1}{2}(C_{11}cos^2\theta - (C_{13} + 2C_{44})cos(2\theta) - C_{33}sin^2\theta)sin(2\theta)$

Table 1.8 gives the values of the parameters A_{ij} and B_{ij}, calculated for both AlN($11\bar{2}2$) and GaN($11\bar{2}2$), from which we can deduce the misfit parameters $\epsilon_{i'j'}$.

We can finally calculate the components ϵ_{ij} expressed into the more commonly used strain tensor in the natural (x, y, z) system (where z values are measured along the c direction and the two in-plane indices are defined such that the x axis is parallel to the x' direction), from the equations:

- $\epsilon_{xx} = \epsilon_{x'x'}$
- $\epsilon_{yy} = \epsilon_{y'y'} \times cos^2\theta + \epsilon_{z'z'} \times sin^2\theta + \epsilon_{y'z'} \times sin2\theta$
- $\epsilon_{zz} = \epsilon_{y'y'} \times sin^2\theta + \epsilon_{z'z'} \times cos^2\theta - \epsilon_{y'z'} \times sin2\theta$
- $\epsilon_{yz} = \epsilon_{y'y'} \times cos^2\theta + \epsilon_{z'z'} \times sin^2\theta + \epsilon_{y'z'} \times sin2\theta$

Parameters (GPa)	AlN(11$\bar{2}$2)	GaN(11$\bar{2}$2)
A_{31}	371	340
A_{32}	27.9	20.5
A_{41}	13.9	10.2
A_{42}	268	264
B_{31}	129	126
B_{32}	126	140
B_{41}	13	14.3
B_{42}	-3.60	-27.2

Table 1.8: *Values of the parameters A_{ij} and B_{ij} calculated for AlN(11$\bar{2}$2) and GaN(11$\bar{2}$2), from the work of Romanov et al. [Rom06].*

Table 1.9 gives the misfit components ϵ_{ij} calculated for AlN(11$\bar{2}$2) and GaN(11$\bar{2}$2) grown on sapphire(1$\bar{1}$00), and GaN(11$\bar{2}$2) grown on AlN(11$\bar{2}$2).

Templates	sapphire(1$\bar{1}$00) template		AlN(11$\bar{2}$2)
Layers	AlN(11$\bar{2}$2)	GaN(11$\bar{2}$2)	GaN(11$\bar{2}$2)
ϵ_{xx}	-0.116	-0.137	0.024
ϵ_{yy}	0.168	0.606	0.035
ϵ_{zz}	-0.063	-0.540	-0.0002
ϵ_{yz}	-0.115	-0.327	-0.688

Table 1.9: *Values of ϵ_{ij} calculated for AlN(11$\bar{2}$2) and GaN(11$\bar{2}$2) grown on sapphire(1$\bar{1}$00), and GaN(11$\bar{2}$2) grown on AlN(11$\bar{2}$2).*

1.3.4 Plastic relaxation via the formation of dislocations or cracks

Dislocations are generated in the material in order to relax the stress and decrease the global energy of the system. They are linear defects which can propagate within the crystal along certain directions. Sugahara *et al.* have shown that the presence of dislocations can strongly alter the performance of optoelectronic devices since they behave as non-radiative recombination centers [Sug98]. Dislocations emerging during the growth due to the difference of lattice parameters between the substrate and the epilayer are called "misfit dislocations" and their Burgers vector, $\vec{b}$, depends on the stress which is accommodated by the formation of the dislocation. The most common dislocation type in wurtzite systems are threading dislocations (TDs) [Kap95, Chi96, Pon96] which are going through the whole film, from the interface with the substrate to the surface of the layer. The three following types of dislocations can be distinguished, depending on the angle formed by the Burgers vector and the dislocation line:

Edge-type dislocations are those with the Burgers vector perpendicular to the dislocation line. As illustrated in Fig. 1.10, half-a-plane is inserted perpendicularly to $\vec{b}$, *i.e.* to the gliding plane. In that way, the region on one side of the dislocation line has one plane more than the region on the other side. In the case of wurtzite nitrides, edge-type TDs are situated within $(1\bar{1}00)$ planes, and their line is along the [0001]-direction. Their Burgers vector is typically 1/3 $<1\bar{2}10>$, 1/3 $<11\bar{2}0>$, or 1/3 $<2\bar{1}\bar{1}0>$. Edge-type TDs are mainly generated at the first stages of the growth, when the islands coalesce [Hir91, Hey96].

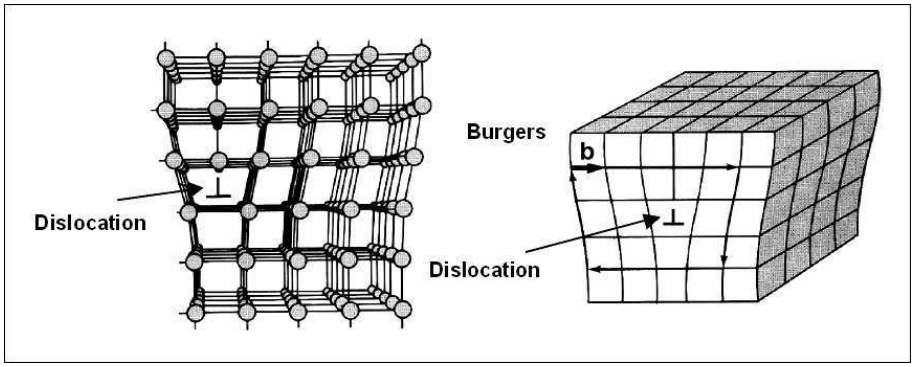

Figure 1.10: *Edge-type dislocation: $\vec{b}$ is perpendicular to the dislocation line.*

Screw-type dislocations present a dislocation line parallel to the Burgers vector. The defect is due to the collinear shift of the two regions separated by the dislocation line. Figure 1.11 represents the gliding plane and the lattice deformation due to a screw dislocation. For wurtzite III-nitrides, screw-type TDs are also within $(1\bar{1}00)$ planes and both their line and the Burgers vector are along $\vec{c}$.

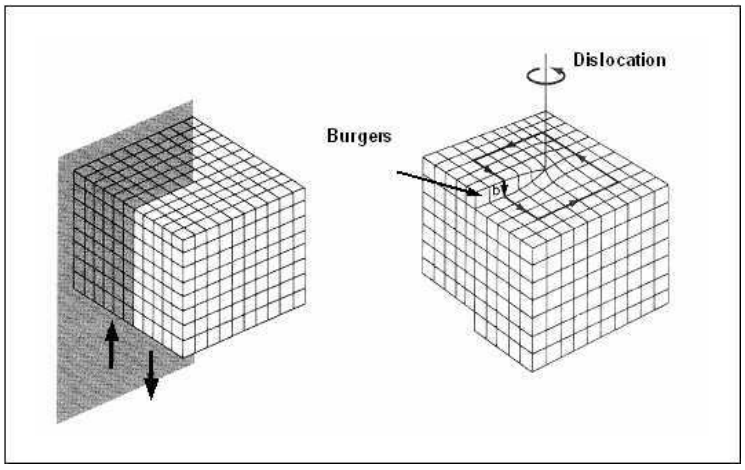

Figure 1.11: *Screw-type dislocation: $\vec{b}$ is parallel to the dislocation line.*

Finally, if $\vec{b}$ is forming an angle different from 0° or 90° with the dislocation line, it is called a **mixed dislocation**. Most of such dislocations can be decomposed into an edge-type and a screw-type dislocation. An example is shown in Fig. 1.12: it

is a screw-type dislocation when it enters the crystal, in (A), and it is an edge-type dislocation when it goes out, in (B). In the particular case of nitrides, the interaction between an edge-type and a screw-type TD automatically creates mixed TDs, so that their Burgers vector results from the two corresponding vectors ($b = 1/3[11\bar{2}3]$ for instance). Wu *et al.* have shown that mixed dislocations represent $\approx 60\%$ of the whole dislocations in the first 1 μm of a GaN epilayer, whereas edge-type TDs dominate in the region between 1 μm and 5 μm [Wu96].

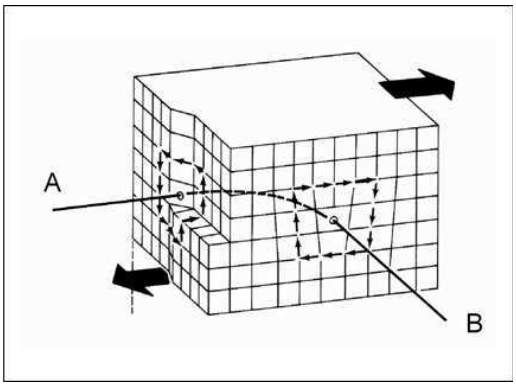

Figure 1.12: *Example of a mixed dislocation showing a screw component in (A) and an edge component in (B).*

Another way to relax the stress is via the creation of cracks in the layer. This process is associated to a plastic deformation in the sense that it is irreversible, but it induces an increase of the free surface, which is typical of the elastic relaxation phenomenon. Cracks can be observed into layers under tensile stress grown on sapphire [Etz01], Si [Sem01] or SiC [Per98].

1.4 Spontaneous and piezoelectric polarization

Since nitrogen atoms are more electronegative than metal atoms, bonds can be considered as an electrostatic dipole. This charge distribution in the tetrahedron is not compensated by the atomic stacking because of the lack of symmetry along the [0001]-direction, which results in a macroscopic spontaneous polarization $\vec{P}_{sp}$ in nitride materials. The values of spontaneous polarization calculated by Bernardini *et al.* are presented in Table 1.10 [Ber97].

	GaN	AlN	InN
P_{sp} (C/m^2)	-0.029	-0.081	-0.032

Table 1.10: *Calculated spontaneous polarization for wurtzite-type GaN, AlN and InN.*

Stress modifies the atomic positions in the crystal leading to a different distribution of the charges, and therefore to piezoelectric polarization ($\vec{P}_{pz}$). Knowing

the strain state of the lattice, it is possible to calculate $\vec{P_{pz}}$ from Eq. 1.9 thanks to the piezoelectric coefficients of the material, e_{ij}. The total polarization of the layer is the sum of the spontaneous and piezoelectric polarization.

$$\vec{P}_{pz} = \begin{pmatrix} 0 & 0 & 0 & 0 & e_{15} & 0 \\ 0 & 0 & 0 & e_{15} & 0 & 0 \\ e_{31} & e_{31} & e_{33} & 0 & 0 & 0 \end{pmatrix} \times \begin{pmatrix} \epsilon_1 \\ \epsilon_2 \\ \epsilon_3 \\ \epsilon_4 \\ \epsilon_5 \\ \epsilon_6 \end{pmatrix} \tag{1.9}$$

	GaN	AlN	InN	Ref
e_{15} (C/m^2)	-0.30	-0.48	-	[Amb00]
e_{31} (C/m^2)	-0.49	-0.60	-0.57	[Ber97]
e_{33} (C/m^2)	0.73	1.46	0.97	[Ber97]

Table 1.11: *Piezoelectric coefficients e_{15}, e_{31} and e_{33} calculated for GaN, AlN and InN.*

Chapter 2

Experimental techniques

The information given in this chapter is intended to serve as a reference for the understanding of the experimental results described in the following chapters.

The first section contains a general presentation of the epitaxial growth process. In particular, we expose the advantages of plasma-assisted molecular beam epitaxy (PAMBE) and the *in-situ* monitoring technique, namely Reflection High-Energy Electron Diffraction (RHEED). To introduce the state of the art in terms of PAMBE of nitrides, we discuss the growth diagram of III-nitride materials as a function of the crystalline orientation.

After a description of our PAMBE equipment and the substrates, the main characterization techniques used in this work will be presented. For the structural part, we will focus on X-ray diffraction (XRD) and Atomic Force Microscopy (AFM). We also depict the optical Photoluminescence (PL) and Time-Resolved Photoluminescence (TRPL) setups. Finally, we address the computational method used to simulate the electronic structures of the samples.

Contents

2.1 Plasma-assisted molecular beam epitaxy 25

2.1.1 Epitaxial growth 25

2.1.2 Heteroepitaxy 27

2.1.3 *In-situ* characterization: RHEED 27

2.2 PAMBE growth of III-nitrides 30

2.2.1 Growth diagram of *c*-plane nitrides 30

2.2.2 Growth of nonpolar nitrides 33

2.3 Description of the growth methods 34

2.3.1 PAMBE equipment 34

2.3.2 *m*-sapphire substrates 37

2.4 Structural and optical characterization 39
2.4.1 X-ray diffraction 39
2.4.1.1 Diffraction theory 39
2.4.1.2 Description of the diffractometer 40
2.4.1.3 Sample alignment 43
2.4.1.4 Symmetrical and asymmetrical reflections 43
2.4.1.5 Effect of the presence of crystalline defects on reciprocal space maps 44
2.4.1.6 Determination of lattice parameters in the case of semipolar nitrides. 47
2.4.2 Atomic-force microscopy 50
2.4.3 Photoluminescence spectroscopy 53
2.5 Simulation of electronic structures 54

2.1 Plasma-assisted molecular beam epitaxy

2.1.1 Epitaxial growth

Epitaxy is defined as the deposition of a monocrystalline film on a monocrystalline substrate, keeping a certain lattice alignment known as epitaxial relationship. We speak about heteroepitaxy when the substrate and the epilayer are different materials.

High quality epitaxial thin films can be synthesized via chemical deposition (Chemical Vapor Deposition, CVD) or physical deposition (Molecular Beam Epitaxy, MBE). In comparison to CVD techniques, MBE presents several advantages which stem from its lower growth temperature and *in situ* monitoring via Reflection High-Energy Electron Diffraction (RHEED):

- Good control of layer thickness, due to a low growth rate (less than one monolayer (ML) per second) and reduced interdiffusion effects.
- Synthesis of a wide range of ternary or quaternary alloys. Even materials that are barely miscible under thermodynamic equilibrium can be dynamically stabilized by MBE.
- Higher dopant concentrations thanks to the minimization of segregation effects.

In the particular case of III-nitrides, additional advantages can be found:

- Possibility to change the material polarity, depending on the substrate or buffer layer.
- Activation of Mg-dopant is not required, because of the H-free growth environment.

The epitaxial growth process depends on the impinging fluxes on the one hand and the substrate temperature on the other hand. The substrate temperature is the key parameter which activates the different phenomena occurring at the growing surface. Figure 2.1 depicts the different atomistic processes that can take place at the surface during epitaxial growth.

The impinging fluxes can be adsorbed at the surface by chemisorption (if chemical bonds are created via a transfer of electrons between impinging atoms and atoms from the surface) or physisorption (if the atoms are adsorbed via Van der Waals forces) [Fig. 2.1(a)]. At a given substrate temperature and concentration, the atoms have a certain mobility. Some of the species will diffuse and be desorbed without being incorporated to the layer [Fig. 2.1(f)], whereas the others will incorporate either by step-edge growth [Fig. 2.1(c)] forming atomic terraces [Fig. 2.1(d)], or by cluster nucleation [Fig. 2.1(e)].

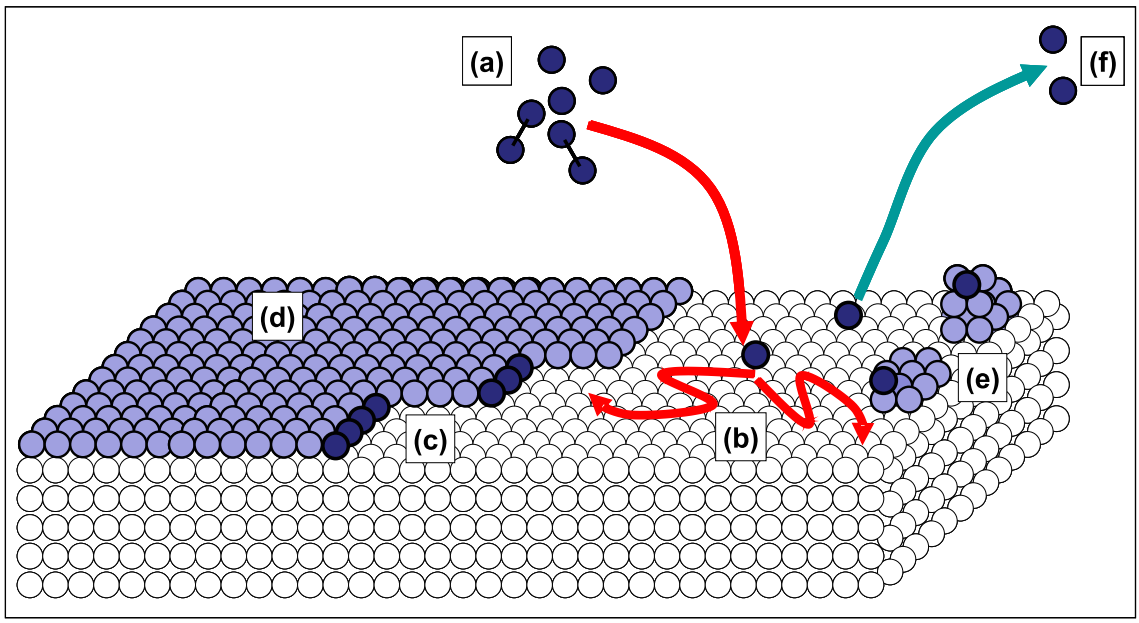

Figure 2.1: *Atomistic processes that can occur at the surface during the growth: (a) adsorption, (b) diffusion, (c) step-edge growth, (d) atomic terraces, (e) nucleation of clusters and (f) desorption.*

Figure 2.2 represents a side view of a growing surface, with the corresponding potential seen by the adatoms. As illustrated, atomic step-edges are often energetically favorable incorporation sites, due to the damping of the potential [point B]. Indeed, for adatoms situated onto the adjacent terrace [position b], a sufficient diffusion length can lead to the incorporation into site in c. Adatoms situated onto an upper terrace face an additional energy barrier (Schwoebel barrier) [position a] for diffusion towards the lower step. If they have enough energy to cross the Schwoebel barrier, they will incorporate into the lower step-edge [position c]. If their diffusion length is shorter than the average distance between steps, adatoms will nucleate to form clusters on the surface, or incorporate into already existing clusters.

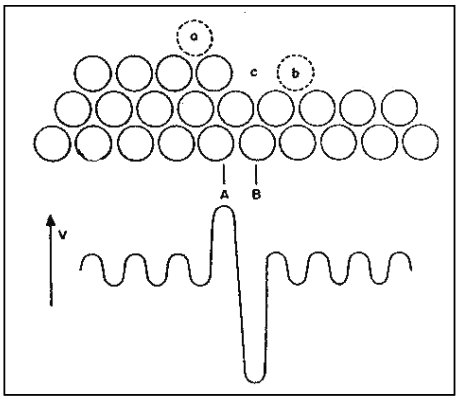

Figure 2.2: *Transversal view of a surface showing atomic steps and the corresponding potential seen by the adatoms.*

2.1.2 Heteroepitaxy

Heteroepitaxy is the deposition of material A on material B. In this case, various growth modes can be observed, depending on the lattice mismatch between the materials and surface energy (see in Fig. 2.3):

- Layer-by-layer growth, also called **Frank Van der Merwe growth** [Fra49], is a two-dimensional (2D) growth process. In the case of lattice mismatch, strain is released via the introduction of dislocations.
- Three-dimensional (3D) growth, called **Volmer-Weber growth** [Vol26] is characterized by the nucleation of small islands directly on the heterointerface.
- **Stranski-Krastanov growth** [Str38] is an intermediate growth mode: the growth starts 2D following the layer-by-layer mode with the formation of one or several monolayers. Once a certain critical thickness θ_{limit} is reached, this 2D growth becomes energetically unfavorable and the growth continues with the formation of islands.

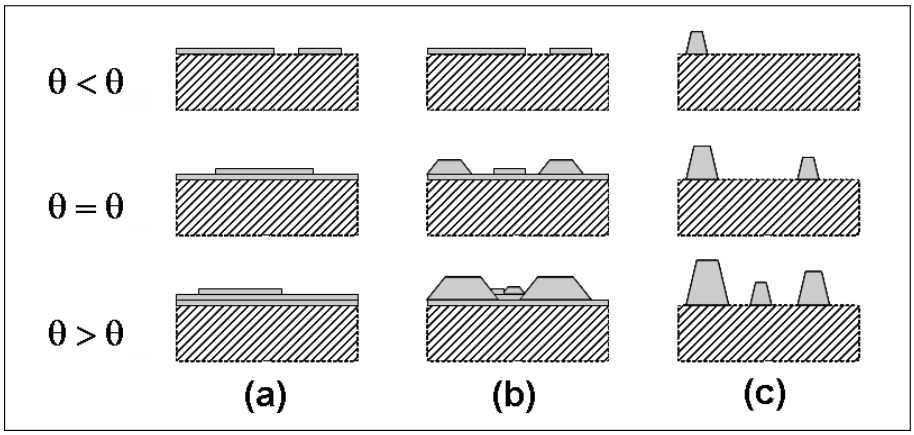

Figure 2.3: *Illustration of (a) Frank Van der Merwe, (b) Stranski-Krastanov and (c) Volmer-Weber growth modes*

2.1.3 *In-situ* characterization: RHEED

RHEED is a characterization technique that presents the advantage of being *in situ* and in real time. As illustrated in Fig. 2.4, the technique is based on the diffraction of an electron beam by the surface of the growing sample. It requires ultra-high vacuum to guarantee that the probability of interaction between the incident beam and particles of the environment must be very low. Electrons are accelerated under high voltage (typically 32 kV in our system) and emitted by a filament excited by a 1.5 A current. The electrons are diffracted by the surface of the growing sample and impinge on a fluorescent screen, so that the image displayed on the screen is the Fourier transformation of the lattice interacting with the beam.

The incident beam forms a small angle $\theta \approx 2°$ with the surface so that it is only diffracted by the first atomic planes below the surface. When the incident beam is parallel to the [*hkil*] crystallographic direction, it is said that the RHEED pattern is observed along the <*hkil*> azimuth.

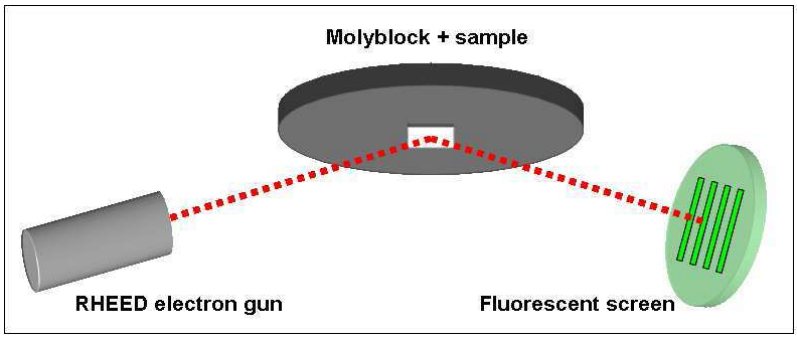

Figure 2.4: *Illustration of the RHEED measurement setup.*

An ideal monochromatic beam with a wavelength λ can be described by the incoming wave vector $\vec{k_i}$, with $||\vec{k_i}|| = \frac{2\pi}{\lambda}$. If the outgoing diffracted beam is denoted by $\vec{k_o}$, the diffraction laws give the following condition of diffraction:

$$\vec{k_o} - \vec{k_i} = \vec{r^*} \tag{2.1}$$

where $\vec{r^*}$ is a reciprocal vector of the surface. Eq. 2.1 can be schematically represented by an Ewald sphere construction illustrated in Fig. 2.5. The Ewald sphere is a sphere centered on the sample with a radius $||\vec{k}||$. The diffraction pattern is the intercept between the Ewald sphere and the representation of the lattice surface in the reciprocal space.

As illustrated in Fig. 2.5, the reciprocal space of a perfect surface is a bidimensional lattice of diffraction rods perpendicular to the surface. The intercept of the Ewald sphere with such a system are spots aligned in circles, called Laue zone. However, a certain broadening of both the rods (originating from the unavoidable roughness of a real surface) and the Ewald sphere (due to the fact that the electron beam is not strictly monochromatic) combined with the large radius of the Ewald sphere with respect to the distance between the rods actually leads to the observation of diffraction lines instead of diffraction spots.

Since the RHEED pattern is an image of the reciprocal space of the surface lattice, the distance between the rods is inversely proportional to the distance between the atomic ranges which diffract the beam [Mah90]. Figure 2.6 is a typical RHEED image of a 2D surface. To determine the relative in-plane lattice parameter, $\Delta a/a_0$, an intensity profile is obtained by integration over a rectangular box. The distance between the outer streaks is measured by fitting the intensity profile with Gaussian curves. This type of measurement provides information on the lattice relaxation processes.

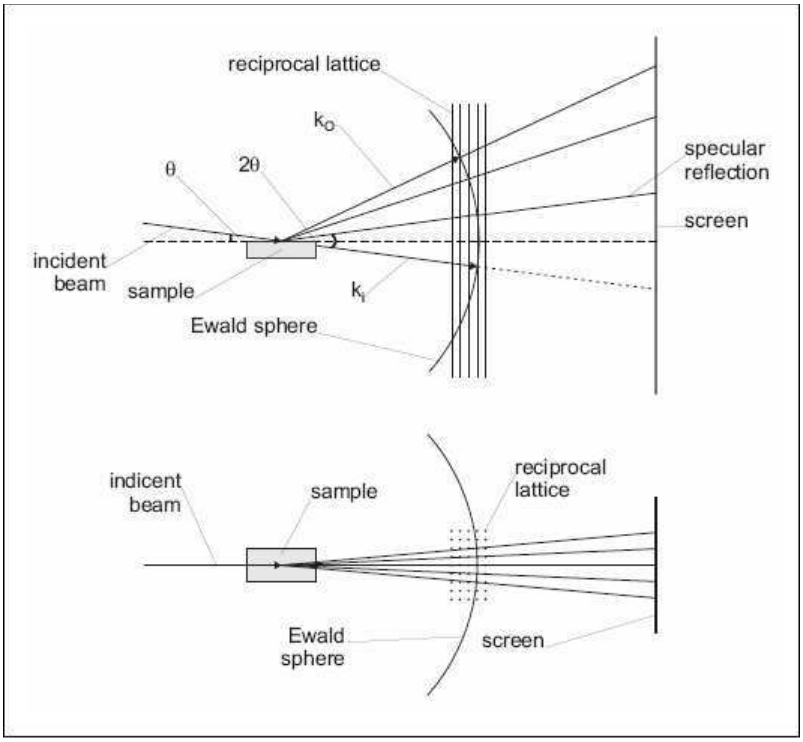

Figure 2.5: *RHEED principle illustrated by the schematic representation of the Ewald construction: side view (top) and top view (bottom) with respect to the sample.*

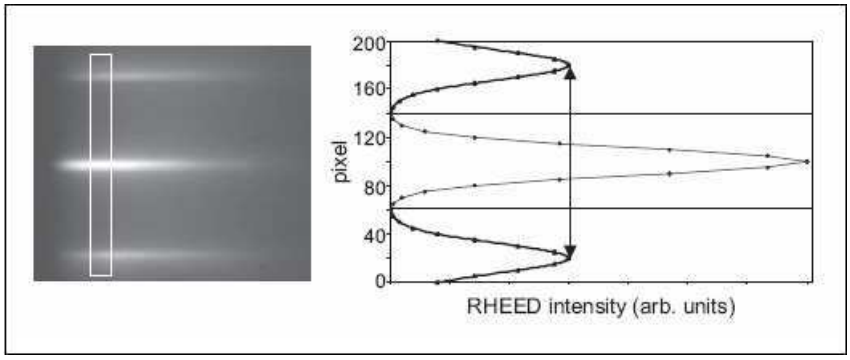

Figure 2.6: *Typical streaky RHEED pattern of a 2D surface. The determination of the in-plane lattice parameter from the intensity profile is schematically shown.*

Besides, another application of RHEED is the measurement of the growth rate from RHEED intensity oscillations. In a layer-by-layer growth mode, the period of these oscillations is equal to the deposition time of one monolayer [Nea83]. This is due to the fact that the intensity of the specular reflection is sensitive to the surface roughness [Cla87]: when a new monolayer grows, the surface roughness increases because of the presence of new nucleation sites. However, once half-coverage is reached the roughness decreases since the quantity of terraces on the first level is higher than the holes to fill (see Fig. 2.7).

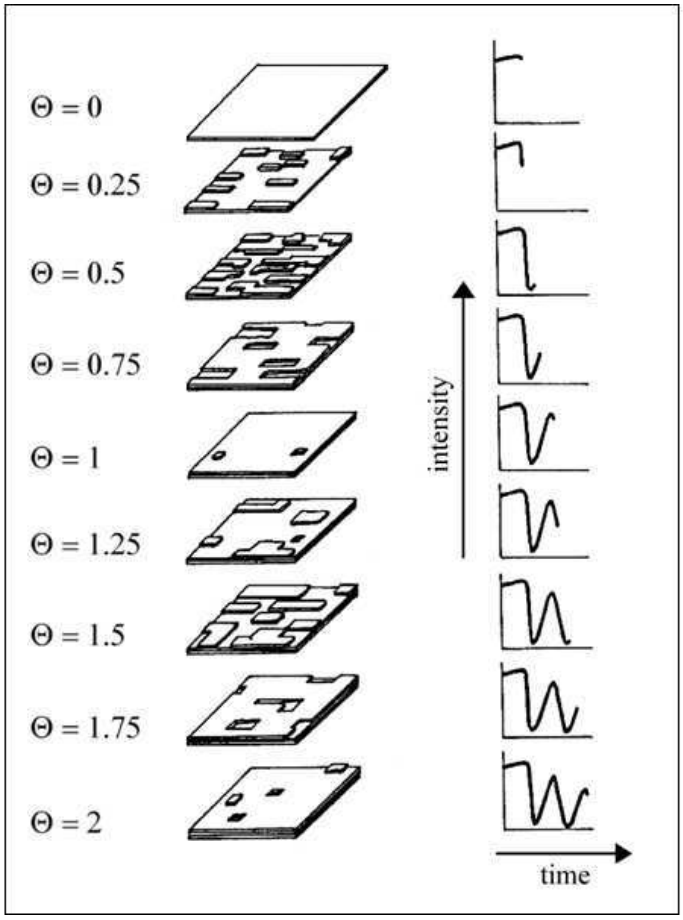

Figure 2.7: *Schematic illustration of the origin of RHEED oscillations: The intensity of the specularly reflected electron beam depends on the step density of the sample surface, which changes with the surface coverage* Θ *of the growing layer [Joy86].*

2.2 PAMBE growth of III-nitrides

The PAMBE growth of III-nitrides is performed under constant nitrogen flux which imposes the growth rate. The key parameters which control the crystalline quality and growth kinetics are the substrate temperature, which determines the adatoms kinetics, and the metallic flux, *i.e.* the III/V ratio. The appropriate growth conditions to obtain a 2D layer depend on the nature (composition, orientation) of the growing surface, and can be influenced by the presence of dopants or pollutants. In this section, I will briefly expose the growth conditions of *c*-plane, *a*-plane and *m*-plane III-nitrides.

2.2.1 Growth diagram of *c*-plane nitrides

a) Growth of GaN(0001)

The III/V ratio is a key parameter for GaN growth [Hey00b] [Ade03]. N-rich conditions (III/V < 1) reduce adatom mobility, which leads to rough surfaces. On

the other hand, high Ga-rich conditions (III/V >> 1) result in Ga accumulation at the surface. It is hence necessary to study the Ga wetting of the GaN surface to determine the appropriate growth conditions for 2D layers. The Ga excess can be quantified *in situ* and in real time by RHEED measurements. With this purpose, the GaN surface is exposed to a certain Ga flux, and we study the desorption of Ga under vacuum after stopping the exposure. The RHEED transient duration depends on the amount of Ga which was on the surface [Ade03].

Figure. 2.8 presents the evolution of Ga coverage depending on Ga flux for a GaN sample at $T_{sub} = 740°C$ and being exposed to Ga for 1 min. Four regimes can be distinguished:

- A: There is a very small coverage of Ga on the surface of less than 1ML ($\phi_{Ga} < 0.3$ ML/s).

- B: The GaN surface is covered with about 1ML of Ga (0.3 ML/s $< \phi_{Ga} <$ 0.5 ML/s).

- C: A Ga bilayer is formed at the GaN surface (0.5 ML/s $< \phi_{Ga} < 1$ ML/s).

- D: Ga accumulates at the surface of the Ga bilayer, forming Ga droplets ($\phi_{Ga} > 1$ ML/s).

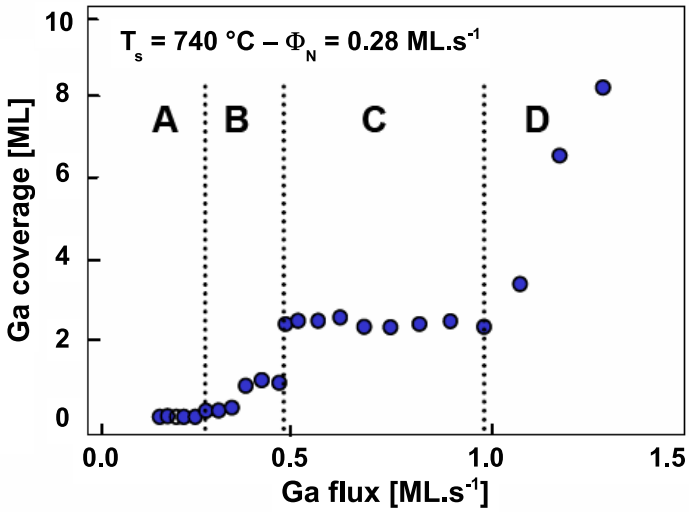

Figure 2.8: *Ga coverage on top of the GaN(0001) surface as a function of Ga flux.*

Figure 2.9 shows the dependence of Ga coverage as a function of both Ga flux and substrate temperature. The four regimes exist for substrate temperatures above 700°C, and the higher the temperature, the higher the flux required to accumulate Ga, due to Ga desorption. However, for $T_{sub} \geq 750°C$, the GaN decomposition becomes important, which makes it more difficult to stabilize the growth.

Adelmann *et al.* have shown that the morphology of the GaN surface strongly depends on the Ga coverage [Ade02]. The AFM images in Fig. 2.9 show that if GaN

is grown with Ga coverage < 2ML, it presents a rough surface, whereas atomic steps can be seen of GaN grown under Ga excess (regime C). This regime is characterized by the formation of a Ga bilayer, as schematized in Fig. 2.10, which consists of two Ga layers adsorbed on top of the Ga-terminated GaN(0001) surface [Neu03, Fee02, Nor00]. The first Ga adlayer is supposed to be pseudomorphic to the GaN surface, but the second Ga adlayer is laterally contracted, presenting an in-plane lattice constant close to the Ga-Ga bond length in bulk Ga (≈ 2.75 $\AA$).

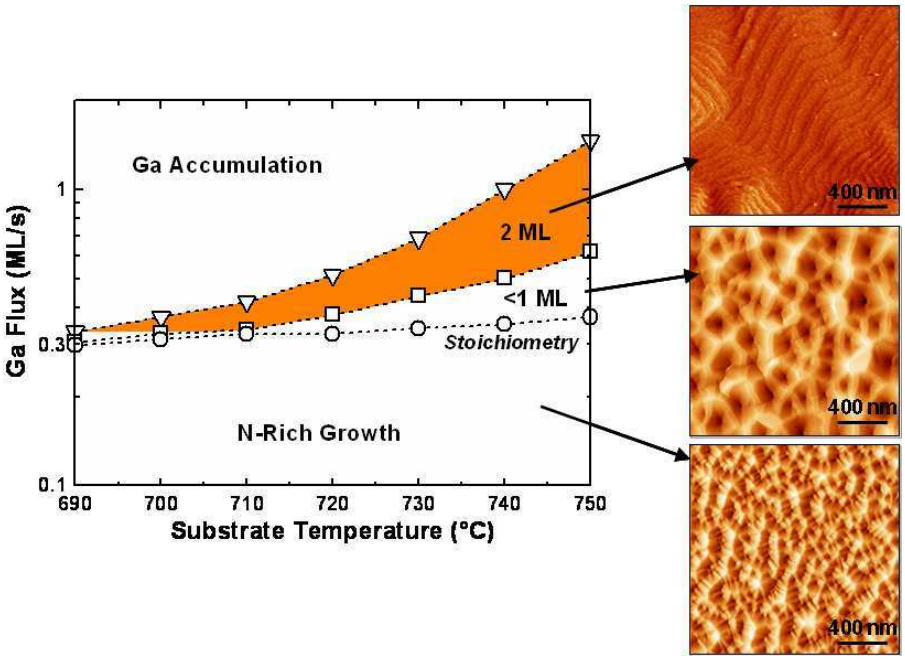

Figure 2.9: *Ga coverage regimes as a function of both substrate temperature and Ga flux [Ade02].*

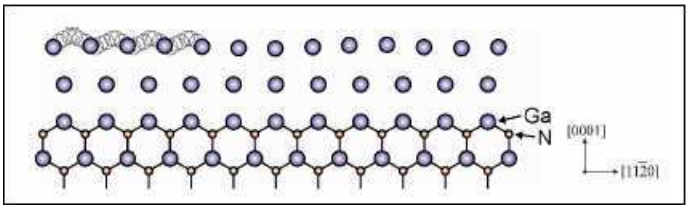

Figure 2.10: *Illustration of the Ga bilayer on top of the GaN surface, viewed along the [1$\bar{1}$00] azimuth.*

b) Growth of AlN(0001)

AlN growth at temperatures lower than $\approx 770°C$ is similar to GaN growth at very low temperatures ($\approx 600°C$), in the sense that the metal is barely desorbed from the surface. Under higher temperatures ($T \geq 800°C$) Al starts to desorb and the growth is optimized with a self-regulated Al coverage on the AlN surface [Kob03]. Since such high temperatures can not be reached in our system, AlN(0001) grown

under Al excess presents Al droplets which are periodically consumed by exposure to nitrogen flux.

Figure. 2.11(a) shows a typical RHEED pattern during 2D AlN growth. We can observe the presence of two additional lines (indicated by the arrows) which indicate the presence of a layer with a smaller lattice parameter, attributed to crystalline incoherent Al. By plotting the intensity profile [Fig. 2.11(b)], we can measure that the difference between the lattice parameter of AlN and Al layers is 11.1%. Hence the Al layer lattice parameter is $a_{Al} = 2.77 \pm 0.03\mathring{A}$. The consumption of this Al excess under nitrogen flux allows us to determine the stoichiometry and to calibrate the Al flux.

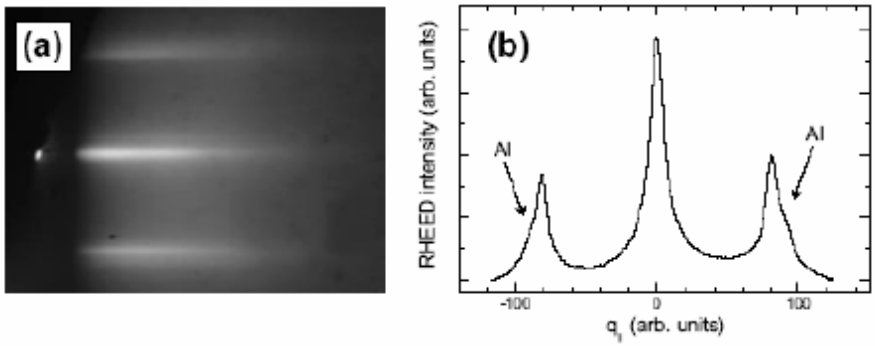

Figure 2.11: *(a) RHEED image of an Al-rich AlN surface (azimuth $11\bar{2}0$). (b) Intensity profile along the [$10\bar{1}0$] direction. One observes two extra streaks due to Al excess.*

2.2.2 Growth of nonpolar nitrides

The interest of nonpolar crystallographic orientations is motivated by the wish to suppress of the internal electric field present in polar *c*-plane structures. Nonpolar planes are those with the *c*-axis in the growth plane. Recent studies have addressed the synthesis of ($11\bar{2}0$) *a*-plane and ($1\bar{1}00$) *m*-plane nitrides. The two following paragraphs describe the PAMBE growth of GaN and AlN on nonpolar *a*-plane and *m*-plane surfaces.

a) Growth of a-plane nitrides

The growth of nonpolar ($11\bar{2}0$) nitrides is usually performed on ($10\bar{1}2$) *r*-plane sapphire [Ng02,Cra02] or ($10\bar{1}2$) *a*-plane 6H-SiC [Ono02,Cra04,Fou05]. When grown on SiC, AlN and GaN present a different stress state: AlN is under compressive stress along [$1\bar{1}00$] and tensile stress along [0001] whereas GaN is under compressive stress along both in-plane directions. This anisotropic stress enhances the anisotropic in-plane properties for AlN layers. In terms of surface roughness, AlN and GaN layers seem to be optimized when grown under nitrogen excess, which is strictly the opposite than for GaN(0001). Based on the work of Founta *et al.* [Fou07],

self-regulated growth conditions equivalent to the Ga bilayer on GaN(0001) do not exist for PAMBE growth of *a*-plane GaN. This corroborates the relevance of the crystalline orientation on the surface energy equilibrium during the growth.

b) Growth of m-plane nitrides

This paragraph is mainly based on the work of Amstatt *et al.*, on the PAMBE growth of $(1\bar{1}00)$ nitrides on 6H-SiC [Ams08]. The strong anisotropy of AlN$(1\bar{1}00)$ leads to the same phenomenon as for AlN$(11\bar{2}0)$, *i.e.* elongation of the surface patterns along [0001]. GaN$(11\bar{2}0)$ also displays isotropic surface roughness, whereas GaN$(1\bar{1}00)$ shows wave-shaped surfaces, with elongated patterns along $[11\bar{2}0]$. *Ab-initio* calculations of the thermodynamics and adatom kinetics on nonpolar GaN surfaces by Lymperakis *et al.* [Lym08, Lym09] explain the anisotropy of the surfaces as resulting from the higher diffusion length of Ga adatoms along $[11\bar{2}0]$ than along [0001]. Figure 2.12 illustrates the kinetics barriers of both *m*-plane and *a*-plane surfaces.

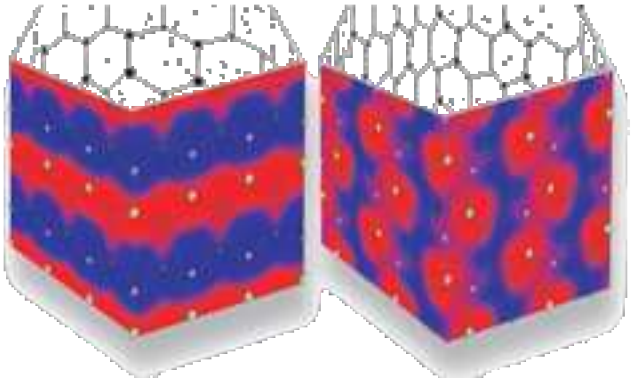

Figure 2.12: *Illustration of the calculated surface kinetics potential of m-plane and a-plane surfaces [http://www.mpie.de/iii-nitride-nanostru/?type=1].*

In terms of growth conditions, both *m*-AlN and *m*-GaN layers present the best surface morphology when grown under metal-rich conditions. For both orientations, the study of GaN growth kinetics have pointed out the existence of a self-regulated regime around 2 ML, equivalent to the Ga bilayer regime for GaN(0001) growth [Fou07, Ams08]. When compared to GaN(0001), this self-regulated regime is shifted towards higher Ga fluxes.

2.3 Description of the growth methods

2.3.1 PAMBE equipment

First MBE systems were developed in the early 70' at Bell Laboratories, by J. R. Arthur for the growth of GaAs layers [Art68] and A. Cho for the fabrication of devices [Cho75a, Cho75b]. Nowadays it is widely used for the synthesis of small objects like quantum wells (QWs), quantum dots (QDs) or nanowires (NWs) based

on different materials. The MBE technique consists on the evaporation of the desired materials and dopants under ultra-high vacuum. The evaporated atoms impinge on a properly heated substrate where they condense and grow epitaxially. Figure 2.13 is an illustration of the plasma-assisted MBE (PAMBE) system I used. It consists of three chambers, each one with its own pumping system. They are separated by gate valves which can only be opened once the pressure at both sides is in the same range.

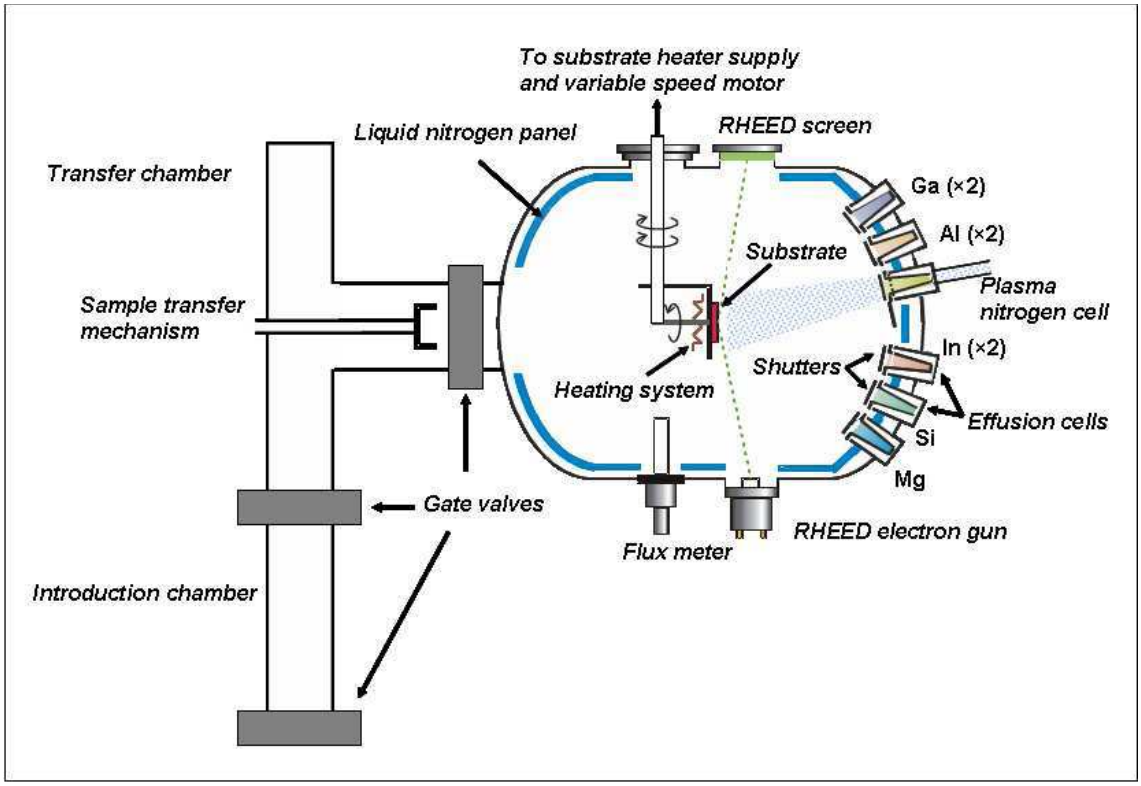

Figure 2.13: *Schematic of a typical MBE growth chamber dedicated to III-nitrides epitaxy.*

The **introduction chamber** is the chamber through which the substrates are entered in the machine. It is pumped thanks to the combination of turbomolecular and ionic pumping systems, reaching $\approx 10^{-8}$ Torr. The chamber is only opened under nitrogen overpressure in order to limit air pollution. The substrates are indium-glued on a 2 inch molybdenum sample holder (molyblock) and introduced in the machine onto a cart which can contain up to 18 molyblocks. The cart is brought from the introduction chamber to the **transfer chamber**, passing through a gate valve. With a ionic pumping system, the transfer chamber pressure is $\approx 10^{-10}$ Torr. Virgin substrates are stocked in this chamber before the growth and the transfer arm allows us to select and enter a new molyblock into the **growth chamber**.

The **growth chamber** is the main body of the machine. It is continuously under both cryogenic pumping and liquid-nitrogen cooling on the walls so that the

pressure in the chamber can be kept in the range of 10^{-11} Torr. As schematized in Fig. 2.13, the molyblock entered in the center of the chamber is mounted onto the manipulator, which can be rotated from transfer position to growth position. In growth position, the substrate is facing the effusion cells providing the elements for the epitaxial growth. The substrate is heated by irradiation of a hot filament and its temperature is controlled using a thermocouple in mechanical contact with the molyblock. To insure a homogeneous deposition, the molyblock is in-plane rotating during the growth. The growth chamber is equipped with a mass spectrometer and a RHEED system whose principle will be described in the following paragraph.

Impinging metal elements (Ga, Al, In, Mg and Si) are provided by **effusion cells** oriented towards the center of the growth chamber. Our chamber is equipped with 2 cells of each group III element (Ga, Al, and In) and one cell for each dopant (Si and Mg). Figure 2.14 shows a typical effusion cell used in our MBE system. The solid charge of the material is placed into a cylindrical or conical crucible heated by a filament, whose current is controlled using a thermocouple in contact with the backside of the crucible. The atomic flux Φ depends on the temperature following Eq. 2.2 where E_F is the effusion energy, characteristic for the evaporated material.

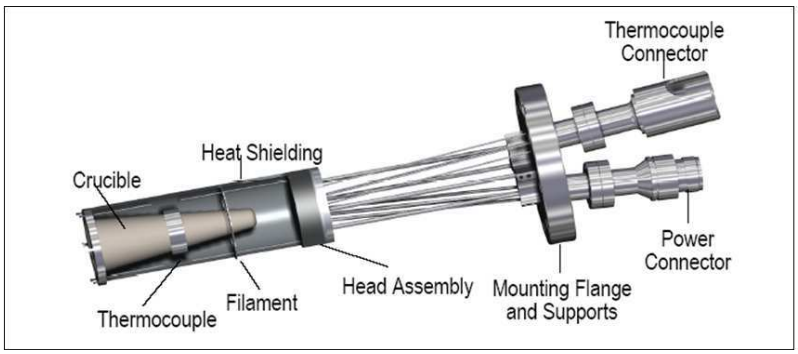

Figure 2.14: *Description of a typical effusion cell.*

$$\Phi = \Phi_0 \exp\left(-\frac{E_F}{k_B T}\right) \tag{2.2}$$

Active nitrogen is provided by a **plasma cell**, whose operating principle is illustrated in Fig. 2.15. Our system is equipped with a radiofrenquency (RF) plasma-cell HD-25 from Oxford Applied Research. Nitrogen molecules coming into the cell are resonantly excited and dissociated by a 13.56 MHz RF electromagnetic wave. To adjust the growth rate, the N flux can be varied from 0.2 sccm to 2 sccm and the excitation power from 300 W to 500 W. For our experiments, the growth rate was $\approx$ 0.27 - 0.30 monolayers per second (ML/s), i.e. $\approx$ 260 nm/h.

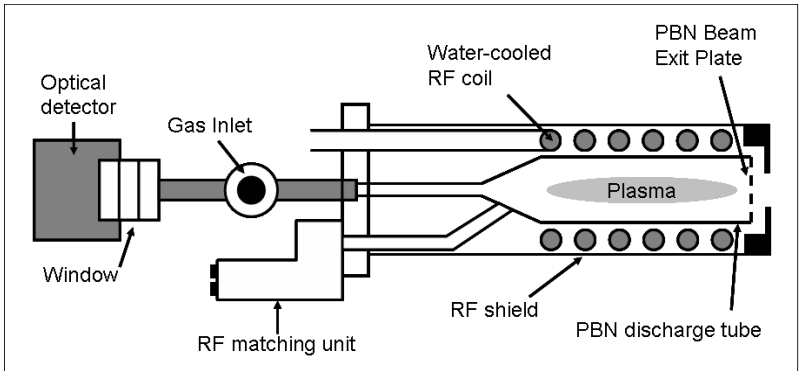

Figure 2.15: *Schematic of the RF plasma cell mounted in our PAMBE system.*

2.3.2 *m*-sapphire substrates

Among the substrates used for the growth of III-nitrides, we can cite sapphire (Al_2O_3), Silicon Carbide (SiC) or even Silicon. Sapphire can be described either in a rhomboedric or hexagonal system. In this latter case, the lattice parameters are a = 4.765 $\AA$ et c = 12.982 $\AA$ at 300 K (Fig. 2.16).

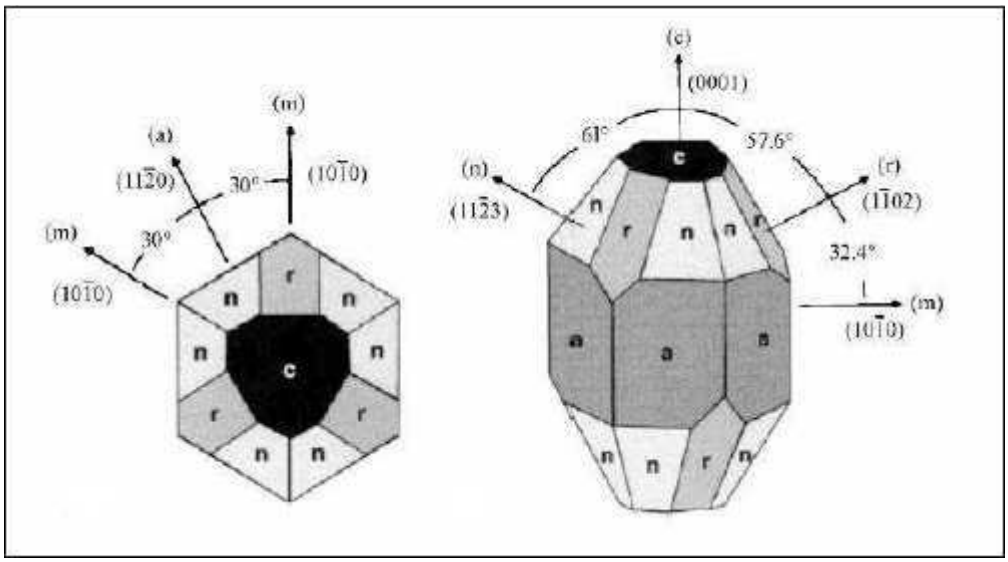

Figure 2.16: *Illustration of the sapphire structure and the particular crystallographic planes noted (a), (m) and (r). The image on the left represents the structure viewed along [0001] direction [Liu02].*

As presented in section 2.2.2, the synthesis of 2D nonpolar heterostructures remains challenging due to the strong surface anisotropy. An alternative approach is the growth of semipolar III-nitrides. Semipolar $(hkil)$ planes are those with a nonzero h, k or i and a nonzero l Miller index. Theoretical studies have shown that semipolar orientations can minimize the internal electric field by compensating the spontaneous and piezoelectric polarization [Tak00]. Several semipolar ori-

entations for films epitaxially grown on spinel or sapphire substrates have been reported: GaN(10$\bar{1}$1) on spinel(100), GaN(10$\bar{1}\bar{3}$) on spinel110 [Bak05], and either GaN(10$\bar{1}\bar{3}$) or GaN(11$\bar{2}$2) on 10$\bar{1}$0-oriented sapphire depending on the growth conditions [Bak06].

In this work, we used (1$\bar{1}$00) *m*-plane sapphire substrates from Kyocera corporation. The atomic arrangement on the *m*-sapphire surface is presented in Fig. 2.17. The two in-plane lattice parameters are a = 4.758 $\mathring{A}$ and c/4 = 3.245 $\mathring{A}$. Note that this former parameter is an average since the atomic distribution is not exactly periodic. This implies a RHEED pattern periodicity larger along $<11\bar{2}0>_{sapphire}$ than along $<0001>_{sapphire}$. Hence the assignment of Fig. 2.18(a) and (b) to $<0001>_{sapphire}$ and $<11\bar{2}0>_{sapphire}$ azimuths respectively.

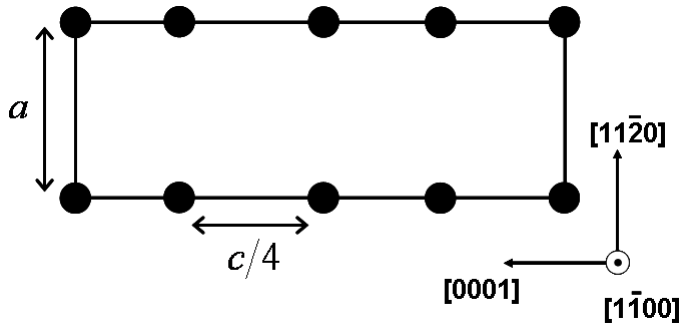

Figure 2.17: *Illustration of Al atomic distribution on sapphire(1$\bar{1}$00) surface.*

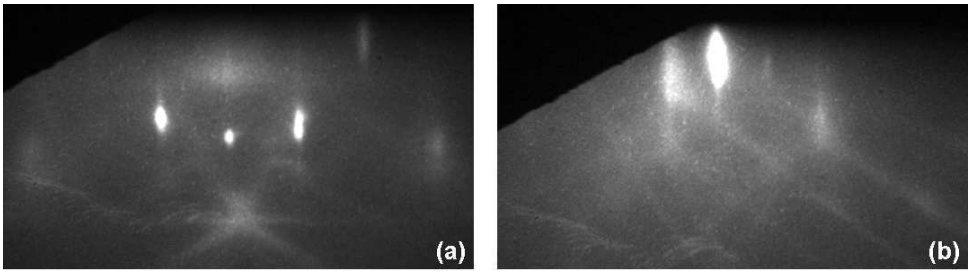

Figure 2.18: *RHEED patterns of m-sapphire viewed along the (a) <0001> and (b) <11$\bar{2}$0> azimuths.*

The AFM image of a typical surface of these substrates is pictured in Fig. 2.19, showing a root mean square (RMS) roughness of about 0.08 nm.

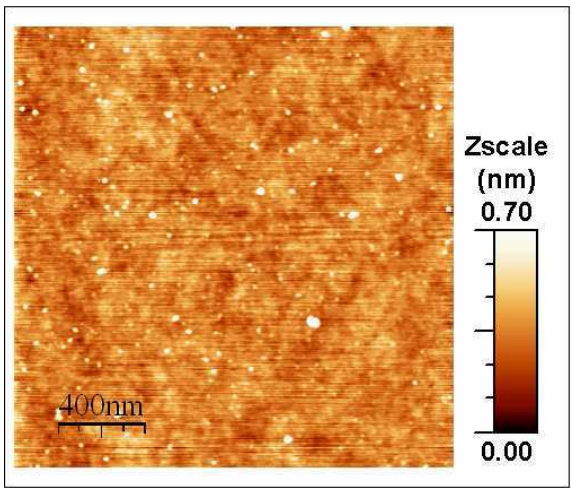

Figure 2.19: *AFM image of a m-sapphire substrate surface.*

2.4 Structural and optical characterization

This section describes the main methods applied to characterize the structural and optical properties of the samples: X-Ray Diffraction (XRD), Atomic Force Microscopy (AFM) and PhotoLuminescence (PL) spectroscopy. All these techniques present the advantage of being non destructive. The defects and fine structure of the samples were also investigated by Transmission Electron Microscopy (TEM) by our collaborators.

2.4.1 X-ray diffraction

XRD has been widely used to probe the crystalline quality of the samples, to verify their crystalline orientation, to identify the epitaxial relationships and to determine the lattice parameters. An X-ray beam impinges on the sample and is diffracted by a selected plane family. The diffraction pattern is analyzed by a punctual detector.

2.4.1.1 Diffraction theory

In kinematical diffraction, the amplitude of the scattered wave ψ is given by

$$\psi(\vec{g}) = \int d^3\vec{x}\rho(\vec{x}) \exp(-i\vec{g}\vec{x}), \tag{2.3}$$

where $\vec{g} = \vec{k_o} - \vec{k_i}$ and $\rho(\vec{x})$ is the electron density of the scattering medium. In a periodic crystal lattice, $\rho(\vec{x}) = \sum_n \rho_n(\vec{x} - \vec{x_n})$, so that the Fourier integral can be written as a discrete Fourier sum:

$$\psi(\vec{g}) = \sum_n f_n \exp(-i\vec{g}\vec{x_n}) \tag{2.4}$$

with the scattering factor of the n^{th} atom, f_n, defined as the Fourier transform of the charge distribution of an individual atom:

$$f_n = \int d^3\vec{x}\rho_n(\vec{x} - \vec{x_n}) \exp(-i\vec{g}(\vec{x} - \vec{x_n})) \tag{2.5}$$

In general, f_n is an increasing function of the nucleus mass Z of the atom, *i.e.* heavier atoms diffract more efficiently. The diffracted intensity $I = \psi^*\psi$ reaches its maximum for $\vec{g} = \vec{r^*}$, where $\vec{r^*}$ is a reciprocal lattice vector defined by $\exp(-i\vec{r^*}\vec{x_n}) = 1$. This leads to the Laue condition for a maximum of the diffracted intensity:

$$\vec{k_o} - \vec{k_i} = \vec{r^*} \tag{2.6}$$

The Laue condition is equivalent to Bragg's law in real space:

$$2d_{hkil} \sin\theta = n\lambda \tag{2.7}$$

where θ is the angle between the incident beam and the planes diffracting it, d_{hkil} is the interplane distance for the $(hkil)$ family, λ is the beam wavelength and n is an integer called the order of diffraction.

2.4.1.2 Description of the diffractometer

XRD studies have been performed on a *Seifert XRD 3003 PTS* system (photographed on Fig. 2.21) which uses the Cu $k_{\alpha 1}$ wavelength, *i.e.* $\lambda = 0.154056$ nm. The equipment consists of three main parts: the beam generator, the sample holder (goniometer) and the detector.

The Cu X-ray beam generated by the tube is transformed into a parallel beam (0.01° divergent) by reflection onto a parabolic mirror (Fig. 2.20) with a parameter gradient, which additionally increases its intensity by a factor of 10.

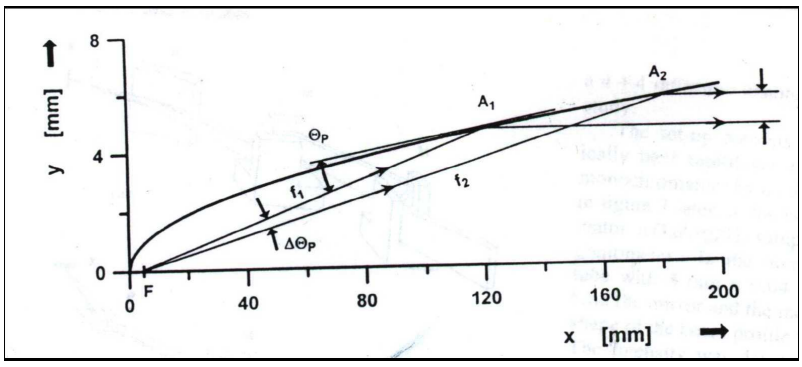

Figure 2.20: *Illustration of the beam concentration by the parabolic mirror.*

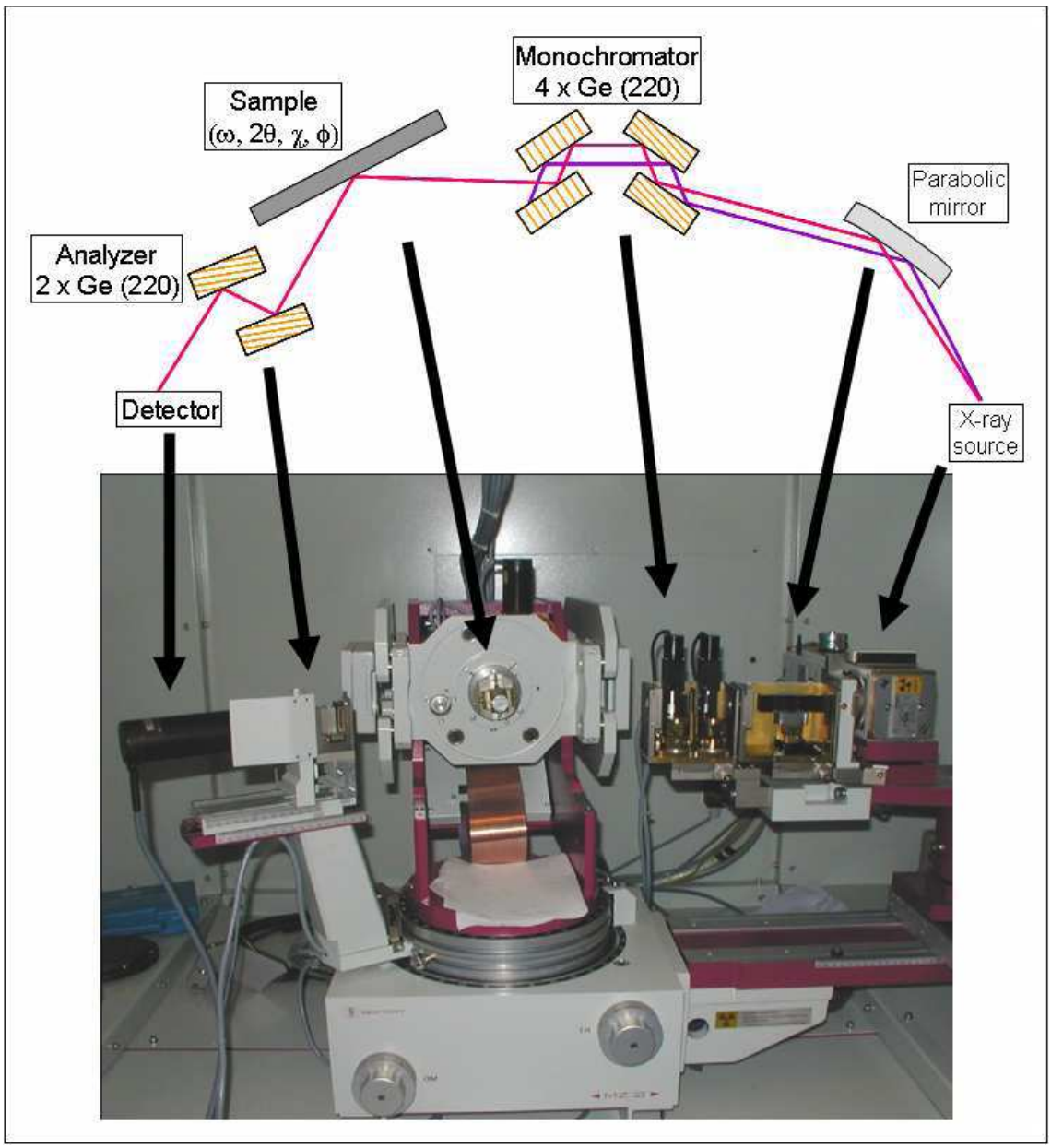

Figure 2.21: *Photograph and illustration of the X-ray diffraction system used in this work.*

Two monochromators, each of them consisting of two Ge(220) monocrystals, are mounted in the so-called "4-crystal" scheme (-n, +n, +n, -n) [Fig. 2.22(c)] [Bow]. This configuration reduces the angular [Fig. 2.22(a)] and wavelength [Fig. 2.22(b)] divergences of the beam. The resolution is improved by the diffraction of the beam by the crystals. Generally, the Ge(220) plane family is placed in diffraction condition, which leads to $\Delta\theta = 0.0033°$ and $\Delta\lambda/\lambda = 1.4 \times 10^{-4}$. It is also possible to select Ge(440) to increase the resolution to $\Delta\theta = 0.0014°$ and $\Delta\lambda/\lambda = 2.2 \times 10^{-5}$, but it decreases the beam intensity. Basically, each monochromator in the Ge(220) configuration reduces the beam intensity by a factor of 5 to 10.

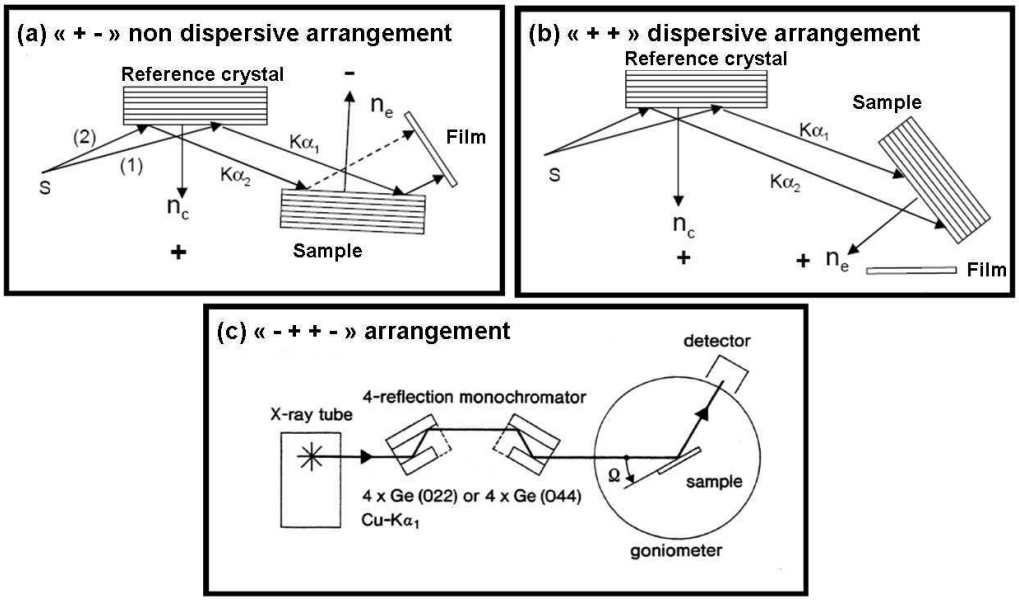

Figure 2.22: *Illustration of the effect of Ge monocrystals on the beam path.*

The goniometer allows selecting the plane family in diffraction condition by changing the orientation of the sample. It is called "4-circle" goniometer because it is possible to rotate independently the 4 angles, $(\omega, 2\theta, \phi, \chi)$, which determine the sample position (Fig. 2.23). The angle ω is the incident angle of the beam with the surface, 2θ the angle between the ingoing and outgoing beams, ϕ and χ the rotations around the normal of the sample (z-axis) and x-axis, respectively. Another part of the goniometer is dedicated to the movement along x, y and z axis, to center the sample. Two additional angles, χ_1 and χ_2, can be rotated around the x-axis and the y-axis, independently from the goniometer, in order to put the normal to the planes exactly along z-axis without using the χ angle. For each reflection, we can measure ω, 2θ or $\omega - 2\theta$ scans. It is also possible to make a two-dimensional scan around a reflection, *i.e.* draw a local mapping of the reciprocal space, by moving both ω and 2θ angles.

The detector has an aperture of 2° which can be reduced by inserting slids in order to improve the resolution of the diffracted beam. For HRXRD measurements, an analyzer is placed between the sample and the diffracted beam (Fig 2.21). It consists of two Ge(220) monocrystals which improve the angular precision of the diffracted beam ($\leq 0.001°$). In this configuration, the direct beam intensity is higher than 10^6 counts per seconds (cps) and the noise is less than 1 cps. When the maximal intensity of the diffracted beam is weak, it can be enhanced by the two following setup modifications:

↪ Replacement of the analyzer by a collimator, in front of the detector to profit from an acceptance of 0.2°. This operation mode does not modify the precision on the ω angle but leads to a broadening of θ and $\theta - 2\theta$ scans and the noise increases to the range of 10 cps. However, if the substrate is glued onto a

disoriented Si holder, the noise is decreased to 1 cps.

↪ Removal of one of the monochromators situated right after the parabolic mirror, in order to enhance the intensity of the impinging beam. We used this so-called low resolution mode for the study of the layers.

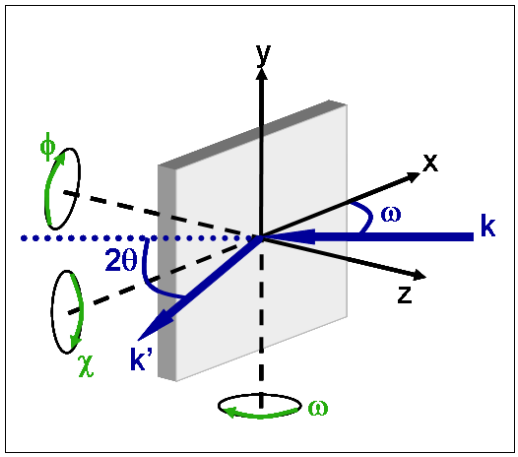

Figure 2.23: *Schematic representation of the angles and axis which allow to position the sample.*

2.4.1.3 Sample alignment

Prior to XRD measurements, it is necessary to center the sample with respect to the fixed impinging beam using x, y and z movements. Then, the planes under study have to be set into Laue diffraction condition (Eq. 2.6). The sample is first aligned by choosing a plane family as a reference, in general the surface planes of the substrate. In the case of samples grown on top of sapphire$(1\bar{1}00)$, we search for the $(3\bar{3}00)$-reflection of sapphire. As described previously (Fig. 2.23), the sample orientation is defined by 4 angles, in addition to x, y and z axis. ω is the incident angle of the beam with the surface and 2θ is the angle formed by the ingoing and outgoing beams directions. ϕ and χ correspond to the rotations around the normal of the sample (z-axis) x-axis respectively. Assuming that the 2θ angle of the substrate is close to its theoretical value [$2\theta = 68.226°$ for sapphire$(3\bar{3}00)$], we find the ω corresponding angle (2θ fixed, scans along ω). The sample misorientation is corrected via the adjustments of the χ_1 and χ_2 angles so that $\omega = \theta_{Bragg}$, where θ_{Bragg} is defined by Bragg's law in Eq. 2.7.

2.4.1.4 Symmetrical and asymmetrical reflections

Figure 2.24 shows the three different configurations used to scan symmetric (a) and asymmetric reflections (b) and (c). Symmetric reflections are those due to the diffraction by the surface plane family. They provide information on the out-of-plane lattice parameter. Asymmetric reflections are those coming from planes

forming an angle with the growth planes, noted α in the figure. Their normal vector has components both along the growth axis and in the growth plane. By combining asymmetric and symmetric measurements, we can determine the in-plane lattice parameters (the method will be described in section 2.4.1.6).

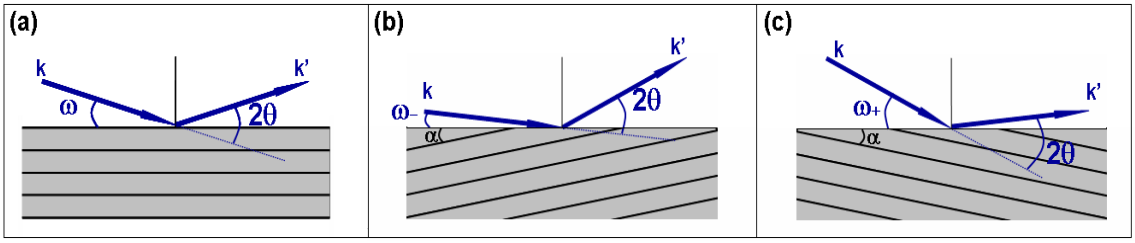

Figure 2.24: *Illustration of the different configurations used to scan (a) symmetrical and asymmetrical reflections on both grazing incidence (b) and emergence (c).*

For (0001)-oriented nitrides under biaxial strain, the in-plane parameter a is isotropic (symmetric by rotation of 60° from one to the other). In contrast, in the case of semipolar or nonpolar surfaces, the in-plane lattice parameters are anisotropic. It is therefore necessary to perform symmetric scans rotated by 90° to alternatively place the two in-plane parameters in the diffraction plane. Figure 2.25 illustrates these two configurations in the case of semipolar $(11\bar{2}2)$-oriented materials, placing either $<1\bar{1}00>$ or $<11\bar{2}\bar{3}>$ in the diffraction plane.

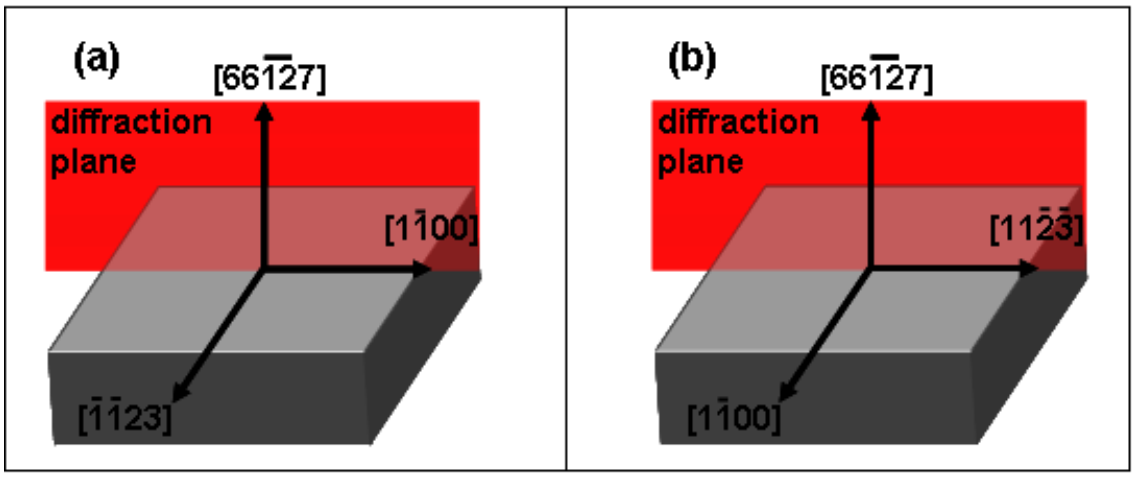

Figure 2.25: *Study of the symmetric diffraction of $(11\bar{2}2)$ by placing $<1\bar{1}00>$ (a) or $<11\bar{2}\bar{3}>$ (b) in the diffraction plane.*

2.4.1.5 Effect of the presence of crystalline defects on reciprocal space maps

When mapping the reciprocal space (RS) of the crystal, the spots corresponding to the reflection by a plane family are broadened because of defects or lattice strain. In this section, I explain the most common sources of this broadening. To

simplify, in Figs. 2.26 and 2.27, I represent the RS of a cubic crystal. The effects described below are equivalent for wurtzite materials.

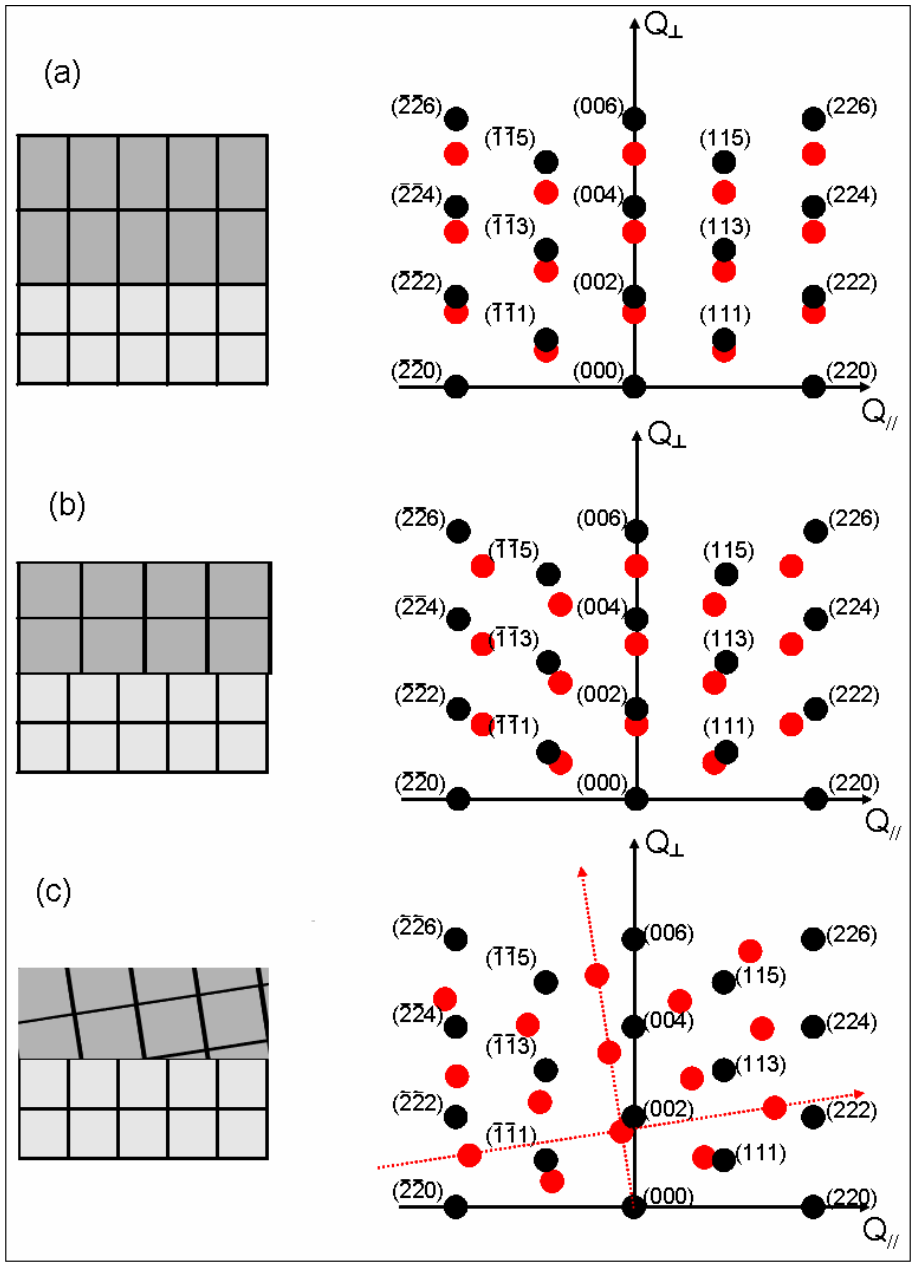

Figure 2.26: *Reciprocal space maps (RSMs) of both the substrate and the layer grown on top, in the case of (a) coherent epitaxy, (b) relaxation of the layer, and (c) tilt of the layer. Black and red dots represent the reflections from the substrate and the layer, respectively.*

Figure 2.26 illustrates the position of the RS of the layer with respect to the RS of the substrate, depending on the relaxation or tilt of the layer. In the case of pseudomorphic growth (a), since the in-plane parameters of both the layer and the substrate are the same, the reflections from the layer are perfectly aligned with the reflections from the substrate along the in-plane reciprocal vector ($Q_{//}$). Along

the out-of-plane reciprocal axis ($Q_\perp$), the reflections are shifted since the lattice parameters are different. When the layer is fully (or partially) relaxed, as shown in (b), the reflections are shifted along the two perpendicular directions. Finally, (c) represents the situation for a relaxed layer with a misorientation (tilt): each reflection is tilted from the reflection of the substrate by the same angle.

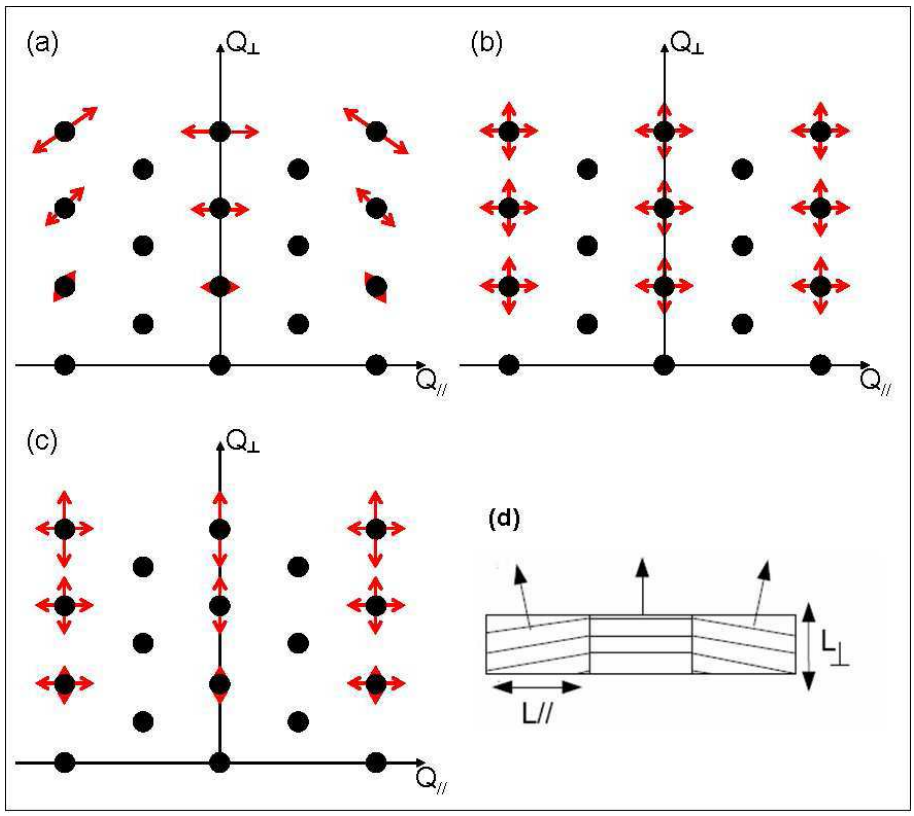

Figure 2.27: *Broadening of the RSM due to (a) tilt, (b) lateral and vertical coherence lengths and (c) lattice parameter gradient. An explicative scheme of the tilt, and coherence lengths is given in (d).*

Figure 2.27 shows how the presence of crystalline defects or relaxation affects the shape of the reflections.

(a) Mosaicity in the layer leads to a broadening perpendicular to $Q_\perp$ (a), *i.e.* along the angle ω. It is then possible to quantify the average tilt of the grains, by studying the broadening of several symmetric reflections. The reflection broadening is proportional to the diffraction vector, *i.e.* it increases with the diffraction order.

(b) In addition to the tilt, we can define both lateral and vertical coherence lengths ($L_{//}$ and $L_\perp$), corresponding to the average size of the grains, as schematized in (d). The vertical and lateral coherence lengths broaden both the symmetric and asymmetric reflections along $Q_\perp$ and $Q_{//}$ respectively, as illustrated in Fig. 2.26(b).

(c) Finally, (c) shows the effect of the relaxation. Since symmetric reflections only correspond to out-of-plane parameter, relaxation only broadens them along $Q_\perp$. On the contrary, asymmetric reflections depend on both in-plane and out-of-plane parameters, so that two perpendicular broadenings can be distinguished: one due to out-of-plane relaxation and the other one due to in-plane relaxation. In all cases, the broadening of the reflection increases with the diffraction vector.

The broadening of a single reflection can present contributions from all these effects. It is hence necessary to record several diffraction patterns to identify the various sources of broadening and to obtain a good idea of the crystalline defect structure of the layer.

2.4.1.6 Determination of lattice parameters in the case of semipolar nitrides.

The determination of the lattice parameters is performed using an extension of Bond method [Bon60,Her02,Geh05], based on the scan of several crystalline (h, k, i, l) reflections which belong to the same crystallographic zone, without modification of the alignment of the sample between the scans. Each reflection is measured twice, in order to correct any misorientation effect. Indeed, symmetric reflections should be 2θ and -2θ scanned. As illustrated in Fig. 2.28(a), the detector is on the other side of the beam for symmetric -2θ measurements (configuration on the right hand side of the picture). In our case, we only performed 2θ scans to determine the out-of-plane parameter, using Eq. 2.7.

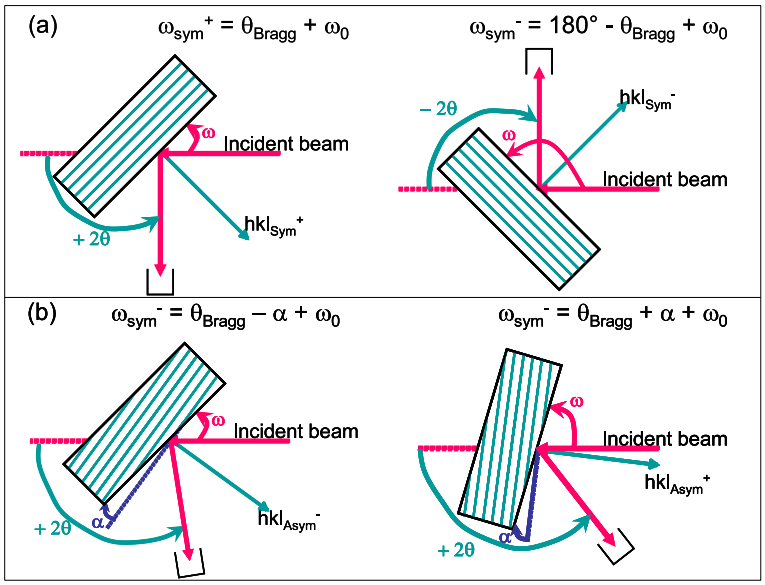

Figure 2.28: *Bond method for (a) symmetric and (b) asymmetric reflections [Her02].*

To determine the in-plane lattice parameters, one has to consider a (*h'*, *k'*, *i'*, *l'*) plane family forming an angle, α, with the (h, k, i, l) surface plane. α directly depends on the lattice parameters a and c via the relation:

$$\cos\alpha = \frac{\frac{4}{3a^2}(hh' + kk' + \frac{h'k+kh'}{2}) + \frac{ll'}{2}}{\sqrt{[\frac{4}{3a^2}(h^2 + k^2 + hk) + \frac{l^2}{2}][\frac{4}{3a^2}(h'^2 + k'^2 + h'k') + \frac{l'^2}{2}]}} \tag{2.8}$$

To get rid of the misorientation, ω_0, these asymmetric reflections should be recorded on both grazing incidence and emergence [see in Fig. 2.24(b) and (c) respectively]. Thus, we measure both $\omega_- = \theta_{Bragg} - \alpha + \omega_0$ (grazing incidence) or $\omega_+ = \theta_{Bragg} + \alpha + \omega_0$ (grazing emergence) [Fig. 2.28(b)], and we extract the angle α as:

$$\alpha = \frac{\omega_+ - \omega_-}{2} \tag{2.9}$$

In the particular case of $(11\bar{2}2)$-oriented materials, we determined the out-of-plane parameter $d_{11\bar{2}2}$ via the measurement of the first order symmetric $(11\bar{2}2)$ reflection (Eq. 2.10). Asymmetric RSMs were recorded around $(20\bar{2}2)$ and $(11\bar{2}4)$ reflections. Since we do not know, *a priori*, the deformation of the hexagonal unit cell, we made two different calculations to determine a and c. On the one hand, we approximate that the hexagonal basal planes are under isotropic strain [Fig. 2.29(a)]. On the other hand, we consider that the basal planes are anisotropically deformed, so that we have to consider two in-plane lattice parameters, a and b, as illustrated in Fig. 2.29(b). Details on these two approaches are given below.

$$2d_{11\bar{2}2}\sin\theta_{11\bar{2}2} = \lambda \tag{2.10}$$

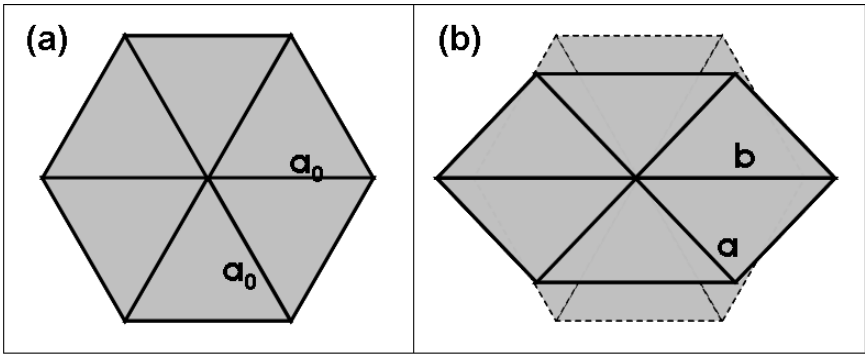

Figure 2.29: *Illustrations of (a) isotropic and (b) anisotropic deformation of the hexagonal basal planes.*

a) Isotropic basal plane deformation

In the following, α_1 refers to the angle between $(11\bar{2}2)$ and $(20\bar{2}2)$ and α_2 refers to the angle between $(11\bar{2}2)$ and $(11\bar{2}4)$. First of all, we perform a symmetric

scan around $(11\bar{2}2)$ reflection, in order to determine $\theta_{11\bar{2}2}$, and hence $d_{11\bar{2}2}$. In the case of an isotropic basal plane, $d_{11\bar{2}2}$ is directly dependent on c/a ratio:

$$d_{11\bar{2}2} = \frac{1}{2\sqrt{\frac{1}{a^2} + \frac{1}{c^2}}} \tag{2.11}$$

It is necessary to study an asymmetric reflection [$(20\bar{2}2)$ or $(11\bar{2}4)$, for instance] to determine a and c independently. The analysis of $(20\bar{2}2)$ reflection gives the parameters a and c via the calculation of α_1:

$$a_{is.1} = \frac{2d_{11\bar{2}2}}{\sqrt{3\tan^2\alpha_1}} \tag{2.12}$$

$$c_{is.1} = 2d_{11\bar{2}2}\sqrt{\frac{\cos^2\alpha_1}{1-4\sin^2\alpha_1}} \tag{2.13}$$

If we scan $(11\bar{2}4)$ reflection, we can calculate α_2, and therefore determine the parameters a and c with the equations:

$$a_{is.2} = 2d_{11\bar{2}2}\sqrt{\frac{7\sin^2\alpha_2 - 1 + \sqrt{\cos^2\alpha_2(1-9\sin^2\alpha_2)}}{5\sin^2\alpha_2 - 1 + \sqrt{\cos^2\alpha_2(1-9\sin^2\alpha_2)}}} \tag{2.14}$$

$$c_{is.2} = 2d_{11\bar{2}2}\sqrt{\frac{7\sin^2\alpha_2 - 1 + \sqrt{\cos^2\alpha_2(1-9\sin^2\alpha_2)}}{2\sin^2\alpha_2}} \tag{2.15}$$

We used the extended Bond method via the determination of the ω position corresponding to the maximum intensity of asymmetric reflections.

b) Anisotropic basal plane deformation

If we assume that the hexagonal basal plane is under compressive stress along one direction and tensile stress along the perpendicular direction [see Fig. 2.29(b)], we need to consider three lattice parameters: the two in-plane parameters a and b and the out-of-plane parameter c. To access these three parameters, we need to scan the two asymmetric reflections [$(20\bar{2}2)$ and $(11\bar{2}4)$] in addition to the symmetric $(11\bar{2}2)$ reflection. Via the determination of $d_{(11\bar{2}2)}$, α_1, α_2, we calculate a, b and c using the following relations:

$$a_{anis.} = d_{11\bar{2}2}\sqrt{\frac{1}{\tan^2\alpha_1} + \frac{7\sin^2\alpha_2 - 1 + \sqrt{\cos^2\alpha_2(1-9\sin^2\alpha_2)}}{5\sin^2\alpha_2 - 1 + \sqrt{\cos^2\alpha_2(1-9\sin^2\alpha_2)}}} \tag{2.16}$$

$$b_{anis.} = 2d_{11\bar{2}2}\sqrt{\frac{7\sin^2\alpha_2 - 1 + \sqrt{\cos^2\alpha_2(1-9\sin^2\alpha_2)}}{5\sin^2\alpha_2 - 1 + \sqrt{\cos^2\alpha_2(1-9\sin^2\alpha_2)}}} \tag{2.17}$$

$$c_{anis.} = 2d_{11\bar{2}2}\sqrt{\frac{7\sin^2\alpha_2 - 1 + \sqrt{\cos^2\alpha_2(1-9\sin^2\alpha_2)}}{2\sin^2\alpha_2}} \tag{2.18}$$

Note that the $(20\bar{2}2)$ reflection only affects the parameter a, whereas $(11\bar{2}4)$ is necessary for the three parameters.

2.4.2 Atomic-force microscopy

AFM provides information on the quality of the surfaces (roughness), but also the distribution and size of QDs. The AFM principle is based on the measurement of the short-range mechanical interaction between the sample and the probe, which depends on the distance [Bin86]. Thus, a 2D AFM scan provides an image of the sample morphology. Figure 2.30 illustrates the AFM measurement setup. The tip is fixed under a cantilever whose bending is proportional to the force between the probe and the surface. A laser beam is reflected by the cantilever towards a 4-sector detector. The bending of the cantilever is kept constant by a feedback insuring a constant distance between the tip and the sample by a piezoelectric system which generates the movement of the sample in the three directions.

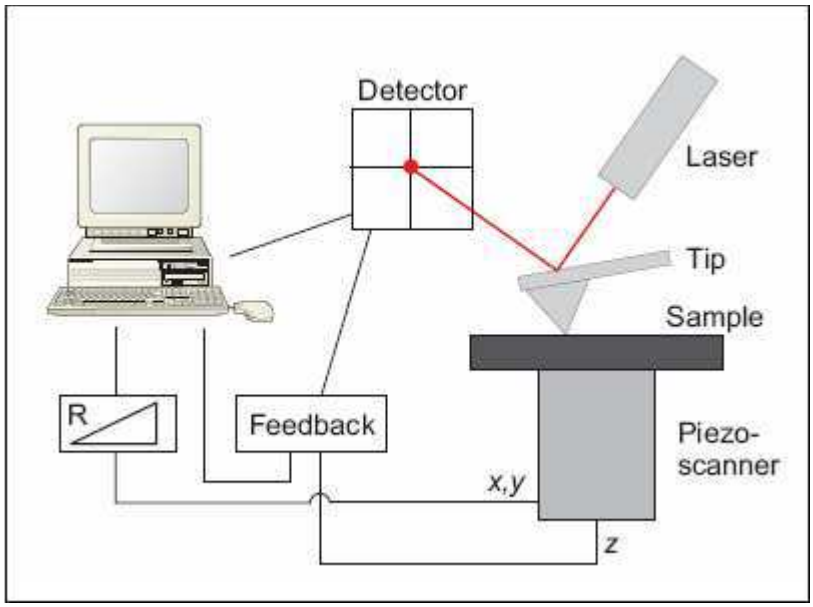

Figure 2.30: *Schematic of an AFM setup.*

Figure 2.31 shows two Scanning Electron Microscopy (SEM) images of the typical tips used in this work. They are pyramid-shaped silicon tips with opening angles around 10°-15° near the apex and with a maximum radius of 5 nm. This type of probes provides images with out-of-plane atomic resolution and in-plane resolution of around 5 nm.

In this work, the AFM measurements were performed in the tapping mode. In this mode, the probe is forced to oscillate slightly above its resonance frequency ω_0 (Eq. 2.19) with a certain amplitude. Usually, a high resonance frequency ($\omega_0 \gg$ 1 kHz) is preferred because it avoids any perturbation on the cantilever oscillations coming from low-frequency noise due to vibrations of the microscope or the building.

$$\omega_0 = \sqrt{\frac{\kappa}{m}} \tag{2.19}$$

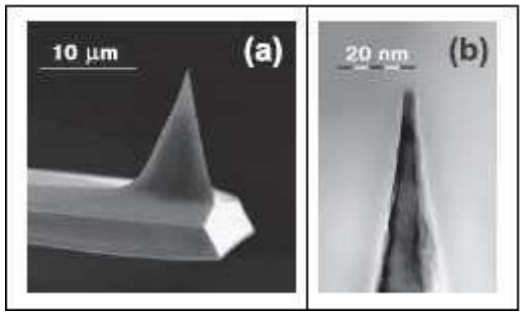

Figure 2.31: *SEM images of AFM tips and cantilevers.*

When the tip is close enough to the surface (less than 10 nm), it is exposed to a Van der Waals interaction gradient which decreases the frequency of the tip as predicted in Eq. 2.20. In addition to this effect, the oscillation amplitude is also damped because of the increase of the interaction between the probe and the surface.

$$\omega = \omega_0 \sqrt{1 - \frac{1}{\kappa}\frac{\partial F}{\partial z}}. \tag{2.20}$$

The oscillation amplitude is kept constant via a piezoelectric actuator and a PID feedback control of the distance between the tip and the surface. Thus, the tapping mode provides a measurement of the force gradient. The minimal detectable force gradient is given by the equation:

$$\left(\frac{\partial F}{\partial z}\right)_{\min} = \frac{1}{A}\sqrt{\frac{4B\kappa k_B T}{\omega_0 Q}} \tag{2.21}$$

where A is the rms (root mean square) oscillation amplitude, B the detection bandwidth, and $Q = \Delta\omega/\omega$ the quality factor of the resonance [Wie94]. From this expression we extract the four main parameters to optimize the resolution:

- $\frac{\kappa}{\omega_0}$ should be as small as possible, which implies the minimization of the cantilever mass (size) [see Eq. (2.19)].
- $Q = \Delta\omega/\omega$ should be high, but size minimization of the cantilever generally increases Q. Another way to decrease Q is to work under vacuum.
- If possible, low temperatures are favorable.
- The oscillation amplitude A, generally limited by the setup, should be as large as possible.

The tapping mode is usually used to scan fragile samples. This mode is preferred in the case of group III nitrides, not to protect the sample but the tip, since they are materials much harder than the silicon tips.

Due to the finite size of the AFM tips we can not access the real size of the small corrugations of the surface. Indeed, the surface not only interacts with the apex of the tip but also with its sidewalls. These side effects can not be neglected as soon as the size of the surface features is comparable to the tip radius. The measured topography is a convolution of the real surface and the tip shape. Figure 2.32 illustrates how the measured lateral size (a) and height (b) of the objects are modified by these effects.

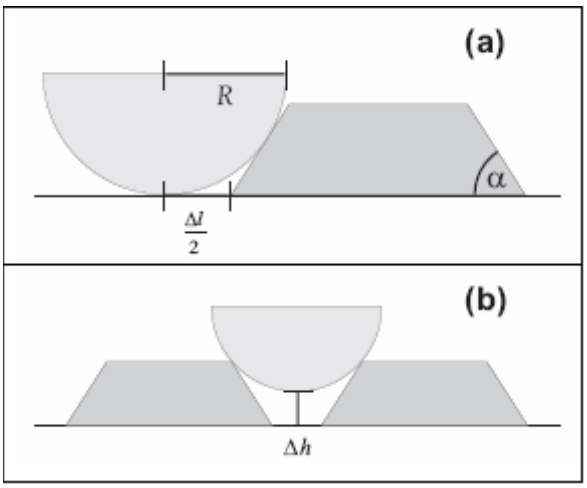

Figure 2.32: *(a) Increase of the lateral size of the islands due to the finite size of the tip. (b) Decrease of the island height when two islands are closer to each other than the tip diameter.*

An exact deconvolution is impossible because it would require to know precisely the surface and the tip shape. However, assuming we have a spheric tip with (radius R), a simple correction Δl of the lateral size, l, of an object can be calculated. If we consider an island with a height h, with facets forming an angle α, the measured size will be larger, as shown in Fig. 2.32(a), and Δl is given by the expressions in Eq. 2.22. It is more difficult to obtain a general expression for the corrected height in the case of high density islands. As illustrated in Fig. 2.32(b), the measured height is smaller than the real one and depends on the separation between the objects. However, this effect is rather difficult to estimate and no general correction exists when the distance between the islands fluctuates.

$$\frac{\Delta l}{2} = \begin{cases} \sqrt{h(2R-h)} - h\cot\alpha & h < R(1-\cos\alpha) \\ R\left[\sin\alpha - (1-\cos\alpha)\cot\alpha\right] & h \geq R(1-\cos\alpha) \end{cases} \tag{2.22}$$

In any case, the opening angle and the apex radius should be as small as possible in order to minimize these measurement artifacts. Typical opening angles of commercial AFM tips are of the order of 15° and typical apex radii of the order of 5 nm.

2.4.3 Photoluminescence spectroscopy

PL spectroscopy consists on the study of the optical emission from a material which is optically stimulated. The laser wavelength is chosen so that the excitation energy is higher than the bandgap of the material, in order to populate as many energy levels as possible via the creation of electron-hole pairs. In general, the return to equilibrium proceeds via phonon emission, to drive the electron down to the conduction band minimum, and radiative (or non radiative) recombination. Radiative recombination of electron-hole pairs leads to the emission of photons whose energy depends on the distance between the levels of the electron and the hole. We can observe interband intrinsic transitions as well as transitions involving donor or acceptor levels introduced within the band gap by the presence of impurities or defects in the material. Hence, the PL spectra provide information about the intrinsic and extrinsic energy levels of the structure. Moreover, the broadening of the luminescence peaks is linked to the crystalline quality and homogeneity of the sample.

Fig. 2.33 illustrates the setup used in this work. The excitation source was a frequency-doubled continuous-wave Ar^+ laser ($\lambda = 488/2 = 244$ nm). The signal was collected into a 45-cm-focal-length Jobin-Yvon monochromator and detected by an ultraviolet-enhanced charge-coupled device (CCD).

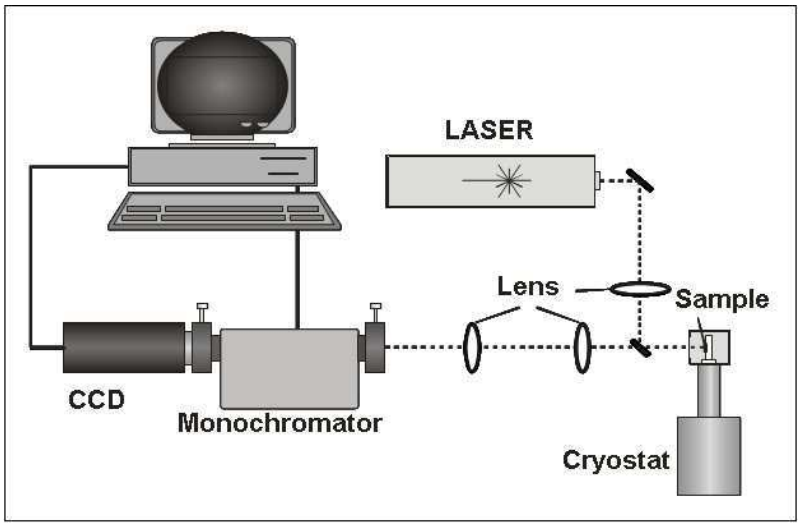

Figure 2.33: *Photoluminescence setup.*

Time-resolved photoluminescence (TRPL) has been used to study the carrier relaxation processes. The principle is to excite the sample with laser pulses and record the evolution of the emission intensity. The measured decay times provide information about the nature of the transition involved. The excitation source was a pulsed frequency-tripled Ti-sapphire laser ($\lambda = 270$ nm) with a pulse width around 200 fs. The repetition rate of the laser could be adjusted from 76 MHz (13 ns period) down to 0.9 MHz (1.1 μs period) by the use of a cavity dumper. Thus, the effective

system resolution depends on the time window used for the analysis. For the shorter pulse periods (13 ns), the signal was analyzed with a 2 ns window, giving a system response of about 10 ps. In the case of longer periods (1.1 μs), we used a 20 ns window, providing a system response of about 500 ps. In this TRPL setup, the monochromator had a focal length of 32 cm. In both PL and TRPL experiments the samples were mounted in a cold finger He cryostat and the diameter of the laser spot was about 50 μm.

2.5 Simulation of electronic structures

Modeling of the electronic structure of III-nitrides is challenging because of the uncertainty in physical parameters, the high density of crystalline defects, which is hard to take into account, and the high piezoelectric constants, which make the band structure very dependent on the strain state of the sample. In this work, I used the next**nano**^{3} solver, created at Walter Schottky Institute in Munich. In this software, the electronic structure is calculated using an 8-band k.p Schrödinger-Poisson solver. The material parameters applied for the simulation are summarized in Table 2.1. The strong advantage of the next**nano**^{3} solver is that it takes into account the spontaneous and piezoelectric polarization coefficients, together with the strain state. It is possible to calculate not only the electronic configuration of common *c*-plane III-nitrides but also other semipolar or nonpolar orientations, by indicating the growth axis. Thus, in the particular case of $(11\bar{2}2)$-oriented nitrides, we use $[66\bar{1}\bar{2}7]$ as the growth axis.

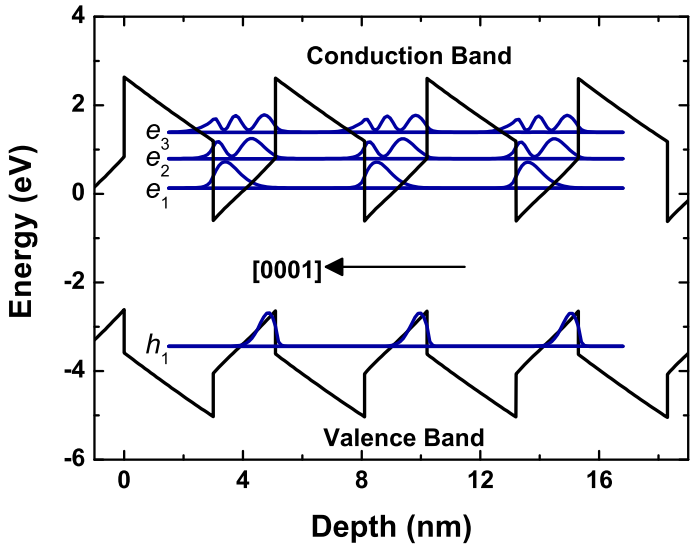

Figure 2.34: *Band diagram of GaN-AlN QWs in a superlattice with 3-nm-thick AlN barriers and 2-nm-thick GaN wells.*

Figure 2.34 shows the band diagram of polar 8-ML-thick GaN QWs embedded in 3-nm-thick AlN barriers, calculated with the next**nano**^{3} 8-band k.p Schrödinger-Poisson solver, using the material parameters given in Table 2.1. In this particular example, the structures are considered to be strained on the AlN substrate. The potential exhibits the characteristic triangular profile due to the internal electric field. The hole wavefunctions of the ground hole state, h_1, the ground electron state, e_1, and the excited electron states, e_2 and e_3, are presented.

The dispersion of GaN and AlN material parameters in the literature leads to significant variations in the simulation results. In order to adjust the simulation parameters, we have compared the results of the calculations with experimental measurements of the intersubband (ISB) transitions in polar GaN/AlN QWs. As an example, Fig. 2.35 shows the ISB absorption of Si-doped GaN multiple quantum well (MQW) structures (20 periods of QWs with thickness varying from 5 ML to 9 ML) embedded in 3-nm-thick AlN barriers [Tch06]. The samples show a pronounced TM-polarized absorption, attributed to the transition from the first to the second electronic levels in the QW ($e_1 - e_2$), while no absorption was observed for TE-polarized light. Besides, the $e_1 - e_3$ transition, which is allowed in polar nitride QWs because the presence of the internal electric field breaks the symmetry of the potential, can be observed in large QW structures as indicated in the figure.

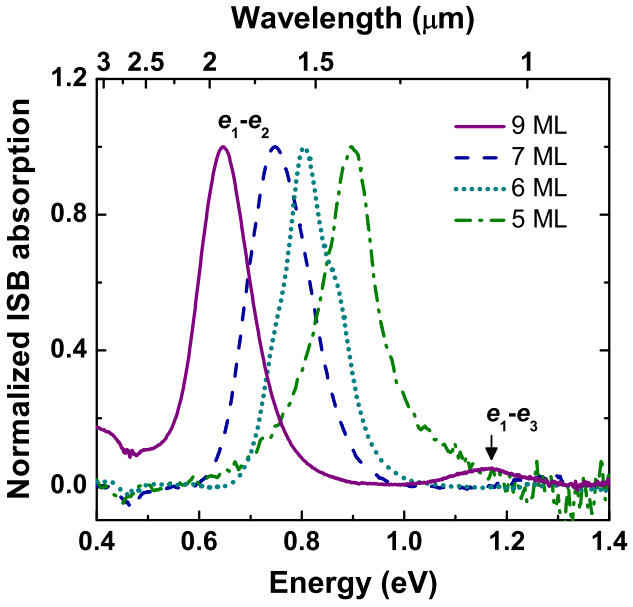

Figure 2.35: *Intersubband absorption in Si-doped GaN/AlN superlattices with different QW thicknesses [Kan08].*

Figure 2.36 compares the experimental values and the simulations of $e_1 - e_2$ and $e_1 - e_3$ transition energies as a function of the QW width. The theoretical transitions have been calculated assuming the structures fully strained on GaN and

on AlN (solid and dashed lines respectively) using the material parameters recorded in Table 2.1. When the structures are strained on GaN, *i.e.* the AlN barriers are under tensile stress, the piezoelectric polarization is enhanced, due the the higher piezoelectric coefficients of AlN compared to GaN. This leads to higher internal electric field, *i.e.* lower ISB transitions. The electric field strongly affects the $e_1 - e_2$ transition in large QWs, since both levels are situated within the triangular part or the potential diagram (see in Fig. 2.34), whereas the $e_1 - e_2$ is mainly determine by the 2D confinement in the smallest QW ($\approx$ 1 nm). On the other hand, the $e_1 - e_3$ transition depends on the GaN/AlN band offset and on the nonparabolicity of the electron effective mass. Therefore, the fit of these two transitions allows us to adjust the different material parameters in Table 2.1.

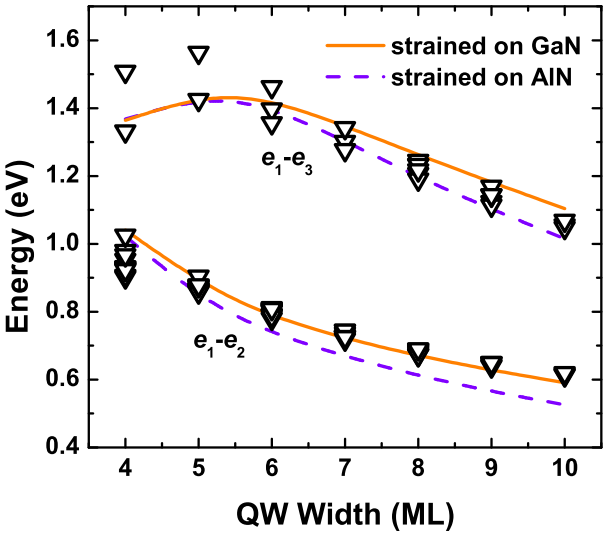

Figure 2.36: *Experimental ISB absorption by Ga/AlN MQW with different QW thickness in comparison with the simulated transitions assuming the structures strained on GaN or AlN [Kan08].*

It is important to notice that next**nano**[3] can be used to calculate the electronic levels in quantum regions using either the effective mass approximation or the k.p solver. In the case of the effective mass approximation, nonparabolic effects are not taken into account, which results in a significant overestimation in the calculation of excited electronic levels.

Parameters		GaN	AlN	References
Lattice constants [nm]	a	0.31892	0.3112	[Vur03]
	c	0.51850	0.4982	
Spontaneous polarization [$C.m^{-2}$]		-0.029	-0.081	[Ber97]
Piezoelectric constants [$C.m^{-2}$]	e_{13}	-0.49	0.60	[Ber97]
	e_{33}	-0.60	1.46	
Elastic constants [GPa]	c_{11}	390	396	[Wri97]
	c_{12}	145	137	
	c_{13}	106	108	
	c_{33}	398	373	
Dielectric constant		10	8.5	[Par00]
Luttinger's parameters	A_1	-5.947	-3.991	[Rin08]
	A_2	-0.528	-0.311	
	A_3	-5.414	3.671	
	A_4	-2.512	-1.147	
	A_5	-2.510	-1.329	
	A_6	-3.202	-1.952	
	A_7	0	0	
	$E_P^{//}$ [eV]	14	17.3	
	$E_P^{\perp}$ [eV]	14	16.3	
Band offset [eV]		1.8		[Tch06]

Table 2.1: *GaN and AlN parameters used for the calculation of band diagrams with the* ***nextnano***^{3} *solver.*

Chapter 3

Analysis of AlN($11\bar{2}2$) grown on *m*-sapphire

The synthesis of heterostructures such as GaN/AlN QWs or QDs requires two semiconductor materials with different band gap energy; the one with larger gap (AlN) is used as the barrier and the one with the smaller gap (GaN) as the active zone (well or dot). Therefore, in order to fabricate GaN/AlN heterostructures, it is necessary to control the two-dimensional (2D) growth conditions of AlN. For polar and nonpolar orientations, the surface morphology of AlN grown by PAMBE depends strongly on the III/V ratio, the flattest surfaces being achieved under Al-rich conditions in the case of AlN(0001) and AlN($1\bar{1}00$), and under N-rich conditions for AlN($11\bar{2}0$).

In this chapter, we present the growth modes and subsequent properties of AlN layers deposited on ($1\bar{1}00$) *m*-sapphire. We demonstrate that, under certain growth conditions, it is possible to isolate the ($11\bar{2}2$) crystallographic orientation. A deep investigation on the structural properties of the layers is exposed. In particular, we demonstrate that the achievement of homogeneous AlN($11\bar{2}2$), as well as its morphology, depends strongly on the earlier steps of the growth. Part of this work was reported in [Lah07].

Contents

3.1 Growth of AlN on *m*-sapphire 61

3.1.1 Effect of the III/V ratio 61

3.1.2 How to understand the RHEED patterns? 64

3.1.3 Crystallographic orientation relationships 67

3.1.4 Synthesis of two-dimensional AlN($11\bar{2}2$) 73

3.1.4.1 Effect of the substrate temperature 73

3.1.4.2 Discussion on *m*-sapphire nitridation 73

3.1.4.3 Starting the growth 76
3.2 Crystalline structure of AlN(11$\bar{2}$2) 77
3.2.1 XRD experiments 77
3.2.2 Estimation of the lattice parameters in thick layers 80
3.2.3 Relaxation analysis 81
3.2.4 Surface morphology 83
3.3 Conclusions 84

3.1 Growth of AlN on m-sapphire

This section presents the effect of the III/V ratio, substrate temperature and substrate nitridation process on the growth of AlN on m-sapphire. We identify the crystallographic orientations which can be found in the layers as a function of the growth conditions. A parenthesis will focus on the crystalline structure of the two main orientations which can be found, AlN($10\bar{1}0$) and AlN($11\bar{2}2$). Finally, I will describe the optimized growth conditions for the synthesis of two-dimensional AlN($11\bar{2}2$).

3.1.1 Effect of the III/V ratio

AlN layers were grown by PAMBE on m-sapphire with an active nitrogen flux corresponding to a growth rate of 0.3 ML/s, *i.e.* $\approx$ 270 nm/h, for AlN(0001) layers grown under Al-rich conditions (unless specified, 1 ML corresponds to the number of atoms arranged in a (0001) wurtzite plane, *i.e.* 1.13×10^{15} atoms/cm^2). For the experiments described in this section, the substrate temperature was kept at 720°C, which is the standard temperature used for the growth of GaN(0001). For all the samples of the series, the substrates were exposed to nitrogen for 30 min prior to AlN deposition. The influence of both substrate temperature and nitridation will be addressed later. In order to determine the appropriate conditions to obtain flat surfaces, I varied the III/V ratio from the Al-rich (III/V $\approx$ 1.15) regime to the N-rich (III/V $\approx$ 0.77) regime. Table 3.1 describes the different layers under study.

Samples	III/V ratio	Thickness	RHEED characteristics
E1011	1.15	490 nm	one streaky pattern one spotty pattern
E1021	1.02	490 nm	one streaky pattern one spotty pattern
E1126	1	670 nm	one streaky pattern one spotty pattern
E1139	0.97	280 nm	spotty pattern
E1020	0.92	490 nm	streaky pattern
E1028	0.84	560 nm	spotty pattern
E1136	0.77	160 nm	diffraction rings

Table 3.1: *Series of samples grown with III/V ratio varying from Al-rich to N-rich conditions.*

Samples grown at the stoichiometry (E1126) or under Al-rich conditions (E1021 and E1011) present the superimposition of two RHEED patterns, as shown in Fig. 3.1(a), where we can observe periodical streaks (continuous lines) and a spotty pattern with a different period (dashed lines). The presence of two periodical patterns indicates the coexistence of two crystallographic orientations in the layers.

On the other hand, samples grown under slightly N-rich conditions display a single periodic pattern at the end of the growth, as illustrated in Figs. 3.1(b) and (c). This means we can assume a highly predominant crystallographic orientation. When close to the stoichiometry, the RHEED remains spotty, as displayed in Fig. 3.1(b) [sample with III/V $\approx$ 0.97 (E1139)]. On the contrary, on Fig. 3.1(c) which corresponds to sample with III/V $\approx$ 0.92 (E1020), only one crystallographic orientation is observed and the streaky pattern indicates 2D growth. Finally, the RHEED pattern of the samples grown under high N-rich conditions (E1136 and E1028) systematically presents diffraction rings, as illustrated in Fig. 3.1(d), which is characteristic of polycrystalline material.

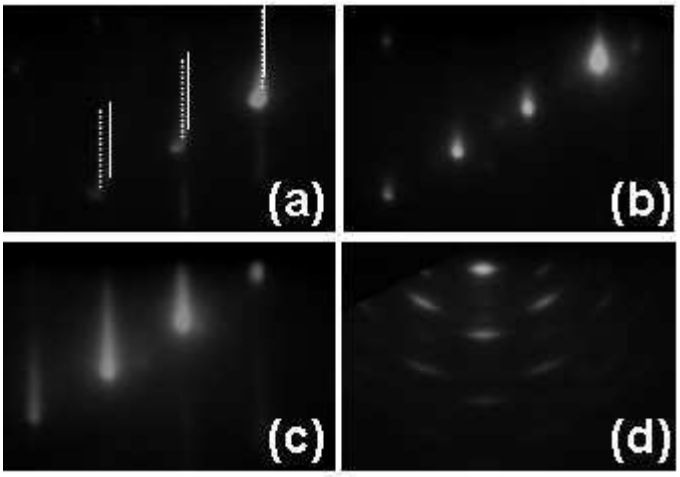

Figure 3.1: *Typical RHEED patterns: (a) superimposition of a streaky and a spotty patterns, (b) spotty pattern, (c) streaky pattern, and (d) diffraction rings. All the images were recorded at the end of the growth along the <11$\bar{2}$0> azimuth of m-sapphire.*

I have analyzed the different crystallographic orientations in the layers using XRD. Figures 3.2 depicts symmetric 2θ-ω scans of five layers grown under different III/V ratio. The main peak in each diffractogram corresponds to the symmetric (3$\bar{3}$00) reflection of *m*-sapphire, occurring for $2\theta = 68.226°$. The reflection around $2\theta = 71.40°$ is attributed to AlN(11$\bar{2}$2) planes and the peak around $2\theta = 69.72°$ corresponds to the (20$\bar{2}$0) reflection of AlN(10$\bar{1}$0). I also indicate the position of the reflection due to AlN(10$\bar{1}$3). Layers grown under Al-rich conditions show two intense peaks attributed to AlN(11$\bar{2}$2) and AlN(10$\bar{1}$0). The presence of these two main peaks is consistent with the RHEED observations previously [Fig. 3.1(a)]. Additionally, sample E1011, with III/V $\approx$ 1.15, presents a reflection originating from AlN(10$\bar{1}$3). When decreasing the III/V ratio below $\approx$ 0.97, the AlN(10$\bar{1}$0) reflection peak tends to disappear, whereas the peak attributed to AlN(11$\bar{2}$2) remains. In this former regime, the predominance of AlN(11$\bar{2}$2) compared to AlN(10$\bar{1}$0) explains the mono-periodic RHEED patterns observed in Figs. 3.1(b) and (c). Finally, under high N-rich ratio, the AlN(10$\bar{1}$3) reflection rises up and the presence of the AlN(10$\bar{1}$0)

domains remains within the error bars of the XRD 2θ-ω scan. However, the intensity of the AlN($11\bar{2}2$) diffraction peaks decreases and the RHEED diffraction rings observed in Fig. 3.1(d) attest a highly polycrystalline growth.

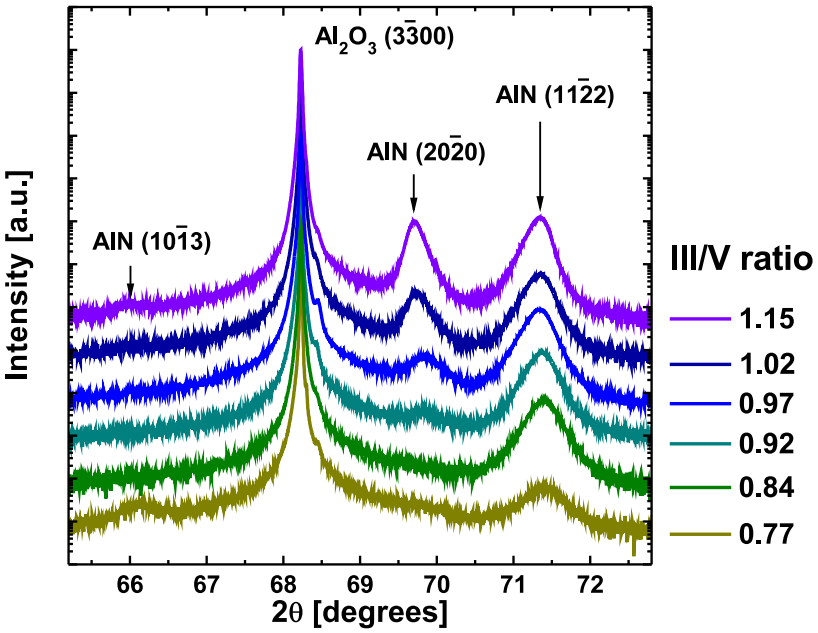

Figure 3.2: *XRD $2\theta - \omega$ scan of AlN layers grown on m-sapphire with different III/V ratio. Data are normalized to the substrate reflection and vertically shifted for clarity.*

From XRD scans, we can estimate the relative proportion of a certain crystallographic orientation in the layer by taking into account their form factor, given the relationship:

$$I_{int}^{(hkil)} \propto V^{(hkil)} \times F^{*}F^{(hkil)} \tag{3.1}$$

where $I_{int}^{(hkil)}$ is the integrated intensity from the (hkil) reflection, $V^{(hkil)}$ is the volume of (hkil) domains within the layer and $F^{*}F^{(hkil)}$ is the atomic structure factor of the (hkil) reflection. The integrated intensity is approximated by the product of the intensity and the full width at half maximum (FWHM) of the reflection. Hence $\frac{V^{(10\bar{1}0)}}{V^{(11\bar{2}2)}}$ and $\frac{V^{(10\bar{1}3)}}{V^{(11\bar{2}2)}}$ ratio calculated from Eq. 3.2 and Eq. 3.3, respectively. Table 3.2 gives the proportion of AlN($10\bar{1}0$) and AlN($10\bar{1}3$) in comparison with AlN($11\bar{2}2$).

$$\frac{V^{(10\bar{1}0)}}{V^{(11\bar{2}2)}} = \frac{I^{(10\bar{1}0)} \times FWHM^{(10\bar{1}0)}}{F^{*}F^{(10\bar{1}0)}} \frac{F^{*}F^{(11\bar{2}2)}}{I^{(11\bar{2}2)} \times FWHM^{(11\bar{2}2)}} \tag{3.2}$$

$$\frac{V^{(10\bar{1}3)}}{V^{(11\bar{2}2)}} = \frac{I^{(10\bar{1}3)} \times FWHM^{(10\bar{1}3)}}{F^{*}F^{(10\bar{1}3)}} \frac{F^{*}F^{(11\bar{2}2)}}{I^{(11\bar{2}2)} \times FWHM^{(11\bar{2}2)}} \tag{3.3}$$

Samples	III/V	$\frac{V^{(10\bar{1}0)}}{V^{(11\bar{2}2)}}$	$\frac{V^{(10\bar{1}3)}}{V^{(11\bar{2}2)}}$	% of AlN(11$\bar{2}$2) in the layers
E1011	1.15	1.78	0.07	$\approx$ 35%
E1021	1.02	0.85	0.12	$\approx$ 51%
E1139	0.97	0.29	-	$\approx$ 78%
E1020	0.92	0.08	-	$\approx$ 93%
E1028	0.84	-	-	$\approx$ 100%
E1136	0.77	-	0.72	$\approx$ 58%

Table 3.2: *Proportion of crystallographic orientations calculated from XRD symmetric diffractograms. The last column gives the AlN(11$\bar{2}$2) content within the layers.*

In conclusion, we can distinguish four growth regimes depending on the Al/N ratio.

- **For III/V $\geq$ 1** (Al-rich conditions), AlN layers show three different crystallographic orientations: AlN(11$\bar{2}$2), AlN(10$\bar{1}$0) and AlN(10$\bar{1}$3). The proportion of AlN(11$\bar{2}$2) and AlN(10$\bar{1}$0) are comparable, whereas AlN(10$\bar{1}$3) seems to be scarce. Besides, we can observe that the AlN(10$\bar{1}$0) orientation becomes predominant for the higher III/V ratio (sample E1011).

- **For 0.97 $\leq$ III/V $\leq$ 1** (slightly N-rich conditions), AlN layers consist of AlN(11$\bar{2}$2) and AlN(10$\bar{1}$0) domains, AlN(11$\bar{2}$2) being highly dominant (less than 30% of AlN(10$\bar{1}$0) domains).

- **For 0.84 $\leq$ III/V $\leq$ 0.97**, the proportion of AlN(10$\bar{1}$0) domains decreases below 5%, indicating that the layers consist mainly of AlN(11$\bar{2}$2) with (10$\bar{1}$0)-oriented clusters.

- **For III/V $\leq$ 0.84** (highly N-rich conditions), the layers are highly polycrystalline, AlN(11$\bar{2}$2) entering in competition with, at least, AlN(10$\bar{1}$3).

3.1.2 How to understand the RHEED patterns?

As mentioned in the former section, three crystallographic orientations can be found when AlN is deposited on *m*-sapphire. In order to exploit the advantages of the RHEED technique during the growth, it is important to be able to identify a certain crystallographic orientation and to know which azimuth we are looking at. Since RHEED patterns can be seen as images of the reciprocal lattice of the surface, I will first present the atomic arrangements of the two main surfaces which can be found [AlN(11$\bar{2}$2) and AlN(10$\bar{1}$0)]. Using this information, we can associate the atomic rows put into diffraction conditions with the corresponding RHEED patterns.

a) AlN(10$\bar{1}$0)

Since the electron beam has a much stronger interaction with metallic atoms, we will not consider nitrogen atoms in the following studies. Figure 3.3 illustrates

the distribution of Al atoms on the AlN($10\bar{1}0$) surface. The rows parallel to the $<0001>_{AlN}$ direction present smaller period (parameter a) than those parallel to the $<1\bar{2}10>_{AlN}$ direction (parameter c). This implies that the RHEED pattern periodicity along the $<0001>_{AlN}$ azimuth will be larger than the periodicity along the $<1\bar{2}10>_{AlN}$. This is verified in the images presented in Fig. 3.4, which were recorded on AlN($10\bar{1}0$) layers grown on SiC [Ams08]. The image on the left corresponds to the RHEED along $<1\bar{2}10>_{AlN}$ azimuth (smaller periodicity), whereas the image on the right has been taken along $<0001>_{AlN}$ azimuth (larger periodicity).

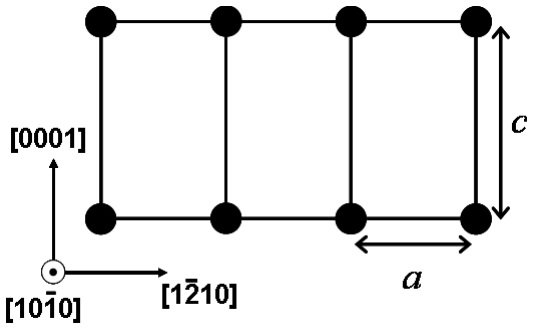

Figure 3.3: *Illustration of Al atomic distribution on the AlN($10\bar{1}0$) surface.*

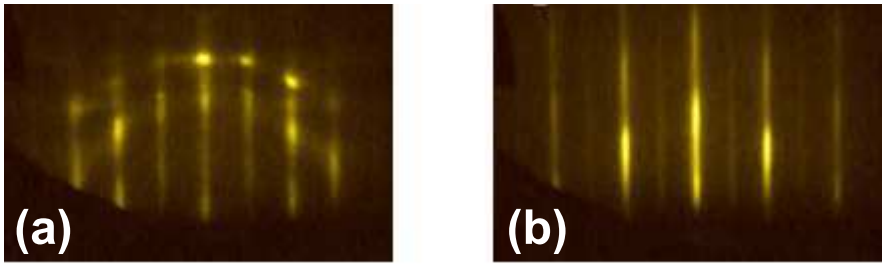

Figure 3.4: *Example of AlN($10\bar{1}0$) RHEED patterns recorded along the (a) $<1\bar{2}10>_{AlN}$ and (b) $<0001>_{AlN}$ azimuths [Ams08].*

b) AlN($11\bar{2}2$)

Figure 3.5(a) presents the Al atomic distribution in the topmost monolayer. Table 3.3 gives the values of the two in-plane parameters $a\sqrt{3}$ and $\frac{\sqrt{a^2+c^2}}{2}$ for both AlN and GaN.

Parameters	AlN	GaN
$a\sqrt{3}$ [$\AA$]	5.390	5.517
$\frac{\sqrt{a^2+c^2}}{2}$ [$\AA$]	2.937	3.044

Table 3.3: *In-plane lattice parameters of relaxed ($11\bar{2}2$)-oriented AlN and GaN.*

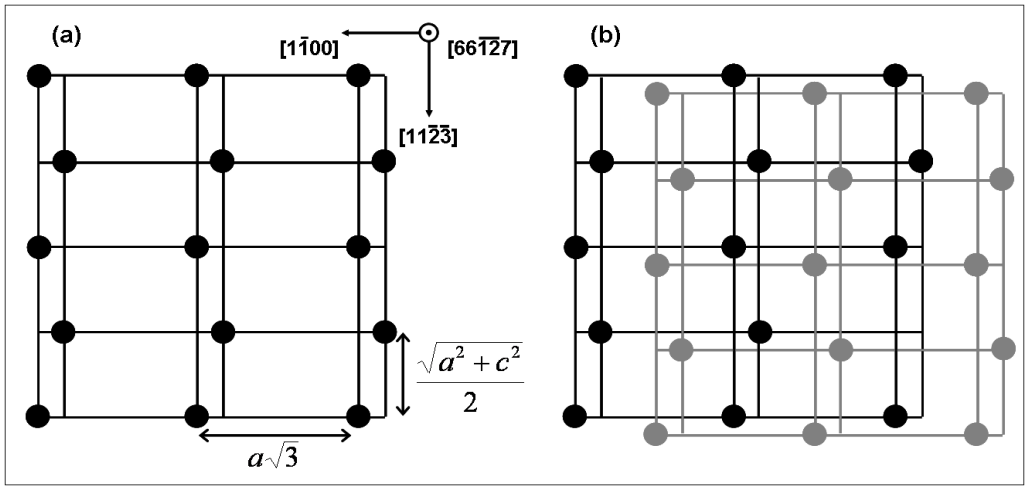

Figure 3.5: *Illustration of the Al atomic distribution on the AlN(11$\bar{2}$2) surface, for the topmost Al monolayer (black) and the following Al monolayer, which is shifted along the growth axis (gray).*

In Fig. 3.5(b), two subsequent (11$\bar{2}$2)-oriented Al atomic planes are represented in order to illustrate the succession of the atomic layers along the growth axis. It is interesting to note that the subsequent atomic layers are not superimposed along the growth axis. They are shifted of $a\sqrt{3}/2$ in the <1$\bar{1}$00> direction and of $a^2/2\sqrt{a^2+c^2}$ in the <11$\bar{2}$3> direction. This particularity results in very specific RHEED patterns. In Fig. 3.6, the image on the left is a schematic illustration of the succession of the (11$\bar{2}$2)-oriented Al atomic planes, viewed along the [$\bar{1}\bar{1}$23] axis. The different gray for the layers indicate that the atoms are not in the same cross-section, but shifted along the [$\bar{1}\bar{1}$23] axis. If we consider one Al plane, the atom distribution present a period $P_1 = a\sqrt{3}$. If we consider the succession of two Al planes, the period is half the previous one, $P_2 = a\sqrt{3}/2$, which should give no additional reflection in the RHEED pattern. Therefore, the RHEED viewed along $[\bar{1}\bar{1}23]_{AlN}$ has a period $P_1^* \propto 1/a$, as illustrated in the image on the right. Because of the shift of the Al layers along the growth axis, we can observe another periodic pattern (P_3) involving atoms from several Al levels, and consequently tilted forming an angle θ with the (11$\bar{2}$2) plane. This gives a third period in the RHEED, forming an angle $\pi - \theta$ with the periodic pattern of the (11$\bar{2}$2) planes, as illustrated in the image on the right.

Figure. 3.7(a) presents a cross-sectional schematic of the Al positions view along [$\bar{1}$100]. We can distinguish 3 different periods, P_1, P_2 and P_3, with P_2 and P_3 tilted from the (11$\bar{2}$2)-oriented P_1 from the angles α and β. Since $\alpha \neq \beta$, the RHEED pattern is not symmetric as previously, but distorted as illustrated in the images on the right. It is important to note that the arrangements of Al atoms when the structure is viewed along the [$\bar{1}$100] and [1$\bar{1}$00] azimuths are not equivalent. This results in two symmetric RHEED patterns, as can be seen in the images on the right.

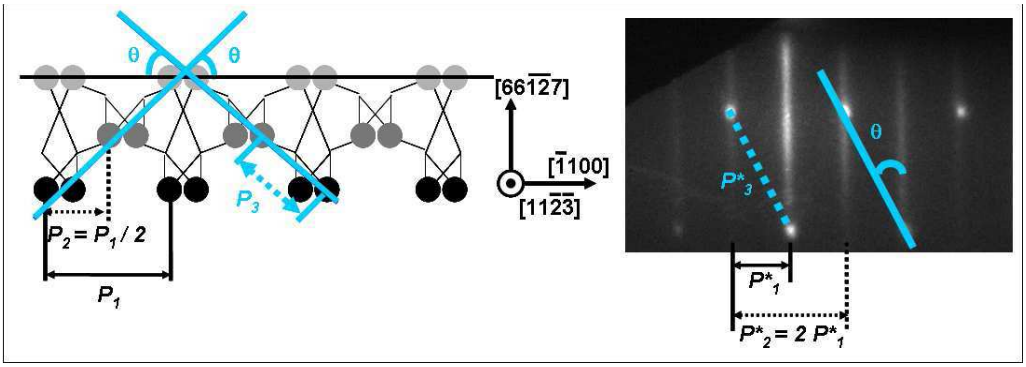

Figure 3.6: *(left) Schematic cross-section view of the Al atomic arrangement observed along the [1$\bar{1}$23] azimuth. The different position of the Al atoms along the azimuth is illustrated by the gray scale. (left) RHEED pattern of an AlN layer viewed along the same azimuth. The atomic periods in the lattice, named P_1, P_2 and P_3, found their counterparts in the RHEED image as P^*_1, P^*_2 and P^*_3.*

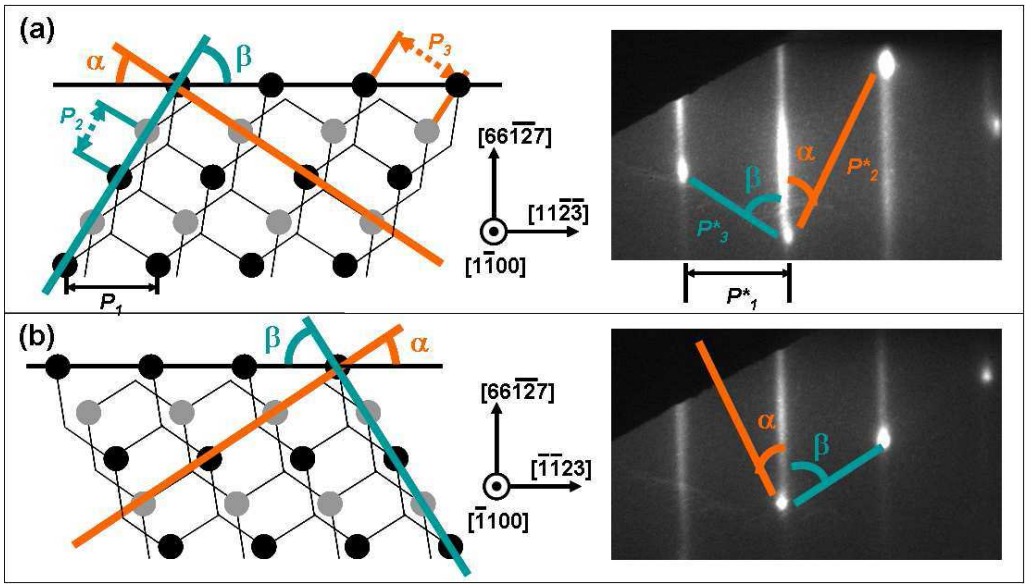

Figure 3.7: *(left) Schematic cross-section views of the Al atomic arrangement observed along the (a) [$\bar{1}$100] and (b) [1$\bar{1}$00] azimuths. The different position of the Al atoms along the azimuth is represented with the gray scale. The images on the right are the corresponding RHEED images.*

3.1.3 Crystallographic orientation relationships

In this section, we will show TEM results and *ab initio* calculations which were very useful to determine the epitaxial relationships between AlN(10$\bar{1}$0), AlN(11$\bar{2}$2), and *m*-sapphire. More particularly, for Figs. 3.11 to 3.13, first-principle DFT calculations were performed using the multiscale library SP/hi/NGX [Boe03].

The epitaxial relationships can be determined by the combination of cross-section transmission microscopy (XTEM) and selected area electron diffraction (SAED).

Figure 3.8(a) is a SAED pattern recorded along the $[0001]_{sapphire}$ azimuth of an AlN layer grown under III/V $\approx$ 1.05 (equivalent to sample E1021), without nitridation. In this image, the most intense reflections emerge from the *m*-sapphire substrate. As indicated by the white arrows "I" and "II", the additional reflections are of two kind, which confirms the coexistence of two main crystallographic orientations. Among them, the less intense spots (named "I") belong to the AlN(10$\bar{1}$0) orientation, and the additional ones are attributed to AlN(11$\bar{2}$2). From the indexation of the reflections, we can verify the surface planes alignment:

$$(\bar{1}100)_{sapphire} \;//\; (10\bar{1}0)_{AlN} \;//\; (11\bar{2}2)_{AlN}.$$

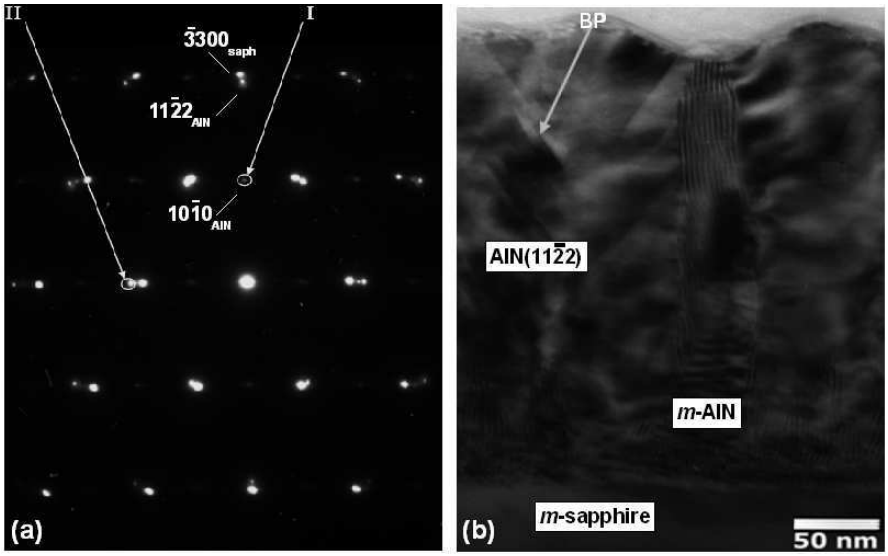

Figure 3.8: *(a) SAED image of an AlN layer grown under Al-rich conditions, recorded along the $[0001]_{sapphire}$ azimuth. The reflections attributed to sapphire($1\bar{1}00$) are the most intense. AlN($10\bar{1}0$) and AlN($11\bar{2}2$) contributions are referred as "I" and "II", respectively. (b) TEM image of the whole layer viewed along the $[0001]_{sapphire}$ axis. The layer shows AlN($11\bar{2}2$) matrix with AlN($10\bar{1}0$) domains at the interface with the sapphire, some of them propagating towards the surface. Images from P. Ruterana et al., CNRS-CAEN, France.*

Figure 3.8(b) is the corresponding TEM image of this sample, viewed along the $[0001]_{sapphire}$ azimuth. We can verify that AlN(10$\bar{1}$0) and AlN(11$\bar{2}$2) domains seem to be in equivalent proportions, which is consistent with the XRD analysis. More particularly, we can observe that the layer presents two types of AlN(10$\bar{1}$0) domains. Some of them are clusters situated at the interface with the sapphire, with an average height around 50 nm. We also see an additional domain propagating through the whole layer up to the surface. The presence of such domains emerging at the surface explains the bi-periodic RHEED patterns observed for Al-rich grown layers at the end of the growth [Fig. 3.1(b)]. Note that in this image, we can also observe the presence of basal plane (BP) defects.

Figures. 3.9(a) and (b) are SAED images recorded at the interface between the sapphire and the layer, on a region presenting only the semipolar AlN. These

diffraction patterns show reflections originating from both the substrate and the epilayer. For better understanding, the sapphire reflections are named in the three-index system, whereas the ($hkil$) notation is used for AlN. With Fig.3.9(a), recorded along the $[\bar{1}\bar{1}20]_{sapphire}$ zone axis, we can further verify that $(11\bar{2}2)_{AlN}$ is parallel to $(\bar{3}300)_{sapphire}$. In Fig. 3.9(b), recorded along the $[0001]_{sapphire}$ zone axis, $(\bar{1}100)_{AlN}$ and $(\bar{1}\bar{1}20)_{sapphire}$ reflections are aligned, which implies $[\bar{1}100]_{AlN}$ // $[\bar{1}\bar{1}20]_{sapphire}$. On the other hand, Fig. 3.9(c) was recorded at the interface with the substrate, where both the nonpolar and semipolar orientations appear. If we compare with the image above, we can see that the diffraction pattern emanating from m-AlN does not display the hexagonal pattern, but a rectangular pattern equivalent to these in Fig. 3.9(a). This indicates an in-plane rotation of 90° of m-AlN with respect to m-sapphire.

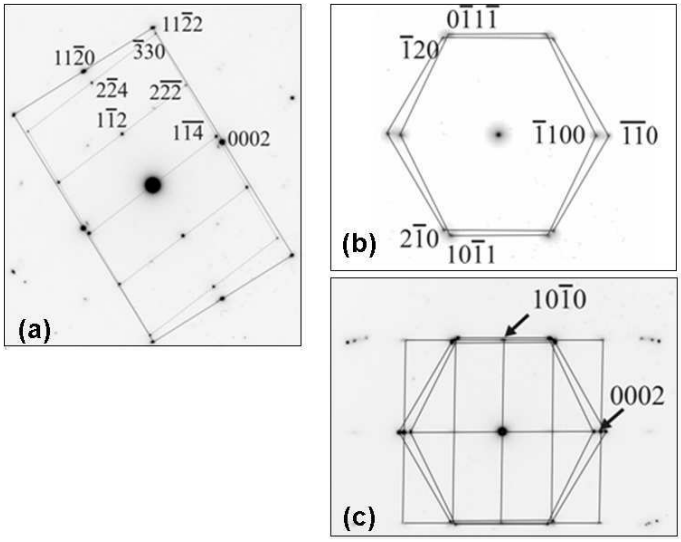

Figure 3.9: *SAED patterns of the epilayer-substrate interface recorded along (a) the $[\bar{1}\bar{1}20]_{sapphire}$ and (b) the $[0001]_{sapphire}$ zone axis on a region containing only semipolar AlN. (c) image recorded along the $[0001]_{sapphire}$ zone axis on a zone presenting both nonpolar and semipolar orientations. To distinguish the reflections from sapphire to those from AlN the 3-index system is used for sapphire. Images from P. Komninou et al., Aristotle University of Thessaloniki, Greece.*

Cross-sectional HRTEM images from m-AlN in Fig. 3.10 corroborate the in-plane epitaxial arrangement, which is illustrated schematically in Fig. 3.11. In Figs. 3.10(a) and 3.11(a), viewed along the $[0001]_{sapphire}$ zone axis, we can see the stacking of the $(0001)_{AlN}$ planes along $[11\bar{2}0]_{sapphire}$, which indicates that $[0001]_{AlN}$ lies perpendicular to $[0001]_{sapphire}$. On the contrary, the hexagonal distribution of the atoms in Figs. 3.10(b) and 3.11(b), viewed along $[11\bar{2}0]_{sapphire}$, is typical from the $(0001)_{AlN}$ planes, which confirms that $[0001]_{AlN}$ is parallel to $[11\bar{2}0]_{sapphire}$. Hence the in-plane epitaxial relationships between AlN($10\bar{1}0$) and m-sapphire:

$[0001]_{AlN}$ // $[11\bar{2}0]_{sapphire}$ and $[\bar{1}\bar{1}20]_{AlN}$ // $[0001]_{sapphire}$.

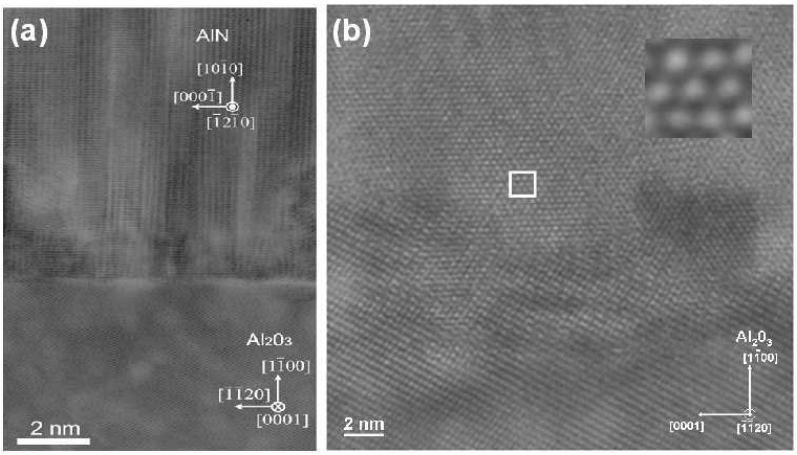

Figure 3.10: *HRTEM image of the interface between m-AlN and m-sapphire viewed along (a) $[0001]_{sapphire}$ and (b) $[11\bar{2}0]_{sapphire}$ axis. The 90° in-plane rotation of AlN with respect to sapphire can be deduced from the atomic arrangement. Images from P. Komninou et al., Aristotle University of Thessaloniki, Greece.*

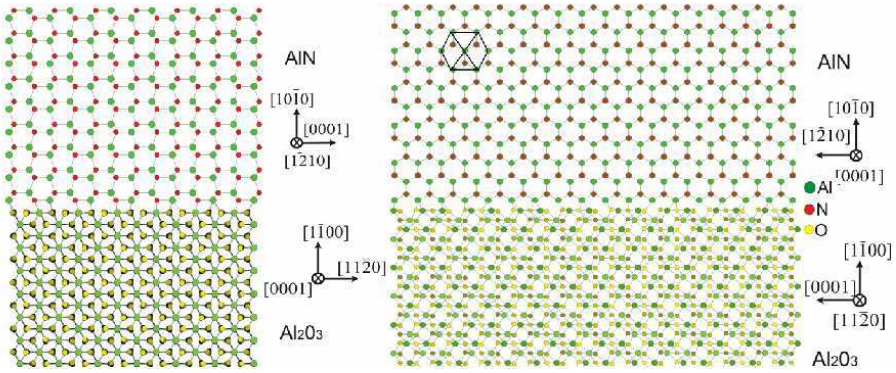

Figure 3.11: *Schematic illustration of the epitaxial relationships of m-AlN with respect to m-sapphire. To be compared with the HRTEM images in Fig. 3.10, the structures are viewed along $[0001]_{sapphire}$ and (b) $[11\bar{2}0]_{sapphire}$. Images from P. Komninou et al., Aristotle University of Thessaloniki, Greece.*

In the case of AlN(11$\bar{2}$2), we have seen with SAED that $[\bar{1}100]_{AlN}$ lies parallel to $[\bar{1}\bar{1}20]_{sapphire}$. The cross-sectional HRTEM image viewed along $[0001]_{sapphire}$ and the corresponding calculated structure are pictured in Fig. 3.12 and attest this epitaxial alignment. However, it is important to note that the direction of $[11\bar{2}\bar{3}]_{AlN}$ is not *a priori* determined. Fig. 3.13 illustrates the two possible ways AlN(11$\bar{2}$2) can arrange on *m*-sapphire: the AlN basal planes can be close to either the $(1\bar{1}04)_{sapphire}$ planes [Fig. 3.13(a)] or the $(1\bar{1}02)_{sapphire}$ *r*-planes [Fig. 3.13(b)]. Since the *c*-axis has a component along the <11$\bar{2}\bar{3}$> direction, $[11\bar{2}\bar{3}]_{AlN}$ and $[\bar{1}\bar{1}23]_{AlN}$ are not equivalent. Therefore, it is important to determine the alignment of AlN on sapphire along this direction. In both simulation, we assume Al-polarity, which will be later justified in the study of GaN (see in section 4.1.1).

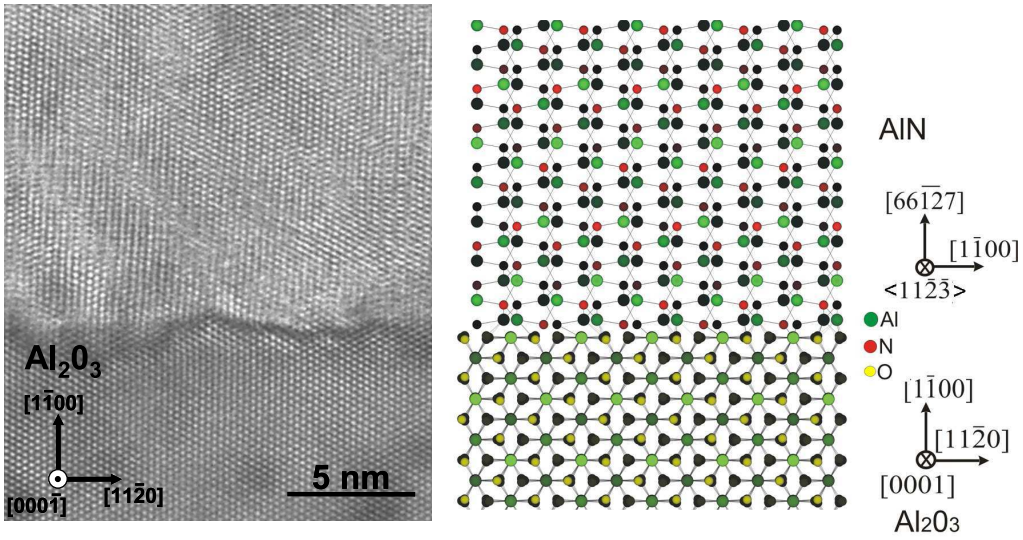

Figure 3.12: *HRTEM image of the AlN(11$\bar{2}$2) viewed [0001]$_{sapphire}$ axis. Image from P. Komninou et al., Aristotle University of Thessaloniki, Greece.*

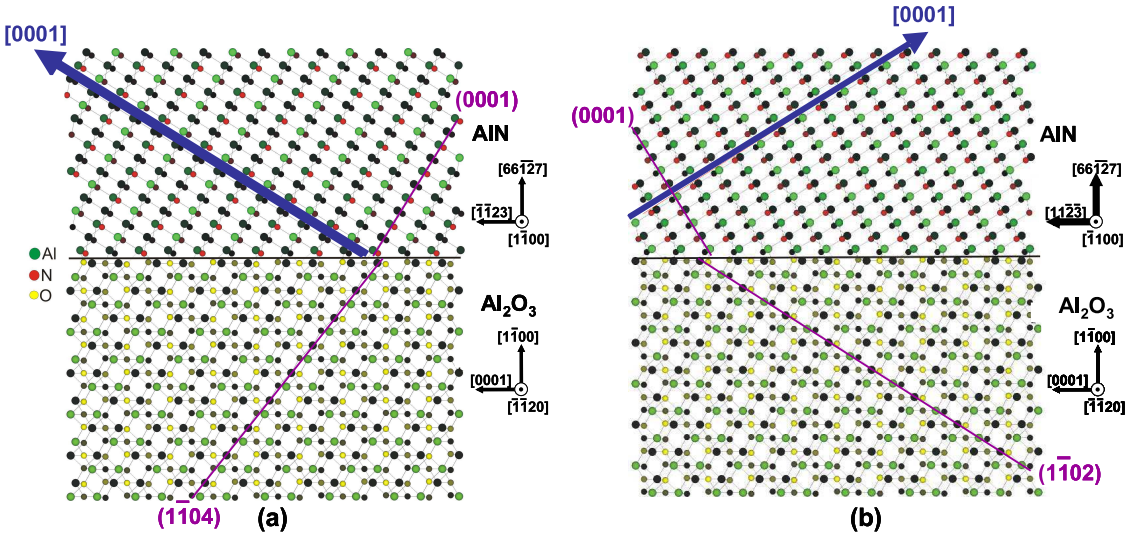

Figure 3.13: *Schematic illustration of the two possible arrangements of AlN(11$\bar{2}$2) on m-sapphire, i.e. with (a) [$\bar{1}\bar{1}$23]$_{AlN}$ // [0001]$_{sapphire}$ or (b)[11$\bar{2}\bar{3}$]$_{AlN}$ // [0001]$_{sapphire}$. Images from P. Komninou et al., Aristotle University of Thessaloniki, Greece.*

When indexing the SAED image in Fig. 3.9(a), recorded along the [$\bar{1}\bar{1}$20]$_{sapphire}$ zone axis, we observed that the (0002)$_{AlN}$ reflection is aligned with those from (1$\bar{1}$04)$_{sapphire}$, which implies [$\bar{1}\bar{1}$23]$_{AlN}$ // [0001]$_{sapphire}$ [image in Fig. 3.13(a)]. This epitaxial relationship is further confirmed by the cross-sectional HRTEM image in Fig. 3.14, in which we can observe that the (1$\bar{1}$02) *r*-planes of sapphire are not aligned with the basal planes of AlN.

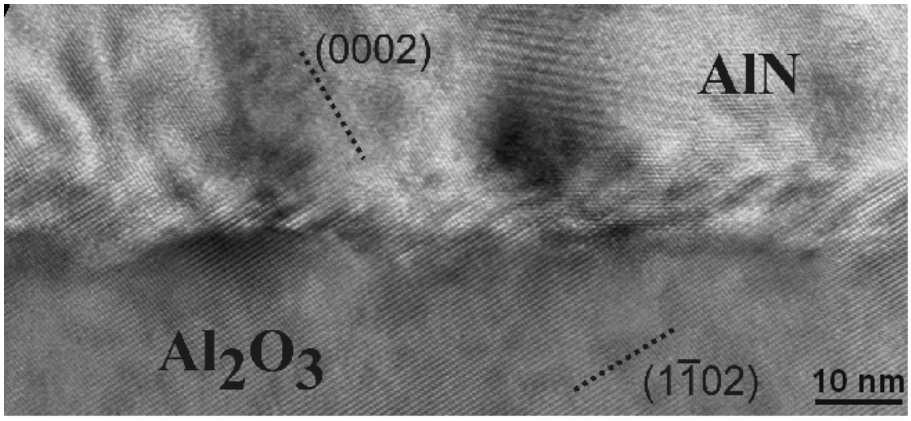

Figure 3.14: *Cross-sectional HRTEM image of the interface between AlN(11$\bar{2}$2) and m-sapphire viewed along <11$\bar{2}$0>$_{sapphire}$. The basal planes of AlN are aligned with the (1$\bar{1}$04) planes of sapphire, which corresponds to the simulation in Fig. 3.13(a).*

Finally, Fig. 3.15 shows cross-sectional HRTEM images of the interface between nonpolar and semipolar AlN domains. If the layer is viewed along the $[\bar{1}100]_{semipolar}/[0001]_{nonpolar}$ zone axis, we can see that $(0002)_{semipolar}$ planes are exactly aligned with the $(01\bar{1}0)_{nonpolar}$ planes. In a similar way, $(0002)_{nonpolar}$ planes are aligned with the $(\bar{1}100)_{semipolar}$ planes. This indicates a rotation of the two domains of about 90° around the $[2\bar{1}\bar{1}0]$ axis with respect with each other. In these two images, we can see the good crystalline arrangement between the domains, which seems to be favored by the introduction of dislocations at their boundary [Fig. 3.15(a)].

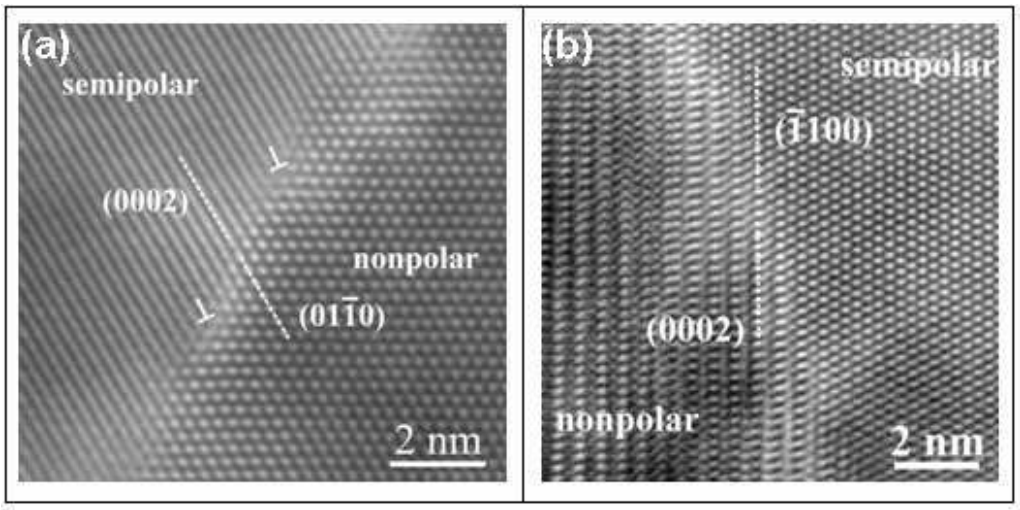

Figure 3.15: *Cross sectional HRTEM images recorded along (a) the $[\bar{1}100]_{semipolar}/[0001]_{nonpolar}$ zone axis and (b) the $[\bar{1}\bar{1}23]_{semipolar}/[\bar{1}\bar{1}20]_{nonpolar}$ zone axis. Images from P. Komninou et al., Aristotle University of Thessaloniki, Greece.*

As a conclusion from this section, we have shown that m-AlN can appear either as small clusters at the interface with the sapphire or as larger domains propagating throughout the whole layer. The analysis of AlN by the combination of HRTEM and SAED measurements made it possible to identify the following in-plane relationships for AlN($11\bar{2}2$) and AlN($10\bar{1}0$) on m-sapphire:

- AlN($10\bar{1}0$): $[0001]_{AlN}$ // $[\bar{1}\bar{1}20]_{sapphire}$ and $[\bar{1}\bar{1}20]_{AlN}$ // $[0001]_{sapphire}$.
- AlN($11\bar{2}2$): $[1\bar{1}00]_{AlN}$ // $[\bar{1}\bar{1}20]_{sapphire}$ and $[\bar{1}\bar{1}23]_{AlN}$ // $[0001]_{sapphire}$.

3.1.4 Synthesis of two-dimensional AlN($11\bar{2}2$)

From the study of AlN growth as a function of the III/V ratio, we can assume that the most stable AlN crystallographic orientation deposited on m-sapphire should be AlN($11\bar{2}2$). In order to verify this assertion and thus optimize the growth conditions of AlN($11\bar{2}2$), I analyzed the influence of the nitridation of m-sapphire, the substrate temperature, and the earlier steps of the growth.

3.1.4.1 Effect of the substrate temperature

Several AlN layers were deposited at various substrate temperatures, from 580°C to 850°C. The samples were grown without nitridation under constant III/V ratio ($\approx$ 0.92). Temperature below 600°C leads to polycrystalline growth with RHEED patterns similar to Fig. 3.1(d). On the contrary, an increase of the substrate temperature above $\approx$ 800°C leads to spotty RHEED patterns, identical to those in Fig. 3.1(b). Therefore, we decided to keep the substrate temperature to 720°C which corresponds to the growth temperature of GaN(0001), and hence easily reproducible.

3.1.4.2 Discussion on m-sapphire nitridation

The nitridation process consists on the exposure of the substrate (Al_20_3) to an active nitrogen flux for a certain time. It has been previously demonstrated that the nitridation effect on c-plane sapphire by PAMBE strongly depends on the substrate temperature [Los01, Geo01]. When performed under temperature lower than 200°C, it induces the formation of a homogeneous c-oriented AlN thin layer. High temperature nitridation favors the creation of AlN domains with additional NO domains, whose formation/desorption equilibrium is directly related to the temperature. However, regarding m-sapphire substrates, there is no report on the effect of PAMBE nitridation, to the best of our knowledge.

Figures 3.16(a) and (b) present the RHEED patterns of m-sapphire along $<0001>_{sapphire}$ and $<11\bar{2}0>_{sapphire}$ azimuths, respectively. Additionally, the RHEED images of the nitridated substrate are presented in Figs. 3.16(c) and (d), recorded after 15 min of nitridation, and in Figs. 3.16(e) and (f) after 30 min of nitridation. After nitridation, the RHEED images present the same patterns and periodicity as

the RHEED images from AlN(10$\bar{1}$0): Figures. 3.16(c) and (e) are similar to those of *m*-AlN viewed along <11$\bar{2}$0>$_{AlN}$ azimuth in Fig. 3.4(a), whereas Figs. 3.16(d) and (f) are similar to Fig. 3.4(b). We can therefore conclude that the nitridation induces the formation of an AlN(10$\bar{1}$0) layer at the *m*-sapphire surface, which presents the in-plane epitaxial relationships enunciated in the former section: <0001>$_{sapphire}$ // <11$\bar{2}$0>$_{AlN}$ and <11$\bar{2}$0>$_{sapphire}$ // <0001>$_{AlN}$.

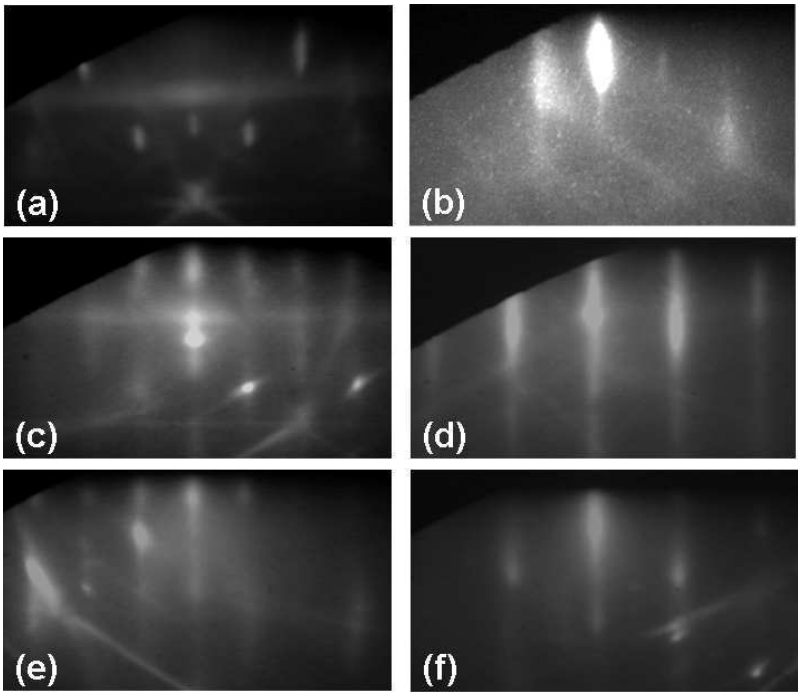

Figure 3.16: *RHEED patterns of m-sapphire viewed along (a) <0001>$_{sapphire}$ and (b) <11$\bar{2}$0>$_{sapphire}$, and RHEED images illustrating its evolution [(c), (d)] after 15 min and [(e), (f)] 30 min of nitridation.*

Figure 3.17(a) is a weak-beam TEM image off the <0001>$_{sapphire}$ zone axis recorded on sample E1769, grown directly on *m*-sapphire. This sample exhibits a polycrystalline interface with the substrate, with ≈ 30-nm-high grains. On the other hand, Fig. 3.17(b), which was recorded on E1768 shows the presence of nonpolar domains higher than 50 nm, and often exceeding 100 nm in other zones. Thus, the nitridation seems to help the formation of the nonpolar *m*-AlN. An interesting feature in Fig. 3.17(b) is the presence of v-shaped defects on the sapphire. On the magnification in Figs. 3.14 and 3.18(a), the v-defects seem to have facets aligned with the (10$\bar{1}$4) and (10$\bar{1}$2) *r*-planes. These v-defects exist independently of the nitridation process. When viewed along <0001>$_{sapphire}$, the v-defects are also identified [Fig. 3.17(b)] and they present (11$\bar{2}$0)-oriented facets. We observed that the nonpolar domains are mainly present at the surrounding of the v-defects and surface roughness (pointed out by the white arrows). This image also shows the presence of additional misoriented domains in the same area.

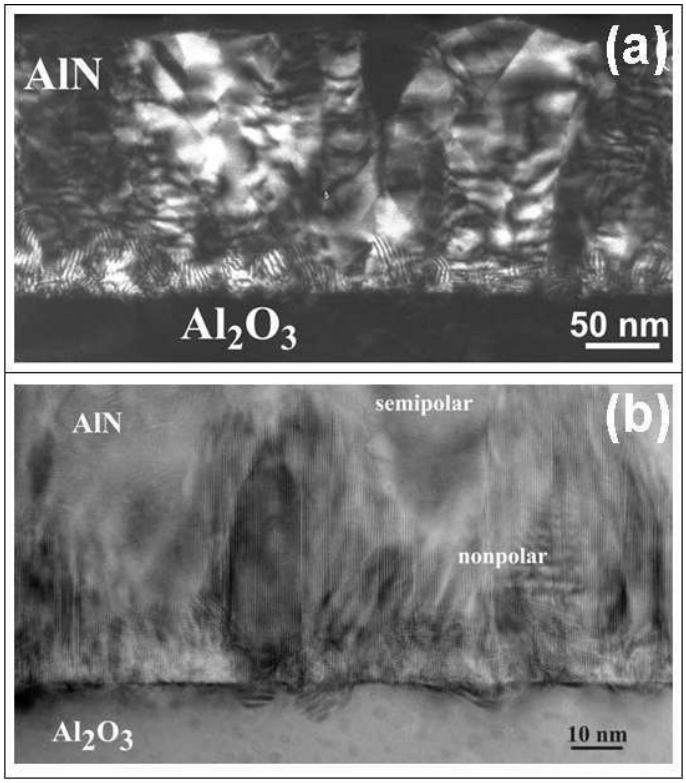

Figure 3.17: *(a) Weak-beam g/3g dark-field image obtained on sample E1769, off the* $[11\overline{2}\overline{3}]_{AlN}/[0001]_{sapphire}$ *zone axis with* $g = [\overline{1}100]$. *(b) Cross-sectional HRTEM image of sample E1768 recorded along the* $[11\overline{2}\overline{3}]_{AlN}/[0001]_{sapphire}$. *Images from P. Komninou et al., Aristotle University of Thessaloniki, Greece.*

At this stage, we assume that the growth of nonpolar AlN is enhanced by the roughness and the presence of v-defects at the sapphire surface. The facets of these defects may act as growth catalysts depending on they orientation. The origin of the v-shaped defects and surface roughness requires further investigation on the evolution of sapphire at different stages of the growth, since these features were not observed on AFM images of the substrates prior to growth.

As a conclusion of this study, the nitridation process should be suppressed since it favors the nucleation of large domains of AlN$(10\overline{1}0)$.

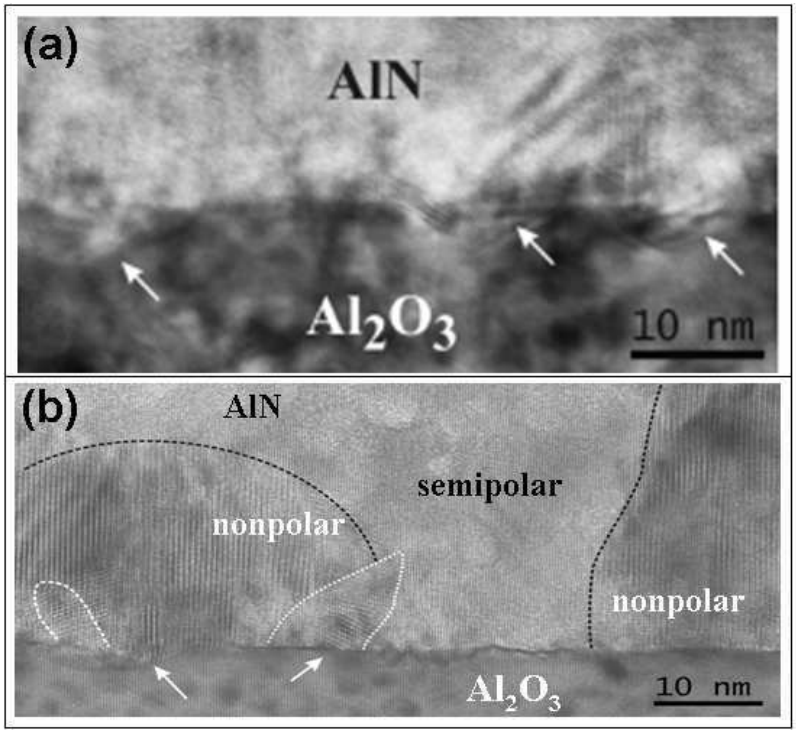

Figure 3.18: *Cross-sectional HRTEM images of the interface between AlN and sapphire to show the presence of v-shaped defects on the sapphire surface. (a) Viewed along <11$\bar{2}$0>$_{sapphire}$ axis and (b) along <0001>$_{sapphire}$ axis. Both images were recorded on a sample with no nitridation of the substrate before the growth. Images from P. Komninou et al., Aristotle University of Thessaloniki, Greece.*

3.1.4.3 Starting the growth

When following the RHEED evolution, I noticed that AlN(11$\bar{2}$2) growth is highly sensitive to the initial stages of the growth, even under constant III/V ratio ≈ 0.92 and equivalent substrate temperatures. However, reproducible results were achieved with the following sequence:

- 10 s Al
- 20 s AlN
- 30 s N
- 15 s AlN + 15 s N
- 30 s AlN + 30 s N

The growth starts with 10 s of Al ($\approx$ 3ML), to saturate the surface with metallic atoms and avoid the nitridation reaction which would favor AlN(10$\bar{1}$0) formation. After 20 s of AlN, the RHEED shows typical Al accumulation rings, which disappear after 30 s of nitrogen exposure. The subsequent AlN deposition leads to the same rings after 15 to 20 s, and it takes another 15 s to consume it. The same rings appear again after 30 s of AlN, and it takes the same time under N to disappear. At this time, the RHEED is clearly polycrystalline, but we can distinguish the

diffraction patterns coming from both AlN(11$\bar{2}$2) and AlN(10$\bar{1}$0). You can see typical RHEED images recorded along <11$\bar{2}\bar{3}$>$_{AlN}$ azimuth in Fig. 3.19. In (a), which corresponds to 3 min of growth, we can identify the typical (11$\bar{2}$2), which presents diffuse spots. Figure (b) which was recorded after 6 min of growth has more defined spots and after 9 min, (c), lines start to appear between the spots, indicating an improvement of the morphology. Finally, after 25 min of deposition, (f), the lines are predominant.

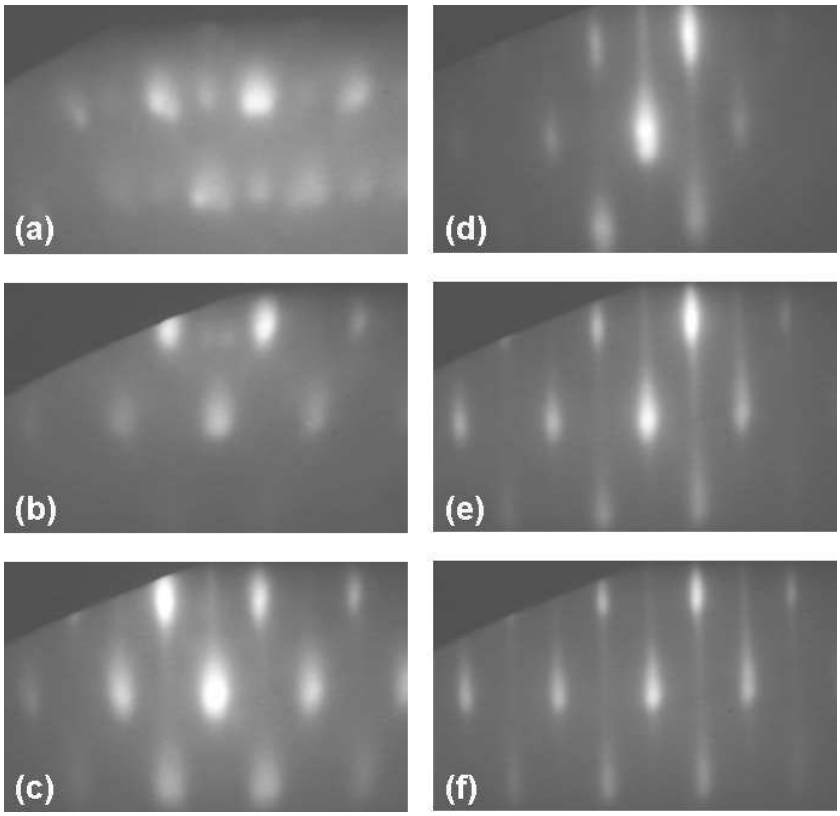

Figure 3.19: *Evolution of the RHEED pattern during the optimized growth of AlN(11$\bar{2}$2). Images were recorded along <11$\bar{2}\bar{3}$>$_{AlN}$ azimuth after (a) 3 min, (b) 6 min, (c) 9 min, (d) 14 min, (e) 18 min, (f) 25 min.*

3.2 Crystalline structure of AlN(11$\bar{2}$2)

This section describes the study of the strain state of semipolar AlN layers using both XRD and TEM measurements, and the characterization of the typical surface morphologies by AFM.

3.2.1 XRD experiments

First of all, I will give a detailed overview of the XRD method I used to estimate the strain state and relaxation of the layers. This part is based on the

data recorded on sample E1529, which is described later, in Table 3.5. Unless mentioned, all the directions indices in this part correspond to those of AlN. As explained in Fig. 2.25, the reflections can be scanned either with <1$\bar{1}$00> or <11$\bar{2}\bar{3}$> in the diffraction plane. In the following, ϕ_0 and ϕ_{90} refer to the configurations with <1$\bar{1}$00> and <11$\bar{2}\bar{3}$> in the diffraction plane, respectively. Additionally, since the *c*-axis is not perpendicular to the <11$\bar{2}$3> direction, we have to differentiate ϕ_{90} and ϕ_{-90} configurations. As illustrated in Fig. 3.20(b) and (c), they differ from the direction of [11$\bar{2}$3] relatively to the setup.

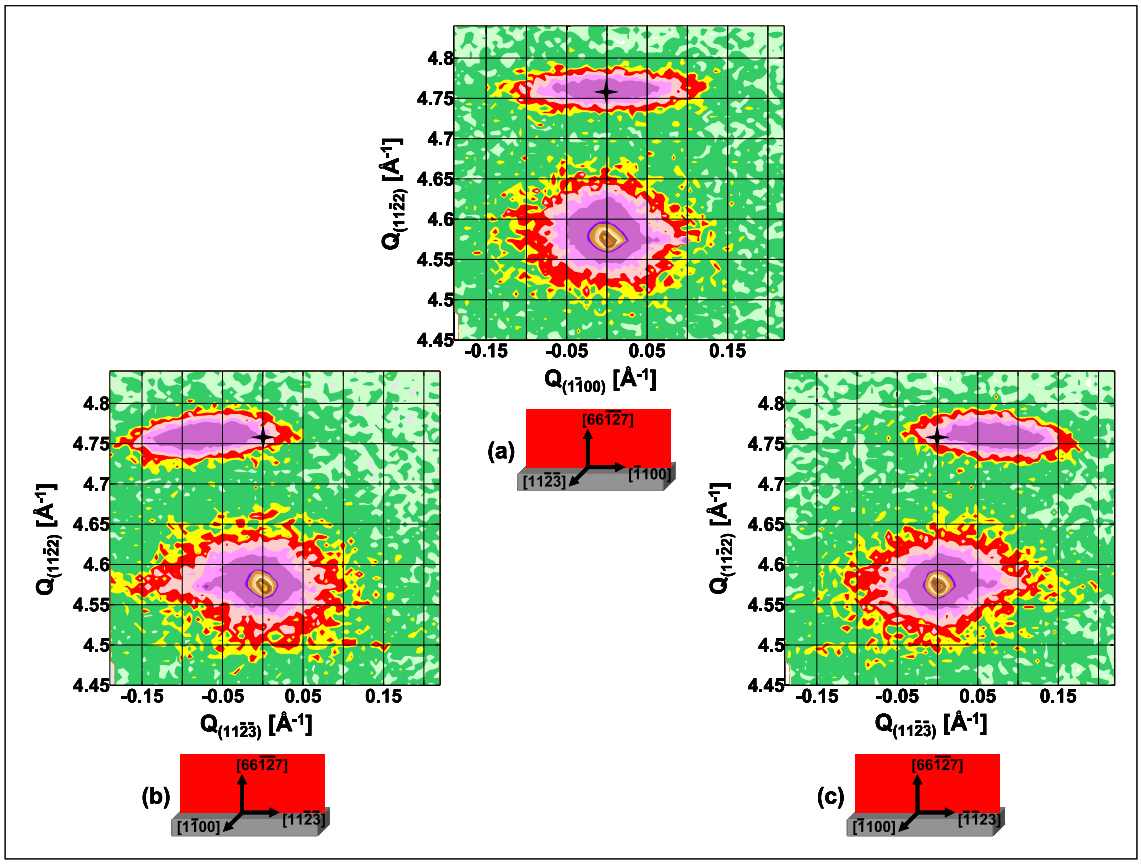

Figure 3.20: *Symmetric RSMs recorded under (a) Φ_0, (b) Φ_{90}, and (c) Φ_{-90} configurations. Note that the direction of [0001] relatively to the setup is the opposite in Φ_{90} and Φ_{-90} configurations.*

Symmetric $2\theta - \omega$ scans provide an accurate value of the out-of-plane parameter, $d_{11\bar{2}2}$ (*cf.* Eq. 2.10). The error bar is in the range of 0.002° for 2θ, so that the determination of $d_{11\bar{2}2}$ is precise with an error of less than 0.001 Å. Symmetric RSMs give information on both the misorientation and the mosaicity. It is therefore important to record them in both configurations, both with <1$\bar{1}$00> and <11$\bar{2}\bar{3}$> in the diffraction plane. As an example, Fig. 3.20 shows the RSMs recorded under the three configurations ϕ_0, ϕ_{90}, and ϕ_{-90} configurations. In each map, the star-symbol indicates the theoretical position of relaxed AlN(11$\bar{2}$2). In Fig. 3.20(a), the AlN reflection is aligned with the reflection from the substrate, which means that the

out-of-plane misorientation of the <1$\bar{1}$00> axis is negligible. On the contrary, in Fig. 3.20(b), the center of the AlN reflection is misaligned with those of the substrate. This indicates a misorientation of the layer around the <1$\bar{1}$00> axis, *i.e.* a certain tilt angle between $<11\bar{2}\bar{3}>_{AlN}$ and $<0001>_{sapphire}$. The mirror-like position of the AlN reflection in Fig. 3.20(c) is due to the opposite direction of [11$\bar{2}\bar{3}$] in both configurations. The FWHM along $Q_{//}$ is similar in both configurations ($\approx 1.3°$), but the FWHM along $Q_{\perp}$ is larger for $\phi_{\pm 90}$ than for ϕ_0. This implies an isotropic lateral coherence length whereas the vertical coherence length is larger along the <1$\bar{1}$00> axis.

Since they have components along the out-of-plane and in-plane directions, the asymmetric reflections can only be recorded on one of the configurations. In the case of AlN(11$\bar{2}$2), (20$\bar{2}$2) and (11$\bar{2}$4) are the two asymmetric reflections under study.

(20$\bar{2}$2) can be decomposed as: (20$\bar{2}$2) = 1×(11$\bar{2}$2) + 1×(1$\bar{1}$00), so that it is only observed on ϕ_0 configuration. Figures 3.21(a) and (b) show the asymmetric RSMs around the AlN(20$\bar{2}$2) reflection, in both grazing incidence and emergence respectively. In each map, the most intense reflection is attributed to sapphire(4$\bar{2}\bar{2}$0). The intensities of the peaks recorded in grazing emergence is very weak and do not provide accurate information. However, we can see that the AlN peak position in (a) is not exactly centered on the relaxed AlN position (star). This means that the layer is stressed on the substrate along <1$\bar{1}$00>. The broadening of the peak is perpendicular to its diffraction vector, which is another indication of the mosaicity along <1$\bar{1}$00>.

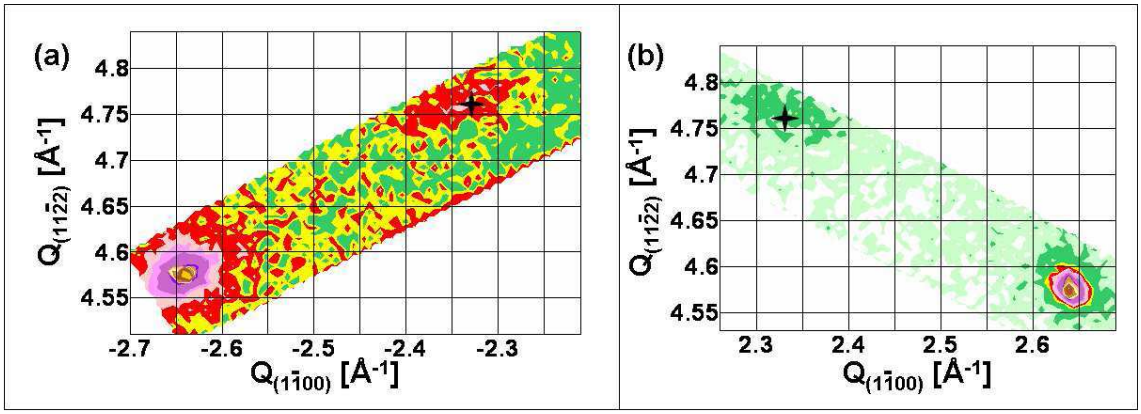

Figure 3.21: *RSMs recorded at ϕ_0 under grazing (a) incidence and (b) emergence around AlN(20$\bar{2}$2) reflections.*

The case of the (11$\bar{2}$4) reflection is different since grazing incidence and emergence do not lead to the scan of the same plane. Indeed, on grazing incidence, with ϕ_{90}, we can record $\frac{7}{5}\times(11\bar{2}2) + \frac{2}{5}\times(\bar{1}\bar{1}23) = (11\bar{2}4)$. The grazing emergence would lead to $\frac{7}{5}\times(11\bar{2}2)$ - $\frac{2}{5}\times(\bar{1}\bar{1}23) = \left(\frac{9}{5}\frac{9}{5}\frac{\bar{18}}{5}\frac{8}{5}\right)$ which is not accessible. However, if we

turn to ϕ_{-90}, the grazing emergence configuration leads to ($\frac{7}{5}\times(11\bar{2}2)$ - $\frac{2}{5}\times(11\bar{2}\bar{3})$ = $(11\bar{2}4)$. Therefore, Figs. 3.22 and 3.23 are the RSMs of the $(11\bar{2}4)$ reflection recorded under grazing incidence (ϕ_{90}) and grazing emergence (ϕ_{-90}) respectively. In both figures, the most intense reflection is attributed to sapphire$(4\bar{4}04)$. In (a), which is the map corrected with respect to sapphire, we can observe the important misorientation of AlN reflection compared to the relaxed AlN theoretical position. In order to access the lattice parameters and the stress in $(11\bar{2}2)$ domain, we need to correct the RSMs by subtracting the tilt measured in the symmetric RSMs ($\pm$ 0.9° in this sample). This gives the RSMs in Figs. 3.22(b) and 3.23(b), in which the reflection is not centered on the star, which means a certain stress along <11$\bar{2}\bar{3}$> axis.

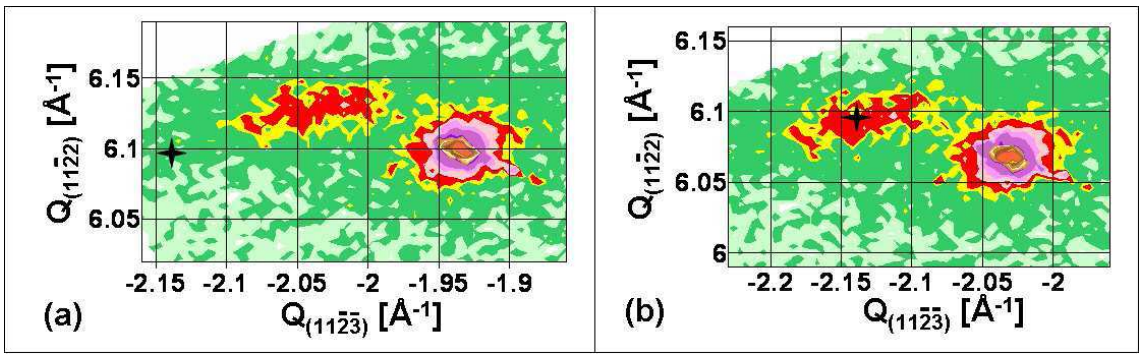

Figure 3.22: *RSMs around AlN(11$\bar{2}$4) recorded under grazing incidence, at ϕ_{90}, corrected to (a) sapphire and (b) AlN.*

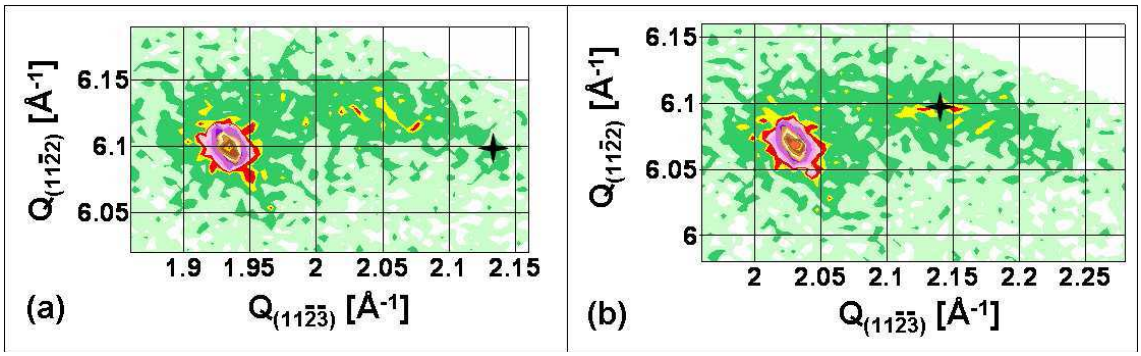

Figure 3.23: *RSMs around AlN(11$\bar{2}$4) recorded under grazing emergence, at ϕ_{-90}, corrected to (a) sapphire and (b) AlN.*

3.2.2 Estimation of the lattice parameters in thick layers

The lattice mismatch between AlN(11$\bar{2}$2) and *m*-sapphire is -9.61% and 13.35% along the *c* axis and the *a* axis of the *m*-sapphire, respectively. Therefore, it is not obvious whether the resulting in-plane stress should induce an equibiaxial or non-equibiaxial deformation of the hexagonal lattice. Consequently, I have considered

the three lattice parameters, a, b and c presented in Fig. 2.29. Given the non-zero components of the strain tensor calculated in Table 1.9, we expect $a \leq a_0$, $b \geq a_0$, and $c \leq c_0$, where a_0 and c_0 are the lattice parameters of relaxed AlN.

From the series of layers grown under different III/V ratio, we can compare the samples with an equivalent thickness of $\approx$ 500 nm, *i.e.* E1011, E1021, E1020 and E1028 (cf. Table 3.1). The calculated lattice parameters are given in Table 3.4. The lattice parameters a and b are consistent with the expected deformation of the hexagonal plane ($a \leq a_0$ and $b \geq a_0$). However, the relaxed values reported in Table 3.3 are within the corresponding error bars of the three parameters a, b and c. Therefore, we can conclude that layers with a thickness in the range of 500 nm are approximately relaxed, whatever the III/V ratio used for the growth.

Samples	III/V ratio	a $\pm$ 0.014 [$\AA$]	b $\pm$ 0.002 [$\AA$]	c $\pm$ 0.004 [$\AA$]
E1011	1.15	3.101	3.117	4.968
E1021	1.02	3.106	3.113	4.993
E1020	0.92	3.112	3.117	4.993
E1028	0.84	3.102	3.117	4.969

Table 3.4: *Lattice parameters a, b and c depending on the III/V ratio.*

3.2.3 Relaxation analysis

To study the relaxation mechanisms involved in the growth of AlN(11$\bar{2}$2), I have chosen three AlN layers with different thickness, from 65 nm to 260 nm presented in Table 3.5. The evolution of the crystalline quality of the layers with their thickness can be accessed by the comparison of the ω-scan FWHM of the symmetric (11$\bar{2}$2) reflections. The values of the FWHM of ω scans rocking towards <11$\bar{2}$3> and <1$\bar{1}$00> are given in Table 3.5. The narrowing of the reflections when increasing the thickness of the layers indicates an improved quality. This is consistent with the TEM observations previously described, showing a poor quality of the interface between AlN(11$\bar{2}$2) and m-sapphire due to the presence of the parasitic AlN(10$\bar{1}$0) domains. Another important feature, is the larger FWHM for ω scans rocking towards <11$\bar{2}$3> compared to those towards <1$\bar{1}$00>. This is consistent with the systematic presence of a tilt angle between $<11\bar{2}3>_{AlN}$ and $<0001>_{sapphire}$ [see in Fig. 3.20(b) and (c)]. Thus, the value of the misorientation of the layers around <1$\bar{1}$00>, reported in Table 3.5, does not seem to follow a specific trend. The presence of this tilt is probably related to the lattice mismatch accommodation. However, at this point, theoretical calculations are not conclusive.

Table 3.6 gives the estimated values of the lattice parameters of the layers, considering an anisotropic in-plane deformation. When increasing the deposition time, the parameters b and c tend towards their relaxed values. This behavior im-

plies a gradual relaxation of the hexagonal cell in both b and c parameters. However, the error bars in the determination of parameter a towards lower values do not allow to explain its evolution at this point. We can compare these values to the values calculated assuming an isotropic deformation recorded in Table 3.7. The parameters a_{is} and c_{is} are close to the parameters b and c, respectively, which is consistent with gradual relaxation. Within the error bars of the measurements, the parameters a_{is} and c_{is} can be considered as relaxed for E1529 and E1533.

Samples	Thickness	Misorientation	ω scan FWHM	
			$< 10\bar{1}0 >$	$< 11\bar{2}3 >$
E1531	65 nm	1°	1.401°	2.151°
E1529	130 nm	0.9°	1.158°	1.597°
E1533	260 nm	1.4°	0.991°	1.192°

Table 3.5: *Misorientation and ω scan FWHM of AlN layers with different thickness. The decrease of the FWHM values in the two perpendicular in-plane directions can be interpreted as an evidence of the improvement of the layers quality with the thickness.*

Samples	Thickness [nm]	a $\pm$ 0.014 [Å]	b $\pm$ 0.002 [Å]	c $\pm$ 0.004 [Å]
E1531	65 nm	3.076	3.104	5.005
E1529	130 nm	3.069	3.109	4.987
E1533	260 nm	3.068	3.114	4.981

Table 3.6: *Lattice parameters of AlN layers, calculated assuming an anisotropic deformation of the basal plane.*

Samples	Thickness [nm]	a_{is} $\pm$ 0.007 [Å]	c_{is} $\pm$ 0.004 [Å]
E1531	65 nm	3.105	5.006
E1529	130 nm	3.109	4.987
E1533	260 nm	3.114	4.980

Table 3.7: *Lattice parameters of AlN layers, calculated assuming an isotropic deformation of the basal plane.*

In order to understand the gradual deformation of the hexagonal unit cell, we can study the evolution of the in-plane parameters of the (11$\bar{2}$2) surface. Their values have been calculated for all the layers and their difference with the relaxed values, Δ, are reported in Table 3.8. The opposite sign for Δ indicates an anisotropic deformation, due to the opposite mismatch along both directions. The evolution of the two in-plane parameters can be compared and completed for the earlier stages of growth by RHEED observations along the corresponding azimuths. As an example,

Fig. 3.24 shows the evolution of the period of the streaky pattern recorded on sample E1533, along <11$\bar{2}\bar{3}$> azimuth. In this azimuth, the distance between RHEED reflections is inversely proportional to the in-plane parameter $\sqrt{3}a$. a rapidly increases during the first $\approx$ 7 minutes, and it takes another 15 to 20 minutes to reach a stable value, which is consistent with the XRD conclusion that AlN(11$\bar{2}$2) layers with thickness higher than $\approx$ 130 nm are relaxed.

Samples	$\sqrt{3}a$ [$\AA$]	Δ_1 [%]	$\frac{\sqrt{b^2+c^2}}{2}$ [$\AA$]	Δ_2 [%]
E1531	5.378	-0.23	2.945	0.27
E1529	5.385	-0.09	2.938	0.05
E1533	5.393	0.05	2.937	0.004

Table 3.8: *Calculated values of the in-plane lattice parameters* $\sqrt{3}a$ *and* $\frac{\sqrt{a^2+c^2}}{2}$ *depending on the thickness of the layer.*

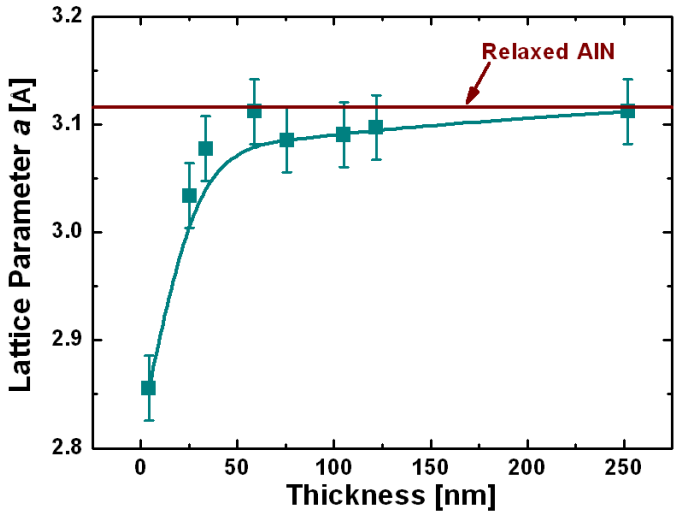

Figure 3.24: *Evolution of the in-plane parameter a during AlN growth.*

3.2.4 Surface morphology

This section is an overview of the typical surface morphology of AlN(11$\bar{2}$2). Figure 3.25 compares 1×1 μm^2 AFM images of AlN layers with a thickness of (a) 65 nm (E1531), (b) 90 nm (E1535), (c) 135 nm (E1529) and (d) 260 nm (E1533). The Root Mean Square (RMS) roughness, reported in Table 3.9, is in the range of 2 nm. In each image, the black arrow indicates the direction of $[11\bar{2}0]_{sapphire}$, *i.e.* $[1\bar{1}00]_{AlN}$. In spite of the presence of a tilt in the layers, the surfaces do not show any specific trend. In particular, we do not observe the same anisotropy as those found in nonpolar layer [Fou07, Ams08].

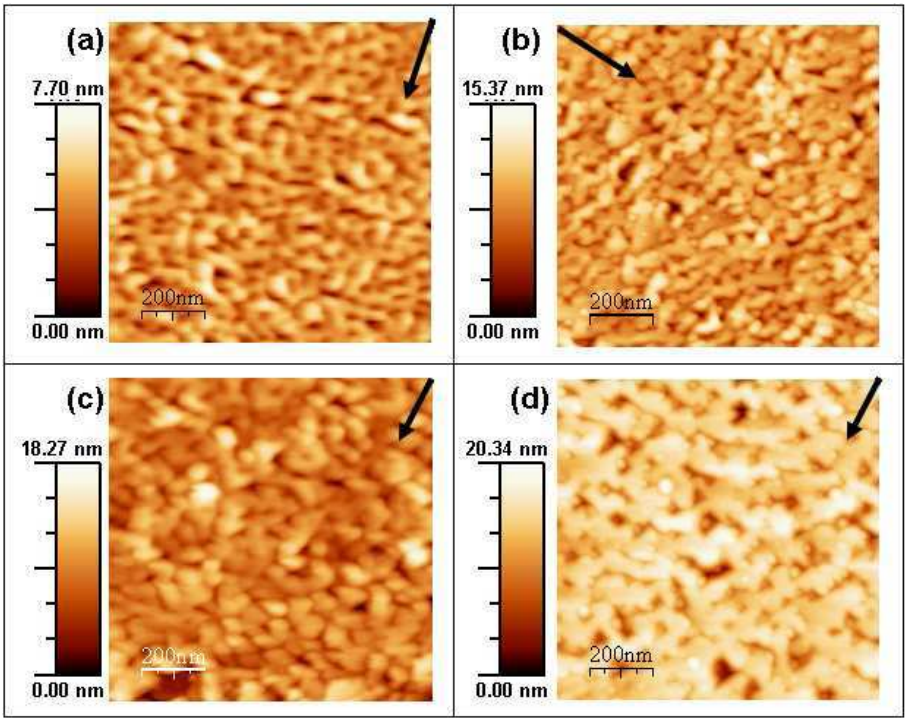

Figure 3.25: *AFM images recorded on AlN layers with a thickness of (a) 65 nm, (b) 90 nm, (c) 135 nm and (d) 260 nm. The black arrow indicates the <$\bar{1}$100> direction.*

Samples	Thickness	RMS roughness
E1531	65 nm	0.90 nm
E1535	90 nm	0.92 nm
E1529	135 nm	1.91 nm
E1533	260 nm	2.28 nm

Table 3.9: *RMS roughness of AlN(11$\bar{2}$2) layers.*

3.3 Conclusions

In this chapter, we demonstrate the synthesis of semipolar (11$\bar{2}$2)-oriented AlN layers on *m*-sapphire, by PAMBE. The AlN crystalline orientation depends strongly on the growth conditions when deposited on *m*-sapphire. The standard Al-rich conditions used for the growth of AlN(0001) lead to the formation of both (11$\bar{2}$2)- and (1$\bar{1}$00)-oriented domains in the layers. However, a III/V ratio of about 0.95 allows to significantly decrease the proportion of AlN(1$\bar{1}$00), so that it only appears in clusters situated at the interface with the substrate.

Substrate nitridation favors the formation of a higher density of AlN(1$\bar{1}$00) domains at the interface with sapphire, so that they tend to propagate over 100 nm. On the contrary, with no nitridation and with an appropriate growth sequence for the first 4 min of AlN deposition under the optimized III/V ratio, we managed to decrease the proportion of nonpolar AlN by the encapsulation of these domains by

AlN($11\bar{2}2$) after $\approx$ 50 nm.

The epitaxial relationships between AlN and m-sapphire for both the semipolar and the nonpolar orientations where identified. AlN($10\bar{1}0$) is twisted by 90° from the substrate, so that $[0001]_{AlN}$ // $[\bar{1}\bar{1}20]_{sapphire}$. For AlN($11\bar{2}2$), we found that $[1\bar{1}00]_{AlN}$ // $[\bar{1}\bar{1}20]_{sapphire}$ and $[\bar{1}\bar{1}23]_{AlN}$ // $[0001]_{sapphire}$. Additionally, images show a good interface between the two AlN orientations, with $(0002)_{semipolar}$ // $(01\bar{1}0)_{nonpolar}$ planes and $(0002)_{nonpolar}$ // $(\bar{1}100)_{semipolar}$ planes.

Chapter 4

Study of GaN(11$\bar{2}$2)

In this chapter, I present the growth and properties of two-dimensional GaN(11$\bar{2}$2). In the first section, I focus on the study of the growth modes of GaN, depending on the Ga/N ratio, considering its deposition directly on *m*-sapphire or on an AlN(11$\bar{2}$2) buffer layer. The structural and optical properties of GaN layers achieved within the best growth window are then analyzed.

The second part of this chapter focuses on the doping of GaN(11$\bar{2}$2) layers. In particular, we have deeply investigated the incorporation of Mg in the layers for *p*-type doping. The modification of the structural and optical properties of the layers is addressed, together with an analysis of their electrical performance. Part of the work presented in this chapter was reported in [Lah08b].

Contents

4.1 Growth of GaN(11$\bar{2}$2) 89

4.1.1 Crystalline orientation 89

4.1.2 Ga wetting on GaN(11$\bar{2}$2) 93

4.1.3 Identification of the growth window 98

4.2 Optical properties of GaN(11$\bar{2}$2) thick layers 103

4.3 Doping of GaN(11$\bar{2}$2) 107

4.3.1 Growth kinetics of doped GaN(11$\bar{2}$2) 108

4.3.2 Mg incorporation in GaN(11$\bar{2}$2) 110

4.3.3 Optical properties Mg-doped layers 114

4.3.4 Electrical characterization of Mg-doped layers 116

4.4 Conclusions 118

4.1 Growth of GaN(11$\bar{2}$2)

In this section, I focus on the PAMBE growth of (11$\bar{2}$2)-oriented GaN. After the analysis of GaN grown directly on *m*-sapphire, I study the Ga wetting of the GaN(11$\bar{2}$2) face and identify the different growth windows.

4.1.1 Crystalline orientation

I first analyzed the deposition of GaN directly on *m*-sapphire by varying the III/V ratio from N-rich to Ga-rich conditions. The description of the samples is given in Table 4.1. They were grown with a N flux corresponding to a growth rate of 0.28 ML/s, *i.e.* $\approx$ 260 nm/h for GaN(0001) layers grown under Ga-rich conditions.

Samples	underlayer	III/V ratio	Thickness	RHEED characteristics
E1033	*m*-sapphire	0.92	300 nm	spotty pattern
E1032	*m*-sapphire	1	300 nm	spotty pattern
E1035	*m*-sapphire	1.24	400 nm	two streaky patterns
E1036	AlN(11$\bar{2}$2)	1.24	300 nm	one streaky pattern

Table 4.1: *Series of GaN samples grown with a III/V ratio varying from N-rich to Ga-rich conditions.*

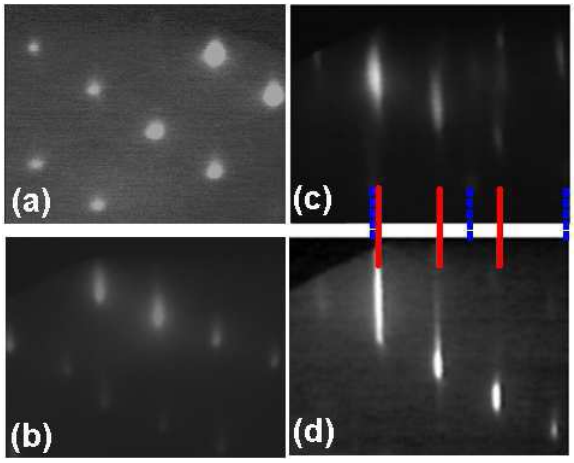

Figure 4.1: *RHEED patterns of GaN layers grown directly on m-sapphire with a III/V ratio of (a) 0.92, (b) 1 and (c) 1.24, and (d) on top of AlN(11$\bar{2}$2) with a III/V $\approx$ 1.24. All images have been recorded at the end of the growth along the <11$\bar{2}$0> azimuth of m-sapphire.*

Figure 4.1 shows the RHEED images recorded at the end of the growth. Under N-rich conditions (E1033) and at the stoichiometry (E1032), the RHEED presents a spotty pattern [Figs. 4.1(a) and (b), respectively] characteristic of three-dimensional (3D) growth. On the contrary, Ga-rich conditions (sample E1035) lead

to two-dimensional (2D) growth, as revealed by the streaky RHEED pattern in Fig. 4.1(c). When increasing the Ga flux to III/V $\approx$ 1.54, the RHEED becomes completely dark after a few minutes, indicating substantial Ga accumulation on the surface. It is important to notice that, whatever the III-N ratio, GaN deposited directly on *m*-sapphire settles into at least two crystalline orientations, as indicated by the superimposition of two RHEED patterns with different period [continuous and dashed lines Fig. 4.1(c)].

In order to identify the crystalline orientations involved, E1035 was characterized by both TEM and XRD. Figure 4.2(a) displays a symmetric reciprocal space map (RSM) of E1035, revealing reflections assigned to GaN(11$\bar{2}$2) and GaN(10$\bar{1}$3).

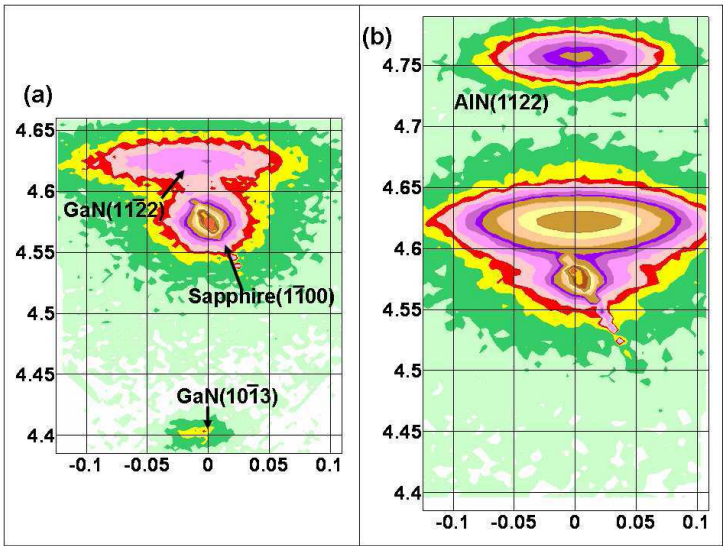

Figure 4.2: *XRD symmetric RSMs of samples grown (a) directly on m-sapphire (E1035) and (b) on top of an AlN(11$\bar{2}$2) buffer layer (E1036).*

Figure 4.3(a) presents a cross-section TEM image of sample E1035 recorded at the GaN/sapphire interface along the $[0001]_{sapphire}$ axis. In the corresponding diffraction pattern [Fig. 4.3(b)], the main reflections are attributed to *m*-sapphire and (11$\bar{2}$2)-oriented GaN. However, the background exhibits additional peaks which have all been indexed so that the (10$\bar{1}$3) plane lies perpendicular to the growth direction. This is in agreement with the above-described XRD results. The streaks along $[0001]_{GaN}$ direction are an indication of a high density of stacking faults in the GaN(10$\bar{1}$3). Figure 4.3(c) has been recorded along the <11$\bar{2}$0> zone axis of GaN(11$\bar{2}$2). In this image, GaN(10$\bar{1}$3) inclusions are no longer in strong diffraction conditions and become easier to identify (white arrows).

Finally, Fig. 4.3(d) depicts a view of the same sample along the <1$\bar{1}$00> zone axis of GaN(11$\bar{2}$2), where it is possible to evaluate the presence of basal plane stacking faults (BSFs). In this sample, we estimate a density of around 3×10^5 cm^{-1}, which is comparable to the values achieved by MOVPE for the same crystallographic orientation ($\approx$ 2 - 4×10^5 cm^{-1} [Ven07]). This high density of BSFs is characteristic

for the growth of nonpolar and semipolar III-nitride films [Ven07, Liu05, Cra02]. Even in layers prepared by the epitaxial lateral overgrowth (ELO) technique, the density of BSFs remains in the 10^5 cm^{-1} range [Ven07].

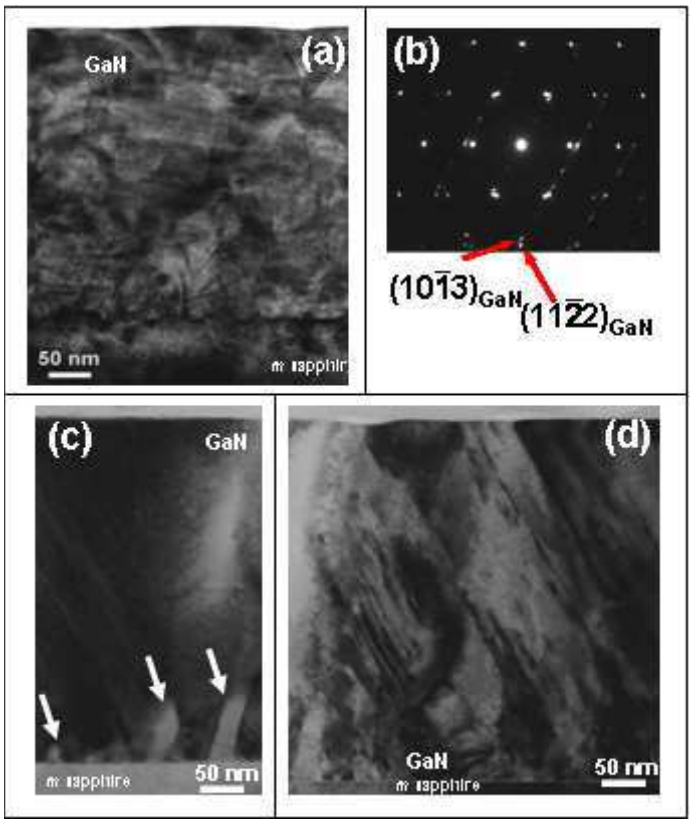

Figure 4.3: *TEM analysis of sample E1035. (a) Image recorded along <0001>$_{sapphire}$. (b) Diffraction pattern corresponding to image (a). (c) View along the <11$\bar{2}$0> axis of GaN(11$\bar{2}$2) to highlight the domains with different crystalline orientation (arrows). (d) View along the <1$\bar{1}$00> axis of GaN(11$\bar{2}$2) to estimate the density of stacking faults. Images from P. Ruterana et al., CNRS - CAEN, France.*

From this first study, we can conclude that the deposition of GaN directly on *m*-sapphire leads to the formation of two crystallographic orientations [GaN(11$\bar{2}$2) and GaN(10$\bar{1}$3)]. In order to minimize the proportion of the GaN(10$\bar{1}$3) domains, I deposited GaN on top of an AlN(11$\bar{2}$2) buffer layer (sample E1036 was grown on top of sample E1020 described in Section 3.1.1), under the same conditions used for E1035. The RHEED pattern of E1036 is presented in Fig. 4.1(d), showing only one periodic streaky pattern (continuous line). Moreover, the symmetric RSM of E1036 [Fig. 4.2(b)] only displays the reflections arising from both the AlN(11$\bar{2}$2) buffer layer and the GaN(11$\bar{2}$2) top layer. The absence of the peak assigned to GaN(10$\bar{1}$3) is consistent with the mono-periodic RHEED pattern. All together, this confirms that GaN(11$\bar{2}$2) becomes the dominant crystallographic orientation when GaN is deposited on top of AlN(11$\bar{2}$2).

In Fig. 4.4(a) and (b), I compare AFM images of the surfaces of samples grown directly on *m*-sapphire under N-rich conditions (E1033) and with a III/V ≈ 1.24 (E1035). On these 2×2 μ m^2 surfaces, I measured a root-mean-square (RMS) roughness of ≈ 11 nm for sample E1033, which is to be compared to ≈ 2.3 nm for E1035. This is consistent with the respective spotty and streaky RHEED patterns observed at the end of the growth.

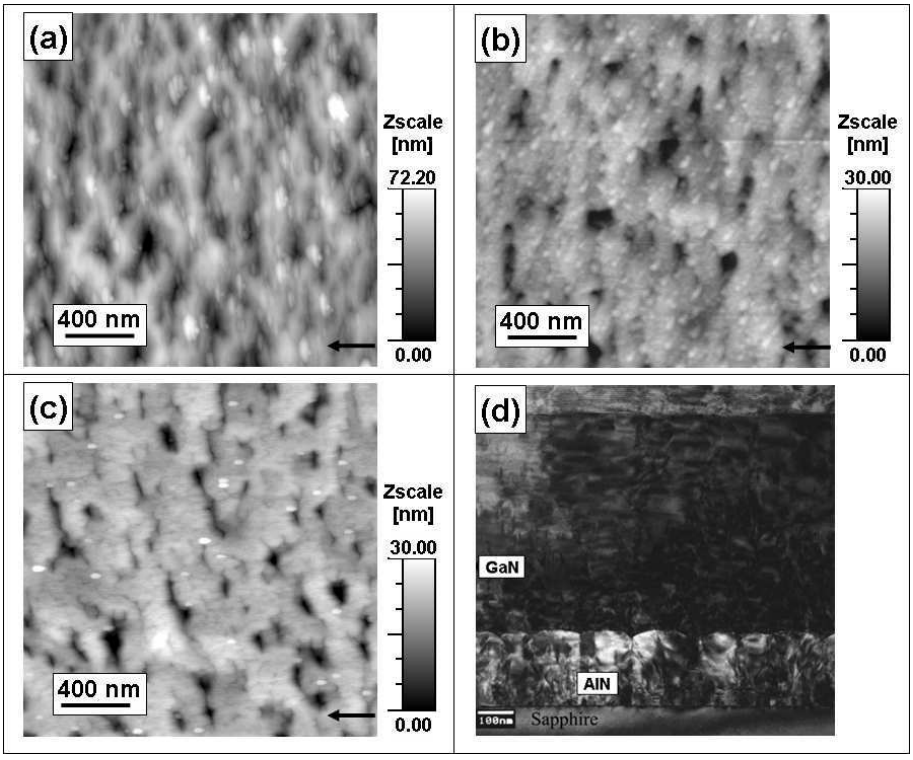

Figure 4.4: *Surface of GaN layers grown on m-sapphire under (a) N-rich conditions (E1033) and (b) III/V ≈ 1.24 (E1035). (c) GaN layer growth with III/V ≈ 1.24 on an AlN(11$\bar{2}$2) buffer layer (E1036). Figures (b) and (c) are normalized to the same z_{scale} in order to compare the surfaces of GaN when it is grown with or without the AlN buffer layer. (d) Example of TEM image of a GaN/AlN interface. The AlN layer has been grown under optimized growth conditions and GaN was deposited under Ga-rich conditions (III/V ≈ 1.24). TEM Image from P. Ruterana et al., CNRS - CAEN, France.*

Additionally, Figs. 4.4(c) and Fig. 4.4(d) show AFM and TEM images, respectively, of a GaN layer deposited on top of an AlN buffer layer, grown with a III/V ratio of ≈ 1.24. In this example, we have measured a RMS roughness of about 3.08 nm on the AlN buffer layer, whereas the growth of GaN on top leads to a RMS roughness of ≈ 1.5 nm (both measured on 3×3 μm^2 surfaces). This indicates that the surface roughness is improved during the growth of the GaN layer as compared to the surface of the AlN buffer layer alone.

An interesting feature revealed by the AFM images is the anisotropy of the surface corrugations, with an outstanding direction on the surface, perpendicularly

to the arrow, *i.e.* along <$\bar{1}\bar{1}$23>. This anisotropy in the growth rate along the two perpendicular directions is drastically reduced in comparison with the growth of nonpolar nitrides exposed in section 2.2.2. Theoretical calculations made by Lymperiakis *et. al.* predict a higher surface energetic potential to cross along <1$\bar{1}$00> than along <0001>, and even a higher one along <11$\bar{2}$0>. This implies longer diffusion lengths along both <11$\bar{2}$0> and <0001> than along <1$\bar{1}$00>. In our case, we have to consider the diffusion of adatoms along <1$\bar{1}$00> and <11$\bar{2}\bar{3}$>. Since <11$\bar{2}\bar{3}$> contains both <11$\bar{2}$0> and <0001>, we can expect that the diffusion would be higher along this direction than along <1$\bar{1}$00> [Lym09].

XRD measurements do not provide information on the polarity of the layers. Thus, I compared the surface of our samples and Ga-polar GaN(11$\bar{2}$2) samples grown by MOVPE after 5 min in a KOH saturated solution, which is a well-known selective etchant for N-polar GaN [Rou98]. The samples grown by MOVPE were previously confirmed to have Ga polarity by CBED measurements [Ven07]. The surface of both kinds of samples remains stable after KOH etching, which supports the Ga polarity for both samples. This assignment implies that GaN(11$\bar{2}$2) synthesized on *m*-sapphire presents metal polarity regardless the growth technique, either PAMBE (this work) or MOVPE [Bak06].

As a conclusion from this section, we have demonstrated the feasibility of (11$\bar{2}$2)-oriented two-dimensional GaN. An AlN(11$\bar{2}$2) buffer layer imposes the (11$\bar{2}$2) crystallographic orientation, when GaN is deposited under Ga-rich conditions.

4.1.2 Ga wetting on GaN(11$\bar{2}$2)

From the previous experiments, we assumed that the growth of two-dimensional GaN(11$\bar{2}$2) requires a certain Ga-excess during the growth. Thus, I have analyzed the Ga-wetting of the GaN(11$\bar{2}$2) surface as a function of the impinging Ga flux, in order to identify the different stability windows of the Ga excess.

The experiments were performed under static conditions (N flux OFF) on a 270-nm-thick GaN(11$\bar{2}$2) layer grown on a 180-nm-thick AlN(11$\bar{2}$2) buffer layer deposited on *m*-sapphire. The exposition of GaN to the Ga flux for a certain time, t_E, leads to the creation of a Ga film on the surface. In this experiment, t_E = 1 min. After closing the Ga cell shutter, at $t = 0$, we can analyze the transient oscillations of the RHEED specular intensity which are due to Ga desorption. The duration of the desorption transient is related to the thickness of the original Ga film. For this study, the desorption time, t_D, is conventionally defined as the time to the first inflexion point of the Ga desorption transient. This choice does not have any influence in the evaluation of the Ga coverage presented below, since the calculations do not use t_D itself but the difference $t_{D,i} - t_{D,j}$, where i and j refer to measurements for different Ga fluxes.

The variation of the RHEED specular intensity during the Ga desorption from

GaN(11$\bar{2}$2) as a function of the Ga cell temperature, *i.e.* Ga flux, is illustrated in Figs. 4.5 (a) and (b), for substrate temperatures T_{sub} = 718°C and T_{sub} = 740°C respectively. For a certain range of Ga flux, illustrated by the gray lines, we can delimit a stable regime where t_D remains independent of the impinging Ga flux. This means that the Ga coverage is constant in such a flux window. If the surface is exposed to higher Ga fluxes ($\phi_{Ga} \geq 0.097$ ML/s at T_{sub} = 718°C or $\phi_{Ga} \geq 0.230$ ML/s at T_{sub} = 740°C), the duration of the transient increases rapidly. This regime corresponds to the accumulation of Ga forming droplets on the surface, which results in a darker and dimmer RHEED pattern. When comparing Figs. 4.5 (a) and (b), we observe that at higher substrate temperatures, higher Ga fluxes are required to reach the stability regime. This is due to the thermal enhancement of the Ga desorption rate.

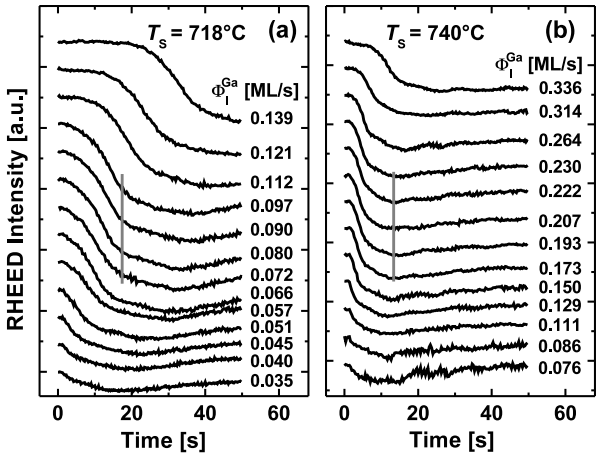

Figure 4.5: *Comparison of the Ga desorption transients for substrate temperatures of (a) 718°C and (b) 740°C. The gray vertical lines indicate a stable region where the transients remain identical for different impinging fluxes.*

From this desorption study, we can quantify the Ga coverage, c_{Ga}, on the GaN surface. The variation of c_{Ga} with time is the difference between the impinging Ga flux, Φ_I^{Ga}, and the Ga desorption flux, Φ_D^{Ga}:

$$\frac{\partial c_{Ga}(t)}{\partial t} = \Phi_I^{Ga} - \Phi_D^{Ga}(t) \tag{4.1}$$

The impinging Ga flux is determined by the temperature of the Ga cell, *i.e.* it is time independent. On the contrary, the Ga desorption flux depends on both the substrate temperature and the Ga coverage, *i.e.* it changes with time. In the case of a self-regulated Ga film ($c_{Ga} = constant$), the desorption flux is equal to the impinging flux during Ga exposition:

$$\Phi_D^{Ga}(t_E \geq t_{S-R}) = \Phi_I^{Ga} \tag{4.2}$$

where t_E is the exposure time and t_{S-R} the time necessary to reach the self-regulated regime. Thus, if the GaN surface is exposed to Ga flux for a time long enough for

the the self-regulated Ga film to be created, *i.e.* $t_E \geq t_{S-R}$, Eq. 4.1 becomes the following equation during Ga desorption:

$$dc_{Ga}(t) = -\Phi_D^{Ga}(t)dt \tag{4.3}$$

For a fixed substrate temperature, T_{sub}, a certain impinging Ga flux, $\Phi_{I,j}^{Ga}$, and after a certain Ga exposure time, $t \geq t_E$, the Ga coverage will reach a dynamically-stable value, c_j^{Ga}. If we assume that we were in a situation of dynamical equilibrium just before closing the Ga shutter, *i.e.* $\Phi_D^{Ga}(t=0) = \Phi_I^{Ga}$, and that the Ga desorption flux, $\Phi_{D,j}^{Ga}$ is only a function of the remaining Ga coverage, we can approximate Eq. 4.3 and deduce the Ga coverage:

$$c_j^{Ga} = c_{j-1}^{Ga} + \Phi_{I,j}^{Ga}(t_{D,j} - t_{D,j-1}) \tag{4.4}$$

where $t_{D,j}$ is the desorption time corresponding to the Ga impinging flux $\Phi_{I,j}^{Ga}$. Thus, for the total Ga coverage, it holds:

$$c_j^{Ga} = c_0^{Ga} + \sum_{k=1}^{j} \Phi_{I,k}^{Ga}(t_{D,k} - t_{D,k-1}) \tag{4.5}$$

where c_0^{Ga} is the Ga coverage corresponding to the lower flux. In general, we start the measurement with a sufficiently low Ga impinging flux so that we can assume $c_0^{Ga} = 0$.

Following this model, I estimated the Ga coverage of the GaN(11$\bar{2}$2) surface. Its evolution when varying the Ga-flux is compared to the situation on GaN(0001), as illustrated in Fig. 4.6 for a substrate temperature of $T_{sub} = 718°$C.

For GaN(11$\bar{2}$2), three different regions can be distinguished. Under low Ga flux ($\Phi_I^{Ga} \leq 0.066$ ML/s), the Ga coverage increases slowly with the Ga flux. Then, it stabilizes around 1.05±0.10 ML for a Ga flux between 0.066 and 0.097 ML/s. Finally, under higher Ga flux ($\Phi_I^{Ga} \geq 0.096$ ML/s), the Ga coverage increases quickly, which is an indication of Ga accumulation in droplets on the surface. An interesting feature of the data is the fact that the accumulation onset in the case of GaN(11$\bar{2}$2) is reached at lower Ga fluxes than in the case of GaN(0001).

In order to validate these results, we need to verify that the Ga exposition time was long enough to form a dynamically stable Ga layer on the GaN surface. Therefore, I analyzed the evolution of the desorption time, t_D, as a function of the Ga exposure time, t_E. Figure 4.7 illustrates this measurement for $\Phi_I^{Ga} = 0.096$ ML/s (just before accumulation) and $\Phi_I^{Ga} \geq 0.096$ ML/s (Ga accumulation). Under $\Phi_I^{Ga} = 0.096$ ML/s, t_D remains constant when increasing the Ga exposure time, *i.e.* longer Ga exposure of the surface has no effect on the amount of Ga deposited. We can therefore conclude that a dynamically-stable Ga film is formed on GaN(11$\bar{2}$2), which is in agreement with our assumption. On the contrary, for higher Ga flux, t_D increases quickly with the Ga exposure time, which is a signature of Ga accumulation

on the surface. In that case, the values of Ga coverage are only an estimation corresponding to $t_E = 1$ min. Indeed, the Ga coverage for $\Phi_I^{Ga} \geq 0.096$ ML/s is a function of the Ga exposition time, *i.e.* Eq. 4.2 is no longer valid.

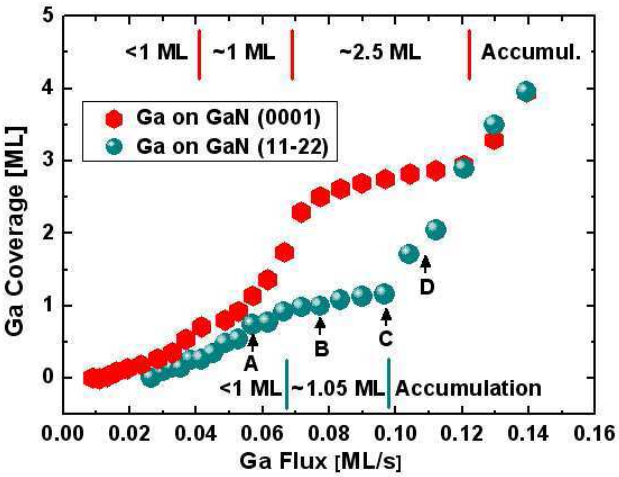

Figure 4.6: *Ga coverage of the GaN(11$\bar{2}$2) surface compared to that of the GaN(0001) surface. In the case of GaN(0001), we differentiate four regimes, corresponding to a coverage of $\leq$ 1 ML, $\approx$ 1 ML, $\approx$ 2.5 ML and Ga accumulation. In contrast, for GaN(11$\bar{2}$2), three regimes are identified, corresponding to a coverage of $\leq$ 1 ML, $\approx$ 1.05 ML and Ga accumulation.*

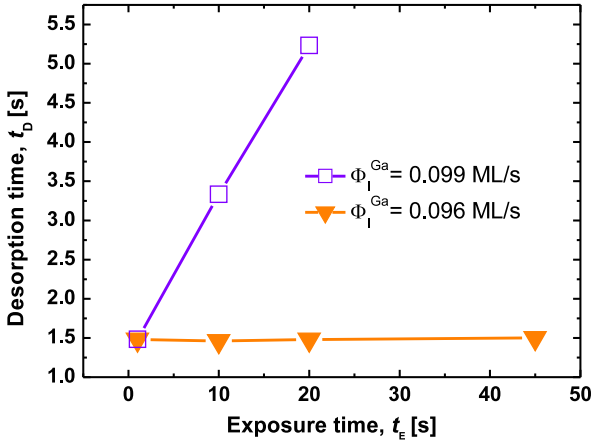

Figure 4.7: *Evolution of the desorption time, t_D, with the exposure time, t_E. Under Ga accumulation ($\Phi_I^{Ga} \geq 0.099$ ML/s), t_D increases rapidly with t_E. Before accumulation and with one Ga monolayer of excess on the surface ($\Phi_I^{Ga} = 0.096$ ML/s), the desorption time is independent of the exposure time.*

From these experiments we conclude that the maximum Ga coverage that we can stabilize on the GaN(11$\bar{2}$2) surface is about 1.05±0.10 ML.

To determine the thermal evolution of the different GaN(11$\bar{2}$2) growth windows, a study of Ga desorption under growth conditions (N flux ON) as a function

of the substrate temperature was performed. In this experiment, I deposited GaN under Ga-rich conditions for 1 min and analyzed the Ga desorption time when stopping the growth. The evolution of the Ga coverage as a function of the impinging Ga flux follows a similar diagram to that in Fig. 4.6, but shifted in Ga flux by 0.28 ML/s: in this case $\Phi_D^{Ga} = \Phi_I^{Ga} + v$, where $v = 0.28$ ML/s is the growth rate. For each measurement, I identified the Ga fluxes corresponding to the starting point of the formation of the Ga monolayer on the surface (point A in Fig. 4.6) and to the Ga accumulation (point C in Fig. 4.6).

Figure 4.8 shows the evolution of these two thresholds as a function of the impinging Ga flux and the substrate temperature. The solid lines are exponential fits to the data, assuming an activation energy $E_A = 2.8$ eV. This activation energy corresponds to the sublimation energy of Ga atoms from liquid Ga [Kit86] which was reported to control the onset of Ga droplet formation on GaN(0001) [Hey00a] and GaN(000$\bar{1}$) [Mon04b].

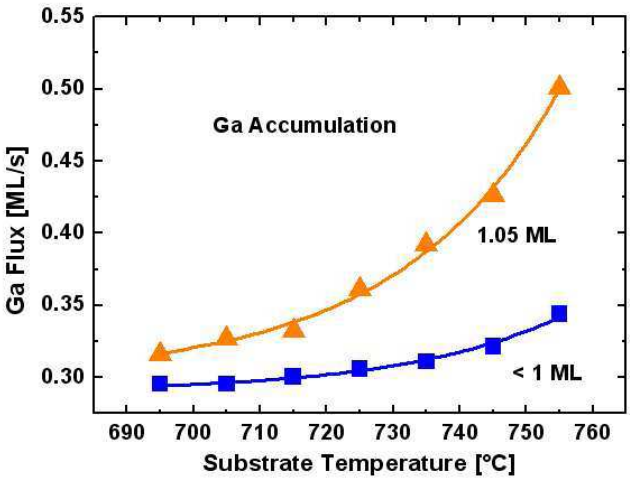

Figure 4.8: *Growth domains of stabilization of 1.05 $ML_{(0001)}$ of Ga, on the GaN(11$\bar{2}$2) surface as a function of both substrate temperature and Ga flux.*

These results can be compared with the desorption studies performed on other crystallographic orientations. In the case of GaN(0001), we have seen in the experimental part that we can distinguished four Ga excess regimes, corresponding to: ≤ 1 ML, $\approx$1 ML, a Ga bilayer and Ga accumulation on the surface. In that case, 2D layers with the best properties are achieved under the self-regulated regime of the Ga bilayer, right before accumulation. For m-plane GaN, it is possible to form a self-regulated Ga adlayer of 2$\pm$0.3 ML on the surface [Ams08]. By comparing with GaN(0001), this regime is shifted towards higher Ga flux, which means that it requires higher Ga rich conditions. On the contrary, when studying the Ga coverage on a-plane GaN, Founta *et al.* have shown that the maximal equilibrium coverage which can be attained is less than 1 ML [Fou07]. They also have demonstrated that there is no self-regulated regime for this orientation. All together, these studies

confirm the importance of the crystalline orientation on the surface equilibrium during Ga adsorption.

It is important to note that, in all these experiments, the Ga coverage is given in units of "monolayers" referring to one monolayer of Ga atoms arranged on (0001)-oriented wurtzite structure, i.e. 1.13×10^{15} atoms/cm^2, since the Ga flux in ML/s was calculated from the growth rate of GaN(0001). As the surface atomic density depends on the crystalline orientation, we need to analyze the Ga atomic distribution on a (11$\bar{2}$2)-oriented surface. Figure 4.9 describes one (11$\bar{2}$2)-oriented monolayer in plane view (a) and viewed along the [1$\bar{1}$00] axis. In this figure, the surface termination has been chosen so as to minimize the number of dangling bonds. The Ga surface atomic density is 1.19×10^{15} atoms/cm^2 in relaxed GaN(11$\bar{2}$2). Thus, a coverage of 1.05 (0001)-oriented monolayers corresponds roughly to one (11$\bar{2}$2)-oriented monolayer. However, we noticed that the atoms are distributed in two levels along the growth axis, forming a pseudo-bilayer.

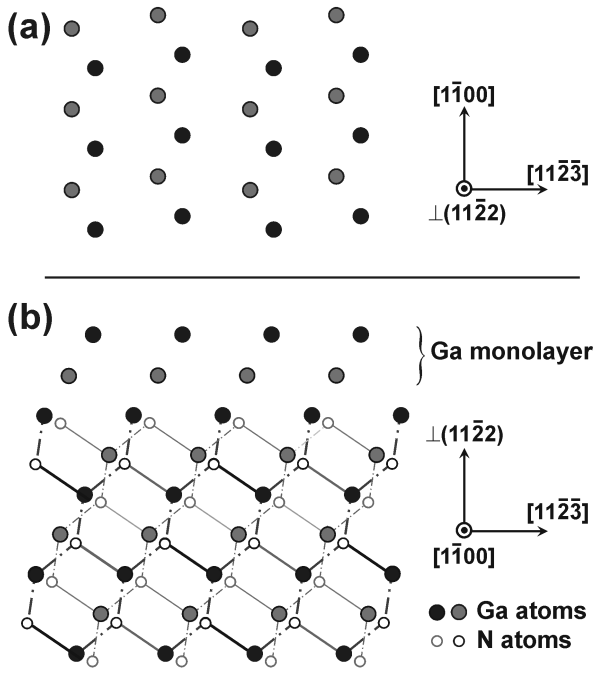

Figure 4.9: *Atomic description of the GaN(11$\bar{2}$2) growing surface, illustrating the Ga excess monolayer. (a) Plane view of the Ga excess monolayer, and (b) atomic distribution of GaN(11$\bar{2}$2) projected along the [1$\bar{1}$00] axis.*

4.1.3 Identification of the growth window

To analyze the effect of the different Ga excess regimes on the GaN layers, I synthesized four GaN samples on top of a ≈140 nm-thick AlN(11$\bar{2}$2) buffer layer under growth conditions indicated in Fig. 4.6 by the points A (less than 1 ML$_{(11\bar{2}2)}$), B (≈1 ML$_{(11\bar{2}2)}$), C (1 ML$_{(11\bar{2}2)}$ at the Ga accumulation limit), and D (in the Ga

accumulation regime). The sample properties are listed in Table 4.2.

Samples	Ga excess	Thickness	RHEED	$\frac{V^{(10\bar{1}3)}}{V^{(11\bar{2}2)}}$
E1246	$\leq$ 1 ML$_{(11\bar{2}2)}$	670 nm	one	0.007
E1240	$\approx$ 1 ML$_{(11\bar{2}2)}$	670 nm		-
E1229	accumulation limit	670 nm	streaky pattern	-
E1260	accumulation	540 nm		0.007

Table 4.2: *Series of GaN samples grown with III/V ratio varying from N-rich to Ga-rich conditions.*

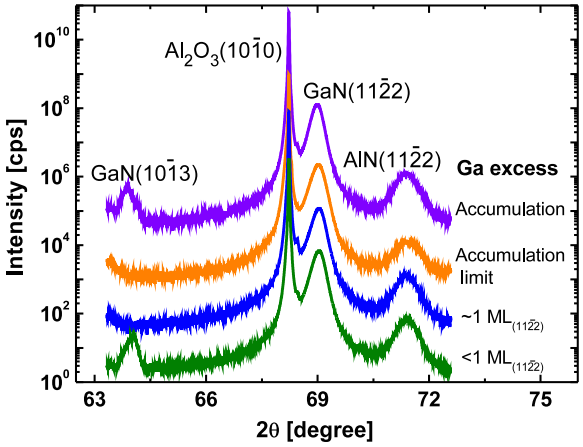

Figure 4.10: *XRD symmetric $2\theta - \omega$ scans performed on samples consisting of a $\approx$ 600 nm-thick GaN layer grown on a 140 nm-thick AlN(11$\bar{2}$2) buffer layer with different Ga excess. Under a Ga excess $\leq$ 1 ML$_{(11\bar{2}2)}$ and under Ga accumulation, the layers contain both the (10$\bar{1}$3) and (11$\bar{2}$2) orientations. Under a Ga excess of $\approx$ 1 ML$_{(11\bar{2}2)}$, only the reflection assigned to the (11$\bar{2}$2)-orientation is detected.*

Figure 4.10 presents the symmetric XRD $2\theta - \omega$ scans recorded for the four samples. As mentioned in the previous chapter (Fig. 3.2), the main peak corresponds to $Al_2O_3(3\bar{3}00)$ and the reflection at $2\theta = 71.40°$ to AlN(11$\bar{2}$2) [Lah07, Bak06]. The reflection around $2\theta = 69.10°$ is attributed to GaN(11$\bar{2}$2) and the additional reflection at $2\theta = 63.43°$ reveals the presence of GaN(10$\bar{1}$3) domains in samples E1246 (grown under a Ga excess of less than one monolayer) and E1260 (grown under Ga accumulation). The percentage of GaN(10$\bar{1}$3) compared to GaN(11$\bar{2}$2) is given in Table 4.2. I calculated $\frac{V^{(10\bar{1}3)}}{V^{(11\bar{2}2)}} \approx 0.53$ for GaN grown directly on *m*-sapphire (sample E1035). In contrast, the $\frac{V^{(10\bar{1}3)}}{V^{(11\bar{2}2)}}$ ratio is much lower for samples E1246 and E1260, which explains the observation of only one crystalline orientation in the RHEED patterns.

From this experiment, we can conclude that when GaN is synthesized with a Ga excess of $\approx$ 1 ML$_{(11\bar{2}2)}$, only the (11$\bar{2}$2)-orientation remains, within the detection limits.

In order to determine the best growth conditions required to achieve two-dimensional GaN(11$\bar{2}$2) layers, I studied the structural properties of the four GaN layers described in Table 4.2. The ω scan of the (11$\bar{2}$2) orientation gives an idea on the crystalline quality of the layers. The values of the full width at half maximum (FWHM) for ω scans around $<10\bar{1}0>_{GaN}$ and $<11\bar{2}3>_{GaN}$ are given in Table 4.3. For samples E1246, E1240 and E1229, the FWHM values around $<1\bar{1}00>_{GaN}$ are in the same range ($\approx 0.5°$) as previously reported results [Ni07, Bak06]. However, the FHWM around $<11\bar{2}3>_{GaN}$ was found to be 0.89° for all samples, which is slightly broader than for the layers grown by HVPE. Sample E1260 (GaN grown under Ga accumulation) presents a poorer crystalline quality compared to the three other layers. Its growth was stopped before reaching the same thickness that the other samples because the growth was no longer controllable: after a certain time, the Ga accumulation leads to a dark RHEED pattern.

Samples	Ga excess	ω scan FWHM	
		$< 10\bar{1}0 >_{GaN}$	$< 11\bar{2}3 >_{GaN}$
E1246	$\leq$ 1 ML$_{(11\bar{2}2)}$	0.46°	0.86°
E1240	$\approx$ 1 ML$_{(11\bar{2}2)}$	0.45°	0.93°
E1229	accumulation limit	0.54°	0.90°
E1260	accumulation	0.80°	0.89°

Table 4.3: *FWHM of the ω scan of the GaN(11$\bar{2}$2) reflection in thick GaN layers grown with different Ga excess.*

The larger FWHM along $<11\bar{2}3>$ is consistent with the larger FWHM along $<11\bar{2}3>$ observed in AlN layers (see in Table 3.5). It can be explained by the presence of a systematic tilt around $<1\bar{1}00>$, as well as in AlN layers. However, an interesting feature of GaN is the fact that the tilt is in the opposite direction compared to AlN layers. This trend is illustrated in Fig. 4.11, for samples E1605 (described in Table 4.4), E1246 and E1036. Some examples of the measured tilt values are given in Table 4.4. No particular trend of the tilt values as a function of the thickness of the AlN or the GaN layers can be extracted from the analyzed samples.

The lattice parameters of the layers have been determined experimentally using reciprocal space maps around the (20$\bar{2}$2) and (11$\bar{2}$4) asymmetric reflections of GaN, together with the $2\theta - \omega$ scans of the GaN(11$\bar{2}$2) reflection. The results are reported in Table 4.5. If we compare the results for samples E1240, E1229 and E1260 to the lattice parameters of relaxed GaN, $a_0 = 3.189$ $\mathring{A}$ and $c_0 = 5.185$ $\mathring{A}$ in Table 1.2, we can conclude that these layers are fully relaxed within the error bars of the measurements. However, the sample grown under a Ga excess of less than

one monolayer, sample E1246, shows a compressive strain along the c-axis ($c \leq c_0$). In that case, I have chosen to describe the (0001)-plane deformation with the two different a and b lattice parameters relatively to $[2\bar{1}\bar{1}0]_{GaN}$ and $[\bar{1}2\bar{1}0]_{GaN}$ directions respectively (Fig. 2.29). The deformation of the hexagonal basal planes is consistent with the expected trend in the case of compressive strain along the c-axis: $a \leq a_0$, $b \geq a_0$.

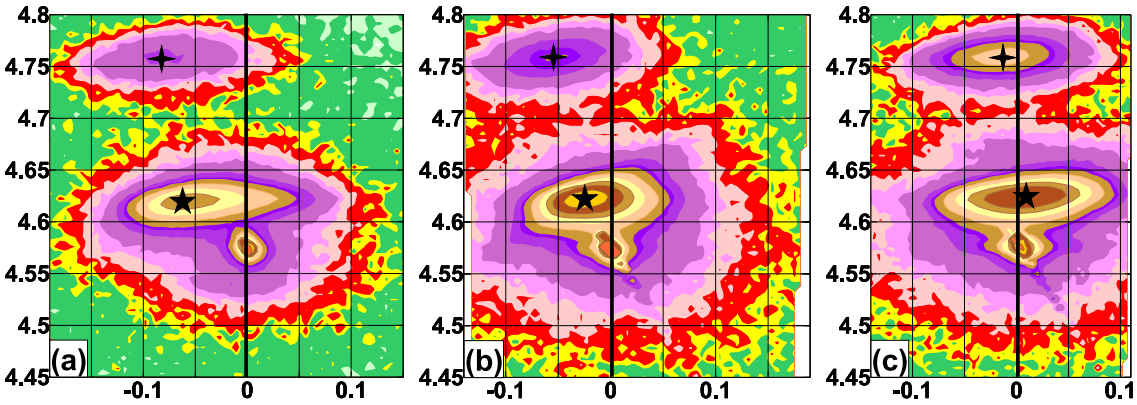

Figure 4.11: *XRD symmetric reciprocal space maps of samples (a) E1605, (b) E1246 and (c) E1036. In each map, the cross and the star represent the centers of AlN and GaN reflections respectively.*

Samples	GaN thickness	AlN thickness	GaN tilt ± 0.01°	AlN tilt ± 0.01°
E1036	360 nm	490 nm	-0.05°	0.22°
E1246	670 nm	140 nm	0.31°	0.68°
E1593	90 nm	260 nm	0.78°	1.05°
E1599	130 nm	130 nm	0.25°	0.60°
E1605	260 nm	130 nm	0.73°	1.02°

Table 4.4: *Values of the tilt angle around <1$\bar{1}$00> for GaN and AlN layers. The values are relative to the substrate.*

Samples	Ga excess	Lattice parameters		RMS roughness
		$a \pm 0.077\mathring{A}$	$c \pm 0.077\mathring{A}$	
E1246	$\leq$ 1 ML$_{(11\bar{2}2)}$	$a = 3.113$ $b = 3.203$	5.135	6.46 nm
E1240	$\approx$ 1 ML$_{(11\bar{2}2)}$	3.185	5.203	6.29 nm
E1229	accumulation limit	3.188	5.208	1.34 nm
E1260	accumulation	3.190	5.205	2.23 nm

Table 4.5: *Structural characteristics of GaN thick layers grown under Ga excess.*

Finally, the surface morphology of the layers was studied by atomic force microscopy (AFM). As an illustration, Figs. 4.12(a) and (b) compare the surfaces of

samples E1246 (Ga excess $\leq$ 1 ML$_{(11\bar{2}2)}$) and E1229 (Ga accumulation limit). Sample E1229 presents an in-plane anisotropy, with domains elongated perpendicularly to the <11$\bar{2}\bar{3}$> direction, which is characteristic of GaN samples grown under the appropriate growth conditions. This is the same anisotropy as the one observed in the AFM images of GaN layers in Fig. 4.4. On the contrary, sample E1246 shows a surface so rough that this anisotropy is not present. The RMS roughness measured from 3×3 μm^2 surfaces are summarized in Table 4.5. The surface roughness decreases markedly when increasing the Ga excess, particularly when approaching the accumulation limit. The optimized sample shows a much flatter surface, the RMS values being slightly better than previous reports on GaN(11$\bar{2}$2) layers grown by HVPE [Bak06, Rom06]. Indeed, they are as low as those measured on GaN(11$\bar{2}$2) substrates cut from *c*-plane GaN grown by HVPE [Fun06] or on homoepitaxial GaN(11$\bar{2}$2) layers grown by low-pressure MOVPE [Ued06].

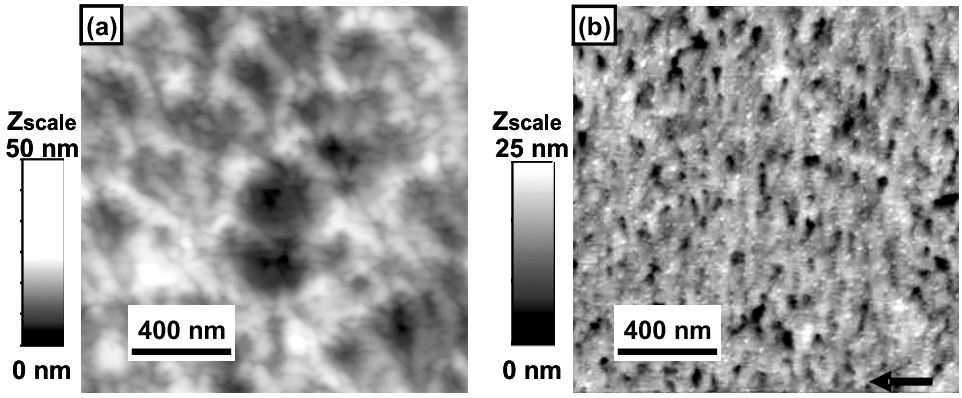

Figure 4.12: *Surface of GaN layers grown under (a) Ga excess $\leq$ 1 ML$_{(11\bar{2}2)}$ (E1246) and (b) Ga excess $\approx$ 1 ML$_{(11\bar{2}2)}$ right before accumulation (E1229). The black arrow in the image on the right indicates the <1$\bar{1}$00>$_{AlN}$ direction*

In conclusion from this section, we can distinguish the following four regimes for the growth of GaN on AlN(11$\bar{2}$2):

- **For III/V $\leq$ 1** (N-rich and stoichiometric conditions), GaN layers show spotty RHEED pattern, characteristic of three-dimensional growth.
- **For Ga excess $\leq$ 1 ML**$_{(11\bar{2}2)}$, GaN layers present small amount of GaN(10$\bar{1}$3) domains embedded in a GaN(11$\bar{2}$2) matrix.
- **For Ga excess $\approx$ 1 ML**$_{(11\bar{2}2)}$, (11$\bar{2}$2)-orientation is isolated and a dynamically-stable Ga film is formed on top of the surface during the growth. Optimum surface morphology is attained.
- **For Ga excess $\geq$ 1 ML**$_{(11\bar{2}2)}$, the Ga accumulation regime is reached (formation of Ga droplets at the surface during the growth). GaN(10$\bar{1}$3) domains are present and the surface morphology degrades.

These results differ from the work of Iwata *et al.*, who reported that the PAMBE growth of GaN on m-sapphire resulted in a competition between (0001)- and (1$\bar{1}$00)-oriented domains [Iwa97]. However, in that work the authors used a low-temperature (400°C) GaN buffer layer, which should be highly polycrystalline and probably favor the (0001) orientation in the subsequent layer. More recent reports on GaN epitaxy on *m*-sapphire by MOVPE or HVPE techniques show a competition between {10$\bar{1}$3} and (11$\bar{2}$2) domains whose ratio depends on the nitridation process and the growth conditions [Bak06, Wer08].

4.2 Optical properties of GaN(11$\bar{2}$2) thick layers

The optical properties of the samples described in Table 4.2 have been investigated using time-integrated photoluminescence (PL) and time-resolved photoluminescence (TRPL).

Figure 4.13 compares room temperature photoluminescence (PL) spectra of samples E1246 (Ga excess $\leq$ 1 ML$_{(11\bar{2}2)}$), E1240 ($\approx$ 1 ML$_{(11\bar{2}2)}$), and E1229 (Ga accumulation limit). The three spectra are dominated by the band-edge emission at 3.39 eV. An important feature of these spectra is the absence of the yellow-band which peaks typically around 2.2-2.3 eV in GaN(0001) grown on *c*-sapphire [Res05]. Thus, by varying the Ga excess, we note no significant difference on the band-edge luminescence peak position or line width ($\approx$ 95 meV). Regarding the sample grown on the Ga accumulation regime (E1260), the room temperature PL was below the detection limit of our setup. This can be explained by the presence of a high density of nonradiative recombination centers, which is a sign of poor crystal quality.

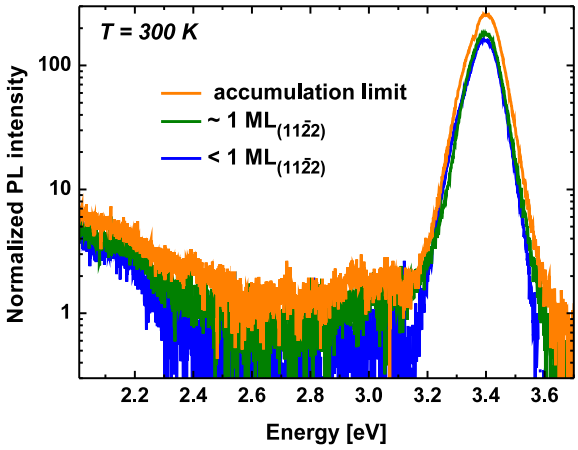

Figure 4.13: *Room-temperature PL spectra obtained from GaN layers grown under Ga excess $\leq$ 1 ML$_{(11\bar{2}2)}$ (E1246), $\approx$ 1 ML$_{(11\bar{2}2)}$ (E1240) and $\approx$ 1 ML$_{(11\bar{2}2)}$ right before accumulation (E1229).*

To get more insight into the optical properties of the GaN(11$\bar{2}$2) layers, I will

detail the study of the sample with the best morphological properties (E1229). The thermal evolution of the near-band-edge PL emission measured with an excitation power of 1 mW (corresponding to about 40 W/cm^2) is illustrated in Fig. 4.14. The low-temperature ($T = 7$ K) PL spectrum is dominated by a line at 3.42 eV, labeled D_1. At higher energy, we observe a shoulder around 3.473eV, attributed to excitons bound to neutral donors, D^0X. At lower energy we observe two broad bands around 3.35 eV and 3.30 eV, labeled D_2 and D_3, respectively. At room temperature, we can estimate the energy location of the free exciton, FX_A, thanks to the Varshni parameters from Romanov *et al.* [Rom06]. The FX_A transition should be located as indicated in the figure, *i.e.* around 3.43 eV. Hence, we can draw the conclusion that in this sample, room temperature PL is dominated by the D_1 line and not by the free exciton.

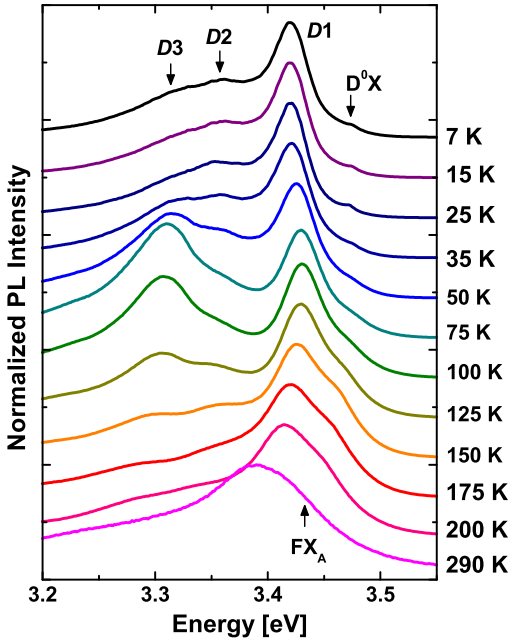

Figure 4.14: *Thermal evolution of the luminescence from sample E1229. The spectra are normalized to the maximum of the emission and vertically shifted for clarity.*

The thermal evolution of the PL intensity from the different emission lines is plotted in Fig. 4.15. The D^0X is the transition involving the A-band exciton localized on a shallow neutral donor level [Cht99]. Its energy confirms that the layer is fully relaxed [Vur03], which is consistent with the above-described X-ray analysis. Its thermal evolution first presents a small blue shift at low temperature as a result of thermal untrapping towards the free exciton band. Then, the emission follows a redshift due to temperature-induced band gap shrinkage. The thermal quenching of the D^0X intensity is fitted by Eq. 4.6. In this equation, *I(T)* is the PL intensity, C is a fitting constant, E_A is an activation energy, and k is the Boltzmann constant.

The fit depicted in Fig. 4.16 indicates an activation energy $E_A = 10 \pm 2$ meV, which is consistent with the interpretation of this line as a donor bound exciton [Cht99].

$$I(T) = \frac{I(T = 0K)}{1 + Cexp\left(\frac{-E_A}{kT}\right)} \tag{4.6}$$

It should be stressed that in these measurements we are not able to resolve D^0X and FX_A lines, and thus the extracted activation energy reflects both the thermalization of D^0X towards FX_A and the effect of nonradiative recombination for FX_A.

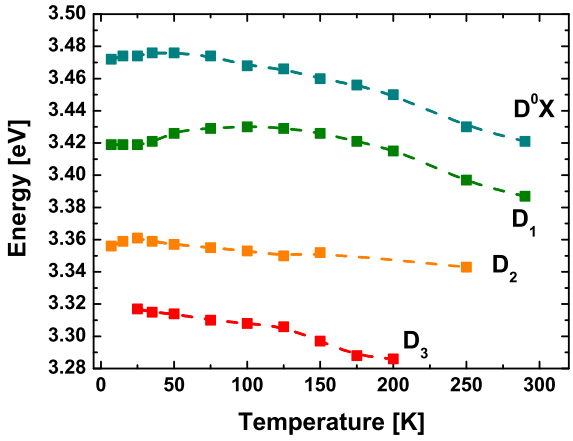

Figure 4.15: *Thermal evolution of the energy of the different emission lines, D^0X, D_1, D_2 and D_3, from sample E1229. The lines are guides for the eyes.*

Regarding the D_1 emission, its energy position displays a clear S-shaped behavior (blue-shift followed by red-shift) with increasing temperature. Its thermal extinction can be fitted by considering two activation energies, as in Eq. 4.7.

$$I(T) = \frac{I(T = 0K)}{[1 + C_2exp\left(\frac{-E_{A1}}{kT}\right)][1 + C_1exp\left(\frac{-E_{A2}}{kT}\right)]} \tag{4.7}$$

As depicted in Fig. 4.16, best fit is obtained for $E_{A1} = 16 \pm 6$ meV and $E_{A2} \geq 90$ meV. The luminescence lines around 3.42 eV have been frequently observed in GaN(0001) [Ni07, Rom06, Liu05, Res05]. In some particular cases, it has been reported as the dominant PL line from GaN(11$\bar{2}$0) nonpolar films [Ler99]. Regardless the crystalline orientation, these lines present similar behavior than the D_1 emission: two activation energies in the temperature quenching, one of them rather small (between 12 meV and 40 meV). The small activation energy can be accounted by assuming that the peak arises from recombination of excitons bound to some structural defects. A model has been proposed for this transition, assigning it to recombination of an exciton bound to an I_1-type basal stacking fault (BSF) [Ler99, Res05, Liu05]. It could be consistent given the density of SFs encountered in these layers [Fig. 4.3(d)].

Hence, we can conclude that the initial blue-shift and small activation energy observed are related to the exciton thermal delocalization. The subsequent red-shift when increasing the temperature follows the GaN band gap evolution.

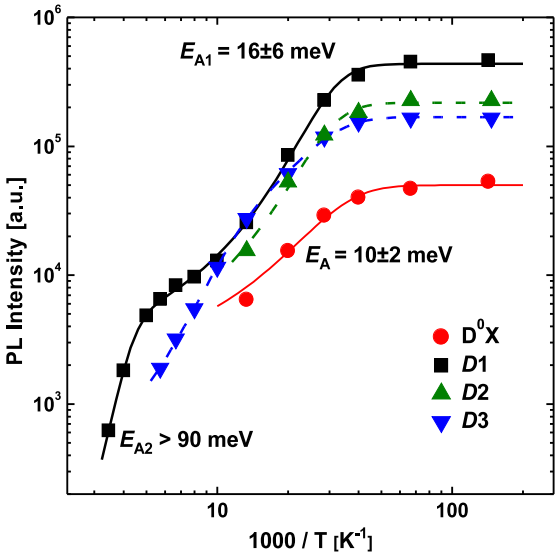

Figure 4.16: *Thermal quenching of the D^0X, D_1, D_2, and D_3 lines. Solid lines correspond to fits to the PL thermal quenching equations (Eqs. 4.6 for D^0X and 4.7 for D_1), whereas dashed lines are guidelines.*

Finally, the emission bands at 3.35 eV and 3.30 eV (D_2 and D_3, respectively) present a rapid thermal quenching, similar to the D_1 line. These lines have also been reported in the PL from GaN(0001) [Ni07, Sal99] and GaN(11$\bar{2}$0) nonpolar films [Ler99, Liu05], and they have been assigned to transitions related to prismatic SFs on $\{11\bar{2}0\}$ planes only observed in $\{11\bar{2}2\}$-oriented regions [Mei06].

TRPL measurements, performed at low average power density (a few Wcm^{-2}), reveal significant differences between the D^0X, D_1, and the D_2 and D_3 lines. Spectra in Fig. 4.17(a) were obtained by exciting with a pulsed laser with a repetition rate of 76 MHz (13 ns period) and the signal was analyzed on a 2 ns window, giving a system response of about 10 ps. We measured the decay time (1/e decay) for both the D^0X and D_1 emissions in the range of 50-80 ps, as illustrated in the figure. However, the spectra show a larger decay time for the D_1 emission compared to the D^0X emission. This can explained by the high density of SFs in the layers, which induces carrier localization. D_2 and D_3 lines also present a relatively short first time decay of $\approx$ 140 ps. However, an important part of the luminescence decays over much longer time, not accessible with this setup. Hence, we studied this PL quenching with a laser pulsed at a repetition rate of 0.9 MHz (1.11 μs period) and analyzed using a 20 ns window. In this configuration, the system response is about 500 ps. As shown in Fig. 4.17, a decrease of the intensity by two orders of magnitude is only obtained after more than 10 ns for the D_2 and D_3 lines. The strongly non-exponential quenching of these PL lines is interpreted as the result of

a broad distribution of decay times. Indeed, the rapid 1/e decay suggests that the electrons and the holes are not spatially separated. Thus, from this short component of the decay time and the small activation energy extracted for both lines, we can conclude that they are not donor-acceptor pair transitions. We can further assume that D_2 and D_3 lines are related to electrons and holes bound to structural defects whose oscillator strength is related to the precise geometry of the defect.

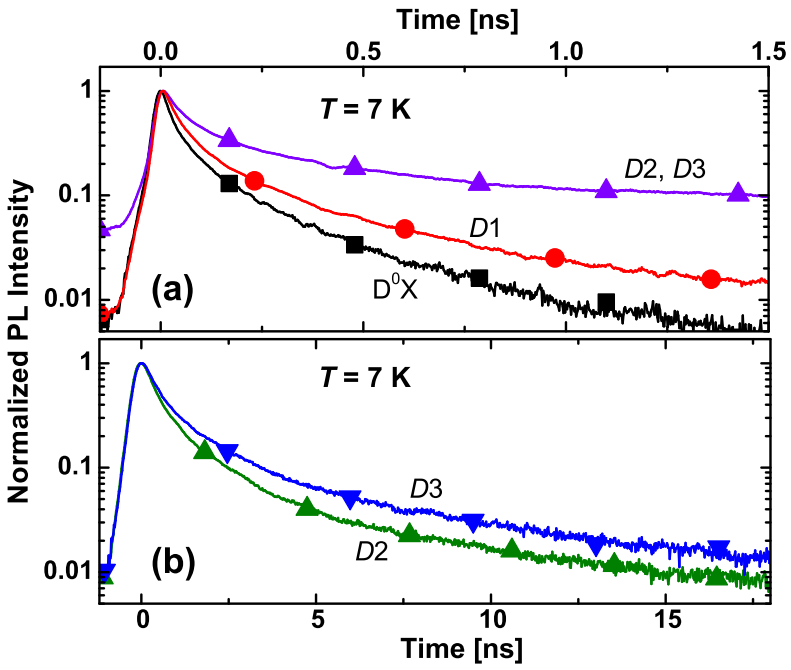

Figure 4.17: *Time-resolved PL measured at T = 7 K. (a) decay times measured with a pulsed laser at a repetition rate of 76 MHz (13 ns). D_2 and D_3 low energy peaks show the same behavior. (b) D_2 and D_3 decay time measured using a repetition rate of 0.9 MHz (1.1 µs) for the pulsed laser.*

These optical studies demonstrate that GaN(11$\bar{2}$2) layers show intense room-temperature bandedge luminescence with no evidence of the yellow band emission usually observed in polar GaN. The investigation of the thermal evolution of the emission lines shows that the room temperature luminescence is dominated by a line attributed to excitons bound to stacking faults (SF^0X).

4.3 Doping of GaN(11$\bar{2}$2)

In this section, I focus on the doping of GaN layers. I first compare the growth conditions of Si-doped and Mg-doped GaN, and continue with a deeper analysis of the dopant incorporation and the optical and electrical properties of Mg-doped layers.

4.3.1 Growth kinetics of doped GaN(11$\bar{2}$2)

In order to study of Si-doped and Mg-doped GaN growth kinetics we analyzed the Ga wetting of the GaN(11$\bar{2}$2) surface during the growth, comparing undoped, Si-doped and Mg-doped layers. Prior to the analysis, a 200-nm-thick AlN(11$\bar{2}$2) buffer layer was deposited on *m*-sapphire, followed by a non-intentionally-doped (n.i.d.) 100-nm-thick GaN(11$\bar{2}$2) layer grown with a Ga excess of 1 $ML_{(11\bar{2}2)}$. The Ga coverage was determined under dynamic conditions, *i.e.* by the analysis of the evolution of the specular RHEED intensity transient when stopping the growth after 1 min of exposure. The measurements were performed successively for n.i.d., Si-doped and Mg-doped GaN. In the case of doped GaN, a thin undoped GaN layer of approximately 3 nm was deposited in between the different Ga fluxes in order to have the same initial condition for each measurement. The substrate temperature was kept at 686°C for the whole experiment, the Si-cell temperature was 1150°C and the Mg-cell temperature was 350°C, both corresponding to a dopant atomic incorporation of about 10^{19} cm^{-3}.

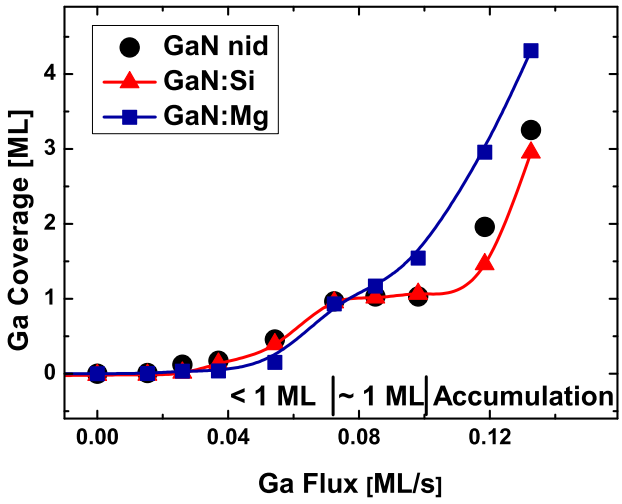

Figure 4.18: *Comparison of the Ga coverage depending on Ga impinging flux for undoped, Si-doped and Mg-doped GaN(11$\bar{2}$2) surfaces.*

Figure 4.18 presents the calculated Ga coverage on n.i.d., Si-doped and Mg-doped GaN(11$\bar{2}$2) surfaces depending on the Ga impinging flux. Eyeguides are given for the coverage on Si-doped and Mg-doped surfaces. In the case of n.i.d GaN, we observe the behavior previously described in section 4.6, with a self-regulated (11$\bar{2}$2)-oriented adlayer formed for $0.072 \leq \Phi_{Ga} \leq 0.101$ ML/s (circles). This stable regime is also observed for Si-doped GaN (triangles), and it occurs for nearly the same range of Ga fluxes, $0.072 \leq \Phi_{Ga} \leq 0.107$ ML/s. In contrast, the formation of the Ga adlayer is inhibited for Mg-doped GaN (squares), and Ga accumulation starts for weaker Ga impinging flux (0.07 ML/s). This can be compared to measurements

performed on GaN(0001) surfaces [Mon04a], showing that Si-doping does not affect the formation of the Ga bilayer, whereas no Ga bilayer can be observed in the case of Mg-doped GaN. However, the Ga accumulation threshold is reached for the same impinging flux in this latter case.

The stability of the doped surfaces has been studied by growing thick layers and analyzing the Ga desorption after certain deposition times, typically 30 min, 1 h and 3 h. In the case of Si-doped GaN(11$\bar{2}$2), I found that the surface remains stable for Ga fluxes below the Ga accumulation threshold ($\Phi \approx 0.101$ ML/s in the former example). In the case of Mg-doped layers, the same Ga impinging flux leads to darker RHEED images whose pattern can barely be distinguished, which is an evidence of Ga accumulation. The stable regime is reached when the Ga impinging flux corresponds to a coverage of 1 $ML_{(11\bar{2}2)}$ on the surface ($\Phi \approx 0.072$ ML/s in the former example).

In the case of Mg-doped GaN(11$\bar{2}$2), the inhibition of Ga adlayer can be due to the perturbation of the surface energy balance by the presence of Mg adatoms, which is not significant when Si atoms are incorporated. To my knowledge, no theoretical calculation has been performed on this orientation yet. However, this result is similar to observations [Mon04b] and theoretical calculations [Ram99, Ros02, Pta01] on Mg-doped GaN(0001).

Applying the optimum growth conditions, we have synthesized $\approx$ 800-nm-thick Si-doped layers containing [Si] $\approx 6.01\times10^{19}$ cm^{-3}. Figure 4.19(a) is a typical AFM image from one of theses Si-doped samples. The surface is rather flat (RMS $\approx$ 2.9 nm), similar to the typical GaN surfaces, observed previously in Fig. 4.12, which present an asymmetry along <11$\bar{2}\bar{3}$>.

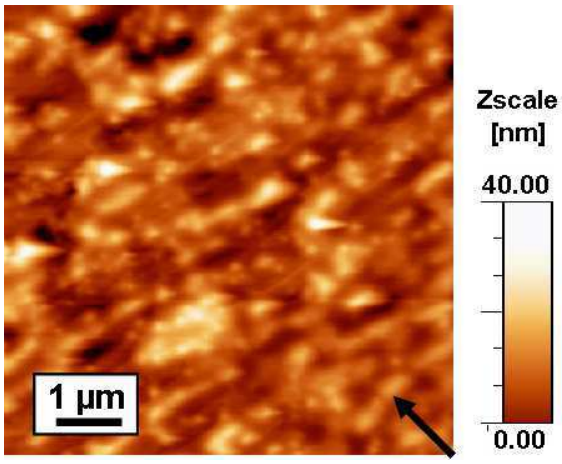

Figure 4.19: *AFM image of a Si-doped GaN(11$\bar{2}$2) layer. The arrow indicates the [11$\bar{2}$0]$_s$apphire direction.*

The properties of Mg-doped GaN layers, which have been deeply investigated, are presented in the following sections.

4.3.2 Mg incorporation in GaN(11$\bar{2}$2)

In order to study the Mg incorporation in GaN(11$\bar{2}$2), 800-nm-thick Mg-doped GaN layers were grown on top of a 260-nm-thick AlN buffer layer, with 1 $ML_{(11\bar{2}2)}$ of Ga in excess. Table 4.6 details the Mg-cell and substrate temperatures used for each sample. The amount of Mg atoms incorporated in the layer has been determined by Secondary Ion Mass Spectroscopy (SIMS), using an O^{2+} primary ion beam. The depth profile depicted in Fig. 4.20 demonstrates that the Mg atoms are uniformly incorporated throughout the whole layer (E1699).

Samples	T_{sub}	T_{Mg}	[Mg] [cm^{-3}]
E1697	697°C	350°C	6.0×10^{19}
E1698	697°C	300°C	2.5×10^{19}
E1699	697°C	325°C	3.5×10^{19}
E1700	677°C	350°C	6.5×10^{19}
E1701	657°C	350°C	8.5×10^{19}
E1702	697°C	275°C	1.4×10^{19}

Table 4.6: *Series of Mg-doped layers obtained by varying both the substrate temperature and the Mg flux.*

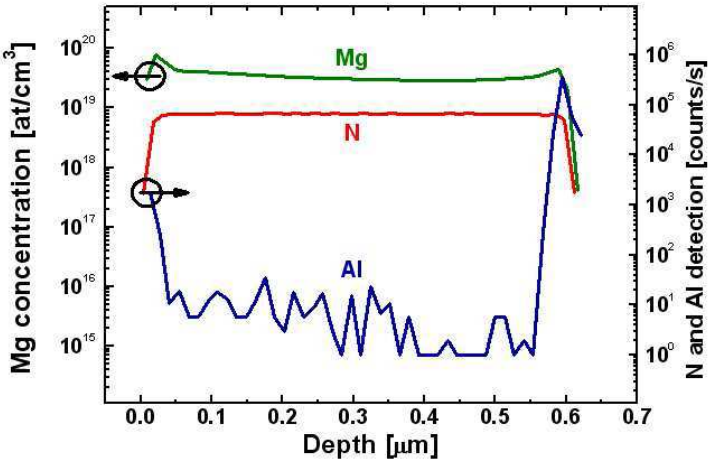

Figure 4.20: *Typical SIMS profile of a Mg-doped sample attesting the uniform incorporation of Mg atoms in the GaN layer.*

As illustrated in Fig. 4.21, the amount of Mg atoms in the layer increases exponentially with the Mg-cell temperature and decreases exponentially with the substrate temperature. No saturation effect up to has been observed up to [Mg] = 8.5×10^{19} cm^{-3}. From the variation of the Mg incorporation with the Mg impinging

flux, we can access the activation energy which should correspond to Mg sublimation. I calculate $E_a = 0.55$ eV, which is consistent with previous work on Mg-doped GaN(0001) by Haus *et. al.* ($E_a = 0.47$ eV) [Hau02], but rather far from the results of Monroy *et. al.* ($E_a = 1.25$ eV) [Mon04a] and the actual value of Mg sublimation energy (≈ 1.53 eV). This lower energy implies that, given a certain substrate temperature, the incorporation of Mg increases superlinearly with the Mg flux. To explain that, we can assume that the segregation of Mg is strongly attenuated for increasing Mg fluxes. Furthermore, the dependence of Mg incorporation on the substrate temperature gives an estimation of the energetic barrier to Mg incorporation. For this semipolar series, I found $E_{inc} = 0.69$ eV, which is much lower than the energies calculated for GaN(0001), 3.05 eV [Hau02] or 2.57 eV [Mon04a]. This small activation energy indicates that the incorporation of Mg is enhanced in the case of GaN(11$\bar{2}$2) compared to GaN(0001).

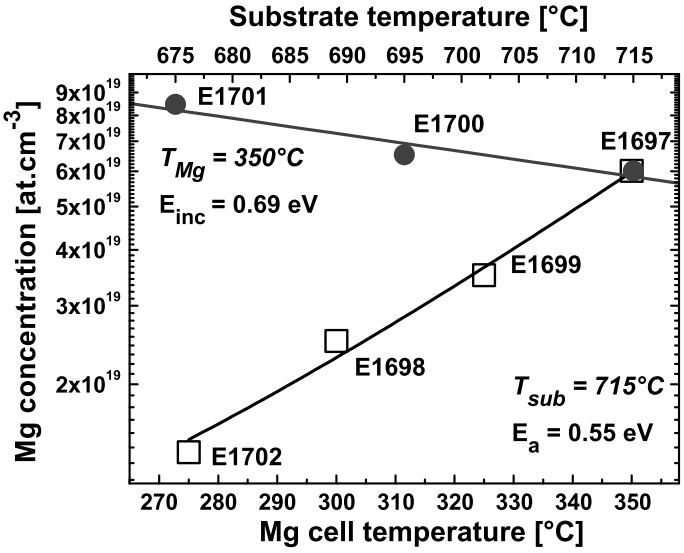

Figure 4.21: *Mg concentration versus both the Mg cell temperature and the substrate temperature. The activation energies are determined from Arrhenius plots of the Mg incorporation as a function of the corresponding 1/T values.*

Mg-doped samples were studied by TEM in order to identify the possible effects of Mg on the GaN matrix. The image in Fig. 4.22(a) has been recorded on sample E1697, which consists of 800 nm of GaN:Mg deposited on 260 nm of AlN with $T_{Mg} = 350$°C. We observed the common vertical defects found in GaN(11$\bar{2}$2) layers but no additional features. Figure 4.22(b) is a HRTEM image recorded on sample E1698. In these two images, we do not see the signature of specific defects usually due to Mg doping, such as polarity inversion [Pez04, Gra03] or cubic domains [Mon04b].

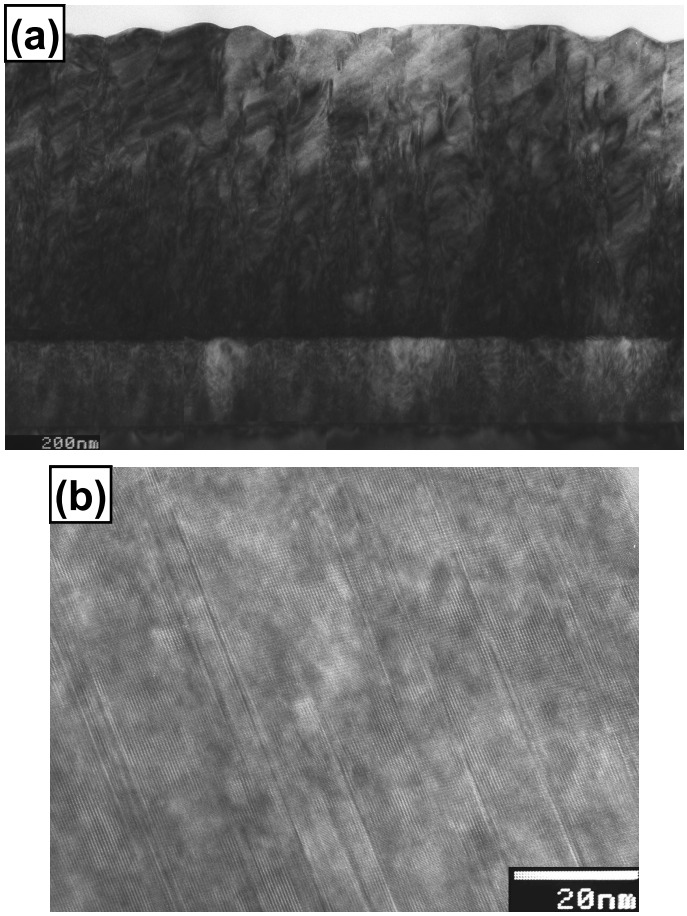

Figure 4.22: *(a) TEM image recorded along <10$\bar{1}$0>$_{GaN}$ azimuth and (b) HRTEM taken along <11$\bar{2}$0>$_{GaN}$ showing no evidence of particular defect related to the presence of Mg atoms.*

Table 4.7 presents a second series of Mg-doped samples, very interesting for their surface morphologies and electrical properties exposed in section 4.3.4. An important feature of the series is the high values of Mg concentration achieved under low temperature, and especially the lower value measured for E1876 than for E1875. This can be an indication of the saturation of the surface with Mg atoms at a certain low temperature, resulting in a barrier to Mg diffusion in the layer. The surface morphology of these samples is presented in Fig. 4.23. Images (a) to (d) correspond to samples with decreasing Mg concentration. We can distinguish three different surface morphologies. Sample E1876, grown at the lowest temperature, presents an isotropic surface with RMS roughness of 8.7 nm, and an average grain diameter of $\approx$ 250 nm. The poor quality of the surface can be attributed to the reduced adatom mobility due to the low substrate temperature. The surface of sample E1875 presents a clear anisotropy, with features extended along the <11$\bar{2}\bar{3}$> direction, with an average length of $\approx$ 500 to 600 nm. The measured RMS roughness is about 7.7 nm on this image. I contrast, the surfaces of samples E1874 and E1873, grown at higher temperature, show grooves along <10$\bar{1}$0>. The flat domains between the grooves extends of $\approx$ 400 nm along <11$\bar{2}\bar{3}$> and are several micrometers long along

the perpendicular direction. The RMS of the flat areas is ≈ 2.6 nm, but they are separated by holes with an average depth of ≈ 100 nm.

Samples	T_{sub}	T_{Mg}	[Mg] [at.cm^{-3}]
E1873	705°C	350°C	$3.4 \pm 0.6 \times 10^{19}$
E1874	705°C	300°C	$7 \pm 1 \times 10^{18}$
E1875	685°C	350°C	$1.0 \pm 0.2 \times 10^{20}$
E1876	665°C	350°C	$9 \pm 2 \times 10^{19}$

Table 4.7: *Second series of Mg-doped layers obtained by varying both the substrate temperature and the Mg flux.*

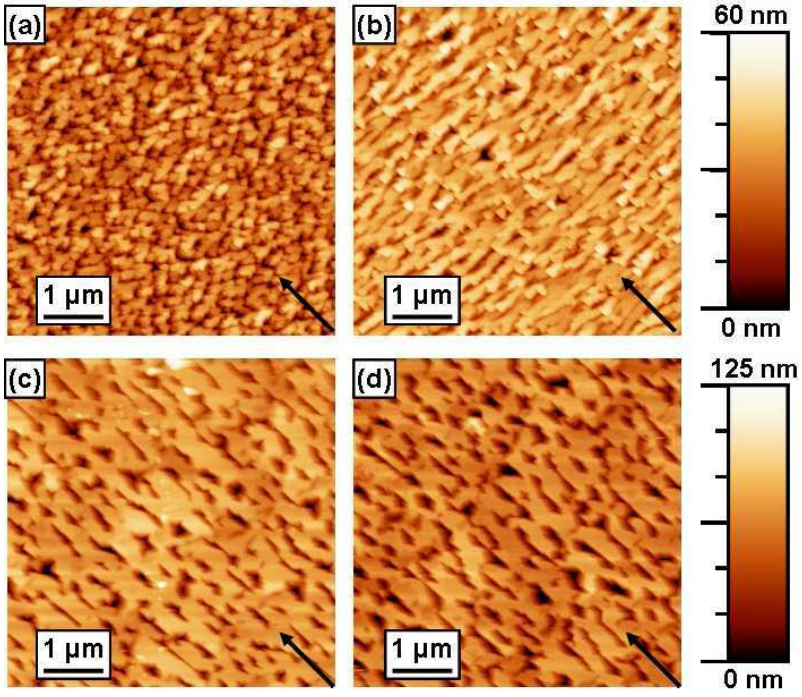

Figure 4.23: *AFM images of Mg-doped samples grown with T_{Mg} = 350°C (a) at T_{sub} = 665°C (E1876) and (b) at T_{sub} = 685°C (E1875). Samples grown at T_{sub} = 705°C with (c) T_{Mg} = 300°C (E1874) and (d) with T_{Mg} = 350°C (E1873). The arrows indicate the [11$\bar{2}$0]$_s$apphire direction.*

These surface specificities, indicate a clear modification of the surface kinetics with Mg-doping. Its effect is not well understood yet, but it seems that the adatom mobility is strongly modified by the presence of Mg, even leading to a privilege diffusion length different than in the case of undoped GaN. At this stage, the surfaces of GaN:Mg grown at low temperature can not be interpreted in comparison with undoped GaN since no low temperature GaN layers have been grown yet.

4.3.3 Optical properties Mg-doped layers

The optical properties of the series of samples in Table 4.6 were studied using time-integrated PL and TRPL measurements. Figure. 4.24(a) compares the luminescence spectra of n.i.d. GaN(11$\bar{2}$2) (sample E1229 described in Table 4.2), Mg-doped GaN(11$\bar{2}$2) (E1698) and Mg-doped GaN(0001), recorded at low temperature (T = 7K). The luminescence of the Mg-doped samples is dominated by the *DAP* line around 3.27 eV, which involves the light hole acceptor level from Mg [Ler99]. The peak corresponding to excitons bound to stacking faults, SF^0X, which is dominant in undoped semipolar layers (labeled D_1 in Fig. 4.14), remains present in E1698. The excitonic transition labeled I_1 is much more pronounced in the case of Mg-doped samples. The lines attributed to excitons bound to neutral donors (D^0X) or neutral acceptors (A^0X) are found around 3.472 eV and 3.466 eV, respectively, in relaxed GaN [Mon09]. In our Mg-doped samples, taking into account the high Mg concentration and the achievement of p-type conductivity, we would expect to the bandedge emission to correspond to the A^0X transition, which might be shifted from the expected value due to the strain state of the layer

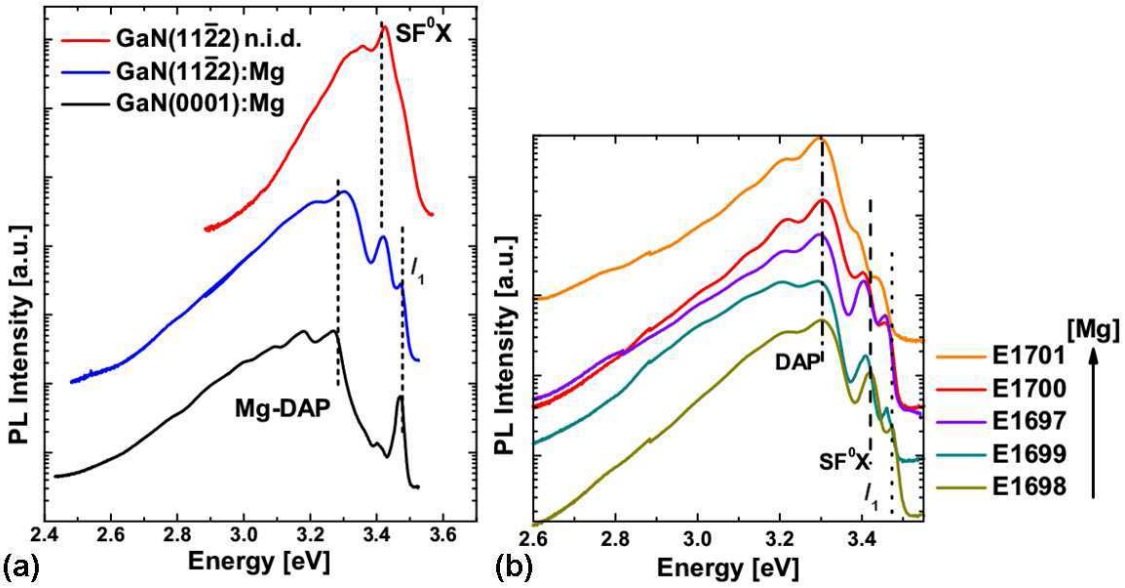

Figure 4.24: *(a) Comparison of the low temperature (T = 7 K) PL spectra of n.i.d. GaN(11$\bar{2}$2), Mg-doped GaN(11$\bar{2}$2) and Mg-doped GaN(0001). (b) Comparison of the low temperature (T = 7 K) luminescence from Mg-doped GaN(11$\bar{2}$2) layers with different Mg concentration. The spectra are vertically shifted for clearer visibilty.*

Figure 4.24(b) compares the luminescence spectra of layers with different Mg incorporation. The position of the *DAP* transition remains the same for all the samples, only its relative intensity increases when increasing the amount of Mg (E1701). The energy location of the excitonic lines is red-shifted for higher quantities of Mg, which can be attributed to a gradual evolution of the strain in the layers when

increasing the incorporation of Mg. However, the error bars of the lattice parameters determined by XRD does not permit a reliable confirmation of the strain evolution.

The optical properties of sample E1699 have been further investigated by time-resolved PL. Figure 4.25 compares the decay times of the excitonic SFX line and the DAP line, both recorded at 5 K. Strictly speaking, the SF^0X evolution corresponds to the integrated intensity of the bandedge emission, containing both the SF^0X and I_1. For this line, we measured a short decay time of 140 ps, which is 2 to 3 times higher than these found for the SF^0X and I_1 lines in undoped GaN [Fig. 4.17(a)]. This can be explained by the fact that the presence of Mg in the layers induces more localization of the carriers. The decay time of the DAP line is 50 μs, over five orders of magnitude larger than the one of the SF^0X. Moreover, the DAP shifts to lower energies with time, as illustrated in Fig. 4.26. To explain this shift, we have to consider that the donor-acceptor transition probability decreases exponentially with the distance between the two ionized atoms. First, the transition involves the closer pairs with higher energies. They recombine faster than the separated pairs which have lower energies.

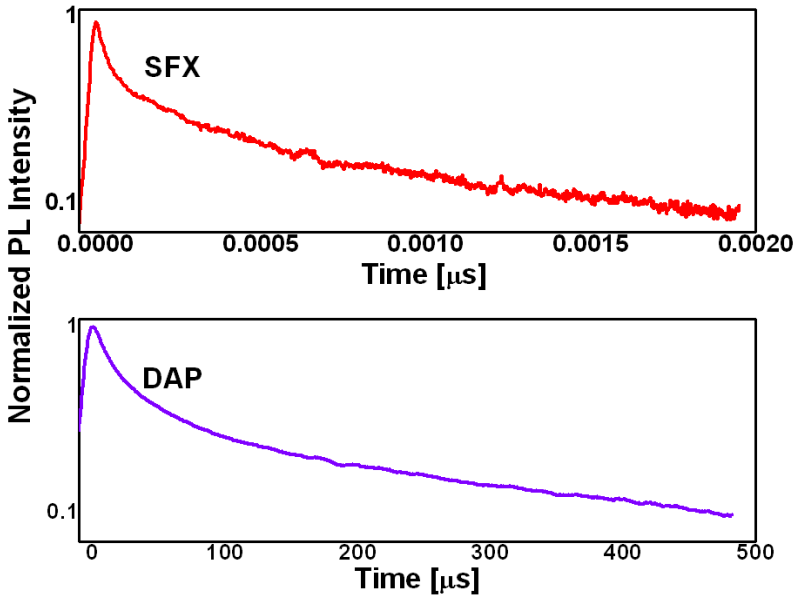

Figure 4.25: *Comparison of the low temperature (T = 5 K) luminescence decay of the bandedge luminescence, SFX, and the donor-acceptor broad band, DAP.*

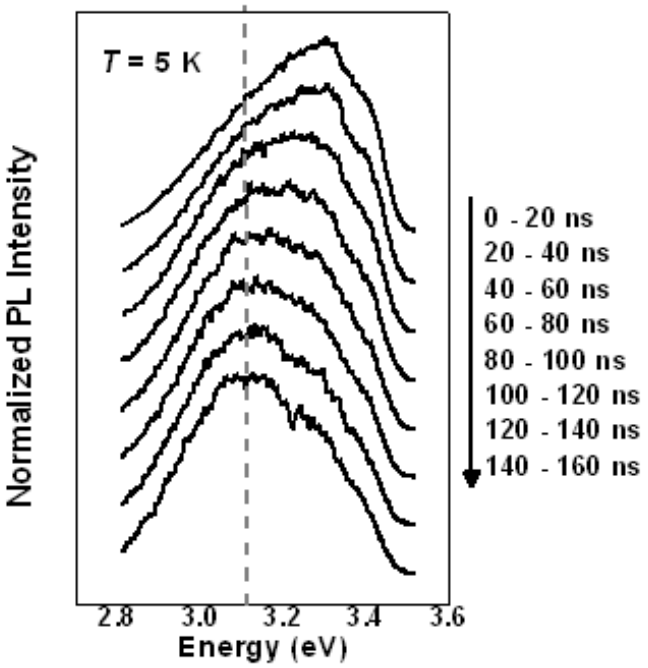

Figure 4.26: *Evolution the low temperature (T = 5 K) TRPL spectra from the DAP along the first 160 ns of the excitation pulse, recorded every 20 ns.*

4.3.4 Electrical characterization of Mg-doped layers

In this section, we focus on the electrical properties of the samples listed in Table 4.7. Hall effect measurements have been performed using the Van Der Pauw method, under temperatures ranging from room temperature to 800 K. Van der Pauw measurements provide the resistivity of the layers, ρ. The hole concentration is deduced from the Hall scattering factor, R_H, with Eq. 4.8, and the hole mobility, μ, depends on both the resistivity and the hole concentration by Eq. 4.9.

$$p = \frac{1}{qR_H} \tag{4.8}$$

$$\mu = \frac{1}{qp\rho} \tag{4.9}$$

The values of the hole concentration and mobility at room temperature are given in Table 4.8, showing evidence of p-type conductivity. Looking in details at the room temperature activation (quantity of holes compared to the amount of Mg atoms in the layers measured by SIMS), we observe a drastic degradation of the electrical performance for GaN:Mg grown at low temperature (samples E1875 and E1876). On the contrary, samples grown at high substrate temperatures (E1873 and E1874) show an activation of nearly 4%. Together with the enhanced Mg incorporation previously demontrated in Fig. 4.21, these are promising results for the p-type doping of the layers.

Samples	T_{sub}	[Mg] [cm^{-3}]	p [cm^{-3}]	μ [cm^2.V^{-1}.s^{-1}]
E1873	705°	$3.4 \pm 0.6 \times 10^{19}$	$5.7 \pm 0.5 \times 10^{17}$	1.3 ± 0.2
E1874	705°	$7 \pm 1 \times 10^{18}$	$2.8 \pm 0.5 \times 10^{17}$	2.4 ± 0.2
E1875	685°	$1.0 \pm 0.2 \times 10^{20}$	$9.0 \pm 0.5 \times 10^{17}$	1.5 ± 0.2
E1876	665°	$9.0 \pm 2 \times 10^{19}$	$6.7 \pm 0.5 \times 10^{17}$	0.8 ± 0.2

Table 4.8: *Electrical properties of Mg doped samples at room temperature.*

In the case of a partially compensated p-doped layer, the hole concentration depends on the system temperature, T, by the equation:

$$\frac{p(p+N_D)}{N_A - N_D - p} = \frac{N_V}{g} \exp\left(\frac{-E_A}{kT}\right) \tag{4.10}$$

where N_A and N_D are the acceptor and donor concentrations, respectively, k is the Boltzmann constant, g is the acceptor degeneracy factor, E_A is the ionization energy and N_V is the effective valence band density of states, given by the relation:

$$N_V = \frac{2(2\pi m_h^* kT)^{3/2}}{kT} \tag{4.11}$$

where h is the Planck constant, and m_h^* the hole effective mass (see values in Table 1.4). This model does not consider the formation of an impurity band or of valence band-tail states. If we consider that the effect of the holes is not compensated by the electrons, Maxwell - Boltzmann statistic implies Eq. 4.12. However, given the high n-type residual typically measured in the layers ($\approx 10^{16}$ - 10^{17} cm^{-3}), it is more correct to consider that the compensation is important, and in this case the hole concentration given by Eq. 4.13. The study of the hole concentration with temperature permit to determine the thermal activation energy of the holes, characteristic of the depth of the acceptor band.

$$p = \sqrt{\frac{N_V N_A}{g}} \exp\left(\frac{-E_A}{2kT}\right) \tag{4.12}$$

$$p = N_V \frac{N_A - N_D}{g N_D} \exp\left(\frac{-E_A}{kT}\right) \tag{4.13}$$

Figure 4.27 shows the evolution with the temperature of the hole concentration and the mobility for a sample with [Mg] = 6×10^{19} cm^{-3} measured by SIMS. For better understanding, the concentrations are represented in logarithmic scale and the temperatures are represented in reciprocal scale. At high temperatures, we observe the linear trend of the hall concentration expected in the approximation from Eq. 4.13. The activation energy, acceptor concentration, and compensating donor concentration, were extracted by fitting the high-temperature data to the formula in Eq. 4.10, where g was assumed equal to four, and N_V was calculated

assuming a hole effective mass $m_h^* = 2.2\ m_0$. The value of the activation energy, $E_A = 170 \pm 20$ meV is within the values typically found for GaN(0001) or m-plane GaN [Koz00, McL06]. The deviation from the fit for temperatures below 350 K, together with the drop of the mobility, is consistent with the activation of hopping transport in the defect band.

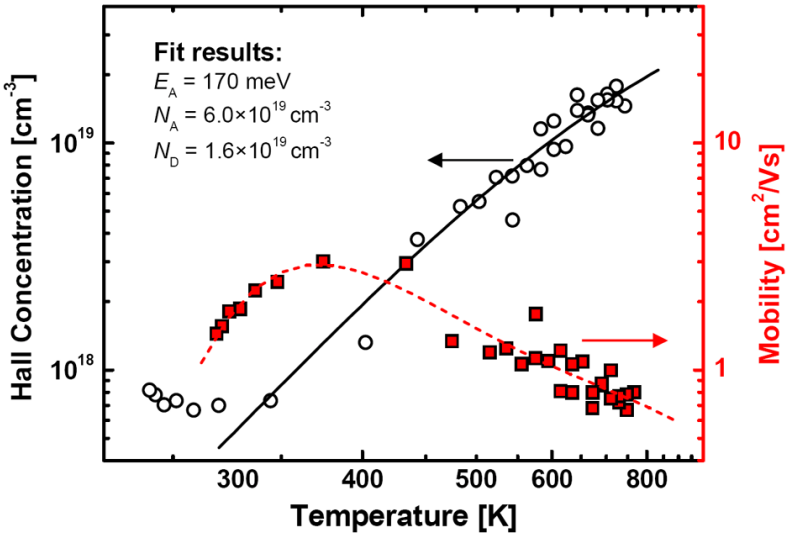

Figure 4.27: *Dependence of (a) the hole concentration and (b) the hole mobility with the temperature measured on sample E1873.*

The thermal evolution of the hole mobility in sample E1873 is illustrated in Fig. 4.27(b), showing an important decrease for increasing temperature. According to the work of Anderson and Apsley [And86], this tendency can not be explained by the presence of ionized impurities which induce an increase of the mobility with temperature ($\mu \propto T^{3/2}$). The decrease might be related to scattering by neutral impurities (μ constant with T), combined with scattering by dislocations ($\mu \propto T^{-1/2}$) and polar optical phonons ($\mu \propto T^{-3/2}$).

4.4 Conclusions

In the first part of this chapter, I analyzed the growth and properties of undoped GaN(11$\bar{2}$2). When studying the growth of GaN directly on m-sapphire, we observed that GaN deposited under N-rich conditions follows a three-dimensional growth, whereas two-dimensional growth is possible under Ga-rich conditions. However, the (11$\bar{2}$2) crystallographic orientation can not be isolated from the (10$\bar{1}$3)-oriented parasitic domains, mostly located at the GaN/sapphire interface. We found that this problem could be solved by growing GaN under Ga excess and on top of an AlN(11$\bar{2}$2) buffer layer. The resulting GaN(11$\bar{2}$2) layer grows epitaxially on AlN(11$\bar{2}$2).

We analyzed the Ga wetting of the GaN(11$\bar{2}$2) surface in order to determine

the different growth regimes under Ga-excess. We have observed that the maximum Ga coverage that we can stabilize on this surface is one (11$\bar{2}$2)-oriented monolayer, and the onset of Ga accumulation occurs at a lower Ga flux than in the case of the GaN(0001) face. XRD investigation showed that growth with a Ga excess of less than 1 ML of Ga or in the Ga accumulation regime leads to the formation of rough layers with inclusions of (10$\bar{1}$3)-oriented domains. On the contrary, GaN grown with exactly 1 ML of Ga in excess only shows the (11$\bar{2}$2) orientation, within the detection limits of our experimental setups.

The best surface morphology (RMS roughness of $\approx$ 2 nm) is achieved with 1 ML of Ga in excess, right before the accumulation limit. Under these growth condition TEM measurements gave us an estimation of the basal stacking fault density in the layers, around 3×10^{15} cm^{-1}, which is comparable to the values in MOVPE grown semipolar layers. From the chemical behavior of the samples, we conclude that they present Ga polarity.

The optical studies of thick layers demonstrate that GaN(11$\bar{2}$2) shows room temperature bandedge luminescence dominated by excitons bound to SFs, with no evidence of the yellow band emission.

The comparison of Ga desorption during the growth of undoped, Si-doped and Mg-doped layers revealed that Si doping does not change the growth kinetics, whereas Mg doping enhances Ga accumulation on the surface during growth. Mg-doped samples present a different surface morphology: grooves appear perpendicular to <11$\bar{2}\bar{3}$> direction, whereas they are parrallel to <11$\bar{2}\bar{3}$> for undoped or Si-doped layers.

We verified by SIMS that Mg incorporation is uniform along the layers up to [Mg] = 1.6×10^{20} cm^{-3}. From the estimation of Mg concentration and its dependence on the substrate temperature and the impinging Ga flux, we found that its incorporation is enhanced in GaN(11$\bar{2}$2) compared to GaN(0001). TEM shows no evidence of the pyramidal defects or polarity inversion domains that can be found Mg-doped GaN(0001).

Chapter 5

GaN/AlN quantum wells

In this chapter, I focus on the analysis of GaN/AlN quantum wells. A short introduction explains the effect of internal polarization in (0001)-oriented III-Nitride heterostructures.

After a structural description of the samples under study, I will demonstrate the strong reduction of the internal electric field using interband optical characterization. Furthermore, I will show the first observation of intersubband absorption in semipolar QWs. All the optical measurements will be discussed in comparison with theoretical calculations of the electronic structure using an 8-band k.p Schrödinger-Poisson solver. The work presented here is based on [Lah08a].

Contents

5.1 Quantum Confined Stark Effect 123

5.2 Structural analysis of semipolar quantum wells 124

5.3 Optical investigation 128

5.3.1 Demonstration of the reduction of the QCSE 128

5.3.2 Intersubband transitions 132

5.4 Conclusions 134

5.1 Quantum Confined Stark Effect

As it is shown in Tables 1.7 and 1.10, the spontaneous polarization along the [0001] axis have different values for GaN, AlN and InN. Moreover, the large lattice mismatch between the binary compounds and their huge piezolectric constants result in giant piezoelectric polarization fields. The growth of heterostructures along the [0001] axis imposes polarization discontinuities at the interfaces, which lead to fixed charge sheets. These electrically charged planes create an internal electric field in the heterostructures [Ber98] (Figure 5.1), whose value can be as high as 10 MV/cm in (0001)-oriented GaN/AlN quantum wells [Ber97, Tch06].

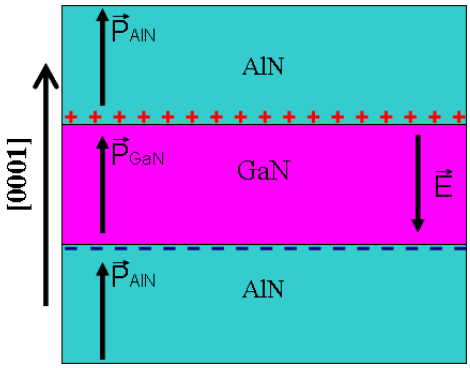

Figure 5.1: *Illustration of the presence of the polarization and the electric field in (0001)-oriented wurtzite structures.*

The presence of an electric field strongly modifies the band diagram of the structure. As an example, Fig. 5.2 illustrates the band diagram of a (0001)-oriented GaN quantum well embedded into AlN barriers. This triangular shape induced by the electric field has significant consequences on the optical properties of the structure. In a first approximation, the energy of the fundamental interband transition in a single QW is given by:

$$E = E_g^{GaN} + E_{e1} + E_{h1} - qFL \tag{5.1}$$

where E_g^{GaN} is the bandgap of GaN, E_{e1} and E_{h1} the first confinement energies of the electron and hole, respectively, q the electron charge, F the internal electric field and L the thickness of the well. In Eq. 5.1, we can see that for extremely thin wells, the quantum confinement effects are larger than the electric field component, and the energy of the transition is close to those from a quantum well with no internal electric field. However, for thick wells, the energy of the transition linearly decreases with the thickness of the wells due to the electric field. Besides, as can be seen in the schema, the band bending spatially separates the wave functions of electrons and holes, which implies lower oscillator strength, and therefore Hence, lower radiative efficiency and longer radiative life times. These features are what is called the quantum confined Stark effect (QCSE).

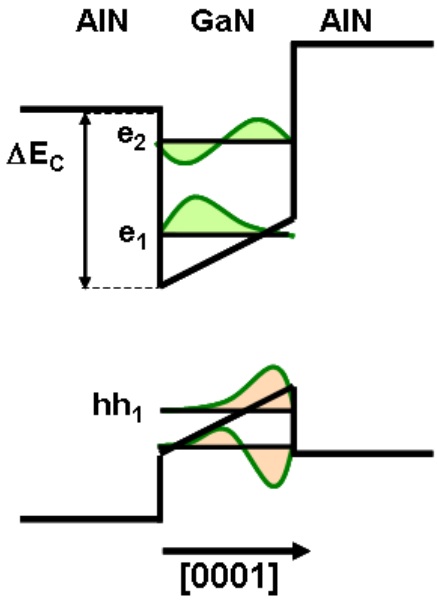

Figure 5.2: *Typical triangular shape of a (0001)-oriented GaN/AlN quantum well. The quantum confined Stark effect separates the electron and hole wave functions so that the optical properties of the well are modified.*

The QCSE induces a limitation to the performance of nitride-based devices such as electroluminescent diodes. In addition to the lower radiative efficiency, any small fluctuation in the thickness of the nanostructures induces a significant shift of the interband transitions, resulting in a broadening in the luminescence peaks. Moreover, the electric field in the diodes can be partially screened by the injected carriers, whose desnity depends on the current. This means that the energy of the optical emission is strongly dependent on the current [Fio99].

Motivated by the idea to reduce the QCSE, I have synthesized semipolar heterostructures, whose properties will be detailed in this chapter and the following one.

5.2 Structural analysis of semipolar quantum wells

All the samples under study in this chapter were grown under the appropriate growth conditions for 2D AlN and GaN. An AlN buffer layer was first deposited on the *m*-sapphire substrate with an Al/N ratio of ≈ 0.95. In order to improve the surface quality, a GaN layer was grown on the AlN, with the optimal Ga excess of 1 $ML_{(11\bar{2}2)}$. The superlattices were grown on top, at the same substrate temperature and using these later conditions for both AlN and GaN.

The crystalline quality of semipolar GaN/AlN QWs has been studied by XRD and TEM. Prior to the growth of the superlattices a $\approx$ 100-nm-thick GaN buffer layer was deposited on an AlN buffer layer with the same thickness. The active structures consist of 40 periods of GaN/AlN QWs with 4.80-nm-thick AlN barriers

and GaN QW thickness varying from 1.3 nm to 3 nm, as summarized in Table 5.1. A similar MQW series was grown along the c-axis on AlN on *c*-sapphire templates in order to compare the internal polarization effects on semipolar and polar structures.

Samples	Nominal QW thickness	Measured thickness
E1364	1.33 nm	1.52 nm
E1363	1.72 nm	-
E1367	1.90 nm	-
E1361	2.31 nm	-
E1366	2.81 nm	3.44 nm

Table 5.1: *Semipolar multiple quantum well samples: the expected thicknesses of the wells is deduced from the growth conditions. For samples E1364 and E1366, the actual thickness is determined via the analysis of XRD and TEM measurements.*

Figure 5.3 shows a cross-sectional TEM view of the whole structure, viewed along the $<11\bar{2}\bar{3}>$ axis of the superlattice. The good periodicity of the structure can be observed. However, the BSFs present in the AlN and GaN buffer layers propagate throughout the entire structures and bend the wells, so that, locally, the thicknesses of the well and barriers are modified. In the following, the studies of the out-of-plane parameter will be performed on "clean" areas, *i.e.* areas with no strong modification of the stack due to defects.

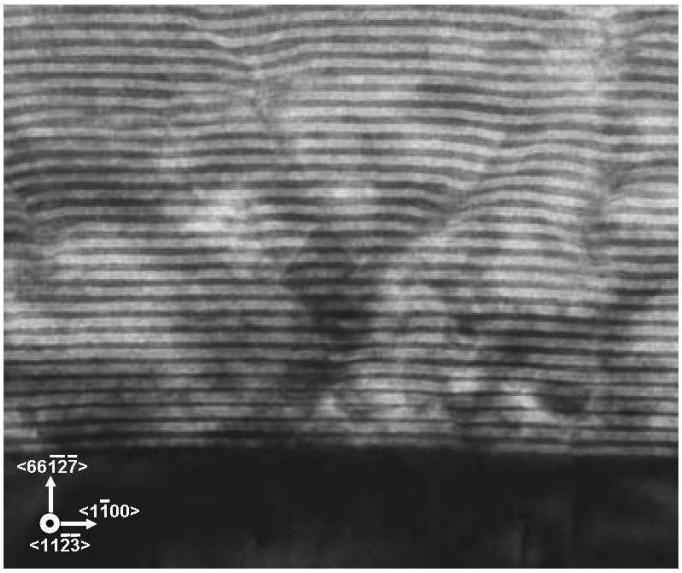

Figure 5.3: *Cross-sectionnal TEM image of a GaN/AlN multiple-quantum-well structure with 40 periods of ≈ 2.8-nm-thick GaN QWs embedded in ≈ 4.8-nm-thick barriers. We can see the good reproducibility in the quantum well thickness, except in the zones stressed by stacking faults. Image from P. Ruterana et al., CNRS - CAEN, France.*

Figure 5.4 shows typical symmetric 2θ-ω scans of multiple quantum well (MQW) structures around the $(3\bar{3}00)$ reflection of the sapphire substrate. As previously indicated (Figs. 3.2 and 4.10), the main peak at $2\theta = 68.226°$ is attributed to the $(3\bar{3}00)$ reflection of the sapphire substrate. The superlattice reflection presents several satellites, named SL$\pm i$, which further confirm the good periodicity of all the samples. The arrows serve as eyeguides to observe the trends when decreasing the GaN well thickness. Indeed, since the proportion of AlN increases, the zero order reflection from the superlattice shifts towards higher 2θ. Additionally the spacing between the superlattice reflections increases, as a result of a thinner period {AlN barrier + GaN well}. For the interpretation of these measurements, the MQW structures are considered as equivalent to $Al_xGa_{1-x}N$ layers, where x is the proportion of Al in the stack. The difference between the n order satellite peak position, $2\theta_n$, and the zero order peak position, $2\theta_0$, is inversely proportional to $\frac{L}{n}$, where L is the thickness of the period.

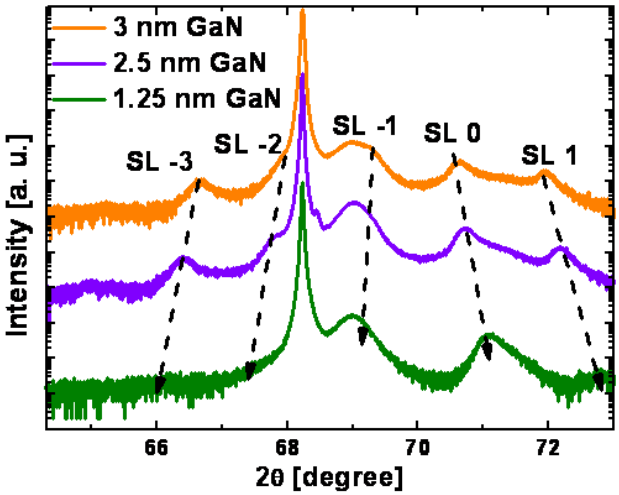

Figure 5.4: *X-ray diffraction 2θ-ω scans of semipolar superlattices with various GaN quantum well thickness.*

XRD scans do not permit the determination of thickness of AlN and GaN independently, so that TEM analysis is required. Figures 5.5(a) and (b) are HRTEM images recorded on samples E1366 and E1364, the samples with the thicker and thinner quantum wells, respectively. These images attest the good epitaxial alignment of GaN and AlN along the growth axis. From these TEM magnifications, we can measure the thickness of AlN and GaN independently, with an error bar of 1 to 2 monolayers. Therefore, by combining the TEM and XRD analysis, we can access the actual thickness of the wells and barriers. We found a barrier thickness of 4.87 nm and 4.76 nm for samples E1364 and E1366, which is consistent with the expected values, given the monolayer thickness fluctuations. The values of the well thickness, reported in Table 5.1. The error in the well thickness stems from the growth rate determination on the one hand (≈ 10 %), and from the TEM observation on the other

hand. Indeed, since the HRTEM images are local magnifications into the structure, we should make a statistical analysis on the with several pictures of the structure to obtain a mean value of the out-of-plane parameter.

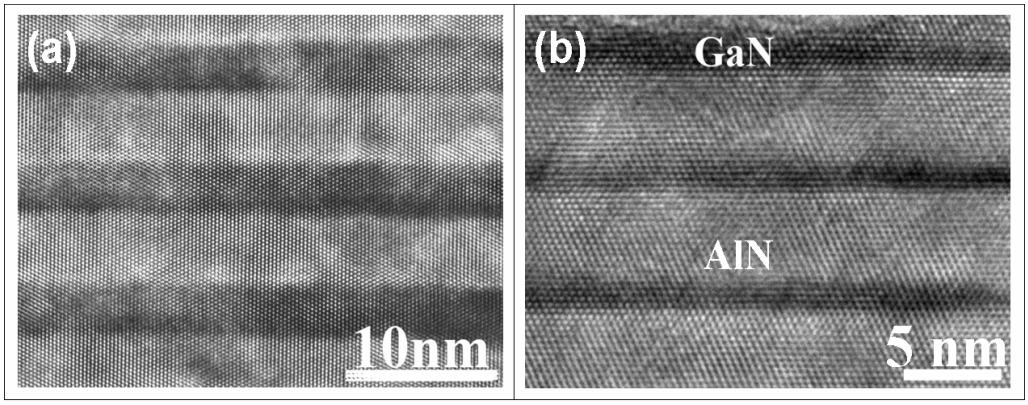

Figure 5.5: *High resolution TEM images of the samples (a) E1366 and (b) E1364. The magnification on the structures makes it possible to count the atomic planes in both the barrier and the well. Image from P. Ruterana et al., CNRS - CAEN, France.*

It is important to note that we did not compare the actual position of *SL0* peak to the position it should have given the measurement of GaN and AlN thickness. For instance, in the case of 1.52-nm-thick wells, the stacking corresponds to an $Al_{76}Ga_{24}N$ layer, whose diffraction peak should occur at $2\theta = 70.79°$, whereas the XRD reflection is shifted towards higher 2θ angles, *i.e.* towards the AlN reflection. In a first approximation, it points to the superlattices being in-plane strained on GaN. The analysis of the asymmetric reciprocal space maps around the $(11\bar{2}4)$ and $(20\bar{2}2)$ reflections would provide average values of the three lattice parameters and allow determining the actual strain state of the structures. However, this is not possible due to the broadening of the reflections. Additionally, conclusions can be drawn on the strain state of the single layer only if the in-plane lattice parameter is the same throughout the whole layer, *i.e.* if GaN and AlN layers have the same lattice parameter, which is not, *a priori*, the case. Furthermore, in the symmetric RSM recorded on E1366 sample around the $<1\bar{1}00>$ axis of the layer shown in Fig. 5.6, we can see that the AlN, the GaN and the superlattice present different tilt. In particular, the higher value of the tilt of the superlattice would imply a complex mechanism in the relaxation of the structure and consequently not one constant parameter for the superlattice.

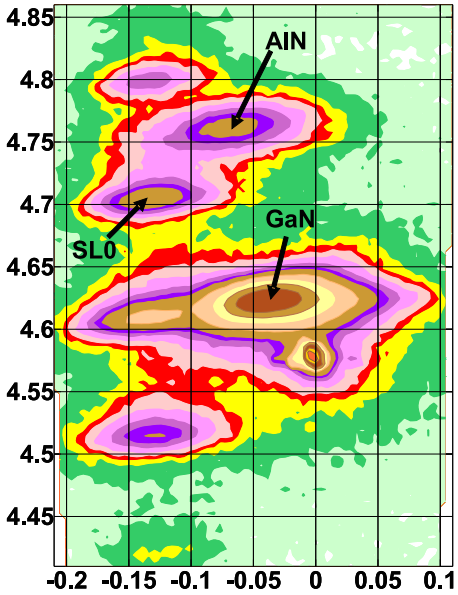

Figure 5.6: *Typical symmetric Reciprocal Space Map recorded around <1$\bar{1}$00> on a QW sample, to illustrate the different misorientations of the AlN, GaN and superlattices.*

5.3 Optical investigation

In this section, I detail the optical measurements performed on the series of multiple-quantum-well structures. We will see the effect of the reduction of the internal electric field on the intraband properties of the superlattices and go into deeper analysis with the evidence of intersuband (ISB) absorption.

5.3.1 Demonstration of the reduction of the QCSE

The fundamental interband transition, $e_1 - h_1$, was investigated by photoluminescence (PL) spectroscopy and time-resolved PL (TRPL) for both semipolar and polar series. Figure 5.7 compares the PL spectra from semipolar and polar GaN/AlN MQWs with different QW thickness recorded at low temperature ($T = 7\ K$). In the case of the polar structures (dashed lines), the PL shows a strong red shift when increasing the QW thickness. For the samples with thin QWs (≤ 2 nm), the PL is blue shifted with respect to the GaN bandgap (light gray line), due to quantum confinement. However, in the structures with thicker wells, the internal electric field screens the quantum confinement and the transition energy is shifted below the GaN bandgap. In the case of (11$\bar{2}$2)-oriented MQWs, the PL energy peak remains systematically above the GaN band gap, attesting the reduction of the internal electric field in the QWs.

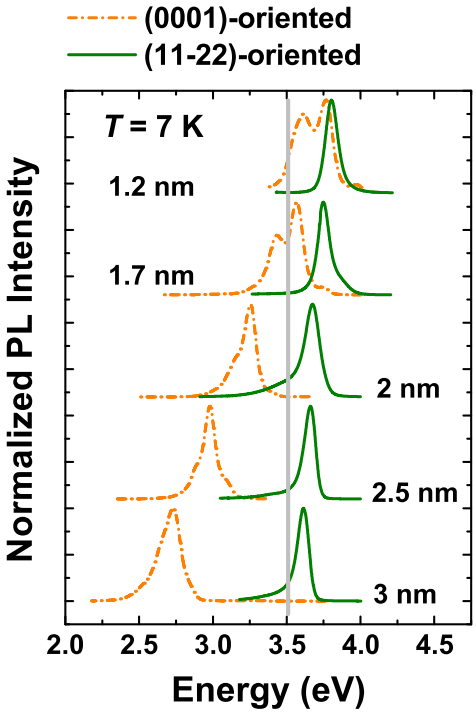

Figure 5.7: *Low-temperature ($T = 7K$) PL spectra from polar and semipolar GaN/AlN MQWs with a QW thickness varying from 1.2 to 3 nm.*

Another important feature of the PL spectra from polar samples is the presence of several non-periodical peaks for thin wells, or shoulders for thicker wells. Since their discrete energy locations correspond to the expected values of the PL line in QWs with thickness equal to an integer number of GaN monolayers, we can attribute their presence to monolayer fluctuations in the wells [Tch06]. For the very narrow QWs, a variation of the thickness by 1 ML implies an important shift of the PL due to the position of the fundamental levels in the triangular zone of the well (see in Fig. 5.2). The shift is about 150 meV for QWs of 4-5 ML, *i.e.* 1-nm to 1.25-nm-thick wells. This value is larger than the line width of the PL ($\approx$ 100 meV) which can explain the presence of well-resolved PL peaks [Tch06]. As a consequence of the reduction of the QCSE, the monolayer thickness fluctuations in the wells would induce a smaller shift of the PL transition, of $\approx$ 50 meV for the thinner wells. However, since the full width at half maximum (FWHM) of the emission lines is typically 100 meV, this phenomenon is only contributing to the broadening of the PL lines.

The PL extinction at low temperature ($T = 7\ K$) has been measured on polar and semipolar series MQWs. For instance, Fig. 5.8 presents the TRPL results obtained for both semipolar and polar GaN/AlN (3 nm / 5 nm) MQW structures. In this particular case, we observe a PL decay time $\approx$ 10 ns for the polar sample, whereas for the semipolar structure we measure a decay time $\approx$ 300 ps. The faster

decay times found for the $(11\bar{2}2)$-oriented structures further confirms the strong reduction of the QCSE.

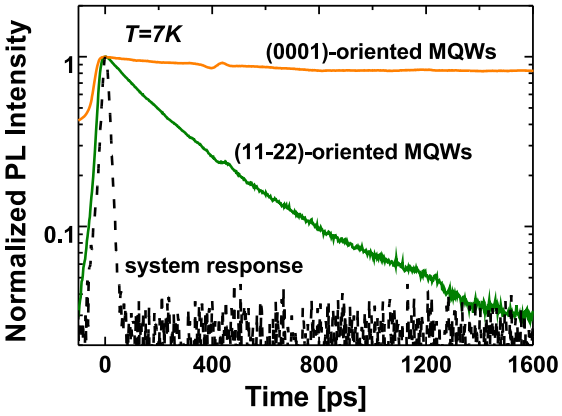

Figure 5.8: *Low temperature $T = 7$ K PL extinction measured on polar and semipolar GaN/AlN (3 nm / 5 nm) MQWs.*

It is interesting to interpret the PL results by comparison with theoretical calculations of the electronic structure. We used the next**nano**[3] 8-band k.p Schrödinger-Poisson solver described in section 2.5, with the material parameters given Table 2.1 to simulate the semipolar and polar structures.

As an example and to evaluate differences between semipolar and polar structures, Fig. 5.9 presents the band diagrams of GaN/AlN (2.5 nm / 5 nm) QWs grown on (0001) and $(11\bar{2}2)$ planes. For both orientations, we assumed either that the structures are fully strained on GaN or fully strained on AlN. The envelope functions of the h_1 ground hole state, the e_1 ground electron state, and the e_2 and e_3 excited electron states are plotted. In polar samples, the band diagrams show the characteristic sawtooth profile due to the presence of the internal electric field. By the simulation, we estimate the value of the electric field to ≈ 6.7 MV/cm in QWs strained on AlN and ≈ 8 MV/cm in QWs strained on GaN. The higher electric field in MQWs strained on GaN is due to the larger piezoelectric constants of AlN compared to GaN (see values of the piezoelectric coefficients in Table 1.11). The spatial separation of the e_1 electron envelope function and the h_1 hole envelope function along the [0001] axis leads to the PL red shift and long radiative lifetimes of polar QWs compared to semipolar QWs, as experimentally observed in Figs. 5.7 and 5.8. The increase of the $e_1 - h_1$ transition energy in MQWs strained on AlN is mostly due to the increase of the GaN bandgap under compressive in-plane strain, *i.e.* tensile strain along the c-axis, as illustrated in Fig. 5.10.

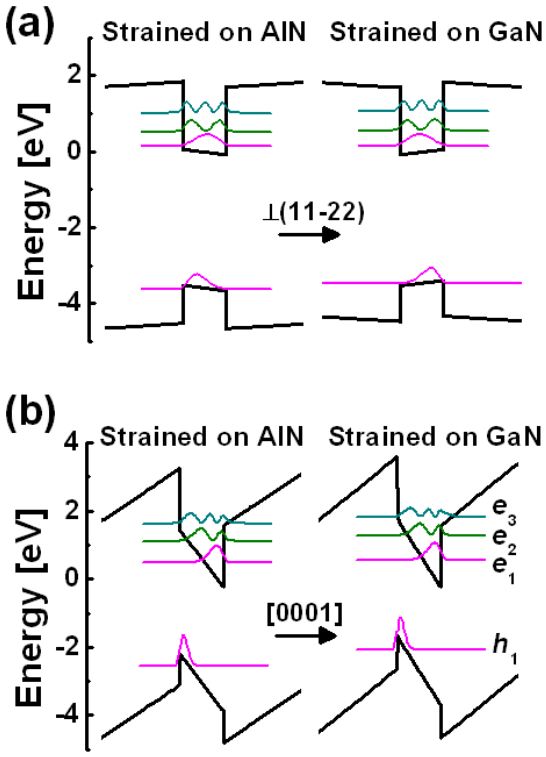

Figure 5.9: *Band diagrams of (0001)- and (11$\bar{2}$2)-oriented GaN/AlN MQWs assuming the structures fully strained on AlN and on GaN. This next**nano**^{3} simulation corresponds to 2.5-nm-thick GaN quantum wells embedded in 5-nm-thick AlN barriers.*

In the case of the semipolar structures, the band diagram exhibits a quasi-squared potential profile in the QWs. We calculate an internal electric field of -0.9 MV/cm for MQWs strained on AlN and of 0.1 MV/cm for MQWs strained on GaN, which confirms the strong reduction of the electric field. Actually, in the semipolar case, the spontaneous and piezoelectric polarization differences at the interfaces between AlN and GaN have opposite signs, so that the global polarization is reduced. The piezoelectric component becomes dominant in the MQWs strained on AlN, which leads to negative electric field.

Figure 5.11 displays the evolution of the $e_1 - h_1$ transition energy as a function of the QW thickness, for polar and semipolar structures and both strained on GaN and AlN, deduced from the simulation of the band structures. In order to compare these calculations with the experimental values, I assumed a lattice temperature of $T = 7\ K$. For the polar QWs, the experimental results fit well the theoretical calculations corresponding to a superlattice strain on AlN. XRD characterization of these structures further confirms an in-plane lattice parameter close to that of AlN [Kan08]. In the case of semipolar samples, the PL measurements fit well to the theoretical evolution of the $e_1 - h_1$ transition if the superlattices were strained on GaN.

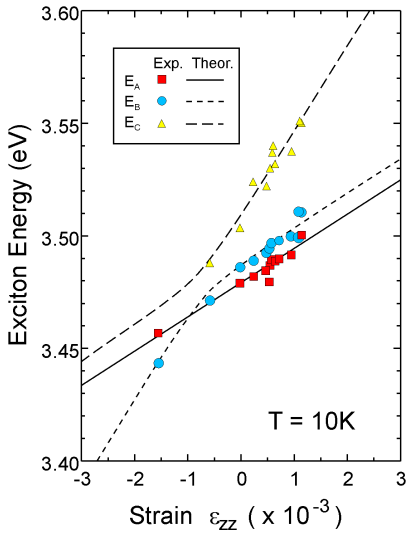

Figure 5.10: *Evolution of the energy of the excitonic lines in undoped GaN depending on the strain state along [0001] axis [Shi97].*

Let me point out that the PL peak energy of the semipolar structures does not permit drawing a direct conclusion on the strain state of the superlattices. The difference in $e_1 - h_1$ energy between a superlattice fully strained on GaN and another one strained on AlN is of about 120 meV, which is is comparable to the FWHM of the peaks. Furthermore, the emission peak energy might be slightly red-shifted due to carrier localization on structural defects or thickness fluctuations.

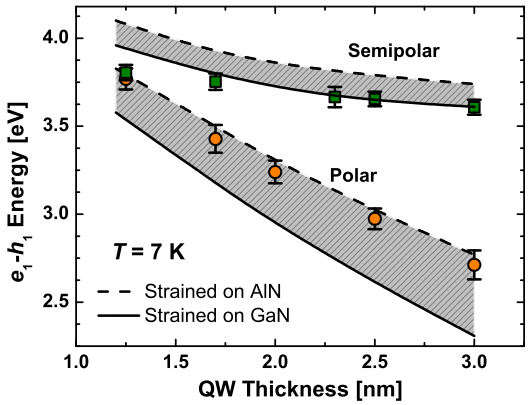

Figure 5.11: *Evolution of $e_1 - h_1$ as a function of the QW thickness and strain state for both semipolar and polar structures.*

5.3.2 Intersubband transitions

The intersubband properties of the samples were studied by the group of Dr F. H. Julien (Intitut d'Etudes Fondamentales, Paris-Sud, France). The MQWs

electronic structure was probed by photoinduced intersubband absorption (PIA) using Fourier transform infrared spectroscopy at room temperature. The sample facets were polished at 45° angle to form a multipass waveguide with 4-6 total internal reflections. During the experiment, the samples were illuminated by a laser at $\lambda = 244$ nm to populate the ground state of the MQWs with electrons. The structures under study for these experiments consist of 40 periods of 2-nm-thick and 2.5-nm-thick GaN:Si QWs embedded in 3-nm-thick AlN barriers. The concentration of Si dopants was estimated to be approximately 5×10^{19} cm^{-3}. The active structure was deposited on top of a 280-nm-thick GaN layer grown on a 100-nm-thick AlN buffer layer. For this series, the GaN buffer layers are thicker than for the previous series in order to prevent Fabry-Pérot oscillations from being superimposed to ISB absorption peaks. Additionally, a 10-nm-thick GaN cap layer was deposited at the end of the growth to fit the Fermi level at the surface and avoid depletion effect in the upper wells.

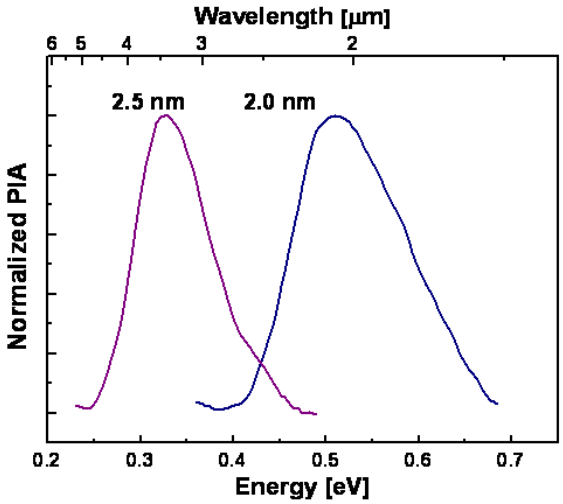

Figure 5.12: *Room-temperature photoinduced intersubband absorption spectra for TM-polarized light measured in (11$\bar{2}$2)-oriented GaN/AlN MQWs with 3-nm-thick AlN barriers and Si-doped GaN QWs with a thickness of 2 nm and 2.5 nm.*

Figure 5.12 displays the TM-polarized PIA spectra of the two structures. Since no absorption was found for TE-polarized light (within the experimental accuracy), we can assign the emission to ISB transitions between electron states confined in the QWs. The FWHM of the lines was found to be around 80-110 meV, which is comparable to results in polar structures [Tch06].

As previously described for the fundamental interband transitions, we calculated the theoretical $e_1 - e_2$ ISB transitions for semipolar and polar samples. The comparison with the experimental values is presented in Fig. 5.13. In the case of polar QWs, the energies of the ISB absorption further confirm that the superlattices are strained on AlN. In the case of semipolar QWs, the strong reduction of

the internal electric field results in a red shift of the ISB energy. Additionally, given the nearly squared shape of the band diagram, the energy of $e_1 - e_2$ intersubband transition does not depend on the strain state of the superlattice.

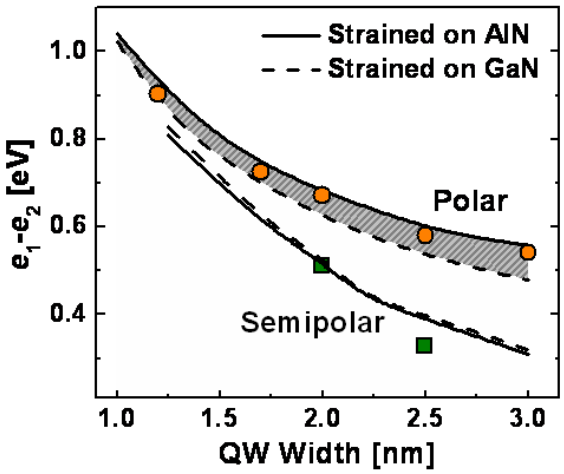

Figure 5.13: *Comparison between calculated and experimental ISB energy for semipolar and polar structures.*

5.4 Conclusions

The control of the two-dimensional growth of AlN and GaN on m-plane sapphire has allowed us to synthesize semipolar GaN/AlN($11\bar{2}2$) multiple-quantum-well structures. The good crystalline quality of the samples is supported by XRD and TEM measurements. In particular, TEM images show sharp interfaces between AlN and GaN, and no interdiffusion within the layers.

The comparison of the PL lines of similar semipolar and polar series show a strong red shift of the polar emission compared to the semipolar emission, which remains above the GaN bandgap as a first indication of a reduction of the internal electric field. TRPL measurements show decay times of hundred of picoseconds for the semipolar MQWs, in comparison with the nanosecond decay usually found in polar structures. All together, the combination of optical studies and simulation confirm the significant reduction of the QCSE in comparison with polar structures.

Finally, it was possible to observe the first intersubband absorption in semipolar nitride nanostructures, redshifted in comparison to the polar intersubband absorption, which stands for another evidence of the reduction of the electric field in the structures.

Experimental results are in good agreement with theoretical calculations of the electronic structure, which show that the potential profile of semipolar QWs is almost square. An original feature is the compensation of the spontaneous polarization by the piezoelectric polarization in the case of semipolar wells. This leads

to an opposite band bending if the wells are strained on GaN, due to the higher piezoelectric constants of AlN. The simulation on semipolar and polar structures points to a reduction of the internal electric fields by a factor of ≥ 10.

Chapter 6

GaN/AlN quantum dots

This chapter focuses on the study of semipolar GaN/AlN quantum dots (QDs). I first describe the growth process which leads to the formation of $(11\bar{2}2)$-oriented QDs, and continue with the analysis of their structural and optical properties. Part of the work presented here has been published in [Lah09].

Contents

6.1 Synthesis of semipolar GaN QDs on AlN$(11\bar{2}2)$ 139

6.1.1 Growth of nitride quantum dots 139

6.1.2 Growth of semipolar GaN quantum dots 140

6.2 Structural description of semipolar GaN quantum dots 141

6.3 Optical properties of $(11\bar{2}2)$-oriented QDs 145

6.4 Conclusions 148

6.1 Synthesis of semipolar GaN QDs on AlN(11$\bar{2}$2)

After a brief overview of the growth mechanisms of polar and nonpolar GaN/AlN QDs, I will describe the growth procedure to synthesize semipolar GaN/AlN QDs.

6.1.1 Growth of nitride quantum dots

The most common approach to synthesize self-assembled QDs is the so-called Stranski-Krastanow (SK) growth mode (described in section 2.1.2), which is characterized by the formation of a two-dimensional (2D) pseudomorphic wetting layer, followed by spontaneous islanding at a certain critical thickness of the deposit. If the elastic energy accumulated in the 3D islands remains below a certain threshold, the formation of extended defects, such as misfit dislocations, is energetically unfavorable.

In the specific case of (0001)- or (000$\bar{1}$)-oriented GaN QDs grown on AlN by plasma-assisted molecular-beam epitaxy (PAMBE), the SK growth mode is observed when GaN is deposited at high temperature ($\geq$ 700°C) under N-rich conditions. The critical thickness is about 2 ML for the (0001) crystallographic orientation [Dau97, Gui06] and 1 ML for the (000$\bar{1}$) face [Gog04]. These self-assembled GaN QDs are hexagonal truncated pyramids with {1$\bar{1}$03}-oriented facets. On the other hand, it is also possible to synthesize (0001)- or (000$\bar{1}$)-oriented GaN/AlN QDs by GaN deposition under Ga-rich conditions followed by a growth interruption in vacuum [Dam99, Gog04, Bro04]. The QDs obtained by this latter method present similar characteristics (critical thickness, facet orientation, and wetting layer) to those of GaN QDs grown by the SK growth mode. In general, polar GaN/AlN QDs are defect-free structures [Cha04].

The growth of nonpolar QDs has also been demonstrated for the GaN/AlN system. In particular, a strong reduction of the internal electric field was observed for QDs grown on the (11$\bar{2}$0) *a*-plane [Fou05] and the (1$\bar{1}$00) *m*-plane [Ams07]. In the case of the (11$\bar{2}$0) orientation, the Stranski-Krastanow transition occurs under Ga-rich conditions leading to the formation of QDs after reaching the critical thickness of about 2 to 3 ML. For *m*-plane GaN, the formation of QDs occurs under Ga-rich conditions, for amount of GaN of less than 7 ML deposited on a 300-nm-thick (at least) AlN buffer layer. However, the integration of such nonpolar nanostructures in complete devices is challenging due to the difficulties to achieve nonpolar 2D layers with flat morphology [Fou05, Ams07], and to the strong dependence of the QD morphology on the AlN underlayer [Ams07].

6.1.2 Growth of semipolar GaN quantum dots

With the motivation to investigate the structural properties and the optical performance of QDs with a different orientation, we have studied the three-dimensional growth mode of GaN on AlN(11$\bar{2}$2). To the best of our knowledge, this chapter stands as the first demonstration of (11$\bar{2}$2)-oriented GaN/AlN QDs.

GaN deposition on AlN(11$\bar{2}$2) can follow either the layer-by-layer (Frank Van der Merwe) mode or the Stranski-Krastanov (SK) growth mode illustrated in Fig. 2.3, by proper tuning of the growth parameters. As explained in Chapter 4, 2D GaN thick layers are achieved with 1 $ML_{(11\bar{2}2)}$ of Ga in excess. On the contrary, GaN deposited under N-rich conditions results in spotty RHEED patterns, which is an indication of a 3D growth.

A deeper analysis of the beginning of the GaN growth on AlN(11$\bar{2}$2) under N-rich conditions revealed that the growth starts 2D, followed by spontaneous islanding at a critical thickness of $\approx$ 3.5 ML. This two-step transition is characteristic of the SK growth mode. Figure 6.1(a) illustrates the spotty RHEED pattern recorded along the <11$\bar{2}$0> azimuth of the sapphire substrate after the deposition of 5 ML of GaN under a Ga/N ratio of $\approx$ 0.83. In addition to the reflections from GaN(11$\bar{2}$2), some dimmer spots can be observed (indicated by white arrows in Fig. 6.1), corresponding to a second crystallographic orientation. As a comparison, Fig. 6.1(b) shows the typical streaky RHEED pattern of a 2D GaN(11$\bar{2}$2) layer taken along the same <11$\bar{2}$0> azimuth of the sapphire substrate. We found that the additional spots in Fig. 6.1(a) present the same pattern as the additional reflections present in thick GaN layers epitaxially grown on *m*-sapphire, attributed to {10$\bar{1}$3}-oriented GaN by XRD measurements. Thus, the SK growth of semipolar QDs under N-rich conditions is possible, but it does not lead to a unique crystallographic orientation.

A 2D-3D transition is observed under slightly Ga-rich conditions (close to the stoichiometry), if the deposition of a few GaN monolayers is followed by a growth interruption in vacuum. As shown in Figs. 6.1(c) and (d), the RHEED pattern becomes spotty, indicating that the surface becomes dimensional. Besides, some additional streaks, enhanced by the continuous lines in the figure, appear at this stage in the RHEED pattern, related to the QD facets. However, when the amount of GaN deposited is lower than 3 ML, such re-arrangement of the layer is not observed, and the GaN layer remains 2D even for extended annealing times.

To study the structural properties and optical performance of semipolar GaN QDs, we have fabricated several series of superlattices of GaN QDs embedded in an AlN matric. The QDs were synthesized by deposition of a 2D GaN layer under Ga-rich conditions, followed by a 90 s growth interruption in vacuum, that makes the reflections corresponding to the QD facets to appear in the RHEED pattern.

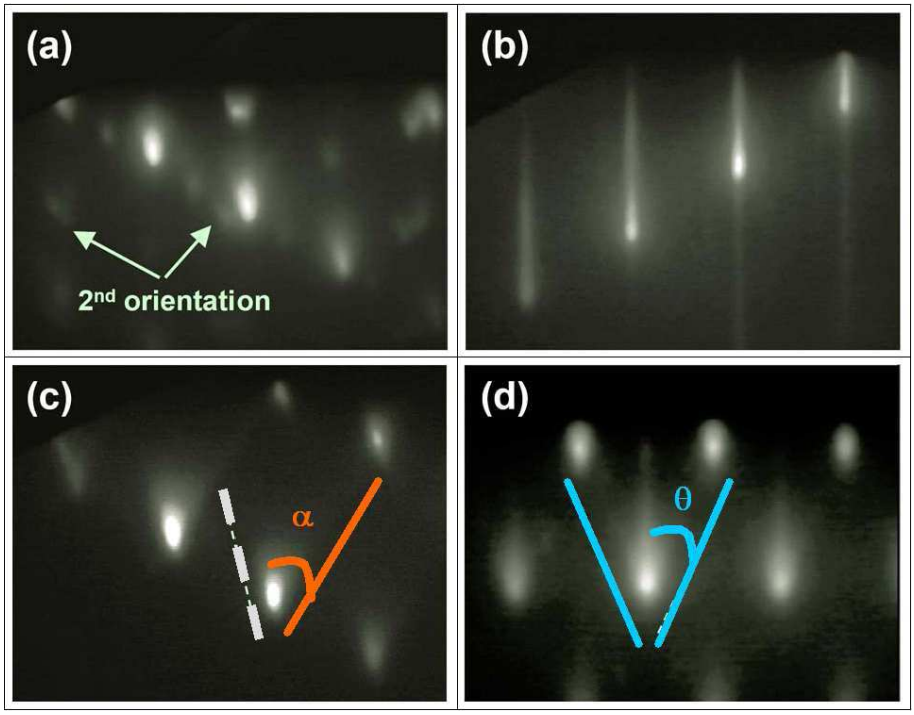

Figure 6.1: *RHEED patterns taken along the <11$\bar{2}$0> [(a), (b) and (c)] and <0001> (d) azimuths of the sapphire substrate in the case of (a) 3D GaN grown under N-rich conditions, (b) typical 2D GaN growth, (c) and (d) GaN deposited under slightly Ga-rich conditions and after growth interruption under vacuum.*

6.2 Structural description of semipolar GaN quantum dots

In this section, the structural characteristics of (11$\bar{2}$2)-oriented semipolar quantum dots will be discussed. For this investigation, several series of samples were grown under the previously described growth conditions, with a nominal amount of GaN in the QD layers varying from 3 ML to 10 ML. For all the superlattices, an additional QD plane was deposited on the surface to enable AFM characterization to estimate the QD density in the layers. Additionally, the crystallographic arrangement and shape of the dots were studied by TEM measurements by our collaborators, the group of Prof. P. Komninou at Aristotle University of Thessaloniki (Greece).

The formation of QDs has been verified by AFM analysis of the last QD layer which was not covered by AlN. For instance, the AFM micrograph in Fig. 6.2(a) illustrates the surface of a sample with nominally 5 ML of GaN in each QD layer. This image is to be compared to Fig. 6.2(b), which shows the typical surface of a $\approx$ 200-nm-thick 2D AlN(11$\bar{2}$2) layer. In Fig. 6.2(a), we measured an island density of approximately 5×10^{10} cm^{-2}, with an average island height of 2.5$\pm$0.4 nm. However, it is important to remind the difficulty to quantify precisely the dimension of surface corrugations from AFM characterization, since the measured topography is a convolution of the real surface and the tip shape. Moreover, it is not possible to

determine if a continuous 2D GaN wetting layer persists between the islands.

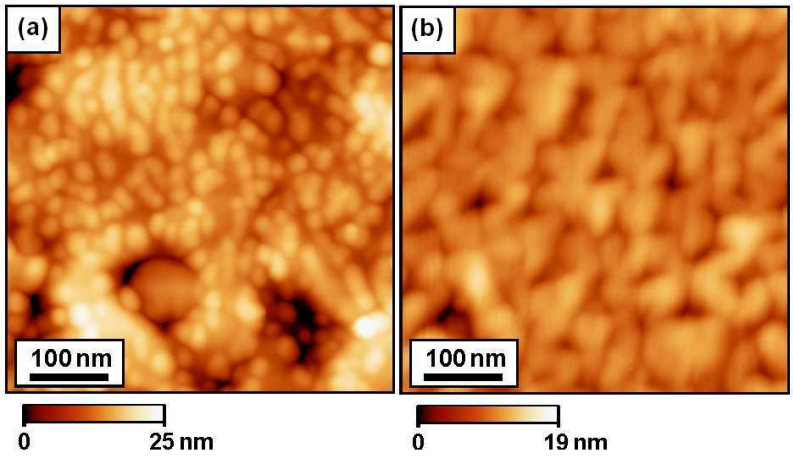

Figure 6.2: *AFM images of (a) GaN(11$\bar{2}$2) QDs synthesized by deposition of 5 ML of GaN and (b) a typical 200-nm-thick AlN(11$\bar{2}$2) layer.*

The structural properties of two semipolar GaN/AlN QD superlattices were further investigated using a combination of electron microscopy techniques to access information on the crystalline orientation of the dots and their shape. The samples consisted of 20 periods of GaN QDs embedded in 10-nm-thick AlN barriers, deposited on a ≈ 170-nm-thick AlN(11$\bar{2}$2) buffer layer. The nominal amount of GaN in the dot layers was equivalent to 5 and 10 monolayers of GaN. In the following, these two samples will be named as "A" and "B", respectively.

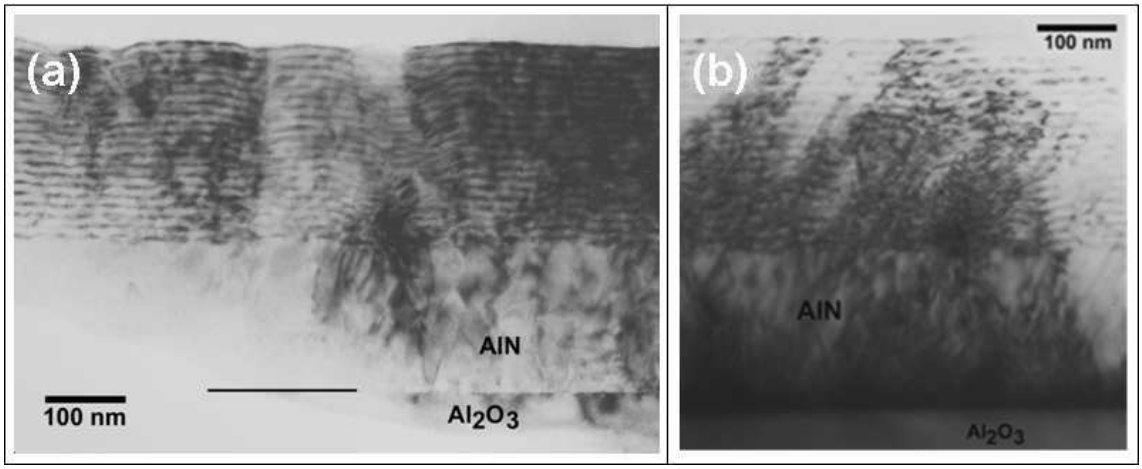

Figure 6.3: *Cross-sectional TEM images of the superlattice with 20 periods of nominally 5 ML GaN QDs embedded in 10-nm-thick AlN barriers (sample "A"), viewed along (a) $[\bar{1}\bar{1}23]_{layer}$ and (b) $[\bar{1}100]_{layer}$ axis.*

Figures 6.3(a) and (b) are cross-section TEM bright-field images showing the whole structure of a GaN/AlN QD superlattice with 5 ML of GaN in the QD layers, viewed along the $[\bar{1}\bar{1}23]_{layer}$ and $[\bar{1}100]_{layer}$ axis, respectively. The AlN(11$\bar{2}$2) buffer layer and the 20 periods are visible. In both images, we can see the same distortion

of the superlattice due to the defects as it was already observed in the QW structures (Fig. 5.3). In particular, the dominant defects are threading dislocations (TDs) and BSFs, emanating from the AlN/sapphire interface.

Figure 6.4 presents cross-section high-resolution TEM images taken on superlattices with nominally (a) 5 ML and (b) 10 ML of GaN in the QD layers. In these images, we can verify that the GaN islands present a good epitaxial relationship with the AlN matrix, keeping the same $(11\bar{2}2)$ crystallographic orientation. By comparing Figs. 6.4(a) and (b) we observe a significant enhancement of the QD height and diameter when increasing the amount of GaN in the QD layers. Another important feature is the presence of a wetting layer, clearly resolved in the sample with 5 ML of GaN. The wetting layer is not distinguished in the sample with 10 ML, due to the higher QD density.

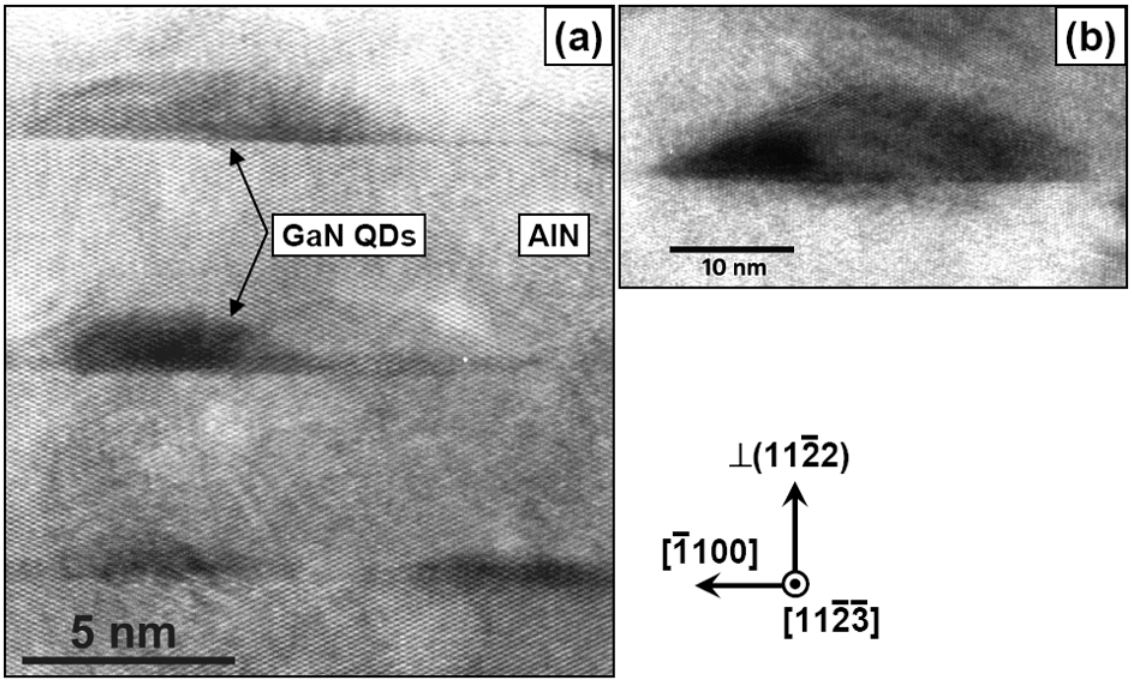

Figure 6.4: *High-resolution TEM images of $(11\bar{2}2)$-oriented GaN/AlN QDs synthesized by the deposition of (a) 5 ML and (b) 10 ML of GaN, viewed along $<11\bar{2}\bar{3}>_{layer}$ axis.*

The TEM image viewed along $[\bar{1}\bar{1}23]_{layer}$ in Fig. 6.5(a) provides information on the local atomic chemistry of the QD layers by Z-contrast imaging. Two different families of QDs are identified, as illustrated in the magnification in Fig. 6.5(b). The QDs sit either on the $(11\bar{2}2)$ or the $\{10\bar{1}1\}$ planes. We can see in Fig. 6.5(c) and (d) that both families of dots present the same crystallographic structure, both being $(11\bar{2}2)$-oriented in good epitaxial relationship with the matrix. This sort of "QD bimodality" should be related to a preferential $(10\bar{1}1)$ facet in the surface roughness. The vertical correlation of the QDs along the *c*-axis might be related to the same phenomenon.

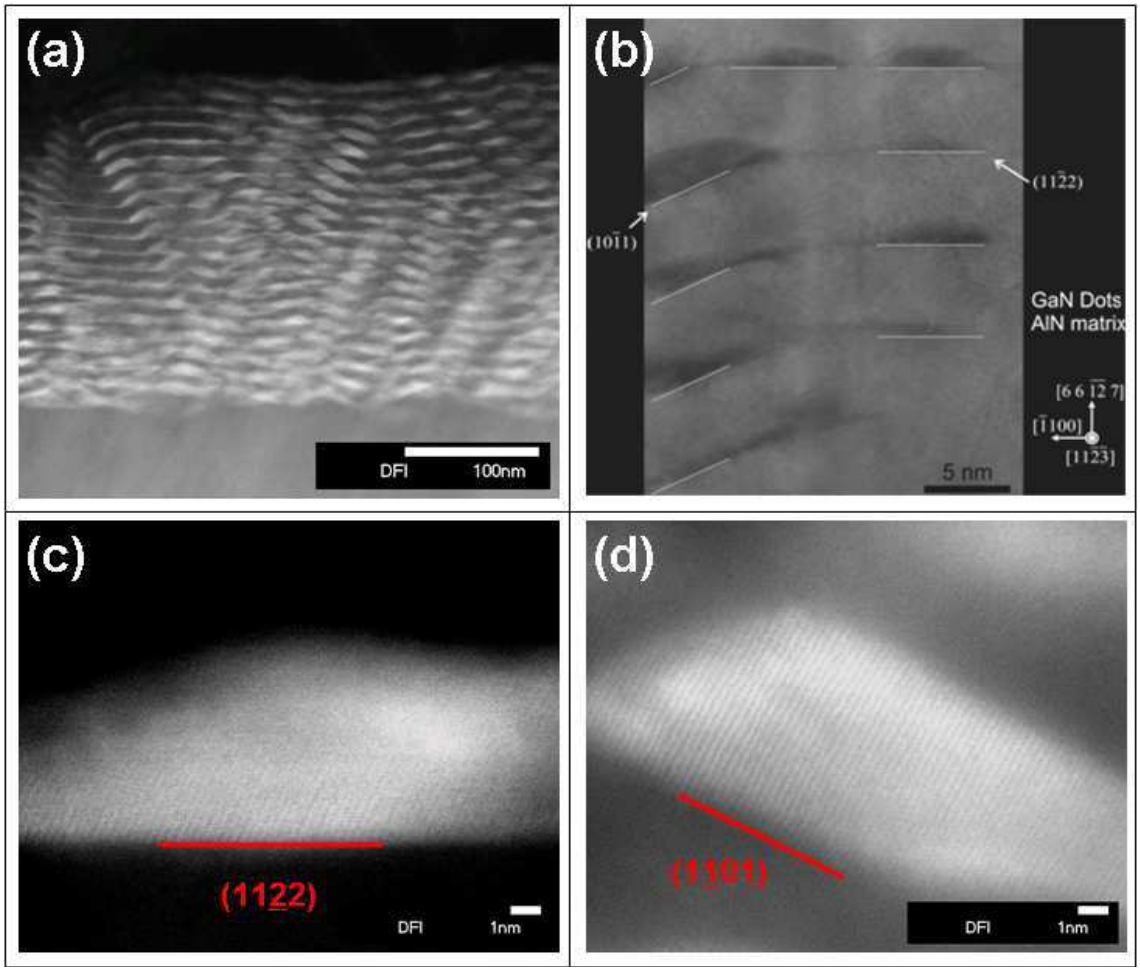

Figure 6.5: *(a) Z-contrast image of sample "A" viewed along the common $[\bar{1}\bar{1}23]_{layer}$ zone axis where we can observe the distribution of the QDs on two different families. (b) Cross-sectional TEM image, viewed along the $[\bar{1}\bar{1}23]_{layer}$ zone axis. The two growth planes of GaN QDs are identified to be (c) (11$\bar{2}$2) and (d) (10$\bar{1}$1).*

Z-contrast TEM images can provide information about the orientation of the facets of the dots. In Fig. 6.6(a), we present a plane view of a QD layer. First of all, we can see that there is no in-plane alignment of the dots, and that there is a certain dispersion in their size. The in-plane shape of the objects is nearly square. The measurements on an ensemble of dots gave in-plane angles ranging from 85° to 93°. Additionally, we can note that the dots have well defined facets, which becomes obvious in the cross-section view along $[\bar{1}\bar{1}23]$ in Fig. 6.6(b). Indeed, the QDs have (01$\bar{1}$1)- and (10$\bar{1}$1)-oriented facets, forming an angle of about 26° with the (11$\bar{2}$2) planes. It is interesting to note that the facets are the same preferential plane of the AlN surface roughness, which suggests a low surface energy of the (10$\bar{1}$1) plane close to stoichiometric conditions. When the structure is viewed along $[\bar{1}100]$, the dots are strongly asymmetric and the facets are the (11$\bar{2}$0) plane (forming an angle of 32° with the (11$\bar{2}$2) plane), and either the (11$\bar{2}$5) plane or the (11$\bar{2}$6) plane (forming an

angle of 25° and 30°, respectively). These QD facets are consistent with the RHEED observations: The reflections from the facets are asymmetric along the $<\bar{1}100>_{layer}$ azimuth [Fig. 6.1(a)], and symmetric along the $<11\bar{2}\bar{3}>_{layer}$ azimuth [Fig. 6.1(b)].

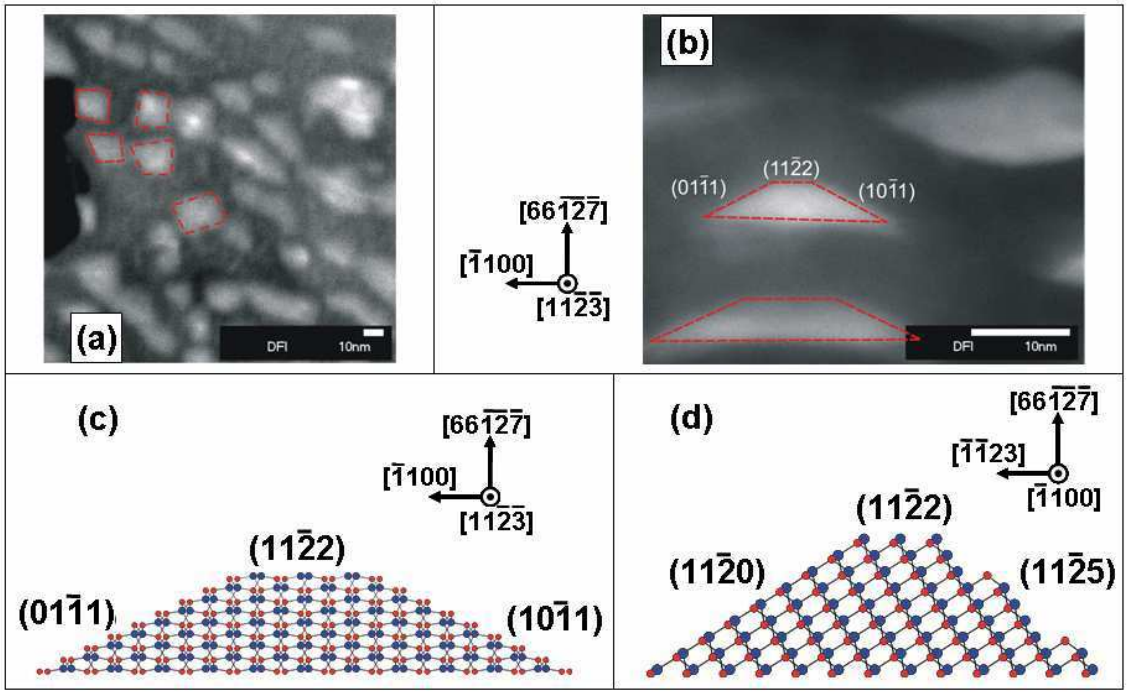

Figure 6.6: *STEM images of GaN QDs in AlN matrix. (a) Plane view image and (b) cross section view of along $[\bar{1}\bar{1}23]_{layer}$ zone axis. Modeling of the crystalline structure of (11$\bar{2}$2)-oriented QDs, viewed along (c) $[\bar{1}\bar{1}23]_{layer}$ and (d) $[\bar{1}100]_{layer}$ zone axis. The (10$\bar{1}$1) planes could also be the (10$\bar{1}$2) planes, and the (11$\bar{2}$5) planes could also be the (11$\bar{2}$6) planes.*

This structural analysis corroborates the interpretation of the RHEED patterns given in section 3.1.2. Indeed, we can verify that the diffraction patterns of the dots along the $<\bar{1}\bar{1}23>$ axis show symetric diffraction lines due to the symmetric $\{01\bar{1}1\}$-oriented facets of the dots. This planes are those generating the P_3 periodicity in Fig. 3.6. In the same way, we can identify, along the $<\bar{1}100>$ azimuth, the (11$\bar{2}$0) facet which is also the plane family generating the P_2 periodicity in Fig. 3.7.

6.3 Optical properties of (11$\bar{2}$2)-oriented QDs

The optical properties of the QDs superlattices were investigated by PL and TRPL measurements.

Figure 6.7 presents the low temperature (T = 7 K) PL spectra from samples with 20 periods of nominally 3 ML, 5 ML, 8 ML and 10 ML of GaN QDs embedded in 10-nm-thick AlN barriers. As a result of the quantum confinement, the PL peak energy shifts to higher energies when the amount of GaN in the QDs is decreased. The full width at half maximum (FWHM) is in the range of 265 meV to 105 meV,

which is comparable to the values obtained from *c*- and *m*-oriented GaN/AlN QDs [Ams08, Gui06]. However, in contrast to results obtained for polar GaN/AlN QDs [Sim03], the PL energy peak remains systematically above the GaN band gap. As described for the semipolar QWs, this attests the reduction of the QCSE in semipolar QDs.

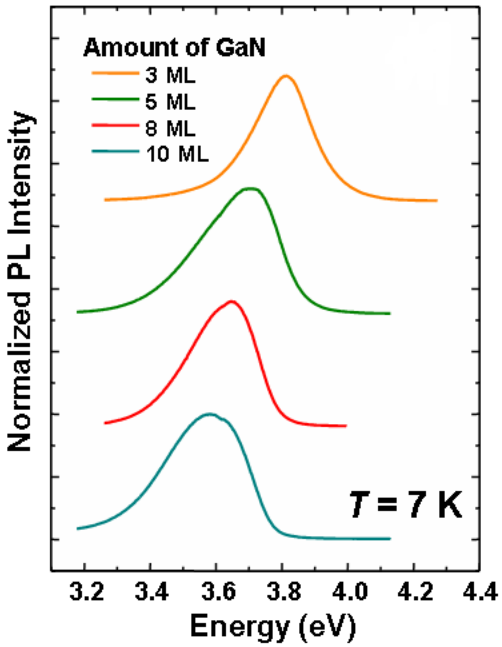

Figure 6.7: *Low temperature PL spectra from 20 periods of GaN/AlN QD stacks with the amount of GaN deposited in the QD layers varying from 3 ML to 10 ML.*

The attenuation of the electric field in the semipolar QDs is further confirmed by time-resolved PL measurements, illustrated in Fig. 6.8(a). The measured decay times are in the range of 350 to 500 ps. These decay times are slightly longer than those from the *a*-plane GaN/AlN QDs presented in Ref. [Fou07] (around 250 ps) because the reported nonpolar emission occurs at higher energies (smaller dots). However, they are one order of magnitude shorter than those measured on polar QDs with similar height, due to the strong attenuation of the electric field [Sim03].

The thermal stability of the luminescence of the samples has been studied. Figure 6.9 presents the evolution of the PL intensity versus temperature. To compare the intensity drop with semipolar multi-QW structures, we have chosen QD and QW samples with PL peak at the same energy ($\approx$ 3.65 eV). We compare the sample with nominally 5 ML of GaN in the QDs to the GaN/AlN (1.7 nm / 5 nm) multi-QW structure studied in the previous chapter. The PL intensity of the QD sample drops by a factor of $\approx$10 between T = 5 K and room temperature, whereas it drops by a factor of $\approx$100 for the QW sample. This improved thermal stability in the QDs is an indication of the 3D carrier confinement in the dots, which makes them relatively insensitive to defects in the surrounding matrix. On the contrary, the carrier recombination in QWs is much more sensitive to the defects present in the

layers, which act as non radiative recombination centers.

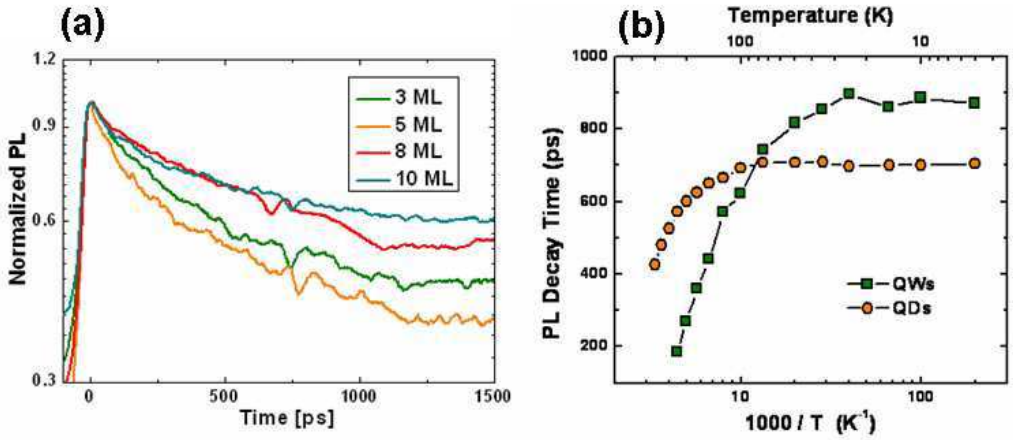

Figure 6.8: *(a) Time-resolved PL measurements of the semipolar GaN/AlN QD stacks with different nominal amount of GaN recorded at T = 5 K. (b) Comparison of the evolution of the decay time with the temperature for both a QD and a QW superlattice.*

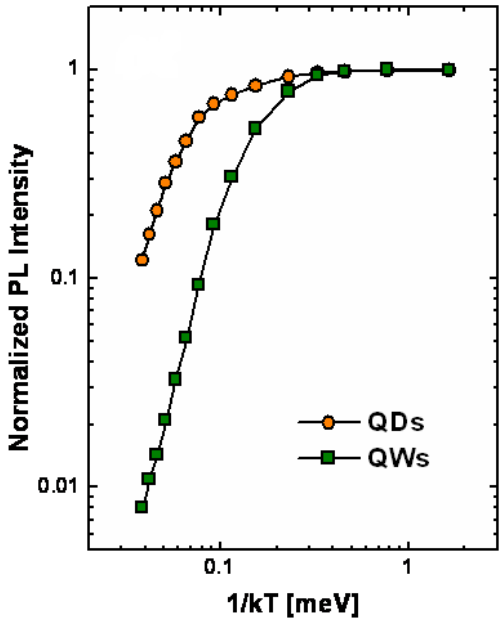

Figure 6.9: *Evolution of the PL intensity with the temperature in semipolar GaN/AlN multi-QD and multi-QW structures, both emitting at ≈ 3.65 eV.*

The thermal evolution of the PL intensity is consistent with the graph in Fig. 6.8(b), which compares the evolution of the decay times of these two samples with temperature. Whereas the QW decay time rapidly decreases for temperatures above ≈ 35 K, the decay time of the QDs remains stable until 80 to 100 K. We can compare these results with those obtained for *a*-plane QDs, where the decay times of QWs and QDs are equivalent and start to decrease around 80 - 100 K [Fou07]. The

enhanced thermal stability of the nonpolar QWs might be attributed to the presence of additional localization centers in the wells, probably related to the presence of defects or thickness fluctuations [Fou07]. In the case of semipolar systems we observe a strong difference in the behavior of QDs and QWs, which a lateral delocalization of the carriers in the QWs, and therefore a lower density of structural defects in comparison to *a*-plane QWs.

Finally, we found an interesting feature of these semipolar QD structures when looking at the dependence of PL peak energy with temperature. As illustrated in Fig. 6.10, the evolution of the luminescence energy presents an S-shape between room temperature and $T = 7$ K. Besides, if we compare the samples with nominally 3 ML, 5 ML and 8 ML of GaN in the QD layers, we can observe that this energy shift increases with the amount of GaN. This behavior might be attributed to the thermalization of the carriers from big dots to smaller dots. Another possible interpretations stem for their thermalization towards excited electronic levels or to transition involving first bound excitons and then free excitons.

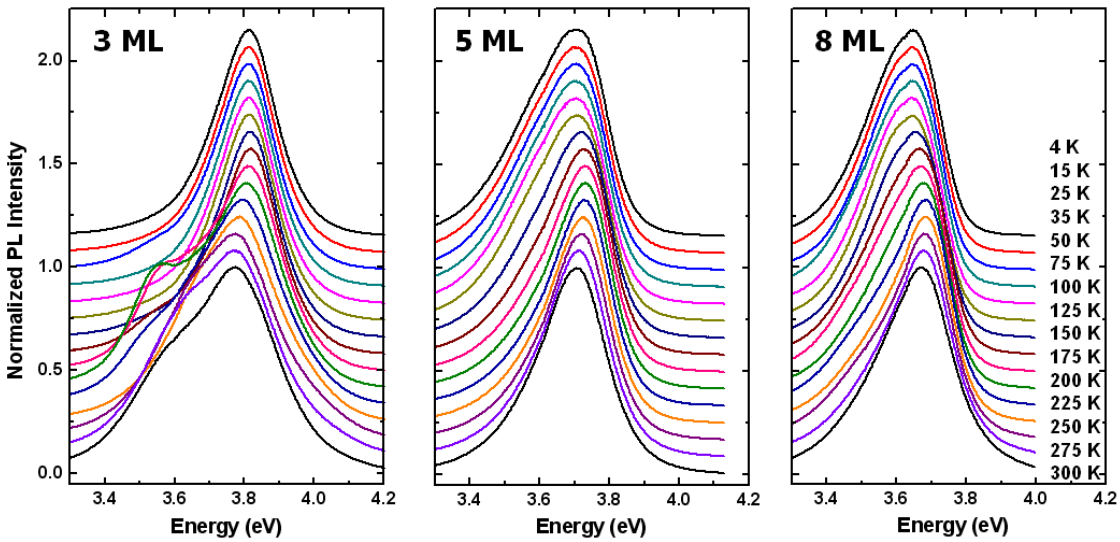

Figure 6.10: *Evolution with temperature of the PL emission from QD structures with nominally 3 ML, 5 ML and 8 ML of GaN in the dot layers*

6.4 Conclusions

We have demonstrated the growth of $(11\bar{2}2)$-oriented GaN QDs on AlN$(11\bar{2}2)$ by deposition of a thin 2D GaN layer under slightly Ga-rich conditions, followed by a growth interruption in vacuum.

High resolution TEM images confirm the $(11\bar{2}2)$ orientation of the dots, but show two types of QDs, sitting either on the $(11\bar{2}2)$ or the $(10\bar{1}1)$ plane of AlN. The dominant QD morphology is that of a truncated tetragonal pyramid with chemically sharp interfaces. When viewed along the $<11\bar{2}\bar{3}>$ zone axis of the superlattice, the

dots have $(10\bar{1}1)$-oriented symmetric facets, whereas they are highly asymmetric along the $<\bar{1}100>$ zone axis, one facet being the $(11\bar{2}0)$ a-planes and the other $(11\bar{2}5)$ planes. The QDs present a tendency to correlate vertically along the c-axis, inclined with respect to the growth direction.

As in the case of $(11\bar{2}2)$-oriented QWs, the comparison of the PL emission of QD superlattices with different nominal amount of GaN shows no evidence of the typical redshift expected in polar structures: The PL lines remain above the GaN bandgap, as a confirmation of the QCSE attenuation. The second evidence of the reduction of the internal electric field lies in the short decay times measured by TRPL measurements.

Finally, the thermal evolution of the PL intensity and PL decay time demonstrates an enhanced carrier confinement and reduced non radiative recombination sensitivity of the QDs in comparison to QWs.

Conclusions and perspectives

The main objective of this work was to study the growth of $(11\bar{2}2)$-oriented III-nitrides thin films and nanostructures, in order to assess their optical and structural properties in comparison with those of polar and nonpolar structures and thus their potential performance in terms of applications.

Conclusions

The growths mechanisms of AlN and GaN depend strongly on the crystalline orientation. Chronologically, the manuscript starts with the description of AlN since it serves as a buffer layer for all the samples, in order to settle the $(11\bar{2}2)$ crystallographic orientation.

AlN deposited on m-sapphire arranges into two main crystalline orientation domains, AlN$(11\bar{2}2)$ and AlN$(10\bar{1}0)$. Therefore, the main challenge of AlN growth lies in the isolation of the $(11\bar{2}2)$ orientation from the parasitic $(10\bar{1}0)$ domains, whose ratio decreases with decreasing III/V ratio and increasing layer thickness. By proper adjustment of the III/V ratio around 0.95 and for layers thicker than 90 nm, we managed to isolate the semipolar orientation: Traces of non polar AlN$(10\bar{1}0)$ domains can be found, but they remain at the interface with the substrate, being rapidly encapsulated by the AlN$(11\bar{2}2)$ matrix. Under these conditions, the layers grow two-dimensional, and both XRD and RHEED studies attest full strain relaxation after deposition of 260 nm. These growth conditions are very different from those of polar and nonpolar AlN, which should be synthesized under Al-rich conditions to be two-dimensional.

The epitaxial relationships between AlN and m-sapphire for both the semipolar and the nonpolar phase where identified: AlN$(10\bar{1}0)$ is twisted by 90° from the substrate, so that $[0001]_{AlN}$ // $[\bar{1}\bar{1}20]_{sapphire}$. For AlN$(11\bar{2}2)$, we found that $[1\bar{1}00]_{AlN}$ // $[\bar{1}\bar{1}20]_{sapphire}$ and $[\bar{1}\bar{1}23]_{AlN}$ // $[0001]_{sapphire}$. Additionally, images show a good interface between the two AlN orientations, with $(0002)_{semipolar}$ // $(01\bar{1}0)_{nonpolar}$ planes and $(0002)_{nonpolar}$ // $(\bar{1}100)_{semipolar}$ planes.

The growth of GaN directly on m-sapphire leads to a GaN$(11\bar{2}2)$ matrix with $\{10\bar{1}3\}$ precipitates. An AlN$(11\bar{2}2)$ buffer layer deposited on m-sapphire prior to the growth of GaN makes it possible to reduce the $\{10\bar{1}3\}$-orientation, so that the GaN$(11\bar{2}2)$ layer grows epitaxially on the AlN. Regarding the III/V ratio, N-rich

conditions lead to three-dimensional growth, whereas Ga-rich conditions tend to flatten the surface. A study of the Ga wetting of the GaN(11$\bar{2}$2) surface shows that the maximum Ga coverage that can be stabilized on the surface during the growth is one (11$\bar{2}$2)-oriented monolayer of Ga atoms. The atomic arrangement of this Ga monolayer forms a pseudo-bilayer (atoms distributed in two levels along the growth axis), which can be compared to the bilayer observed on top of GaN(0001) or GaN(1$\bar{1}$00) surfaces. GaN layers grown with a Ga-excess high enough to form the self-regulated Ga monolayer exhibit the best surface morphology (RMS roughness lower than 1.5 nm), with minimized amount of GaN(10$\bar{1}$3). The study of the photoluminescence behavior attributes the main emission to excitons bound to stacking faults, which are present with a density around 3×10^5 cm^{-1} in the layers.

Si-doping barely affects the growth kinetics of GaN neither its structural properties. On the contrary, Mg-doping inhibits the formation of the self-regulated Ga monolayer during the growth, so that the accumulation regime is reached for lower impinging Ga fluxes than for undoped GaN. Consequently, the surface morphology of GaN-Mg doped layers is altered, even if, in volume, no evidence of inversion domains or cubic inclusions, typically found in Mg-doped GaN(0001) have been observed. We have achieved homogeneous Mg incorporation up to 10^{20} cm^{-3} and demonstrated that Mg incorporation in semipolar GaN is enhanced in comparison to the usual GaN(0001). We measured a dopant activation of 4%, leading to holes concentrations in the range of 10^{18} cm^{-3}.

By applying the growth conditions identified for two-dimensional AlN and GaN, we have synthesized QW heterostructures displaying sharp interfaces between the materials. Time-integrated and time-resolved photoluminescence studies confirm a significant reduction of the QCSE, in comparison with polar structures. The experimental results in the semipolar MQWs are consistent with simulations of the electronic structure, which predict an internal electric field between 0.6 MV/cm and -0.55 MV/cm, depending on the strain state of the superlattice. Finally, we have shown the first demonstration of intersubband absorption in semipolar MQW structures. The reduction of the internal electric field results in a red shift of the intersubband absorption transitions with respect to polar materials.

The growth of GaN/AlN QDs is achieved by the deposition of a few 2D GaN monolayers under slightly Ga-rich conditions followed by an interruption under vacuum. High-resolution TEM images confirm the (11$\bar{2}$2) orientation of the QDs, and show that they sit either on the (11$\bar{2}$2) or the (10$\bar{1}$1) plane of AlN. Their dominant morphology is that of a truncated tetragonal pyramid with chemically sharp interfaces. The QDs present a tendency to correlate vertically along the *c*-axis, inclined with respect to the growth direction. Semipolar GaN/AlN QD superlattices synthesized by this method display a strong reduction of the internal electric fields in comparison with polar structures.

Perspectives

Judging by the increasing number of groups involved in the research on the $(11\bar{2}2)$ orientation within the last three years, several perspectives should be addressed, both from an academic point of view, and for potential applications.

In terms of growth optimization, there are certain issues that should still be addressed. Particularly, the nucleation process of AlN on *m*-sapphire and the strain relaxation mechanisms should be analyzed in more detail. Along these lines, an interesting feature of AlN and GaN semipolar layers is the presence of a misorientation of their $<11\bar{2}\bar{3}>$ axis relatively to the <0001> axis of sapphire, which is larger for AlN than for GaN. The origin of this tilt is under investigation. Some hypothesis tend to explain it as a consequence of the misfit accommodation along the $<11\bar{2}\bar{3}>$ direction. In this sense, it would be interesting to study the growth of AlN on *m*-sapphire substrates with a certain miscut in the <0001> direction.

Semipolar GaN layers still present a density of defects twice higher than polar materials, which is a major drawback for the fabrication of high performance components. With the motivation to reduce the amount of defects density, we have a collaboration to use MOVPE and HVPE grown GaN$(11\bar{2}2)$ templates as the substrates, which should also improve the surface quality. Moreover, in the last year $(11\bar{2}2)$-oriented GaN templates have been introduced in the market, as an indication of the growing interest in these materials.

Beyond the understanding of new physical phenomena, semipolar nitrides are promising materials for the fabrication of optoelectronic devices. We can mention the demonstration of HVPE growth of thick semipolar layers by the group of S. Nakamura at the University of California at Santa Barbara, and the fabrication of yellow LEDs with efficiency higher than commercial devices made of phosphide materials. In this context, the know-how of this work will be useful for the synthesis of the nanostructures used as active media in optoelectronic components. In addition, we have started the growth of $(11\bar{2}2)$-oriented AlGaN layers, with 30% and 50% of Al content. The study of ternary alloys, AlGaN and InGaN, will become a priority, and parrallel developements of technological process will be held for the integration of thin films and nanostructures in devices.

Bibliography

[Ade02] H. C. Adelmann, *Growth and strain relaxation mechanisms of group III-nitride heterostructures*. Ph.D. thesis, Université Joseph Fourier - Grenoble 1 (2002).

[Ade03] C. Adelmann, J. Brault, G. Mula, B. Daudin, L. Lymperakis, and J. Neugebauer, *Gallium adsorption on (0001) GaN surfaces.* Physical Review B **67**, 165419 (2003).

[Aka07] I. Akasaki, *Key inventions in the history of nitride-based blue LED and LD*. Journal of Crystal Growth **300**, 2 (2007).

[Ama89] H. Amano, M. Kito, K. Hiramatsu, and I. Akasaki, *P-type conduction in Mg-doped GaN treated with low-energy electron beam irradiation (LEEBI)*. Japanese Journal of Applied Physics **28**, L2112 (1989).

[Amb98] O. Ambacher, *Growth and applications of Group III-nitrides*. Journal of Physics D: Applied Physics **31**(20), 2653 (1998).

[Amb00] O. Ambacher, B. Foutz, J. Smart, J. R. Shealy, N. G. Weimann, K. Chu, M. Murphy, A. J. Sierakowski, W. J. Schaff, L. F. Eastman, R. Dimitrov, A. Mitchell, and M. Stutzmann, *Two dimensional electron gases induced by spontaneous and piezoelectric polarization in undoped and doped AlGaN/GaN heterostructures*. Journal of Applied Physics **87**, 334 (2000).

[Ams07] B. Amstatt, J. Renard, C. Bougerol, E. Bellet-Amalric, B. Gayral, and B. Daudin, *Growth of m-plane GaN quantum wires and quantum dots on m-plane 6H-SiC*. Journal of Applied Physics **102**, 074913 (2007).

[Ams08] B. Amstatt, *Croissance d'hétérostructures non-polaires de GaN/AlN plan m sur 6H-SiC plan m*. Ph.D. thesis, Université Joseph Fourier - Grenoble 1 (2008).

[And86] D. A. Anderson and N. Apsley, *The Hall effect in III-V semiconductor assessment*. Semiconductor Science Technology **1**, 187 (1986).

[Art68] J. R. Arthur, *Interaction of Ga and As_2 molecular beams with GaAs surfaces*. Journal of Applied Physics **39**(8), 4032 (1968).

[As97] D. J. As, F. Schmilgus, C. Wang, B. Schottker, D. Schikora, and K. Lischka, *The near band edge photoluminescence of cubic GaN epilayers.* Applied Physics Letters **70**(10), 1311 (1997).

[Bak05] T. J. Baker, B. A. Haskell, F. Wu, P. T. Fini, J. S. Speck, and S. Nakamura, *Characterization of Planar Semipolar Gallium Nitride Films on Spinel Substrates.* Japanese Journal of Applied Physics **44**, L920 (2005).

[Bak06] T. J. Baker, B. A. Haskell, F. Wu, J. S. Speck, and S. Nakamura, *Characterization of Planar Semipolar Gallium Nitride Films on Sapphire Substrates.* Japanese Journal of Applied Physics **45**, L154 (2006).

[Ber97] F. Bernardini, V. Fiorentin, and D. Vanderbilt, *Spontaneous polarization and piezoelectric constants of III-V nitrides.* Physical Review B **56**(16), R10024 (1997).

[Ber98] F. Bernardini and V. Fiorentin, *Macroscopic polarization and band offsets at nitride heterojunctions.* Physical Review B **57**(16), R9427 (1998).

[Bin86] G. Binnig, C. Quate, and C. Gerber, *Atomic force microscope.* Physical Review Letter **56**(9), 930 (1986).

[Blo74] S. Bloom, G. Harbeke, E. Meier, and I. Ortenbur, *Band-structure and reflectivity of GaN.* Physica Status Solidi B-Basic Research **66**(1), 161 (1974).

[Boe03] S. Boeck, A. Dick, C. Freysoldt, F. Grzegorzewski, T. Hammerschmidt, L. Ismer, L. Lymperakis, and M. Wahn, *SFHIngX Users Guide* (S. Boeck and J. Neugebauer, Berlin, 2003).

[Bon60] W. L. Bond, *Precision lattice constant determination.* Acta Crystallographica **13**, 814 (1960).

[Bow] K. Bowen and B. K. Tanner, *High resolution X-ray diffractometry and topography.*

[Bro04] J. Brown, F. Wu, P. M. Petroff, and J. S. Speck, *GaN quantum dot density control by rf-plasma molecular beam epitaxy.* Applied Physics Letter **84**, 690 (2004).

[Cae07] C. Caetano, L. K. Teles, M. Marques, A. D. Pino, and L. G. Ferreira, *Theoretical support for the smaller band gap bowing in wurtzite InGaN alloys.* AIP Conference Proceeding **893**, 257 (2007).

[Cal97] F. Calle, F. J. Sanchez, J. M. G. Tijero, M. A. Sanchez-Garcia, E. Calleja, and R. Berenford, *Exciton and donor-acceptor recombination in undoped GaN on Si(111).* Semiconductor Science Technology **12**, 1396 (1997).

[Cha04] V. Chamard, T. Schülli, M. Sztucki, T. H. Metzger, E. Sarigiannidou, J.-L. Rouvière, M. Tolan, C. Adelmann, and B. Daudin, *Strain distribution in nitride quantum dot multilayers*. Physical Review B **69**, 125327 (2004).

[Cha05] A. Chakraborty, T. J. Baker, B. A. Haskell, F. Wu, J. S. Speck, S. P. DenBaars, S. Nakamura, and U. K. Mishra, *Miliwatt power blue InGaN/GaN Ligh-emitting diodes on semipolar GaN templates*. Japanese Journal of Applied Physics **44**, L954 (2005).

[Cha06] A. Chakraborty, B. A. Haskell, H. Masui, S. Keller, J. S. Speck, S. P. DenBaars, S. Nakamura, and U. K. Mishra, *Nonpolar m-plane blue-light-emitting diode lamps with output power of 23.5 mW under pulsed operation*. Japanese Journal of Applied Physics **45**, 739 (2006).

[Chi96] F. R. Chien, X. J. Ning, S. Stemmer, P. Pirouz, M. D. Bremser, and R. F. Davis, *Growth defects in GaN films on 6H–SiC substrates*. Applied Physics Letters **68**(19), 2678 (1996).

[Chi04] A. Chitnis, C. Chen, V. Adivarahan, M. Shatalov, E. Kuokstis, V. Mandavilli, J. Yang, and M. A. Khana, *Visible light-emitting diodes using a-plane GaN-InGaN multiple quantum wells over r-plane sapphire*. Applied Physics Letter **84**, 3663 (2004).

[Cho75a] A. Y. Cho, *Device fabrication by molecular beam epitaxy*. Electron Devices Meeting, 1975 International (1975).

[Cho75b] A. Y. Cho and J. R. Arthur, *Molecular beam epitaxy*. Progress in Solid State Chemistry **10**(157) (1975).

[Cht99] D. G. Chtchekine, Z. C. Feng, G. D. Gilliland, S. J. Chua, and D. Wolford, *Donor-hydrogen bound exciton in GaN*. Physical Review B **60**(23) (1999).

[Cla87] S. Clarke and D. D. Vvedensky, *Origin of reflection high-energy electron-diffraction intensity oscillations during molecular-beam epitaxy : a computational modeling approach*. Phys. Rev. Lett. **58**(21), 2235 (1987).

[Cra02] M. D. Craven, S. H. Lim, F. Wu, J. S. Speck, and S. P. DenBaars, *Structural characterization of nonpolar (11$\bar{2}$0) a-plane GaN thin films grown on (1$\bar{1}$02) r-plane sapphire*. Applied Physics Letter **81**, 469 (2002).

[Cra03] M. D. Craven, P. Waltereit, F. Wu, J. S. Speck, and S. P. DenBaars, *Characterization of a-Plane GaN/(Al,Ga)N Multiple Quantum Wells Grown via Metalorganic Chemical Vapor Deposition*. Japanese Journal of Applied Physics **42**, L253 (2003).

[Cra04] M. D. Craven, F.Wu, A. Chakraborty, B. Imer, U. K. Mishra, S. P. DenBaars, and J. S. Speck, *Microstructural evolution of a-plane GaN*

grown on a-plane SiC by metalorganic chemical vapor deposition. Applied Physics Letter **84**, 1281 (2004).

[Dam99] B. Damilano, N. Grandjean, F. Semond, J. Massies, and M. Leroux, *From visible to white light emission by GaN quantum dots on Si(111) substrate.* Applied Physics Letter **75**, 962 (1999).

[Dam07] B. Damilano, J. Brault, A. Dussaigne, and J. Massies, *Fabrication and performance of GaN electronic devices.* Images de la physique (2007).

[Dau97] B. Daudin, F. Widmann, G. Feuillet, Y. Samson, M. Arlery, and J. L. Rouvière, *Stranski-Krastanov growth mode during the molecular beam epitaxy of highly strained GaN.* Physical Review B **56**, 7069 (1997).

[Dau98] B. Daudin, G. Feuillet, J. Hübner, Y. Samson, F. Widmann, A. Phillipe, C. Bru-Chevallier, G. Guillot, E. Bustarret, G. Bentoumi, and A. Deneuville, *How to grow cubic GaN with low hexagonal phase content on (001) SiC by molecular beam epitaxy.* Journal of Applied Physics **84**, 2295 (1998).

[Deg98] C. Deger, E. Born, H. Angerer, O. Ambacher, M. Stutzmann, J. Hornsteiner, E. Riha, and G. Fischerauer, *Sound velocity of $Al_xGa_{1-x}N$ thin films obtained by surface acousticwave measurements.* Applied Physics Letter **72**(19), 2400 (1998).

[Dre95] M. Drechsler, D. M. Hoffman, B. K. Meyer, T. Detchprohm, H. Amano, and I. Akasaki, *Determination of the conduction band electron effective mass in hexagonal GaN.* Japanese Journal of Applied Physics Part 2 **34**(9B), 1178 (1995).

[Etz01] E. V. Etzkorn and D. R. Clarke, *Cracking of GaN films.* Journal of Applied Physics **89**(2), 1025 (2001).

[Fee02] R. M. Feenstra, J. E. Northrup, and J. Neugebauer, *Review of Structure of Bare and Adsorbate-Covered GaN(0001) Surfaces.* MRS Internet Journal of Nitride Semiconductor Research **7**, 3 (2002).

[Fic07] F. Fichter, *Über Aluminiumnitrid.* Z. Anorg. Chem. **54**, 332 (1907).

[Fio99] V. Fiorentini, F. Bernardini, F. D. Sala, A. D. Carlo, and P. Lugli, *Effects of macroscopic polarization in III-V nitride multiple quantum wells.* Physical Review B **60**(12), 8849 (1999).

[Fou05] S. Founta, F. Rol, E. Bellet-Amalric, J. Bleuse, B. Daudin, B. Gayral, H. Mariette, and C. Moisson, *Optical properties of GaN quantum dots grown on nonpolar (11$\bar{2}$0) SiC by molecular-beam epitaxy.* Applied Physics Letter **86**, 171901 (2005).

[Fou07] S. Founta, *Croissance d'hétérostructures GaN/AlN à champ électrique interne réduit.* Ph.D. thesis, Université Joseph Fourier - Grenoble 1 (2007).

[Fra49] F. C. Frank and J. H. V. der Merwe, *One-dimensional dislocations. II. Misfitting monolayers and oriented overgrowth.* Royal Society of London Proceedings Serie A **198**, 216 (1949).

[Fun06] M. Funato, M. Ueda, Y. Kawakami, Y. Narukawa, T. Kosugi, M. Takahashi, and T. Mukai, *Blue, Green, and Amber InGaN/GaN Light-Emitting Diodes on Semipolar $11\bar{2}2$ GaN Bulk Substrates.* Japanese Journal of Applied Physics **45**, L659 (2006).

[Gar05] N. F. Gardner, J. C. Kim, J. J. Wierer, Y. C. Shen, and M. R. Krames, *Polarization anisotropy in the electroluminescence of m-plane InGan/GaN multiple-quantum-well light-emitting diodes.* Applied Physics Letter **86**(11), 111101 (2005).

[Geh05] S. Gehrsitz, H. Sigg, N. Herres, K. Bachem, K. Kohler, , and F. K. Reinhart, *Compositional dependence of the elastic constants and the lattice parameter of $Al_xGa_{1-x}As$.* Physical Review B **60**, 11601 (2005).

[Geo01] A. Georgakilas, S. Mikroulis, V. Cimalla, M. Zervos, A. Kostopoulos, P. Komninou, T. Kehagias, and T. Karakostas, *Effects of the Sapphire Nitridation on the Polarity and Structural Properties of GaN Layers Grown by Plasma-Assisted MBE.* Physica Status Solidi (a) **188**(2), 567 (2001).

[Gog04] N. Gogneau, E. Sarigiannidou, E. Monroy, S. Monnoye, H. Mank, and B. Daudin, *Surfactant effect of gallium during the growth of GaN on AlN($000\bar{1}$) by plasma-assisted molecular beam epitaxy.* Applied Physics Letter **85**, 1421 (2004).

[Gra03] T. Graf, S. T. B. Goennenwein, and M. S. Brandt, *Prospects for carrier-mediated ferromagnetism in GaN.* Physica Status Solidi (b) **239**, 277 (2003).

[Gui06] F. Guillot, E. Bellet-Amalric, E. Monroy, M. Tchernycheva, L. Nevou, L. Doyennette, F. H. Julien, L. S. Dang, T. Remmele, M. Albrecht, T. Shibata, and M. Tanaka, *Si-doped GaN/AlN quantum dot superlattices for optoelectronics at telecommunication wavelengths.* Journal of Applied Physics **100**, 044326 (2006).

[Guo94] Q. Guo and A. Yoshida, *Temperature dependence of band gap change in InN and AlN.* Japanese Journal of Applied Physics **33**, 2453 (1994).

[Hau02] E. Haus, I. P. Smorchkova, B. Heying, P. Fini, C. Poblenz, T. Mates, U. K. Mishra, and J. S. Speck, *The role of growth conditions on the p-doping*

of GaN by plasma-assisted molecular beam epitaxy. Journal of Crystal Growth **246**, 55 (2002).

[Her02] N. Herres, L. Kirste, H. O. K. Kohler, J. Wagner, and P. Koidl, *X-ray determination of the composition of partially strained group-III nitride layers using the Extended Bond Method.* Material Science and Engineering **B91-92**, 425 (2002).

[Hey96] B. Heying, X. H. Wu, S. Keller, Y. Li, D. Kapolnek, B. P. Keller, S. P. D. Baars, and J. S. Speck, *Role of threading dislocation structure on the x-ray diffraction peak widths in epitaxial GaN films.* Applied Physics Letter **68**(643) (1996).

[Hey00a] B. Heying, R. Averbeck, L. F. Chen, E. Haus, H. Riechert, and J. S. Speck, *Control of GaN surface morphologies using plasma-assisted molecular beam epitaxy.* Journal of Applied Physics **88**, 1885 (2000).

[Hey00b] B. Heying, I. Smorchkova, C. Poblenz, C. Elsass, P. Fini, S. D. Baars, U. Mishra, and J. S. Speck, *Optimization of the surface morphologies and electron mobilities in GaN grown by plasma-assisted molecular beam epitaxy.* Applied Physics Letter **77**, 2885 (2000).

[Hir91] K. Hiramatsu, S. Itoh, H. Amano, I. Akasaki, N. Kuwano, T. Shiraishi, and K. Oki, *Growh mechanism of GaN grown on sapphire with AlN buffer layer by MOVPE.* Journal of Crystal Growth **115**(1-4), 628 (1991).

[Im97] J. S. Im, A. Moritz, F. Steuber, V. Haerle, F. Scholtz, and A. Hangleiter, *Radiative carrier lifetime, momentum matrix element and hole effective mass in GaN.* Applied Physics Letter **70**(5), 631 (1997).

[Iwa97] K. Iwata, H. Asahi, K. Asami, R. Kuroiwa, and S. Gonda, *Growth and applications of Group III-nitrides.* Japanese Journal of Applied Physics **36**, L661 (1997).

[Joh32] W. C. Johnston, J. B. Parsons, and M. C. Crew, *Nitrogen compound of Gallium.* Journal of Physics and Chemistry **234**, 2651 (1932).

[Joy86] B. A. Joyce, P. J. Dobson, J. H. Neave, J. Zhang, P. K. Larsen, and B. Boelger, *RHEED studies of heterojunction and quantum well formation during MBE growth — from multiple scattering to band offsets.* Surf. Sci. **168**(1-3), 423 (1986).

[Kam05] S. Kamiyama, A. Honshio, T. Kitano, M. Iwaya, H. Amano, I. Akasaki, H. Kinoshita, and H. Shiomi, *GaN growth on (30$\bar{3}$8) 4H-SiC substrate for reduction of internal polarization.* Physica Status Solidi C **2**(7), 2121 (2005).

[Kan08] P. K. Kandaswamy, F. Guillot, E. Bellet-Amalric, E. Monroy, L. Nevou, M. Tchernycheva, A. Michon, F. H. Julien, E. Baumann, F. R. Giorgetta, D. Hofstetter, T. Remmele, M. Albrecht, S. Birner, and L. S. Dang, *GaN/AlN short-period superlattices for intersubband optoelectronics: A systematic study of their epitaxial growth, design, and performance*. Journal of Applied Physics **104**, 093501 (2008).

[Kap95] D. Kapolnek, X. H. Wu, B. Heying, S. Keller, B. P. Keller, U. K. Mishra, S. P. DenBaars, and J. S. Speck, *Structural evolution in epitaxial metalorganic chemical vapor deposition grown GaN films on sapphire*. Applied Physics Letters **67**(11), 1541 (1995).

[Kim96] K. Kim, W. R. L. Lambrecht, and B. Segall, *Elastic constants and related properties of tetrahedrally bonded BN, AlN, GaN, and InN*. Physical Review B **53**(24), 16310 (1996).

[Kim97] K. Kim, W. R. L. Lambrecht, B. Segall, and M. V. Schilfgaarde, *Effective masses and valence band splittings in GaN and AlN*. Physical Review B **56**(12), 7363 (1997).

[Kit86] C. Kittel, *Introduction to solid state physics* (Wiley, New York, 1986).

[Kob03] G. Koblmueller, R. Averbeck, L. Geelhaar, H. Riechert, W. Hosler, and P. Pongratz, *Growth diagram and morphologies of AlN thin films grown by molecular beam epitaxy.* Journal of Applied Physics **93**, 9591 (2003).

[Koz00] P. Kozodoy, H. Xing, S. P. D. Baars, U. K. Mishra, A. Saxler, R. Perrin, S. Elhamri, and W. C. Mitchel, *Heavy doping effects in Mg-doped GaN*. Journal of Applied Physics **87**(4), 1832 (2000).

[Kuo01] Y.-K. Kuo, W.-W. Lin, and J. Lin, *Band-Gap Bowing Parameter of the $In_xGa_{1-x}N$ Derived From Theoretical Simulation*. Japanese Journal of Applied Physics **40**(Part 1, No. 5A), 3157 (2001).

[Kuo02] Y.-K. Kuo and W.-W. Lin, *Band-Gap Bowing Parameter of the $Al_xIn_{1-x}N$ Derived from Theoretical Simulation*. Japanese Journal of Applied Physics **41**(Part 1, No. 9), 5557 (2002).

[Lah07] L. Lahourcade, E. Bellet-Amalric, E. Monroy, and a. P. R. M. Abouzaid, *Plasma-assisted molecular-beam epitaxy of AlN(11$\bar{2}$2) on m-sapphire*. Applied Physics Letter **90** (2007).

[Lah08a] L. Lahourcade, P. K. Kandaswamy, J. Renard, P. Ruterana, H. MAchhadani, M. Tchernycheva, F. H. Julien, B. Gayral, and E. Monroy, *Interband and intersubband optical characterization of semipolar (11$\bar{2}$2)-oriented GaN/AlN multiple-quantum-well structures*. Applied Physics Letter **93**, 111906 (2008).

[Lah08b] L. Lahourcade, J. Renard, B. Gayral, E. Monroy, M. Chauvat, and P. Ruterana, *Ga kinetics in plasma-assisted molecular-beam epitaxy of GaN(11$\bar{2}$2): Effect on the structural and optical properties*. Journal of Applied Physics **103**, 093514 (2008).

[Lah09] L. Lahourcade, S. Valdueza-Felip, T. Kehagias, G. P. Dimitrakopulos, P. Komninou, and E. Monroy, *Stranski-Krastanow growth of (11$\bar{2}$2) oriented GaN/AlN quantum dots*. Applied Physics Letter **94**, 111901 (2009).

[Lee99] S. R. Lee, A. F. Wright, M. H. Crawford, G. A. Petersen, J. Han, R. M. Han, and R. M. Biefeld, *The band-gap bowing of Al_xGa_{1-x}, N alloys*. Applied Physics Letter **74**, 3344 (1999).

[Ler99] M. Leroux, N. Grandjean, B. Beaumont, G. Nafat, F. Semond, J. Massies, and P. Gibart, *Temperature quenching of photoluminescence intensities in undoped and doped GaN*. Journal of Applied Physics **86**, 3721 (1999).

[Li97] Y. Li, Y. Lu, H. Shen, M. Wraback, M. G. Brown, M. Schurman, L. Koszi, and R. A. Stall, *Temperature dependence of energy band gap in GaN thin film studied by thermomodulation*. Applied Physics Letter **70**, 2458 (1997).

[Lio05] B.-T. Liou, S.-H. Yen, Y.-K. Kuo, J. quan Yao, Y. J. Chen, and S. Lee, *Vegard's law deviation in band gaps and bowing parameters of the wurtzite III-nitride ternary alloys*. Semiconductor Lasers and Applications II **5628**(1), 296 (2005).

[Liu02] L. Liu and J. H. Edgar, *Substrates for gallium nitride epitaxy*. Material Science and Engineering R **37** (2002).

[Liu05] R. Liu, A. Bell, F. A. Ponce, C. Q. Chen, J. W. Yang, and M. A. Khan, *Luminescence from stacking faults in gallium nitride*. Applied Physics Letter **86**, 021908 (2005).

[Los01] M. Losurdo, P. Capezzuto, G. Bruno, G. Namkoong, W. Doolittle, and A. Brown, *The Chemistry of Sapphire Nitridation in Relation to the GaN Structural Quality: Why Low Temperature 200°C Nitridation?* Physica Status Solidi (a) **188**(2), 561 (2001).

[Lym08] L. Lymperakis and J. Neugebauer, *Ab initio study of Thermodynamics and adatom kinetics on non-polar GaN surfaces: Consequences on the growth morphology and the formation of nanowires*. Max Planck Society (Germany) (2008).

[Lym09] L. Lymperakis and J. Neugebauer, *Large anisotropic adatom kinetics on nonpolar GaN surfaces: Consequences for surface morphologies and nanowire growth*. Physical Review B **79**, 241308 (2009).

[Mah90] J. E. Mahan, K. M. Geib, G. Y. Robinson, and R. G. Long, *A review of the geometrical fundamentals of reflection high-energy electron diffraction with application to silicon surfaces*. Journal of Vacuum Science Technology A of Applied Physics **8**(5), 3692 (1990).

[Man71] H. M. Manasevit, F. M. Erdmann, and W. I. Simpson, *The use of metalorganics in the preparation of semicondutor materials*. Journal of Electrochemistry Society **118**, 1864 (1971).

[Mar71] H. P. Maruska and J. J. Tietjen, *The preparation and properties of vapor-deposited single-crystalline GaN*. Applied Physics Letter **15**, 327 (1971).

[Mas05] M. Mastroa, O. Kryliouka, T. Andersona, A. Davydovb, and A. Shapirob, *Influence of polarity on GaN thermal stability*. Journal of Crystal Growth **274**(38), 646 (2005).

[McL06] M. McLaurin, T. E. Mates, F. Wu, and J. S. Speck, *Growth of p-type and n-type m-plane GaN by molecular beam epitaxy*. Journal of Applied Physics **100** (2006).

[McN93] L. E. McNeil, M. Grimsditch, , and R. H. French, *Vibrational spectroscopy of aluminium nitride*. Journal of American Ceramic Society **76**(5), 1132 (1993).

[Mei06] J. Mei, S. Srinivasan, R. Liu, F. A. Ponce, Y. Narukawa, and T. Mukai, *Prismatic stacking faults in epitaxially laterally overgrown GaN*. Applied Physics Letters **88**(14), 141912 (2006).

[Mer96] C. Merz, M. Kunzer, U. Kaufmann, I. Akasaki, and H. Amano, *Free and bound excitons in thin wurtzite GaN layers on sapphire*. Semiconductor Science Technology **11**(5), 712 (1996).

[MG02] E. Martinez-Guerrero, *Elaboration en épitaxie par jets moléculaires des nitrures d'éléments III en phase cubique*. Ph.D. thesis, Université Joseph Fourier - Grenoble 1 (2002).

[Mon04a] E. Monroy, T. Andreev, P. Holliger, E. Bellet-Amalric, T. Shibata, M. Tanaka, and B. Daudin, *Modification of GaN(0001) growth kinetics by Mg-doping*. Applied Physics Letter **84**(14), 2554 (2004).

[Mon04b] E. Monroy, E. Sarigiannidou, F. Fossard, N. Gogneau, E. Bellet-Amalric, J.-L. Rouvière, S. Monnoye, H. Mank, and B. Daudin, *Growth kinetics of N-face polarity GaN by plasma-assisted molecular-beam epitaxy*. Applied Physics Letter **84**, 3684 (2004).

[Mon09] B. Monemar, P. P. Paskov, G. Pozina, C. Hemmingsson, J. P. Bergman, T. Kawashima, H. Amano, I. Akasaki, T. Paskova, S. Figge, D. Hommel,

and A. Usui, *Evidence for Two Mg Related Acceptors in GaN*. Physical Review Letters **102**(23), 235501 (2009).

[Mor94] H. Morkoç, S. Strite, G. B. Gao, M. E. Lin, B. Sverdlov, and M. Burns, *Large-band-gap SiC, III-V nitride, and II-VI ZnSe-based semiconductor device technologies*. Journal of Applied Physics **76**(3), 1363 (1994).

[Nak97] S. Nakamura, M. Senoh, S.-I. Nagahama, N. Iwasa, T. Yamada, T. Matsushita, Y. Sugimoto, and H. Kiyoku, *Room temperature continuous-wave operation of InGaN multi-quantum-well-structure laser diodes with a long lifetime*. Applied Physics Letter **70**, 868 (1997).

[Nea83] J. H. Neave, B. A. Joyce, P. J. Dobson, and N. Norton, *Dynamics of film growth of GaAs by MBE from RHEED observations*. Appl. Phys. A **31**(1), 1 (1983).

[Neu03] J. Neugebauer, T. Zywietz, M. Scheffler, J. E. Northrup, H. Chen, and R. M. Feenstra, *Adatom Kinetics On and Below the Surface: The Existence of a New Diffusion Channel*. Physical Review Letter **90**, 056101 (2003).

[Ng02] H. M. Ng, *Molecular beam epitaxy of GaN/$Al_xGa_{1-x}N$ multiple quantum wells on r-plane ($10\bar{1}2$) sapphire substrates.* Applied Physics Letter **80**, 4369 (2002).

[Ni07] X. Ni, . Özgür, A. A. Baski, H. Morkoç, L. Zhou, D. J. Smith, and C. A. Tran, *Epitaxial lateral overgrowth of ($11\bar{2}2$) semipolar GaN on ($1\bar{1}00$) m-sapphire by metalorganic vapor deposition*. Applied Physics Letter **90** (2007).

[Nis06] A. Nishikawa, K. Kumakura, and T. Makimoto, *High breakdown voltage with low on-state resistance of p-InGaN/n-GaN vertical conducting diodes on n-GaN substrates.* Applied Physics Letter **89**, 153509 (2006).

[Nor00] J. E. Northrup, J. Neugebauer, R. M. Feenstra, and A. R. Smith, *Study of GaN(0001): the laterally contracted Ga bilayer.* Physical Review B **51**, 9932 (2000).

[Och99] T. J. Ochalski, B. Gil, P. Lefebvre, N. Grandjean, J. Massies, S. Nakamura, and H. Morkoç, *Photoreflectance investigations of the bowing parameter in AlGaN allows lattice-matched to GaN*. Applied Physics Letter **74**, 3353 (1999).

[Ono02] N. Onojima, J. Suda, and H. Matsunami, *Growth of AlN ($11\bar{2}0$)) on 6H-SiC ($11\bar{2}0$) by Molecular-Beam Epitaxy.* Japanese Journal of Applied Physics **41**, L1348 (2002).

[Onu04] T. Onuma, S. F. Chichibu, , A. Uedono, T. Sota, P. Cantu, T. M. Katona, J. F. Keading, S. Keller, U. K. Mishra, S. Nakamura, and S. P. DenBaars, *Radiative and nonradiative processes in strain-free $Al_xIn_{1-x}N$ films studied by time-resolved photoluminescence and positron annihilation techniques*. Journal of Applied Physics **95**(5), 2495 (2004).

[Pan75] J. L. Pankove, S. Bloom, and G. Harbeke, *Optical properties of GaN*. RCA Review **36**, 163 (1975).

[Par00] S. H. Park, *Crystal Orientation Effects on Electronic Properties of Wurtzite GaN/AlGaN Quantum Wells with Spontaneous and Piezoelectric Polarization*. Japanese Journal of Applied Physics **39**, 3478 (2000).

[Per96] P. Perlin, E. Litwin-Staszewska, B. Suchanek, W. Knap, J. Camassel, T. Suski, R. Piotrzkowski, S. Grzegory, E. Porowski, E. Kaminska, and J. C. Chervin, *Determination of the effective mass of GaN from infrared reflectivity and Hall effect*. Applied Physics Letter **68**(8), 1114 (1996).

[Per98] W. G. Perry, M. B. Bremser, T. Zheleva, K. J. Linthicum, and R. F. Davis, *Biaxial strain in AlxGa1-xN/GaN layers deposited on 6H-SiC*. Thin Solid Films **324**(1-2), 107 (1998).

[Pez04] S. Pezzagna, P. Vennéguès, N. Grandjean, and J. Massies, *Polarity inversion of GaN(0001) by a high Mg doping*. Journal of Crystal Growth **259**, 69 (2004).

[Pon96] F. A. Ponce, D. Cherns, W. T. Young, and J. W. Steeds, *Characterization of dislocations in GaN by transmission electron diffraction and microscopy techniques*. Applied Physics Letters **69**(6), 770 (1996).

[Pta01] A. J. Ptak, T. H. Myers, L. T. Romano, C. G. V. de Walle, and J. E. Northrup, *Magnesium incorporation in GaN grown by molecular-beam epitaxy*. Applied Physics Letters **78**(3), 285 (2001).

[Pug99] S. K. Pugh, D. J. Dugdale, S. Brand, and R. A. Abra, *Electronic structure calculations on nitride semiconductors*. Semiconductor Science Technology **14**(23), 631 (1999).

[Ram99] V. Ramachandran, R. M. Feenstra, W. L. Sarney, L. Salamanca-Riba, J. E. Northrup, L. T. Romano, and D. W. Greve, *Inversion of wurtzite GaN(0001) by exposure to magnesium*. Applied Physics Letters **75**(6), 808 (1999).

[Res05] M. A. Reshchikov and H. Morkoç, *Luminescence properties of defects in GaN*. Journal of Applied Physics **97**, 061301 (2005).

[Rez06] B. Rezaei, A. Asgari, and M. Kalafi, *Electronic band structure pseudopotential calculation of wurtzite III-nitride materials*. Physica B **371**, 107 (2006).

[Rin08] P. Rinke, M. Winkelnkemper, A. Qteish, D. Bimberg, J. Neugebaeur, and M. Scheffler, *Consistent set of band parameters for the group-III nitrides AlN, GaN, and InN*. Physical Review B **77**, 075202 (2008).

[Rom06] A. E. Romanov, T. J. Baker, S. Nakamura, and J. S. Speck, *Strain-induced polarization in wurtzite III-nitride semipolar layers*. Journal of Applied Physics **100**, 023522 (2006).

[Ros02] A. L. Rosa, J. Neugebauer, J. E. Northrup, C.-D. Lee, and R. M. Feenstra, *Adsorption and incorporation of silicon at GaN(0001) surfaces*. Applied Physics Letters **80**(11), 2008 (2002).

[Rou98] J. Rouvière, J. Weyher, M. Seelman-Eggebert, and S. Porowski, *Polarity determination for GaN films grown on (0001) sapphire and high-pressure-grown GaN single crystal*. Applied Physics Letter **73**, 668 (1998).

[Sal95] A. Salvador, G. Liu, W. Kim, O. Aktas, A. Botchakarev, and H. Morkoç, *Properties of a Si-doped GaN/AlGaN quantum well*. Applied Physics Letter **67**(22), 3322 (1995).

[Sal99] G. Salviati, M. Albrecht, C. Zanotti-Fregonara, N. Armani, M. Mayer, Y. Shereter, M. Guzzi, Y. V. Melnik, K. Vassilevski, V. A. Dmitriev, and H. P. Strunk, *Cathodoluminescence and Transmission Electron Microscopy Study of the Influence of Crystal Defects on Optical Transitions in GaN*. Physica Status Solidi (a) **171**, 325 (1999).

[Sem01] F. Semond, P. Lorenzini, N. Grandjean, and J. Massies, *High-electron-mobility AlGaN/GaN heterostructures grown on Si(111) by molecular-beam epitaxy*. Applied Physics Letters **78**(3), 335 (2001).

[Sem07a] C. Semiconductor, *Audi*. Compound Semiconductor (2007).

[Sem07b] C. Semiconductor, *PS3 is now in full production, says Sony*. Compound Semiconductor (2007).

[Sha98] W. Shan, J. W. A. III, K. M. Wu, W. Walukiewicz, E. E. Haller, M. C. Martin, W. R. McKinney, and W. Yang, *Dependence of the fundamental band gap of Al_xGa_{1-x}, N on alloy composition and pressure*. Applied Physics Letter **84**, 4452 (1998).

[Shi97] A. Shikanai, T. Azuhata, T. Sota, S. Chichibu, A. Kuramata, K. Horino, and S. Nakamura, *Biaxial strain dependence of exciton resonance energies in wurtzite GaN*. Journal of Applied Physics **81**, 417 (1997).

[Sim03] J. Simon, N. Pelekanos, C. Adelmann, E. Guerrero, R. André, B. Daudin, L. Dang, and H. Mariette, *Direct comparison of recombinaison dynamics in cubic and hexagonal GaN/AlN quantum dots*. Physical Review B **68**, 035312 (2003).

[Str38] I. N. Stranski and L. V. Krastanow, *Zur Theorie der orientation Ausscheidung von Ionenkristallen aufeinander*. Math.-Naturwiss. K1 Abt. IIb **146**(797) (1938).

[Sug98] T. Sugahara, H. Sato, M. Hao, Y. Naoi, S. Kurai, S. Tottori, K. Ymashita, K. Nishimo, L. T. Romano, and S. Sakai, *Direct evidence that dislocations are non-radiative recombination centers in GaN*. Japanese Journal of Applied Physics **37**(L398) (1998).

[Sun99] X. L. Sun, H. Yang, L. X. Zheng, D. P. Xu, J. B. Li, Y. T. Wang, G. H. Li, and Z. G. Wang, *Stability investigation of cubic GaN films grown by metalorganic chemical vapor deposition on GaAs (001)*. Applied Physics Letters **74**(19), 2827 (1999).

[Tak00] T. Takeuchi and H. A. I. Akasaki, *Theoretical study of orientation dependence of piezoelectric effects in wurtzite strained GaInN/GaN heterostructures and quantum wells.* Japanese Journal of Applied Physics **39**, 413 (2000).

[Tch06] M. Tchernycheva, L. Nevou, L. Doyennette, F. H. Julien, E. Warde, E. Monroy, E. Bellet-Amalric, T. Remmele, and M. Albrecht, *Systematic experimental and theoretical investigation of intersubband absorption in GaN/AlN quantum wells*. Physical Review B **73**, 125347 (2006).

[Tri99] S. Tripathy, R. K. Soni, H. Asahi, K. Iwata, R. Kuroiwa, K. Asami, and S. Gonda, *Optical properties of GaN layers grown on C-, A-, R-, and M-plane sapphire substrates by gas source molecular beam epitaxy*. Journal of Applied Physics **85**(12), 8386 (1999).

[Tya07] H. Z. Tyagi, R. B. Chung, D. F. Feezel, M. Saito, K. Fujito, J. S. Speck, S. P. Denbaars, and S. Nakamura, *Semipolar ($10\bar{1}\bar{1}$) InGaN/GaN laser diodes on bulk GaN substrates*. Japanese Journal of Applied Physics **46**, L444 (2007).

[Ued06] M. Ueda, K. Kojima, M. Funato, Y. Kawakami, Y. Nakamura, and T. Mukai, *Epitaxial growth and optical properties of semipolar ($11\bar{2}2$) GaN and InGaN/GaN quantum wells on GaN bulk substrates*. Applied Physics Letter **89**, 21 (2006).

[Ven07] P. Vennéguès, Z.Bougrioua, and T. Guehne, *Microstructural Characterization of Semipolar GaN Templates and Epitaxial-Lateral-Overgrown*

Films Deposited on M-Plane Sapphire by Metalorganic Vapor Phase Epitaxy. Japanese Journal of Applied Physics **46**, 4089 (2007).

[Vol26] M. Volmer and A. Weber, *Keimbildung in übersättigten Gebilden*. Z. Phys. Chem. **119**(277) (1926).

[Vur01] I. Vurgaftman, J. R. Meyer, and L. R. Ram-Mohan, *Band parameters for III-V compound semiconductors and their alloys*. Journal of Applied Physics **89**(11), 8815 (2001).

[Vur03] I. Vurgaftman and J. R. Meyer, *Band parameters for nitrogen-containing semiconductors*. Journal of Applied Physics **94**, 3675 (2003).

[Wal00] P. Waltereit, O. Brandt, A. Trampert, H. T. Grahn, J. Menniger, M. Ramsteiner, M. Reiche, and K. H. Ploog, *Nitride semiconductors free of electrostatic fields for efficient white light-emitting diodes*. Nature **406**, 865 (2000).

[Wal04] W. Walukievicz, S. X. Li, J. Wu, K. M. Yu, J. W. Ager, E. E. Haller, H. Lu, and W. J. Schaff, *Optical properties and electronic structure of InN and In-rich group III-nitride alloys*. Journal of Crystal Growth **269**, 119 (2004).

[Wan04] X. Wang and A. Yoshikawa, *Molecular beam epitaxy growth of GaN, AlN and InN*. Progress in Crystal Growth and Characterization of Materials **48**, 42 (2004).

[Wer08] T. Wernicke, C. Netzel, M. Weyers, and M. Kneissl, *Semipolar GaN grown on m-plane sapphire using MOVPE*. Physica Status Solidi (c) **5**(6), 1815 (2008).

[Wie94] R. Wiesendanger, *Scanning probe microscopy and spectroscopy* (Cambridge Univ. Press, 1994).

[Wri97] A. F. Wright, *Elastic properties of zinc-blende and wurtzite AlN, GaN and InN*. Journal of Applied Physics **82**, 6 (1997).

[Wu96] X. H. Wu, P. Fini, S. Keller, E. J. Tarsa, B. Heying, U. K. Mishra, S. P. DenBaars, and J. S. Speck, *Morphological and Structural Transitions in GaN Films Grown on Sapphire by Metal-Organic Chemical Vapor Deposition*. Japanese Journal of Applied Physics **35**(Part 2, No. 12B), L1648 (1996).

[Wu03] J. Wu, W. Walukiewicz, K. M. Yu, J. W. Ager, S. X. Li, E. E. Haller, H. Lu, and W. J. Schaff, *Universal bandgap bowing in group-III nitride alloys*. Solid State Communications **127**(6), 411 (2003).

[Wun07] T. Wunderer, P. Brückner, J. Hertkorn, F. Scholz, G. J. Beirne, M. Jetter, P. Michler, M. Feneberg, and K. Thonke, *Time- and locally resolved photoluminescence of semipolar GaInN/GaN facet light emitting diodes*. Applied Physics Letter **90**, 171123 (2007).

[Yam97] M. Yamaguchi, T. Yagi, T. Azuhata, T. Sota, K. Suzuki, S. Chichibu, and S. Nakamura, *Brillouin scattering study of gallium nitride: elastic stiffness constants*. Journal of Physics D: Condensed Matter **Matter 9**(1), 241 (1997).

[Yeh92] C.-Y. Yeh, Z. W. Lu, S. Froyen, and A. Zunger, *Zinc-blende–,wurtzite polytypism in semiconductors*. Physical Review B **46**(16), 10086 (1992).

[Yos75] S. Yoshida, S. Misawa, and A. Itoh, *Epitaxial growth of aluminium nitride films on sapphire by reactive evaporation*. Applied Physics Letter **26**, 461 (1975).

Glossary

You will find here the list of the abbreviations used in this manuscript.

AFM - Atomic Force Microscopy

BSF - Basal Stacking Fault

CBED - Convergent Beam Electron Diffraction

CCD - Charge-Couple Device

EJM - Epitaxie par Jets Moléculaires

FWHM - Fell Width at Half Maximum

HEMT - High Electron Mobility Transistors

HRTEM - High-Resolution Transmission Electron Microscopy

HVPE - Hybrid Vapor Phase Epitaxy

ISB - Intersubband

LED - Luminescent Emitting Diode

LD - Laser Diode

MBE - Molecular Beam Epitaxy

ML - Monolayer

MOCVD - Metal-Organic Chemical Vapor Deposition

MOVPE - Metal-Organic Vapor Phase Epitaxy

MQD - Multiple Quantum Dot

MQW - Multiple Quantum Well

PAMBE - Plasma-Assisted Molecular Beam Epitaxy

PL - Photoluminescence

QCSE - Quantum Confined Stark Effect

QD - Quantum Dot

QW - Quantum Well

RF - Radio frequency

RHEED - Relection High-Energy Electron Diffraction

RMS - Root Mean Square

RS - Reciprocal Space

RSM - Reciprocal Space Map

SAED - Selected Area Electron Diffraction

SF - Stacking Fault

TD - Threading Dislocation

TEM - Transmission Electron Microscopy

TRPL - Time-Resolved Photoluminescence

XRD - X-Ray Diffraction

XTEM - Cross-section Transmission Electron Microscopy